RELATIONSHIP BETWEEN SYNAPTIC DYSFUNCTION AND DEGENERATION IN A RODENT MODEL OF DEMENTIA

Submitted by **Soraya Meftah** to the University of Exeter

as a thesis for the degree of

Doctor of Philosophy in Medical Studies

In October 2020

This thesis is available for Library use on the understanding that it is copyright material and that no quotation from the thesis may be published without the proper acknowledgement.

I certify that all material in this thesis which is not my own work has been identified and that no material has previously been submitted and approved for the award of a degree by this or any other University.

Signature: 

Word Count: 62,392

ABSTRACT

Synaptic degeneration is currently the best biomarker correlate of cognitive decline in dementia. In the years prior to dementia onset, many neurophysiological changes are occurring hypothesised to preserve cognitive function, including alterations in synaptic and neuronal function. This thesis aims to characterise the early synaptic and neurophysiological alterations occurring in a mouse model of tauopathy-driven neurodegeneration (rTg4510). This work was performed in the somatosensory cortex, a well characterised region of the brain in the mouse, which serves as a prototypical model of the neocortex.

The work presented in Chapters two and three revealed alterations in synaptic glutamatergic receptor function (reduced NMDA:AMPA receptor ratio) and intrinsic neuronal properties in prodromal tauopathy in rTg4510 mice, using in vitro whole-cell patch clamp electrophysiology. Increased dendritic branching proximal to the soma was seen in these recorded neurons following post hoc imaging of their structure. In more advanced stages of tauopathy, reductions in putative AMPA receptor-mediated spontaneous synaptic activity was observed. Significant reductions in glutamatergic receptor expression and synaptic markers was detected in both prodromal and more advanced tauopathy, quantified from isolated synaptosomes.

To characterise how glutamatergic receptor dysfunction manifested in vivo, recording paradigms were optimised for in vivo two-photon targeted whole-cell patch clamp electrophysiology, outlined in Chapter four. This technique was used to simultaneously record subthreshold synaptic properties, network activity, and evoked synaptic responses in the rTg4510 model in early neurodegeneration in Chapter five. Whilst spontaneous network activity was similar between genotypes, there was an observable increase in the fast peak response of evoked activity.

This work suggests that synaptic dysfunction is a feature of both prodromal and advanced tauopathy, with different functional and biochemical correlates manifesting at different stages of disease progression. Further characterisation of these processes, and how this contributes to symptomatic decline, can provide a basis to develop novel therapeutic strategies to alleviate tau-mediated synaptic and neuronal dysfunction prior to widespread cell loss.

ACKNOWLEDGEMENTS

None of this work would have been possible without the invaluable support and guidance from my supervisors: Jon Brown, Jon Witton & Mike Ashby. You have all been wonderful supervisors and have each supported my PhD in your own unique way. Thank you for your scientific guidance, help and expertise throughout my PhD, and the many conversations about science and everything else. I am very grateful to you all, you have all pushed me to be a better scientist and made my PhD experience an enjoyable and interesting one.

I would like to acknowledge my funders (MRC GW4 Biomed DTP) for my studentship and the MRC NPIF, ARUK and BNA for additional funding support during my PhD. My research was only possible with the use of animals, so I would like to acknowledge the mice that were used to form my research.

I want to thank all who supported me in Exeter, in particular the Hatherly lab groups who were a wonderful and interesting group of people (special thanks to Francesco and Tom for occasionally dealing with my mice, to Lydia for always feeding me and for letting me stay when I was in-between homes (and Francesco again too)). This also includes my postgrad/pub quiz group & Exe Hockey Club for keeping things light in times of stress. To Mark, thanks for helping me start this journey and for your support beforehand, and for moving with me to Exeter so I could start my PhD. I really appreciate it.

Part of the “joys” of a multi-university programme was splitting my time between Exeter and Bristol. However, I’m very glad this was the case, and thanks to everyone that made my Bristol experience so wonderful. Specifically, a big thanks to the MAshby lab who made it a great environment to work in. As part of this I’d like to thank Jon Witton again separately, for your help in setting up the equipment and sitting through multiple surgeries with me. The work I performed in Bristol would have been very limited without your help! And of course, I couldn’t go without mentioning PPN+/Cheese & Hoodies & the Robin Hood for the intellectual(?) discussions on Friday nights. Thanks also to Firebrands Hockey Club (with a special mention to Leeya, one of the best housemates anyone could ask for).

During my PhD, I was also fortunate enough to have the opportunity to work in multiple labs. Thanks to the Poulet lab for hosting me for two weeks in Berlin, and Jean-Seb Jouhanneau & Leiron Ferrarese for teaching me how to *in vivo* patch. In addition, I had the pleasure of spending 4 months at Eli Lilly. Thanks Suchira & Mike O for helping make that possible, Annalisa for my day to day supervision in the lab, and the Bose lab, Histo lab and the Biology dept for making my visit enjoyable and productive.

Thanks to my friends for their support, especially the poo emoji queens, the A team (extended) with a special mention to Kam for letting me stay during my placement, my Surrey crew (with a special mention to Neil), & the Cool Cambridge Crew.

A special thanks to my mum, dad and brother for making me who I am today, for motivating me to work hard for things in life, and for your kindness, love, and support. I hope I have made you proud. Also, thanks to the rest of my family for their love and support. I know it was long and confusing for you to keep up with my plans and progress, but I am finished now!

I also want to un-acknowledge coronavirus. Thanks for making writing up my thesis and finishing my PhD an awful experience, but at least I can almost work productively from home now.

And lastly, Dr Darren Walsh, I'm sorry that during lockdown I was just constantly talking about figures and thesis progression. I am very glad I could share this whole journey with you. You have been my rock and my number 1 fan. You have helped shape my ideas, been my sounding board and pushed me to be better and more patient(!) as a person. Thanks pet. x

TABLE OF CONTENTS

TABLE OF FIGURES

TABLE OF TABLES

ABBREVIATIONS

3R	Three microtubule binding repeats
4R	Four microtubule binding repeats
µm	Micrometer
Aβ	Amyloid beta
aCSF	Artificial cerebrospinal fluid
AD	Alzheimer's disease
AIC	Akaike information criterion
AMPA	α-amino-3-hydroxy-5-methyl-4-isoxazolepropionic acid
AMPAR	α-amino-3-hydroxy-5-methyl-4-isoxazolepropionic acid receptor
ANOVA	Analysis of variance
AP	Action potential
APP	Amyloid precursor protein
ATP	Adenosine triphosphate
BB	Bottom band
CC	Current clamp
D-APV	D(−)-2-Amino-5-phosphonopentanoic acid
DOX	Doxycycline
EEG	Electroencephalogram
eEPSC	Evoked excitatory postsynaptic current
EPSC	Excitatory postsynaptic current
E	Exon
FTD	Frontotemporal dementia
FTDP-17	Frontotemporal dementia and parkinsonism linked to chromosome 17
GABA	γ-aminobutyric acid

Gabazine	6-Imino-3-(4-methoxyphenyl)-1(6H)-pyridazinebutanoic acid hydrobromide
GLMM	Generalised linear mixed model
H	Homogenate
Hz	Hertz
ICC	Interclass correlation coefficient
JPE	Junction potential error
kHz	Kilohertz
KO	Knock-out
L-689,560	trans-2-Carboxy-5,7-dichloro-4-phenylaminocarbonylamino-1,2,3,4-tetrahydroquinoline
LFP	Local field potential
LP	Lysed pellet
LTP	Long-term potentiation
M	Months
MAPT	Microtubule associated protein tau
MK801	(5S,10R)-(+)-5-Methyl-10,11-dihydro-5H-dibenzo[a,d]cyclohepten-5,10-imine maleate
mM	millimolar
mOsm	miliosmolarity
NFT	Neurofibrillary tangles
NMDA	*N*-Methyl-d-aspartate
NMDAR	*N*-Methyl-d-aspartate receptor
P	Pellet
PB	Phosphate buffer
PBS	Phosphate buffered saline

PBS-T	Phosphate buffered saline with tween
PFA	Paraformaldehyde
POm	Medial posterior thalamic nuclear group
PSD	Post-synaptic density
PSP	Post-synaptic potential
REM	Rapid eye movement
R_i	Input resistance
RMP	Resting membrane potential
RMS	Root mean square
rTg4510	Regulatable Transgene 4510
S	Supernatant
S1	Primary somatosensory
SEM	Standard error of the mean
sEPSC	Spontaneous excitatory postsynaptic current
SWS	Slow-wave sleep
Syn	Synaptic fraction
TB	Top band
TG	rTg4510
ThioS	Thioflavin-S
VC	Voltage clamp
V_m	Membrane potential
VPM	Ventral posterior medial nucleus of the thalamus
WT	Wildtype

1 GENERAL INTRODUCTION

1.1 DEMENTIA

Dementia is a clinical syndrome, characterised by substantial deterioration of one or more cognitive domains such as a decline in executive function, learning and memory, and social cognition (American Psychiatric Association, 2013; Hugo and Ganguli, 2014). There are an estimated 50 million cases worldwide, projected to increase to 152 million cases by 2050 (Alzheimer's Association, 2020; Prince, 2015). It was the 5th leading cause of death in the world in 2016 and causes unprecedented socioeconomic impact, with an estimated cost to society of £26 billion a year in the UK alone (Alzheimer's Association, 2020; Prince, 2015; Prince et al., 2013, 2014).

The biggest cause of dementia is Alzheimer's disease (AD) which accounts for 60-80% of cases (Alzheimer's Association, 2020). There are however, multiple other forms of dementia including but not limited to: vascular dementia, dementia with Lewy bodies, frontotemporal dementia (FTD) (Bang et al., 2015; O'Brien and Thomas, 2015; Walker et al., 2015). A common pathological feature of dementias, which are typically caused by neurodegenerative diseases, is the association with abnormal aggregation of a subset of proteins in the brain which can be used to confirm diagnosis post-mortem (Irvine et al., 2008; Lovestone and McLoughlin, 2002).

1.1.1 Alzheimer's Disease

AD is a progressive neurodegenerative disease which affects approximately 1 in 3 people over the age of 65 (Alzheimer's Association, 2020; Herrup, 2015; Prince et al., 2014). The majority of cases (~99%) of AD are sporadic, with the greatest risk factor for AD being advanced age. The remainder are familial forms of AD (~1%) that are associated with genetic mutations in the amyloid precursor protein (APP) gene, and those that influence APP processing and cleavage (*PSEN1/PSEN2*) (Chartier-Harlin et al., 1991; Goate et al., 1991; Murrell et al., 1991; Randall et al., 2010; Tanzi and Bertram, 2005). The discovery of causal genetic mutations in the *APP* gene, led to the idea that amyloid was crucial in AD pathogenesis (St. George-Hyslop et al., 1987; Glenner and Wong, 1984; Levy et al., 1990; Tanzi and Bertram, 2005). This idea influenced the amyloid cascade hypothesis, which proposed that amyloid aggregation and deposition in the brain

was a causative pathological driver of AD, with the ensuing pathological cascade formed as a direct consequence of this deposition (Hardy and Higgins, 1992). Whilst a lot of research and disease modifying treatments have focussed on this hypothesis, targeting amyloid deposition, no effective therapeutics have been discovered to date (Hardy and Higgins, 1992; Herrup, 2015; Karran et al., 2011).

AD has two core neuropathological hallmarks, amyloid plaques and neurofibrillary tangles (NFTs) (Alzheimer, 1911). These neuropathologies are evident early in the pathological timeline of the disease, and accumulate in a stereotypical and progressive fashion (Alzheimer, 1911; Braak and Braak, 1991; Montine et al., 2012; Figure 1.1). Amyloid protein aggregates, known as amyloid plaques, accumulate within the brain approximately 10-15 years prior to symptomatic onset (Jack Jr et al., 2009; Villemagne et al., 2013; Figure 1.1). The second neuropathological hallmark are NFTs, formed of aggregated tau proteins, which is common to multiple dementias known as tauopathies (Braak et al., 2011; Grundke-Iqbal et al., 1986). The emergence of NFTs in the brain occurs 3-5 years prior to symptomatic onset, and this correlates well with synaptic and neuro-degeneration in AD and other dementia spectrum diseases (Bejanin et al., 2017; Vogel et al., 2020; Figure 1.1). The role of tau in the pathogenesis of AD has been emphasised within the past 10 years, with significant evidence now suggesting that tau accumulation is a key pathological driver of AD and other tauopathies (Busche et al., 2019; DeVos et al., 2018; Iqbal et al., 2010; Ittner and Götz, 2011; Kopeikina et al., 2012; Lao et al., 2019; Wang et al., 2011).

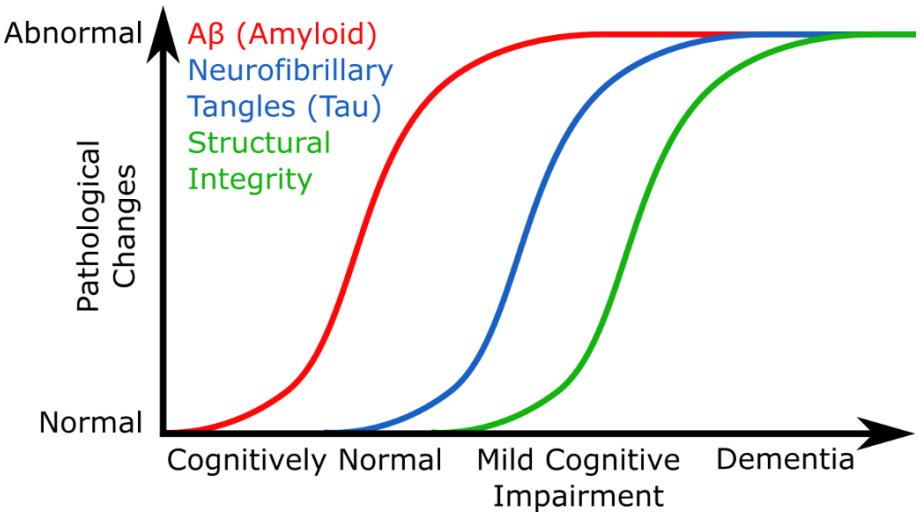

Figure 1.1 Alzheimer's disease: A timeline of the onset of pathological changes and progression within the brain. Lines represent the state of pathological changes that occur within the brain (y-axis) with symptomatic impairment denoted on the x-axis. Amyloid pathology appears early in the brain (10-15 years prior to symptomatic onset), denoted as a red line. Tau pathology is next detectable (3-5 years prior to symptomatic onset), denoted as a blue line. Structural changes such as synaptic and neuro- degeneration occur in parallel with cognitive impairment, denoted as a green line. Adapted from *Jack et al., 2010.*

1.1.2 Tauopathies

Tauopathies are a group of neurodegenerative diseases characterised by abnormal tau protein inclusions within neurons or glia (Kovacs, 2015; Orr et al., 2017). Familial forms of tauopathy are caused by mutations within the microtubule associated protein tau (*MAPT)* gene, which encodes the tau protein (Hutton et al., 1998; Poorkaj et al., 1998; Spillantini et al., 1998). One form of familial tauopathy, frontotemporal dementia and parkinsonism linked to chromosome 17 (FTDP-17), presents with severe behavioural deficits, dementia, and is accompanied by a parkinsonian syndrome (Foster et al., 1997). Brain autopsies performed on these patients revealed frontotemporal atrophy with the presence of tau inclusions (Foster et al., 1997). Causal missense mutations, such as the P301L mutation, were identified within the *MAPT* gene in FTDP-17 (Hutton, 2001; Hutton et al., 1998; Wilhelmsen et al., 1994). This indicated that mutations in the *MAPT* gene were sufficient to cause the formation of tau inclusions and neurodegeneration (Goedert and Jakes, 2005). However, how tau

pathology influences neurophysiological dysfunction, and synaptic and neuro-degeneration, is still a vital unanswered question in dementia research.

1.1.3 Tau

Tau is one of the major microtubule-associated proteins, encoded by the *MAPT* gene on chromosome 17 (Barbier et al., 2019; Weingarten et al., 1975). Six tau isoforms are detectable in the adult human brain, generated from alternate splicing of exon (E) 2, E3, and E10 regions of *MAPT* (Andreadis, 2005; Andreadis et al., 1992; Goedert et al., 1989). Alternate splicing of E10 results in tau isoforms which contain three (3R) or four microtubule binding repeats (4R), with differential and balanced expression of these two groups of isoforms found in normal physiology (D'Souza and Schellenberg, 2005; Liu and Gong, 2008). Dysregulation of balanced 3R/4R isoform expression has been implicated as a pathogenic mechanism in several tauopathies (D'Souza and Schellenberg, 2005; Liu and Gong, 2008).

1.1.3.1 The physiological function of tau

Tau is predominantly expressed in the axons of neurons following maturation, with some expression in other non-neuronal subtypes including oligodendocytes (Binder et al., 1985; Lopresti, 2002; Lopresti et al., 1995). The main physiological function of the tau protein is the stabilisation of microtubule bundles in axons (Barbier et al., 2019; Black et al., 1996; Weingarten et al., 1975; Witman et al., 1976). However, recent work has found that endogenous tau is also present in dendrites and dendritic spines, and interacts with PSD95 at post-synaptic sites (Mondragón-Rodríguez et al., 2012; Xia et al., 2015). Endogenous tau may therefore facilitate normal synaptic function. For example, there is evidence that tau participates in structural reorganisation of dendritic spines following synaptic plasticity (Chen et al., 2012; Frandemiche et al., 2014). This suggests that tau plays diverse physiological roles in both axonal and dendritic neuronal compartments, and is directly involved in normal synaptic physiology.

1.1.3.2 Tau pathology

The degree by which tau promotes microtubule assembly and stability in normal physiological conditions is regulated by post translational modifications such as phosphorylation (Binder et al., 1985; Lindwall and Cole, 1984; Mandelkow et al., 1995). Tau phosphorylation promotes the dissociation of tau from microtubules, and abnormal hyperphosphorylation is thought of as an early event in tauopathies

as a precursor to the accumulation of tau aggregates (Alonso et al., 1994; Iqbal et al., 2005; Kopke et al., 1993; Lindwall and Cole, 1984). Abnormal hyperphosphorylation is also thought to promote the mislocalisation of the tau protein, with these hyperphosphorylated tau species found missorted to the somatodendritic compartment including within synapses (Hoover et al., 2010; Sohn et al., 2016).

Following abnormal hyperphosphorylation, tau undergoes conformational changes prior to self-assembly into insoluble filaments (Serrano-Pozo et al., 2011). These filaments eventually aggregate together to form NFTs (Serrano-Pozo et al., 2011). Markers are used to determine the stage of tau pathology, with antibodies such as AT-8 targeting hyperphosphorylation of specific tau epitopes, and MC-1 detecting a conformational change in the structure of tau equivalent to an early pre-NFT stage (Goedert et al., 1995; Jicha et al., 1997). For the more mature, fibrillar NFTs, Thioflavin-S (ThioS) can be used to detect the β-pleated sheet structure of filaments or silver impregnation methods such as the Gallyas technique can be used for the argyrophilic inclusions (Braak and Braak, 1991; Braak et al., 2006; Serrano-Pozo et al., 2011). The different stages of tau pathology from early pre-NFT pathology to mature and fibrillar NFTs are thought to play different roles in the pathophysiology of tauopathies (Brunello et al., 2020; Dujardin et al., 2018; Spires-Jones et al., 2009).

1.1.4 Animal models of dementia

Historically, the most commonly used experimental models of dementia are transgenic mice that overexpress familial disease-associated mutations, which leads to the development of neuropathological inclusions seen in the disease (LaFerla and Green, 2012; Mullane and Williams, 2019). The generation of tauopathy models, typically by the expression of tau mutations, develop NFTs with associated neuronal dysfunction and degeneration (Götz and Ittner, 2008). These models also recapitulate other aspects of tauopathies such as neuroinflammation and synapse loss (Götz and Ittner, 2008).

However, these models suffer from random integration of the transgene, either with inappropriate transgene disruption following insertion, overexpression effects, or other artificial phenotypes (Gamache et al., 2019; Goodwin et al., 2017). This has led to difficulties in concluding whether the various phenotypes observed are related to the emergence of pathology. Knock-in models have

become the focus for the next generation of models, which express the transgene in a targeted manner to attempt to produce a more physiologically relevant model with less artifacts (Saito et al., 2014, 2019). Some of these newer models show limited disease phenotypes and so irrespective of artifact, the model should be chosen that best fits the experimental hypothesis and disease state in question.

1.1.4.1 Mouse models of tauopathy

Recapitulating tauopathy in mice is not simple as adult mice only express the 4R isoform of tau, compared to balanced 3R/4R expression found in humans. Interestingly, overexpression of all six isoforms of human tau in mice lacking mouse tau (knock-out (KO) for mouse tau) leads to the formation of pre-NFT tau pathology (Andorfer et al., 2003). Overexpression of mutations from familial tauopathies develop more mature NFT pathology and neurodegeneration. For example, the P301S mouse model overexpresses the P301S mutation found in FTDP-17, and develops progressive age-associated tau pathology and neurodegeneration (Allen et al., 2002). A novel tauopathy model, the tau knock-in model, has attempted to overcome some of the mutant overexpression issues by direct and targeted replacement of the *MAPT* mouse gene with the human variant which is expressed at physiological concentrations (Saito et al., 2019).

Other tauopathy models have been generated by infusing pathological species of tau into the mouse brain, to investigate the transsynaptic spread of tau (Ahmed et al., 2014; Clavaguera et al., 2013; Falcon et al., 2015). Whilst these models have been informative on the mechanisms of propagation of tau pathology, these models tend not to develop insoluble NFTs, and the pathology within these models is insufficient to induce neurodegeneration (Götz et al., 2018).

1.1.4.2 The rTg4510 model of tauopathy

The model used for the work in this thesis was the rTg4510 mouse model of tauopathy, generated in 2005 (Ramsden et al., 2005; SantaCruz et al., 2005). This bitransgenic model is generated by the crossing of two genetically modified mouse lines. The responder 4510 line carries a tetracycline operon-responsive element upstream of cDNA with encodes mutant human $MAPT^{P301L}$ on an FVB/NJ background. This is crossed with an activator line which expresses a tetracycline-controlled transactivator under the control of the calcium (Ca^{2+})/calmodulin kinase II α promoter on a 129S6 background. This leads to forebrain restricted transgene expression which can be repressed with

doxycycline treatment (Bailey et al., 2014; Blackmore et al., 2017; Ramsden et al., 2005; SantaCruz et al., 2005). Mutant transgene overexpression can be up to 13x the amount compared to typical murine tau expression (Ramsden et al., 2005; SantaCruz et al., 2005). Recently, it was suggested that transgene insertion lead to insertion deletion artifacts at the site of insertion, disrupting a number of genes important for synaptic and neuronal development (Gamache et al., 2019; Goodwin et al., 2017). However, in comparison with other models including the more recent knock-in models, the rTg4510 model develops a robust and rapid neurodegenerative phenotype associated with tau pathology development. Therefore, for the experimental hypothesis tested within this thesis, this model better recapitulates some of the key aspects of interest. However, with the limitations of the model, conclusions drawn should be interpreted cautiously, with the appropriate transgene controls used when possible.

The rTg4510 mouse model recapitulates some of the key neuropathological aspects of tauopathies including the manifestation of progressive age-associated tau pathology and neurodegeneration. Hyperphosphorylated tau is detectable from ~2.5 months of age, progressing to more mature NFTs at around 4-6 months of age (Blackmore et al., 2017; Ramsden et al., 2005; SantaCruz et al., 2005; Spires et al., 2006; Figure 1.2 A). One key feature of this model is the appearance of progressive and dramatic neurodegeneration which occurs between 6-7 months (Ramsden et al., 2005; SantaCruz et al., 2005; Spires et al., 2006; Figure 1.2 B), which is not seen in many other models of tauopathy. Interestingly, the pathological tau burden and neurodegeneration develop heterogeneously throughout the forebrain, with phenotypes emerging later in the cortex than in the hippocampus (Blackmore et al., 2017; Harrison et al., 2020; Ramsden et al., 2005; SantaCruz et al., 2005). Therefore, this model can provide invaluable information on the pathological relationship between tauopathy and neurodegeneration.

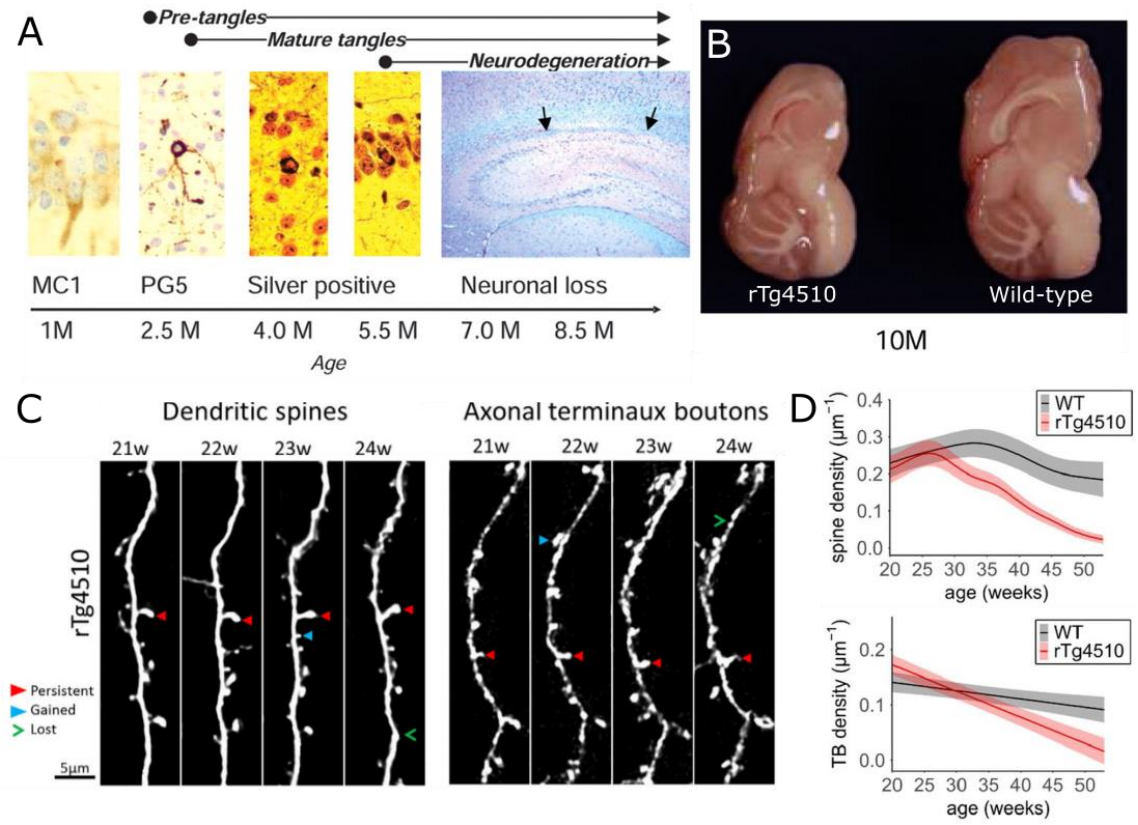

Figure 1.2 The rTg4510 mouse model of tauopathy. A pathological timeline across ages in the rTg4510 model is shown in panel **A**, marking the age of detection of different tau pathologies and neurodegeneration onset. A photograph of the gross anatomy of the brain is shown in **B**, demonstrating the severe neurodegeneration seen at 10 months in the forebrain in comparison to a wild-type mouse brain at the same age. Two-photon images show the progressive loss of dendritic spines and axonal terminal boutons seen in the model (**C**), quantified with age (**D**). Abbreviations: M = months, W = weeks. *Figure **A** & **B** is adapted from SantaCruz et al., 2005, Figure **C** is adapted from Jackson et al., 2017, Figure **D** is adapted from Jackson et al., 2020.*

Alongside the development of pathology, neurophysiological dysfunction is evident in the rTg4510 model. There was a reduction in network activity (measured by imaging spontaneous Ca^{2+} transients) and changes in neuronal excitability (measured using whole-cell electrophysiology) prior to neurodegeneration in the rTg4510 model, suggesting that tau overexpression alone can alter neurophysiological function (Busche et al., 2019; Crimins et al., 2012; Hatch et al., 2017; Jackson et al., 2017; Menkes-Caspi et al., 2015). Interestingly, some functional domains, such as visual processing in the visual cortex, were preserved following neurodegeneration onset (Kuchibhotla et al.,

2014). This implies that some pathways may be more resilient to the pathophysiological changes occurring in tauopathy and neurodegeneration.

In addition, there are demonstratable alterations in synapse number, function, and structural plasticity in the rTg4510 model. Specifically, synapse density was decreased in early neurodegenerative phases of tauopathy, with a skew towards transient synaptic structures compared to more stable ones (Crimins et al., 2011, 2012; Kopeikina et al., 2013a, 2013b). Synapse stability was also altered, with a transient increase in dendritic spine turnover followed by progressive spine loss prior to neurite and neuro- degeneration (~5.5M of age) (Jackson et al., 2017, 2020; Figure 1.2 C & D). Together, this suggests the model displays a synaptic phenotype in early neurodegenerative phases of tauopathy that may mimic that seen in the disease.

Therefore, the rTg4510 model was selected to examine synaptic and neurophysiological function at an age point equivalent to prodromal tauopathy. There are potentially transient and homeostatic functional changes at this age point that could account for observed deficits in cellular and network function prior to the emergence of frank neurodegeneration. These changes were investigated in a tractable and prototypical model of the neocortex, the somatosensory cortex.

1.2 THE MAMMALIAN NEOCORTEX

The outer most layers of the cerebral hemispheres, known as the neocortex, are involved in higher level function including sensory perception and integration, complex behaviours, and memory formation and preservation (Ghazanfar and Schroeder, 2006; Harris and Shepherd, 2015; Kandel et al., 2000). There is a striking degree of similarity across the neocortex with respect to its' cytoarchitecture, microcircuitry, and reciprocal subcortical connectivity (Harris and Shepherd, 2015; Lübke and Feldmeyer, 2007; Mountcastle, 1997).

The neocortex is organised into cortical columns, perpendicular to the pia, which are formed of six horizontal layers of cells based on the laminar structure within the cytoarchitecture (Brodmann, 1909; Heimer, 2012; Mountcastle, 1957, 1997). These cortical columns are thought of as discrete functional units, with cells within a column sharing similar properties such as receptive field tuning (Hubel and Wiesel, 1959, 1962; Mountcastle, 1957, 1997). This structural organisation is

proposed to increase the efficiency of complex cognitive computations (Harris and Shepherd, 2015; Lübke and Feldmeyer, 2007).

The canonical cortical circuit describes the flow of excitatory information within these columns, first described in the visual cortex (Douglas and Martin, 1991; Douglas et al., 1989, 1995). Whilst recent evidence suggests some subtle regional differences, the basic principles seem to be conserved and extend across cortical areas (Capone et al., 2016; Harris and Shepherd, 2015; Kaas, 1987). Most subcortical information enters the column from the thalamus and undergoes local processing in more superficial cortical layers (Douglas and Martin, 2010; Guillery and Sherman, 2002). Reciprocal intralaminar connections allow for recurrent excitation, feedback inhibition and disinhibition, with local translaminar axonal and dendritic collaterals connecting the superficial to the deeper cortical layers (Lübke and Feldmeyer, 2007). Deeper cortical layers project cortical column output to neighbouring neocortical structures and other subcortical regions (Douglas and Martin, 2010).

Overall, cortical columns are broadly similar in structure and connectivity across neocortical regions and species, with differences in cytoarchitecture likely related to differences in connectivity that allows for functional specialisation (Harris and Shepherd, 2015; Rockel et al., 1980). This gives confidence that these units may have similar fundamental roles within information processing, which can be generalised to understand more complex cognitive behaviours (Harris and Shepherd, 2015). As such, the somatosensory cortex has become an attractive model to study the neocortical system and has helped inform some common principles of neocortical function (Lübke and Feldmeyer, 2007; Miller et al., 2001).

1.2.1 The somatosensory cortex

Somatosensory information – sensory perception such as pressure, touch or temperature change felt anywhere on the body – is processed in the brain via the somatosensory pathway. The somatosensory cortex encodes this sensory perception, with areas across the entire body corresponding to specific regions within the brain (somatotopy). In humans, for example, there are specific regions of the brain that will respond to sensation at individual fingers, first described by Penfield and Rasmussen, 1950. The somatosensory cortex in mice was first described by Woolsey and Van der Loos, 1970, with the identification of discrete

clusters of neurons defined as barrels, with receptive fields that corresponded to single whiskers (vibrissae) in a somatotopic fashion.

1.2.1.1 From whisker to the primary somatosensory cortex

The typical pathway for conveying vibrissal information to the primary somatosensory (S1) cortex can be described as follows. A single whisker movement innervates distal axons of trigeminal ganglion in the infraorbital branch of the trigeminal nerve (Lee and Woolsey, 1975; Rice et al., 1986). This innervates trigeminal nuclei of the brain stem which are organised into discrete neuronal clusters termed barrelettes (Belford and Killackey, 1979; Erzurumlu et al., 1980; Veinante and Deschênes, 1999). These project to the thalamus, which is organised into barreloids (Land et al., 1995; Van Der Loos, 1976; Williams et al., 1994). Thalamic axons then project to the S1 cortex (Lee and Woolsey, 1975; Welker, 1971; Woolsey and Van der Loos, 1970). Each structure of this pathway preserves the information flow in a somatotopic fashion (Adibi, 2019; Petersen, 2007).

1.2.1.2 Primary somatosensory cortex cytoarchitecture and circuitry

S1 cortex is separated into six layers as is typical of the neocortex. The majority of neurons within this region are excitatory, constituting 80-85% of all neurons within S1 (Lefort et al., 2009; Markram et al., 2015; Narayanan et al., 2017; Oberlaender et al., 2012). The remainder are a heterogeneous population of interneurons, thought to help shape excitation and define receptive field tuning (Harris and Shepherd, 2015; Markram et al., 2015). The most superficial layer of S1 (layer I) is exclusively comprised of inhibitory cell bodies in addition to apical dendritic arbors and axonal projections (Lefort et al., 2009; Markram et al., 2015; Oberlaender et al., 2012). The deeper layers (II – VI) consist of a mixture of excitatory and inhibitory cells with inter- and intra- laminar connections (Lefort et al., 2009; Markram et al., 2015).

The inputs into S1 from the thalamus can be further split into different parallel pathways, which target distinct nuclei or layers within S1: the lemniscal, paralemniscal, and extralemniscal pathway (Petersen, 2007; Pierret et al., 2000; Yu et al., 2006; Figure 1.3). The well characterised lemniscal pathway is the primary glutamatergic pathway for vibrissal information, thought to convey whisking and touch. This projection enters S1 via the dorsal medial region of the ventral posterior medial nucleus of the thalamus (VPM), whose axons primarily

innervate layer IV (barrels) in S1 with sparse projections to layer VIa (Chmielowska et al., 1989; Lu and Lin, 1993; Mo et al., 2017; Figure 1.3). The excitatory layer IV axons form prominent inputs to layer II/III within the same cortical column (Feldmeyer et al., 1999, 2002). These neurons form transcolumnar intralaminar connections, with axonal arborisations extending well beyond the confines of the cortical column (Petersen, 2007). These neurons form strong descending connections to cell bodies in layer V (Koralek et al., 1990; Reyes and Sakmann, 1999). These innervate layer VI cells, and also the thalamic VPM and the medial part of the posterior thalamic nuclear group (POm), closing the corticothalamic loop (Bourassa et al., 1995; Land et al., 1995; Lübke and Feldmeyer, 2007).

Other whisking related information is conveyed from the paralemniscal pathway, which enters from the POm by forming axon collaterals with layer I and layer Va in S1 (Koralek et al., 1988; Lu and Lin, 1993; Figure 1.3). This pathway is suggested to play a role in active whisking and exploration, and sensorimotor coordination (Petersen, 2007; Yu et al., 2006). The most recently discovered extralemniscal pathway projects via the ventral lateral VPM in the thalamus, whose axons then innervate S1 (layer V) and the secondary somatosensory cortex equally (Pierret et al., 2000; Figure 1.3). This pathway is thought to convey information about whisker contact (Yu et al., 2006).

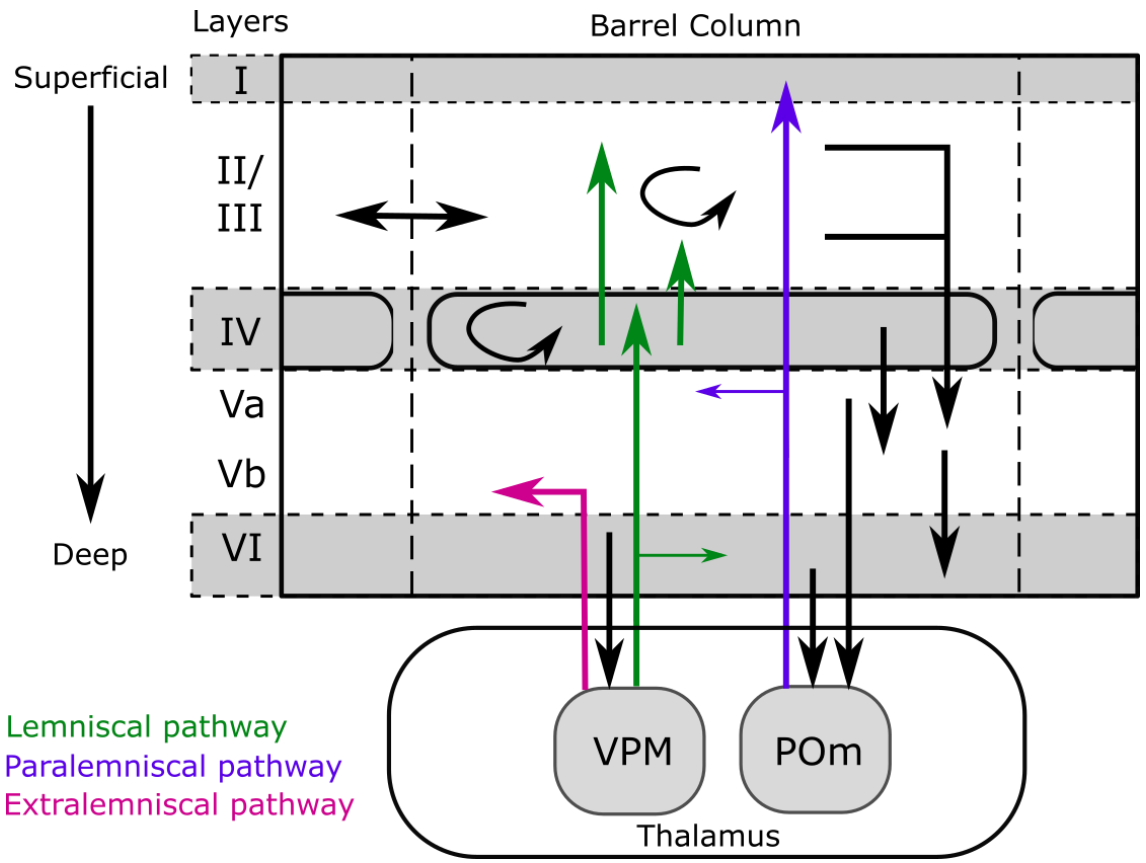

Figure 1.3 The excitatory microcircuitry within the primary somatosensory cortex from thalamic input. A schematic of excitatory information flow within a barrel column. The lemniscal, paralemniscal and extralemniscal pathways are highlighted in green, purple, and pink, respectively. Information enters the cortical column via the VPM and POm thalamic nuclei. Black arrows denote general column microcircuitry such as transcolumnar and descending connections, and includes recurrent connections as curly arrows. Cortical layers are shown as alternating white and shaded grey areas, labelled on the left. The column is marked as dashed vertical lines and the barrel fields are shown in layer IV as rounded rectangles. *Adapted from Adibi, 2019.*

1.2.1.3 The somatosensory cortex as an experimental model system

The rodent somatosensory cortex has been widely used as a neocortical model system. As the barrel fields are visible by eye, this allows for the identification of individual cortical columns within slice preparations that preserve the connections between the column and the thalamus, which is not possible with preparations from other cortical areas (Agmon and Connors, 1991; Lübke and Feldmeyer, 2007; Lübke et al., 2000). The region is also easily accessible for recording and imaging experimentally, with the ability to drive evoked responses using whisker stimulation, which is a behaviourally relevant pathway. This allows the same whisker projection pathways to be studied *in vitro* and *in vivo*. The system has

given invaluable insight into cortical processing and plasticity, and has been well defined within the literature from cellular composition to functional circuity in behaving animals.

Anatomical and functional characteristics of the barrel cortex therefore make it an ideal system to study cortical microcircuit dysfunction in pathophysiological conditions. Using a well-defined microcircuit such as S1 to study the impact of tauopathy allows for more precise characterisation of the specific locus of dysfunction occurring which could then be generalised to other, more complex, microcircuits. Within the rTg4510 mouse model, there is significant tau pathology accumulation from 4-6 months of age in S1, with alterations in synaptic stability from ~5.5 months of age and visible neurodegeneration from ~6 months of age (Blackmore et al., 2017; Harrison et al., 2020; Jackson et al., 2020; Ramsden et al., 2005; SantaCruz et al., 2005). Therefore, S1 in the rTg4510 model is a viable model for studying the effects of tauopathy-mediated dysfunction and degeneration in cortical networks.

1.3 NEURONS

Whilst there are highly diverse and heterogeneous populations of neurons within the brain, they share some common properties in regard to their basic structure and electrical functionality. Characterising how these properties are altered in disease can help guide us towards neurophysiological alterations that underpin complex network and behavioural phenotypes.

1.3.1 The electrophysiology of the neuron

Neurons are electrically specialised cells due to the inherent properties of the phospholipid bilayer membrane, which prevents ion movement between the intracellular and extracellular space producing an electrochemical gradient (Goldman, 1943; Kandel et al., 2000). This lack of ionic mobility can precipitate into an electrical charge, dependent on the extracellular and intracellular ion concentrations (Goldman, 1943; Hodgkin and Katz, 1949). This gradient is maintained by various ion channels embedded within the phospholipid membrane. Overall, the electrical excitability of neurons is dictated by a combination of membrane and ion channel properties, and how these integrate incoming signals to produce an appropriate electrical output.

1.3.1.1 Neuronal excitability: passive properties

The neuronal membrane can be considered as an electrical circuit, with ion channels embedded within the membrane modelled as resistors (Hodgkin and Huxley, 1952; Kandel et al., 2000). Therefore, the passive properties of a neuron refer to the capacitive and resistive functions of the neuronal membrane and the ion channels within this circuit. These properties influence how the neuron responds to voltage change, by altering how current flows across the membrane. This includes the time course, the size, and the amplitude of the response to incoming currents, shaping how this response flows through the neuron (Kandel et al., 2000; Rall, 2011). Together, these passive properties can influence neuronal excitability. Some of these electrical properties can be elucidated using whole-cell patch clamp electrophysiology recordings, by injecting hyperpolarising or subthreshold currents into the cell and measuring the corresponding voltage deflection response.

1.3.1.2 Neuronal excitability: active properties

Active properties refer to the dynamic response of membrane-embedded gated ion channels to a voltage or chemical change (Crill and Schwindt, 1983; Kandel et al., 2000). For example, when the neuron is depolarised past action potential (AP) threshold, the complexity of the response surpasses that of a simple circuit with a capacitance and resistance. Active properties of different voltage gated ion channels work in complement to drive the electrical potential away from the resting membrane potential to produce an all or nothing AP response (Kandel et al., 2000). Hyperpolarising voltage-gated channels also contribute to active properties of the neuron, altering the frequency of APs. Together, active properties influence neuronal excitability by altering the length and size of the AP response, and how often that response can occur.

1.3.2 Neurophysiological dysfunction in tauopathy

Whilst it is difficult to measure changes to passive and active electrical properties in human tauopathy due to cellular accessibility, alterations to the electrical properties of neurons have been seen in multiple models of tauopathy. Acute incubation with tau oligomers have a marked effect on the AP waveform and dynamics, leading to a slower, longer, and reduced amplitude AP (Hill et al., 2019). In the chronic Tau35 model of tauopathy at 14-18M when tau pathology is progressed within the model, hippocampal neurons had a hypoexcitable

phenotype with altered intrinsic neuronal properties such as an increased capacitance, decreased input resistance, and a decrease in AP firing rates (Tamagnini et al., 2017). In another chronic model of advanced tauopathy, the rTg4510 model, there was a hyperexcitable phenotype seen in neurons in the frontal cortex, with a depolarised resting membrane potential, increased input resistance, and increased AP firing rates at 8-9M of age (Crimins et al., 2012; Rocher et al., 2010). Interestingly, neurons recorded in the hippocampus within the rTg4510 model at a similar age (7-8M), also showed an altered neurophysiological phenotype (increased hyperpolarising activated currents and decreased membrane time constant), but this did not affect the core excitability of these cells in comparison (Booth et al., 2016a). Therefore, it seems that there are differential tauopathy-driven phenotypes, likely related to the pathological stage of the model and brain region studied, as the rTg4510 model has a more severe pathological phenotype in comparison to the Tau35 model. This suggests that there are differential mechanisms of dysfunction or compensation at different stages of tauopathy. Whilst the precise mechanisms by which these changes are occurring is unknown, it is obvious that there are likely multiple pathological processes by which tauopathy induces neurophysiological dysfunction.

1.4 SYNAPSES

The synapse is a term coined by Charles Sherrington in 1897, describing the non-continuous contact between one neuron to another, which had been suggested as part of the neuron doctrine (Foster et al., 1897; Kandel et al., 2000; Ramon y Cajal, 1911). These specialised connections allow the transmission of signals, either electrical or more often chemical, between neurons. Typically, synapses are formed of the pre- and post-synapse and the synaptic cleft. Whilst this overview will focus on chemical synaptic connections solely between neurons, it should be noted that astrocytic endfeet are in close contact with the majority of synapses within the brain and play a role in modulating synaptic transmission (Dieterich and Kreutz, 2016; Kandel et al., 2000; Ventura and Harris, 1999). This overview will also focus on the more prevalent chemical synaptic transmission for brevity and relevance for this thesis.

1.4.1 Synaptic structure

The structure of synapses is specialised to ensure efficient and appropriate transfer of information between neurons, with structural disruption leading to

synaptic dysfunction. This specialisation occurs from a vast array of heterogeneous protein machinery, specific to the functional architecture of either the pre- or post-synapse that streamlines the process of synaptic transmission (Dieterich and Kreutz, 2016; O'Rourke et al., 2012).

Proteins at the pre-synaptic terminal facilitate and regulate pre-synaptic transmission (Garner et al., 2000; Figure 1.4). This includes proteins to determine the localisation, tethering, and fusion of synaptic vesicles at the pre-synapse. For example, SNARE and SM proteins dock and prime vesicles at the cytomatrix active zone (Garner et al., 2000); the synaptic vesicle protein synaptophysin is suggested to play a role in the efficient endocytosis of synaptic vesicles (Kwon and Chapman, 2011). Other proteins also tightly regulate synthesis, storage and release of neurotransmitters (Schweizer and Ryan, 2006). Ion channels, such as voltage-gated Ca^{2+} channels, and other receptors are also embedded in the pre-synaptic membrane (Kandel et al., 2000; Schweizer and Ryan, 2006).

At the post-synaptic terminal, there are ~1500 proteins which are specialised to generate the response to neurotransmitter release (O'Rourke et al., 2012; Scannevin and Huganir, 2000; Figure 1.4). A number of these proteins form a complex yet critical structure known as the post-synaptic density (PSD). This dynamic protein lattice helps localise, organise, and traffic receptors and other required molecules within and to the PSD. Receptors and ion channels crucial for generating a response to neurotransmitter release are stabilised within the PSD by scaffold proteins. PSD95 is one such protein scaffold associated with synapse maturation and stabilisation (Ehrlich et al., 2007; El-Husseini et al., 2000).

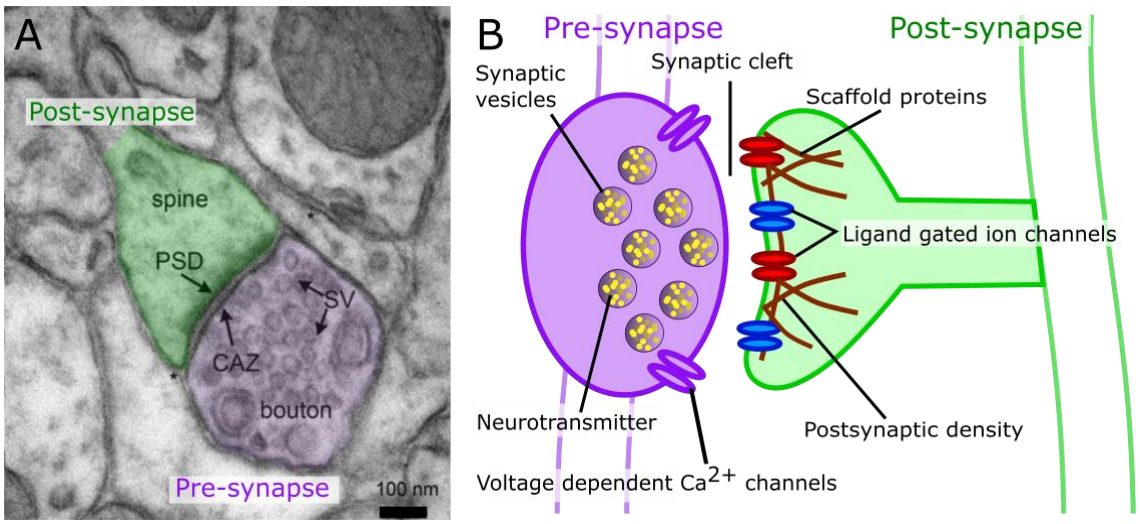

Figure 1.4 The structure of a chemical synapse. An electron micrograph of a synapse (**A**), with the pre-synapse highlighted in purple and the post-synapse highlighted in green. Abbreviations: SV = synaptic vesicles, CAZ = cytomatrix at the active zone, PSD = post-synaptic density. Scale bar = 100 nm. Panel **B** shows a labelled cartoon schematic of a typical chemical synapse. ***A*** *is adapted from Dieterich and Kreutz, 2016*.

1.4.1.1 Assessing the synaptic proteome: synaptosomes

There is a large diversity in the downstream molecular mechanisms of synapses, which is likely a consequence of molecular composition within the synapse, even within traditional neurotransmitter categories (O'Rourke et al., 2012). Synaptosome preparations are the foundation of how we assess the molecular content of synapses, although development of newer technologies such as array tomography, are starting to be favoured for assessing single synapse diversity within small subregions (Busse and Smith, 2013; Dieterich and Kreutz, 2016; O'Rourke et al., 2012). Synaptosomes are sealed terminal ends which preserve the synaptic milieu including vesicles and synapse bound receptors (Evans, 2015; Hebb and Whittaker, 1958; De Robertis et al., 1961; Whittaker, 1959, 1993). Further purification methods such as discontinuous sucrose and percoll gradients can be used to improve purity of the preparations, and the pre- and post- synapse can be further isolated (Dunkley et al., 1986; Gray and Whittaker, 1962; Huttner et al., 1983; Nagy and Delgado-Escueta, 1984; Tenreiro et al., 2017). This process allows for the identification and quantification of protein localisation within pre- and post- synaptic terminals.

1.4.2 Synaptic transmission

The general process of neuronal communication via chemical synapses occurs in a similar manner regardless of subtype (Kandel et al., 2000; Figure 1.5). An AP occurs at the pre-synaptic neuron, where this signal reaches and depolarises pre-synaptic terminals. This depolarisation activates voltage dependent Ca^{2+} channels, leading to a transient influx of Ca^{2+} within the pre-synaptic terminal (Dodge and Rahamimoff, 1967; Katz, 1969). These ions bind to calcium sensors on synaptic vesicles. Neurotransmitters are stored within these vesicles, and are released into the synaptic cleft by exocytosis at the active zone of the pre-synapse (del Castillo and Katz, 1954; Fatt and Katz, 1951; Heuser and Reese, 1973). Neurotransmitters diffuse across the synaptic cleft, to bind to ligand-gated post-synaptic ion channels (del Castillo and Katz, 1956b, 1956a). This binding causes a change in receptor conformation allowing the inflow of specific ions, leading to an electrical change at the post-synaptic neuron (Fatt and Katz, 1952).

Post-synaptic responses to neurotransmitter release are said to be quantal, with “packets” of neurotransmitters released from vesicles activating post-synaptic receptors producing a change in current at the post-synapse (Fatt and Katz, 1951, 1952). These responses can be expressed as a function of the number of active synapses, the probability of release, and the potency of the released neurotransmitter (del Castillo and Katz, 1954). If any of these properties are altered, this can alter the amplitude or frequency of post-synaptic responses. A reduction in the probability of release for example would likely lead to a lowered frequency and perhaps also the amplitude of responses.

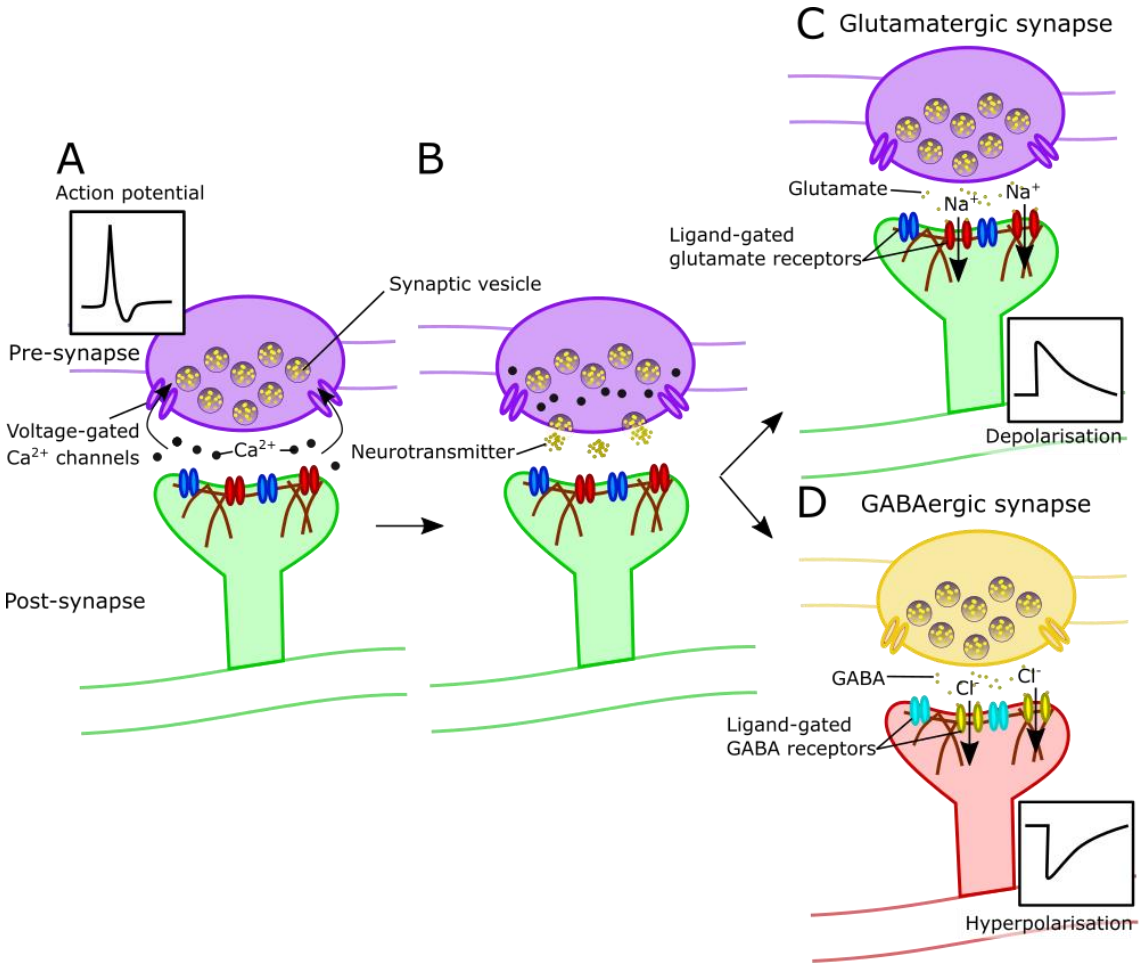

Figure 1.5 Synaptic transmission. An AP (shown in inset) occurs in the pre-synaptic neuron (**A**). This depolarisation within the neuron causes the opening of voltage-gated Ca^{2+} ion channels. Ca^{2+} influx into the pre-synaptic terminal leads to neurotransmitter release (**B**). Then, independent of synapse type, neurotransmitters are released into the synaptic cleft (**C** & **D**). With glutamate release (**C**), post-synaptic glutamate receptors are particularly permeable to sodium (Na^{+}), causing a depolarisation of the post-synapse at resting membrane potentials (shown in inset). With γ-aminobutyric acid (GABA) release (**D**), post-synaptic GABA receptors are typically permeable to chloride (Cl^{-}) causing a hyperpolarisation of the post-synapse at resting membrane potentials (shown in inset). Glutamatergic synapse shown in purple and green in C and GABAergic synapse shown in yellow and red in D.

1.4.2.1 Excitatory and inhibitory synaptic transmission

The major excitatory and inhibitory neurotransmitters in the brain are glutamate and γ-aminobutyric acid (GABA) respectively, formed from their precursor glutamine (Kandel et al., 2000; Sibson et al., 1998). Glutamate binds to glutamate receptors, depolarising the post-synaptic membrane at typical resting membrane

potentials, thus increasing the probability of firing an AP (Figure 1.5 C). GABA and GABA receptors conversely decrease the probability of firing an AP by hyperpolarising membrane potential (Vm), classing it as an inhibitory neurotransmitter in most circumstances (Kandel et al., 2000; Krnjević and Schwartz, 1967; Figure 1.5 D). These electrical changes can be measured using whole-cell patch clamp electrophysiology, and are known as excitatory or inhibitory post-synaptic activity respectively.

Whether an ion channel elicits excitatory or inhibitory activity is dictated by the equilibrium potential of the ion that is permeable through the channel (Kandel et al., 2000). The excitatory glutamate receptors are typically equally permeable to Na^+ and potassium (K^+) ions, with the reversal potential of glutamate receptors being ~0 mV. This results in a depolarisation (inward current) of the membrane at resting membrane potential (Figure 1.5 C). Inhibitory ionotropic GABA receptors are typically permeable to chloride (Cl^-) ions, which have an equilibrium potential of ~-70 mV. Therefore, the influx of Cl^- (outward current) leads to a hyperpolarisation of the membrane at resting membrane potential (Figure 1.5 D).

1.4.2.2 Inhibition & GABA

Whilst this thesis will mainly focus on excitatory neurotransmission, inhibitory neurotransmission is critical to the function of neuronal networks and therefore cannot be overlooked. In the mature brain, GABA is an inhibitory neurotransmitter, acting on both synaptic and extrasynaptic GABA receptors: $GABA_a$, $GABA_b$, $GABA_c$ (Owens and Kriegstein, 2002). These different receptors promote different GABAergic responses, with fast activity mediated by the ionotropic $GABA_a$ and $GABA_c$ receptors, and slower activity mediated by metabotropic $GABA_b$ receptors (Benardo, 1993; Dutar and Nicoll, 1988). GABA releasing neurons are typically classed as inhibitory interneurons. Inhibition within neuronal networks is of critical importance, as a network of pure excitation would only beget further excitation. This balanced network dynamic generates complex properties such as neuronal oscillations, increasing the computational ability of the brain (Haider et al., 2006; Isaacson and Scanziani, 2011).

1.4.2.3 Excitation & Glutamate

Focussing on excitatory neurotransmission, glutamate acts on ionotropic and metabotropic glutamate receptors. The ionotropic glutamate receptors are named after their affinity and selectivity to the synthetic agonists: α-amino-3-hydroxy-5-

methyl-4-isoxazolepropionic acid (AMPA), *N*-Methyl-d-aspartate (NMDA), kainate. Therefore, the receptors are termed AMPA, NMDA and kainate receptors respectively (Collingridge et al., 2009; Kew and Kemp, 2005; Traynelis et al., 2010). There are eight known metabotropic glutamate receptors, termed $mGluR_{(1-8)}$ (Kew and Kemp, 2005; Kunishima et al., 2000; Masu et al., 1991; Niswender and Conn, 2010). Ionotropic glutamate receptors are thought to mediate the majority of excitatory neurotransmission, whereas metabotropic receptors modulate neuronal excitation and neurotransmitter release via secondary messenger signalling cascades.

1.4.2.3.1 Ionotropic glutamatergic receptors: AMPA receptors

AMPA receptors (AMPAR) are heteromeric transmembrane ionotropic receptors that mediate the overwhelming majority of fast glutamatergic synaptic transmission. AMPARs are expressed mainly on neurons, and to a lesser extent glia, and along with NMDA receptors (NMDARs), are thought to dictate the majority of excitatory signalling (Ashby et al., 2008; Hollmann and Heinemann, 1994; Kew and Kemp, 2005). They assemble as tetramers, formed of combinations of four subunits, GluA1-4 (Boulter et al., 1990; Collingridge et al., 2009; Hollmann and Heinemann, 1994; Hollmann et al., 1989; Keinänen et al., 1990). In addition, these receptors form stable complexes with auxillary AMPAR subunits, such as stargazin, and other transmembrane AMPAR regulatory proteins (TARPs). These facilitate appropriate AMPAR trafficking, stabilisation, maturation, and function (Bats et al., 2007; Chen et al., 2000; Opazo et al., 2010; Tomita et al., 2003).

Upon glutamate binding to AMPARs, irrespective of membrane voltage, conformational change of the receptor occurs opening a central transmembrane pore. This leads to the influx of Na^+ (with some K^+ efflux) which depolarises the post-synaptic terminal at typical resting membrane potentials. In some cases, AMPARs are also Ca^{2+} permeable. This is either by alternate splicing and RNA editing of GluA2 containing AMPARs, or in those AMPARs that lack the GluA2 subunit (Hollmann et al., 1991; Isaac et al., 2007; Jonas et al., 1994). Different AMPAR subunits variants can dictate the kinetics of the post-synaptic response. For example, splice variants of the GluA3/4 subunits lead to lowered desensitisation of AMPAR responses (Grosskreutz et al., 2003; Mosbacher et al., 1994). Different AMPAR subunit configurations, such as the inclusion or

exclusion of the GluA2 subunit, can dictate the voltage dependence and conductance of AMPARs (Cecilia Angulo et al., 1997). Combinations of both different subunits and subunit splice variants alters activation, desensitisation and recovery of AMPAR responses (Grosskreutz et al., 2003).

Heteromeric and homomeric receptor subunit conformation undergoes spatiotemporal regulation within the brain. From birth, GluA1-3 expression increases gradually and stabilises early in life (Henley and Wilkinson, 2013; Zhu et al., 2000). Conversely, GluA4 undergoes strict developmental regulation, with high expression in early development to low expression in the adult brain (Zhu et al., 2000). Subunit expression is also regulated within brain regions, with GluA3 present at 10% of the levels of GluA1 and GluA2 in the adult brain (Lu et al., 2009; Sans et al., 2003). There are also differential subunit conformations within different cell types. For example, the most abundant AMPAR subunit in pyramidal neurons in the neocortex is GluA2 with lesser expression of GluA1 and 3, which would likely form GluA1/GluA2 and GluA2/GluA3 heterodimers as seen in hippocampal pyramidal neurons (Jonas et al., 1994; Mansour et al., 2001; Sans et al., 2003; Wenthold et al., 1996). However, other cell types such as inhibitory interneurons, predominantly express GluA2 lacking Ca^{2+} permeable AMPARs (Geiger et al., 1995; Jonas et al., 1994; Mahanty and Sah, 1998). Inhibitory interneurons also express GluA4 containing AMPARs which are key in regulating inhibitory circuit integration, whereas GluA4 is mostly absent in mature excitatory neurons (Pelkey et al., 2015; Zhu et al., 2000).

AMPARs are highly dynamic proteins, that rapidly undergo constitutive and activity-dependent trafficking and recycling at the post-synapse. AMPAR trafficking is linked to subunit composition, with GluA2 containing AMPARs trafficked and recycled with a half-life in the order of minutes, compared to slower constitutive turnover over hours to days of other AMPAR assemblies (Henley, 2003; Nishimune et al., 1998; Noel et al., 1999). The active and dynamic regulation of AMPARs is fundamental in learning and memory mechanisms (Henley and Wilkinson, 2013).

1.4.2.3.2 Ionotropic glutamatergic receptors: Kainate receptors

Along with AMPARs, kainate receptors were termed the non-NMDA glutamate receptors for many years, due to their sensitivity to NBQX, insensitivity to D-APV, and also their structural similarities (Kew and Kemp, 2005; Pinheiro and Mulle,

2006). Kainate receptors are tetrameric assemblies, formed from five possible subunits (GluK1-5) (Bettler et al., 1990; Collingridge et al., 2009; Hollmann and Heinemann, 1994). Kainate receptors are the less abundant glutamate ionotropic receptor and whilst they are structurally and functionally similar to AMPARs, their role in physiology is less clear (Lerma and Marques, 2013).

Kainate receptors have varying affinities for both glutamate and kainate, conferred by subunit assembly. With this, the lack of selective agonists has hampered our understanding of the kainate receptor (Kew and Kemp, 2005; Pinheiro and Mulle, 2006). In contrast to the other ionotropic glutamate receptors, kainate receptors show diverse and non-conventional signalling mechanisms including activation of both canonical ionotropic and non-canonical metabotropic pathways (Lerma and Marques, 2013; Valbuena and Lerma, 2020). Whilst their physiological role is likely widespread, there is paradoxical evidence of their role at the pre- and post-synapse, with kainate receptor activation shown to modulate neuronal excitability and inhibition (Evans et al., 2019; Lerma and Marques, 2013; Pinheiro and Mulle, 2006). Within the brain, their expression is relatively low and restricted to specific pathways, and activation of post-synaptic kainate receptors mediates low amplitude slow currents compared to AMPARs (Castillo et al., 1997; Lerma and Marques, 2013). Thus, the role mediated by kainate receptors in canonical excitatory signalling is still uncertain compared to the other ionotropic glutamate receptors.

1.4.2.3.3 Ionotropic glutamatergic receptors: NMDA receptors

NMDARs are ionotropic glutamatergic receptors with multiple ligand binding sites. In contrast to the other ionotropic receptors, NMDAR activation requires the binding of both the endogenous ligand glutamate and glycine/D-serine as a cofactor (Hansen et al., 2018; Mcbain and Mayer, 1994; Traynelis et al., 2010). It is also unique amongst the other glutamatergic ionotropic receptors as it is a voltage-gated receptor. At hyperpolarised potentials, there is a magnesium (Mg^{2+}) ion in the channel pore that blocks activation. Sufficient depolarisation (> -40 mV) is required to relieve the Mg^{2+} block. Therefore, this receptor has been described as a coincidence detector as it needs both glutamate activation and depolarisation to be maximally active. This also leads to typically slower activation and deactivation kinetics compared to AMPARs. Following activation, NMDARs

are permeable to Na^+, K^+ and Ca^{2+}, with Ca^{2+} influx triggering downstream signalling cascades.

These heteromeric receptors are made up of the constitutive GluN1 subunit plus variants of GluN2 (GluN2A, GluN2B, GluN2C, GluN2D) or the more recently discovered GluN3 (GluN3A, GluN3B) subunits (Chatterton et al., 2002; Ciabarra et al., 1995; Collingridge et al., 2009; Hollmann and Heinemann, 1994; Meguro et al., 1992; Moriyoshi et al., 1991; Sucher et al., 1995). These receptors are typically formed of two glycine-binding GluN1 subunits with either two glutamate-binding GluN2 subunits or less frequently two glycine-binding GluN3 subunits or a mixture of both GluN2/3 (Laube et al., 1998; Monyer et al., 1992; Pachernegg et al., 2012). The most widely expressed NMDARs are typically GluN1 with either GluN2A or 2B (Hollmann and Heinemann, 1994; Traynelis et al., 2010).

Different GluN2 subunits can alter Ca^{2+} permeability and voltage dependence, causing differences in receptor current dynamics in response to pharmacological activation (Kew and Kemp, 2005; Monyer et al., 1992, 1994). For example, NMDARs that contain GluN2C and GluN2D subunits have decreased sensitivity to Mg^{2+} block, lower single channel conductance, and GluN2D containing receptors in particular have slower deactivation kinetics in comparison to GluN2A and GluN2B containing NMDARs (Cathala et al., 2000; Erreger et al., 2007; Monyer et al., 1992). GluN3 is thought to modulate NMDAR activity by modifying the heteromeric receptor structure, leading to reduced Mg^{2+} sensitivity and reduced Ca^{2+} influx, although further corroborating evidence is needed (Pachernegg et al., 2012). GluN1/GluN3 heteromeric NMDARs form excitatory glycine-gated channels which are not Ca^{2+} permeable and are resistant to Mg^{2+} block, and so therefore function in a non-canonical manner in respect to NMDARs (Chatterton et al., 2002; Köhr, 2006).

NMDAR subunit expression undergoes spatiotemporal regulation. In development, GluN2B and GluN2D are abundant, with the progressive addition of GluN2A and GluN2C (Monyer et al., 1994; Standaert et al., 1996). In the adult brain, GluN2A expression is ubiquitous whilst GluN2B expression is restricted to the forebrain (Monyer et al., 1994; Standaert et al., 1996). GluN2C is highly expressed in the cerebellum and GluN2D expression is enriched in interneurons (Monyer et al., 1994; Standaert et al., 1996). Functional NMDARs are also expressed both synaptically and extrasynaptically, with GluN2B containing

NMDARs suggested to be more mobile and are more frequently detected in the extrasynaptic domain (Tovar and Westbrook, 1999, 2002). NMDARs are expressed both pre- and post- synaptically, with pre-synaptic NMDARs playing a functional role in LTD in layer IV to layer II/III synapses in the barrel cortex (Rodríguez-Moreno et al., 2011).

NMDARs have diverse roles in normal neurophysiology. NMDAR activity facilitates non-linear integration of synaptic inputs, which plays a crucial role in regulating sensory perception including the control and refinement of response tuning curves (Lavzin et al., 2012; Lee et al., 2005; Palmer et al., 2014; Smith et al., 2013; Takahashi et al., 2016). This can include the regulation of stimulation detection thresholds (Takahashi et al., 2016), preferred directionality of angular tuning fields (Lavzin et al., 2012) and the selectivity of neuronal orientation tuning (Smith et al., 2013). NMDARs are also implicated in multiple learning and memory processes such as LTP, due to its' function as a coincidence detector and activation of downstream Ca^{2+} dependent signalling pathways (Lau et al., 2009; MacDonald et al., 2006; Müller et al., 2009). In pathophysiological conditions, glutamate excitotoxicity is suspected to be due to NMDAR overactivation, leading to excessive Ca^{2+} entry which is thought to be neurotoxic (Choi, 1988; Rothman and Olney, 1986).

1.4.2.4 Synaptic plasticity and stabilisation

The favouring of one pathway within a circuit, whilst weakening others, now known as plasticity, is an idea that was proposed in the 1940s (Hebb, 1949; Konorski, 1948). Plasticity has been hypothesised as the way that networks, neurons, and synapses can dynamically modulate the network in an efficient manner, and this is thought to be how we learn and adapt to different behaviours. There is increasing recognition that synapses are critical in functional plasticity, compared to other nodes of modulation (Busse and Smith, 2013; Citri and Malenka, 2008). Synapses can undergo high turnover and can change shape, size, or number leading to corresponding changes in synaptic transmission to an experience (Trachtenberg et al., 2002). This can be on rapid or longer timescales and can occur at both excitatory and inhibitory synapses.

Short-term plasticity (STP) is a rapid mechanism, thought to be important in transient short-term adaptation to behaviours, or short-term forms of memory (Citri and Malenka, 2008). STP modulates synaptic filtering, which is the process

of efficiently converting synaptic information with different temporal scales by transformation with either a low- or high-pass filter. STP works by modulating the probability of neurotransmitter release at the synapse, and therefore does not induce changes in the structure or composition of the synapse.

Glutamatergic receptor function and regulation is critical for forming and maintaining longer term plasticity changes within the brain. Long-term plasticity (LTP) occurs on a time scale of hours to days and is thought to be the neural foundation of learning and memory (Bliss and Collingridge, 1993; Bliss and Lømo, 1973). LTP leads to the strengthening of existing spines by increasing the size, and also induces the formation of new spines (Barnes and Finnerty, 2010; Engert and Bonhoeffer, 1999). The most widely studied mechanisms of LTP relate to NMDAR activation, and AMPAR trafficking and regulation at synapse. Other forms of synaptic plasticity include homeostatic plasticity, such as synaptic scaling, and metaplasticity (Abraham and Bear, 1996; Turrigiano, 2008). These forms of plasticity are also regulated in part by glutamatergic receptor expression and trafficking at the synapse. For example, a prevailing mechanism for synaptic scaling is the availability of AMPARs within the whole cell and within different subcellular compartments (Barnes et al., 2017; Gainey et al., 2009; Turrigiano, 2008).

The converse of synaptic potentiation, the process of downscaling of responses, is short- and long-term depression. The mechanisms for these processes typically share common pathways, such as the regulation of excitatory receptor expression. For example, one mechanism of long-term depression (LTD) is endocytosis of AMPARs at the synapse (Beattie et al., 2000; Granger and Nicoll, 2014).

1.4.3 Synaptic dysfunction and degeneration in tauopathy

In the past decade, the synapse has increasingly been viewed as a vulnerable target to tau-mediated disruption (Crimins et al., 2013; Jackson et al., 2019; Jadhav et al., 2015; Pooler et al., 2014; Tracy and Gan, 2018). Whilst tau may have a physiological role at synapses in stabilisation and plasticity for example, hyperphosphorylated tau is abnormally and preferentially located at synapses in post-mortem AD brain tissue (Fein et al., 2008; Perez-Nievas et al., 2013; Tai et al., 2014). In fact, there is evidence that differential post-translational modifications on tau isoforms determines the neuronal and synaptic localisation,

with specific pro-aggregating isoforms promoting synapse loss in models of tauopathy (Eckermann et al., 2007; Sahara et al., 2014; Schaler et al., 2020; Xia et al., 2015). Infusion of tau oligomers into the brains of C57Bl/6 mice also led to a decreased density of synapses (Lasagna-Reeves et al., 2011). In chronic tauopathy models, synaptic markers are lost prior to NFT formation, and large-scale synaptic degeneration is observable (Crimins et al., 2011; Kopeikina et al., 2013a; Yoshiyama et al., 2007).

Tau pathology is also suggested to mediate changes to synaptic function prior to synaptic degeneration. Some suggested mechanisms include pre-synaptic dysfunction by tau association with synaptic vesicles, demonstrated by injection of tau into the pre-synapse (Zhou et al., 2017). However, the overall functional impact of tau pathology on synaptic function is conflicting, with increased, decreased and unchanged excitatory neurotransmission seen in different models of tauopathy (Crimins et al., 2013). In addition, studies investigating how tauopathy can impact synaptic function typically focuses at either very early pre-clinical states, or late degenerative stages. Therefore, despite mounting evident that tauopathy can promote synaptic disruption and degeneration, information on the pathological drivers of this transitionary phase and how this can impact function is lacking.

1.4.3.1 Alterations in the glutamatergic system in tauopathy

The suggestion that glutamate is key in the pathogenesis of AD has been a hypothesis for the past 30 years, with this also being suggested more recently for other tauopathies (Benussi et al., 2019). A prevalent hypothesis is that excitatory circuitry exhibits a greater degree of vulnerability when compared to their inhibitory counterparts in tauopathy post-mortem brain tissue (Dickson et al., 2011; Fu et al., 2018, 2019). This could be accounted for by alterations in inhibitory control of excitability, or loss of glutamatergic or GABAergic neurons or other mechanisms of dysregulation of glutamatergic signalling (Frere and Slutsky, 2018; Palop et al., 2007; Shimojo et al., 2020). Intracortical facilitation, a magnetic transcranial stimulation protocol that relies on intact glutamatergic circuitry, is reduced in patients with presymptomatic familial FTD (Benussi et al., 2016; Gazzina et al., 2018). Within the pR5 mouse model of tauopathy, altered glutamate, glutamine, and GABA metabolism has been observed (Nilsen et al., 2013). As the majority of fast excitatory neurotransmission is mediated by

AMPARs and NMDARs, a considerable amount of research has aimed to deconstruct how tauopathy can influence receptor activity and localisation. However, there is a significant lack of information regarding how glutamatergic receptor dysfunction specifically relates to synaptic and neuro- degeneration in tauopathy. This disease phase is suggested to be when symptomatic impairment occurs, and thus characterising dysfunction at this phase provides an ideal window for symptomatic rescue (Scheff et al., 2006, 2007).

NMDARs are an attractive target for glutamatergic dysfunction and thus therapeutic intervention in tauopathies (Avila et al., 2017; Lao et al., 2019; Liu et al., 2019; Mota et al., 2013; Wang and Reddy, 2017). In chronic models of tauopathy, there have been significant reductions in NMDAR expression, synaptic localisation, and function (Hoover et al., 2010; Kopeikina et al., 2013a; Warmus et al., 2014). In the hT-337M mouse model of tauopathy, enhancing NMDAR activity with an agonist lead to behavioural rescue, suggesting targeting NMDARs could be an effective tauopathy treatment (Warmus et al., 2014). Conversely, Memantine (an NMDAR antagonist) is currently one of the only approved symptomatic treatments for moderate to severe AD (Danysz and Parsons, 2003; Wang and Reddy, 2017). Memantine treatment lacked efficacy in FTD in two small trials, although meta-analysis of these trials suggests possible modest benefits of treatment (Boxer et al., 2013; Kishi et al., 2015; Vercelletto et al., 2011). Therefore, whilst it seems likely that NMDAR dysfunction occurs in tauopathy, it is not clear how and when this dysfunction precipitates at different phases of tauopathy, and these therapeutic strategies outlined likely target different mechanisms.

Glutamate excitotoxicity is thought to be mediated by NMDAR overactivation, which is a hypothesised mechanism of neurodegeneration (Liu et al., 2019; Mota et al., 2013; Wang and Reddy, 2017). Increased extrasynaptic localisation of NMDARs regulated by GluN2B subunit expression is thought to underpin excitotoxicity (Liu et al., 2007). Interestingly, it has been suggested that tau interacts directly with NMDARs at the synapse via fyn kinase, which regulates GluN2B phosphorylation, regulating synaptic localisation (Ittner et al., 2010; Miyamoto et al., 2017; Mondragón-Rodríguez et al., 2012). In fact, in a tau KO mouse model, there was decreased extrasynaptic NMDAR receptor expression and function suggesting that tau may regulate extrasynaptic NMDARs (Pallas-

Bazarra et al., 2019). This mechanism seems to have some validity in human tauopathies as the genetic A152T mutation on the *MAPT* gene, which increases the risk for tauopathies, has also been identified as increasing the risk of NMDAR-mediated excitotoxicity (via the GluN2B subunit) (Decker et al., 2016; Maeda et al., 2016).

Whilst understudied compared to NMDARs, AMPARs are also implicated in tauopathy. In FTD patients, autoantibodies for the AMPAR subunit GluA3 were present in the CSF and serum (Borroni et al., 2017). Application of the autoantibodies to neuronal cultures saw a reduction in spine density, suggesting AMPAR dysfunction mediated by reduced GluA3 expression. Conversely, increased GluA1 expression was observed in the hippocampus in AD post-mortem brain tissue suggesting increased AMPAR expression in the brain (Marcello et al., 2012). In the CHMP2B mouse model of FTD and in FTD patients, there were significantly reduced levels of miRNA for AMPAR subunits GluA2-4 (Gascon et al., 2014).

Work in tau KO cultured neurons revealed mislocalised GluA2 puncta and abnormal GluA2-containing AMPARs being trafficked out of the synapse under normal physiological stimulation, implying a role of tau in regulating AMPAR localisation (Suzuki and Kimura, 2017). Phosphorylation of tau at different sites can differentially reduce AMPAR activity in cultured neurons, suggesting that tau can also mediate reduced AMPAR expression or hypoactivity (Teravskis et al., 2019). In line with this, downregulation of genes that express AMPAR subunits (Alldred et al., 2012) and reductions in AMPAR subunit expression (Hoover et al., 2010; Kopeikina et al., 2013a) have been observed in the rTg4510 model of tauopathy and in cultured rTg4510 neurons. Conversely, AMPAR-mediated activity was increased in the rTg4510 model in the hippocampus and frontal cortex following neurodegeneration onset (Crimins et al., 2011, 2012; Dalby et al., 2014). Overall, it seems that there is reduced expression or hypofunction of AMPARs with mislocalisation from the synapse, induced by tauopathy. One mechanism of tauopathy-induced AMPAR dysfunction could also be a subunit switch from Ca^{2+} impermeable to Ca^{2+} permeable GluA2 containing AMPARs, which could lead to excessive Ca^{2+} influx and synaptic dysfunction contributing to glutamate excitotoxicity (Whitehead et al., 2017). AMPAR activity also

facilitates the release and spread of tau between neurons, promoting the trans-synaptic spread of pathological tau (Pooler et al., 2013).

1.4.3.2 Altered synaptic stability and plasticity in tauopathy

Excitatory networks of connected neurons are highly flexible, with input deprivation leading to restructuring of local networks by recruiting neighbouring silent neurons and by changing the strength, shape, timing, and number of synaptic connections (Albieri et al., 2015; Barnes et al., 2015b, 2015a, 2017; Cheetham et al., 2014). In neurodegenerative diseases such as tauopathies, it is likely that there are similar changes occurring within networks to help preserve established behaviours. In fact, it has been suggested that there is homeostatic compensation in response to loss of synaptic connections by surviving neurons to maintain the network activity, by changing excitability, dendritic restructuring, and the formation of novel synaptic connections (Crimins et al., 2011, 2012, 2013). This could explain why some behaviours are preserved in the rTg4510 model of chronic tauopathy following progressed neurodegeneration (Kuchibhotla et al., 2014).

Within these networks, it has been evidenced that spine and bouton turnover is increased in prodromal tauopathy in the rTg4510 model, suggesting a lack of synaptic stability (Jackson et al., 2017, 2020). In addition, there are an increased proportion of filopodia compared to more mature stable synaptic structures in the same model (Crimins et al., 2011). This would imply a lack of access to functional molecular machinery, such as AMPARs and PSD proteins, required to stabilise and strengthen synapses (Ehrlich et al., 2007). Functional assessment of plasticity in mouse models of tauopathy suggests alterations in both short- and longer-term plasticity mechanisms (Booth et al., 2014, 2016a; Gelman et al., 2018; Hill et al., 2019; Sydow et al., 2011).

1.5 NEURAL NETWORK ACTIVITY

Higher-order mental processes such as cognition require local coordinated activity within microcircuits, and more distal coordinated activity across regional hubs. Synchronisation of such assemblies is thought to be fulfilled by rhythmic oscillations in the brain (Buzsaki, 2006). Oscillations are assumed to be generated via the balance of local excitatory and inhibitory neuronal interactions or by intrinsic cellular mechanisms (Fell and Axmacher, 2011; Schnitzler and Gross, 2005). Subregional oscillations help coordinate the timing of local

neuronal activity, whereas transregional synchronous oscillations are hypothesised to help with the transfer of information by facilitating long-range neuronal communication (Gupta et al., 2016; Schnitzler and Gross, 2005; Singer and Gray, 1995). Oscillations are hypothesised to play a critical role in complex behaviours, temporal coding, information processing and transfer, and neuronal computation and storage (Buzsaki, 2006; Fell and Axmacher, 2011). Non-invasive electrophysiological techniques, such as electroencephalogram (EEG) recordings, can be used to measure this activity at the level of coordinated neuronal ensembles within the human brain.

1.5.1 Up and down states

Anaesthetics such as urethane induce a slow wave oscillation termed up and down states, comparable to those generated in slow wave sleep and quiescent wake, and is used as a model of synchronous cortical network activity (Neske, 2016). This bistable oscillation fluctuates neuronal membrane potentials between hyperpolarised and depolarised membrane voltages at a low frequency (<1 Hz), referred to as down and up states respectively (Steriade et al., 1993a; Wilson and Groves, 1981). It is thought that these two states are generated and maintained due to a balance of excitation and inhibition within neuronal networks, in addition to intrinsic cellular properties (Egorov et al., 2002; Haider et al., 2006; Neske, 2016; Wilson and Cowan, 1972). Studies within the thalamocortical network suggest that up and down states can be self-sustained with a cortical column, but also receive periodic input from the thalamus to help synchronize neuronal populations (Sheroziya and Timofeev, 2014; Steriade et al., 1993b; Timofeev et al., 2000). Therefore, measuring different properties of this oscillation can provide insight into the local excitatory and inhibitory network activity, making it a reasonable model to study cortical network dynamics.

By studying evoked responses under anaesthesia, the contribution of synaptic activity can be more easily isolated in conditions of reduced local and global activity associated with awake states. Evoked responses induced by whisker stimulation in the somatosensory cortex are multicomponent post-synaptic potentials, comprised of glutamatergic and GABAergic components, providing a system to experimentally drive synaptic activity *in vivo* (Gambino et al., 2014; Lavzin et al., 2012; Lebedeva et al., 2019). Evoked responses are modulated by up and down state phase, with reduced amplitude of evoked responses on up

states compared to down states (Ferrarese et al., 2018; Gambino and Holtmaat, 2012; Petersen et al., 2003; Sachdev et al., 2004). Therefore, this system can also be used to measure local network influence on controlling synaptically-driven activity.

1.5.2 Neural network dysfunction in tauopathy

Work within models of tauopathy has tried to ascertain more generalised tauopathy-induced network disruption. Infusion of tau fibrils into a pathology free region within the P301S model of tauopathy, saw a reduction in spontaneous neuronal activity (measured via cellular Ca^{2+} imaging) independent of NFT presence (Marinković et al., 2019). Functional connectivity, as detected using functional magnetic resonance imaging, was also significantly reduced in mouse models which overexpress anti- or pro-aggregant tau isoforms (Green et al., 2019). Network silencing has been observed in the chronic rTg4510 model of tauopathy, as measured by Ca^{2+} imaging of spontaneous neuronal activity (Busche et al., 2019; Jackson et al., 2017). Within the same model, whole-cell recordings revealed a reduction in the principal frequency of up and down states, a reduction in the number of up states, and increased false up state transitions (Menkes-Caspi et al., 2015). These data suggest that there is typically a reduction in network activity in tauopathy. There is also evidence for network compensation in the face of the pathological accumulation of tau (Crimins et al., 2013). Other studies within the rTg4510 model revealed preserved visually evoked responses and head direction cell functionality, when other functionalities that also depend on the network were disrupted (Kuchibhotla et al., 2014; Ridler et al., 2019). These observed differences in neuronal dysfunction between different cortical regions may reflect the level of pathological burden within each region, or the level of dysfunction in cortical and subcortical inputs to these neurons.

1.6 AIMS

The pathogenic accumulation of tau is implicated in cognitive impairment, with tauopathies displaying progressive, age-associated neurodegeneration associated with dementia. It is known that tauopathy can alter synaptic function (Jackson et al., 2017), neuronal excitability (Crimins et al., 2012), and network activity (Menkes-Caspi et al., 2015). However, the sequence of pathophysiological changes occurring early in the neurodegenerative process in tauopathy is unclear. Deconstructing the sequence of events triggered by tauopathy and how this is compensated for functionally, would provide an opportunity to identify mechanisms that can delay cognitive decline. Also, interventions targeting earlier stages of the disease would provide an opportunity for full symptomatic rescue prior to overt cell loss. Therefore, this thesis aims to delineate the relationship between tau pathology, and changes in neuronal morphology and function in the earlier neurodegenerative stages of tauopathy, in addition to characterising how alterations manifest in more advanced stages of tauopathy. This work was performed in the somatosensory cortex of the rTg4510 mouse model of tauopathy with the following aims:

1. To examine the effects of prodromal tauopathy on synaptic and neuronal physiology, neuronal morphology, and receptor expression *in vitro* to identify biomarkers of dysfunction. Whilst it is known that tau can affect both synaptic and neuronal physiology, little is known about what alterations occur early in the neurodegenerative process and how these interact within the brain.

2. To explore how tauopathy-driven dysfunction *in vitro* manifests in neuronal circuits *in vivo,* and the impact this has on network physiology. The local network imposes some regulatory control over intrinsic and synaptic properties, noticeable under up and down state oscillations. Within a functional network, there is likely to be some masking of synaptic and neuronal dysfunction that may be seen *in vitro* providing compensatory control.

By characterising the effects of prodromal tauopathy using multiple *in vitro* and *in vivo* techniques, this work aims to increase our understanding of the functional impact, and structural and biochemical alterations in early tauopathy-mediated neurodegeneration.

2 NEUROPHYSIOLOGICAL CHARACTERISATION OF THE SOMATOSENSORY CORTEX SHOWS SUBTLE SYNAPTIC AND NEURONAL DYSFUNCTION IN RTG4510 MICE IN PRODROMAL TAUOPATHY

2.1 INTRODUCTION

Abnormal tau pathology has been shown to affect neurophysiological function, ranging from synapses to networks (Ahnaou et al., 2017; Marinković et al., 2019; Stancu et al., 2015; Zhou et al., 2017). Different functional phenotypes can be seen within the same mouse model, which would likely be related to the onset and progression of pathology within that cellular population. For example, dysfunctional characteristics identified in the rTg4510 mouse model at a young age (2 months (2M)) in the frontal cortex and hippocampus, either persisted or were absent at older ages (9M) with the emergence of other novel functional changes (Crimins et al., 2011, 2012; Hatch et al., 2017). Recent work characterising pre-neurodegeneration physiology (~5M) in the rTg4510 model revealed specific alterations in synapse dynamics and neuronal activity. This included increased spine turnover and an increase in silent neurons (i.e. non active neurons), eluding to altered synaptic function and reduced neuronal excitability (Busche et al., 2019; Jackson et al., 2017; Menkes-Caspi et al., 2015). However, these studies measured action potential (AP) related Ca^{2+} transients as a proxy of neuronal activity, and therefore synaptic and neuronal electrophysiology were not explicitly measured within these studies. Therefore, this chapter aimed to characterise synaptic and neuronal function in the rTg4510 model of tauopathy at an early neurodegenerative phase (~5.5M) using *in vitro* whole-cell patch clamp electrophysiology in the somatosensory cortex. Characterising changes in synaptic and neuronal function at this age would highlight potential mechanisms that may be underpinning dysfunction. Synaptic function was also examined at more progressed neurodegenerative phases (~7.5M) to assess whether any changes seen in synaptic function persisted following neurodegeneration onset, or whether the changes were a transient and perhaps compensatory response to neurodegeneration.

2.1.1 Synaptic function in rTg4510 mice

Synaptic degeneration is currently the best correlate of cognitive decline in AD (Scheff et al., 2006, 2007), and therefore it is paramount to understand synaptic alterations that likely correspond to degeneration that occurs over the disease (Jackson et al., 2019).

In the rTg4510 mouse model, measures of total synapse density were maintained at 5.5M of age in the somatosensory cortex, with a reduction in synapse density occurring by 8.5M with a corresponding loss of neuropil volume (Jackson et al., 2017; Kopeikina et al., 2013a). Excitatory neurons in the model exhibit reduced dendritic spine density by 8.5M (with inhibitory synapse density still unexplored) (Kopeikina et al., 2013a; Rocher et al., 2010). Prior to reductions in spine density, there is an observable shift from larger, more “mature” mushroom type dendritic spines in favour of thin filopodia spines (less mature, more likely transient), with a significant increase in spine turnover to presumably help compensate for the loss of mushroom type spines (Crimins et al., 2011, 2012; Jackson et al., 2017). A change in the distribution of synapse shape and size from larger more stable mushroom type spines to filopodia and other smaller subtypes would likely correlate with alterations in the composition of glutamatergic receptors in synapses (Araya et al., 2014; Bourne and Harris, 2007). For example, larger mushroom spines typically have increased expression of AMPA receptors (AMPARs) at the synapse leading to increased synaptic strength (Araya et al., 2014; Fischer et al., 2000). Therefore, this shift in the distribution of spine shape is likely to alter glutamatergic signalling in the model, such as AMPAR or NMDA receptor (NMDAR) -mediated activity.

Synaptic activity in the frontal cortex, characterised using whole-cell electrophysiology, revealed an increased frequency of spontaneous excitatory post-synaptic currents (sEPSC) at ~9M in the rTg4510 mouse model (Crimins et al., 2011). However, this increase was specifically in a subpopulation of neurons with a non-atrophic structure compared to atrophic neurons (Crimins et al., 2012). In addition, the distribution of event amplitudes were different between these two subpopulations of neurons, suggesting a homeostatic change in glutamatergic transmission in neurons with differing levels of pathology (Crimins et al., 2012). Cultured neurons from the rTg4510 mouse model have shown reduced sEPSC amplitude and frequency which is related to changes in glutamatergic receptor distribution (Hoover et al., 2010). In addition,

changes in short-term synaptic plasticity, such as a reductions in the paired-pulse ratio, has been seen in the hippocampus at age points prior to the onset of neurodegeneration in the rTg4510 model (Gelman et al., 2018; Hoover et al., 2010). Further characterisation of glutamatergic synaptic activity and short-term plasticity in the somatosensory cortex is therefore needed to define and clarify the changes that are specifically occurring in this model in relation to neurodegeneration.

2.1.2 Neuronal function in rTg4510 mice

Studies performed in aged rTg4510 mice (7+ months old) have revealed a hyperexcitability phenotype in neurons in the hippocampus and cortex (Booth et al., 2016a; Crimins et al., 2011, 2012). Neurons in the hippocampus and medial entorhinal cortex have altered firing rate synchrony to local oscillations and a change in phase encoding to oscillations (Booth et al., 2014, 2016b; Witton et al., 2016). Reductions in AP related Ca^{2+} transients, measured by fluorescence imaging techniques, suggests a reduction in AP firing earlier in the model (4/5M) (Busche et al., 2019; Jackson et al., 2017). Changes in excitation would alter signal encoding and shape the dynamics of network activity (Booth et al., 2016a; Johnston and Wu, 1994). This could have consequences for complex cognitive behaviours that require coordinated neural activity between multiple brain regions.

Whole-cell recordings in the hippocampus revealed a hyperexcitable phenotype (increased rheobase) pre- but not following neurodegeneration onset (Hatch et al., 2017). However, a hypoexcitable phenotype was observed (decreased input resistance and rheobase) in the frontal cortex pre-neurodegeneration (Crimins et al., 2012). Interestingly, one paper saw a decrease in AP amplitude only at the more advanced age points (9-13M), suggesting that different neurophysiological alterations can appear in a progressive manner in the rTg4510 mouse model (Crimins et al., 2012). A depolarised resting membrane potential, alterations in hyperpolarisation-activated currents (sag) and changes in the AP waveform have been shown across ages within the rTg4510 model in the hippocampus and frontal cortex, with some of these changes unrelated to mature tau pathology (Crimins et al., 2012; Hatch et al., 2017; Kuchibhotla et al., 2014; Rocher et al., 2010). Defining any changes in intrinsic neuronal properties in the early neurodegenerative phase of tauopathy in the rTg4510 mice in the somatosensory cortex may identify changes that precipitate into progressed dysfunction with neurodegeneration.

2.2 AIMS

From work by Jackson et al., 2017, it is likely that synaptic function is altered at ~5.5M of age in rTg4510 mice in relation to the observed changes in dendritic turnover and degeneration. Therefore, this work aimed to characterise excitatory synaptic function early (~5.5M) and at more progressed neurodegenerative age points (~7.5M) using *in vitro* whole-cell patch clamp electrophysiology in littermate rTg4510 and wildtype control mice. This would provide a more definitive picture of the changes occurring in single cells by directly measuring synaptic function using whole-cell patch clamp electrophysiology. In addition, this work characterised neuronal function (passive and active intrinsic neuronal properties) at an early neurodegenerative phase (~5.5M) of tauopathy using *in vitro* whole-cell patch clamp electrophysiology in littermate rTg4510 and wildtype control mice. Neuronal excitability, for example, may be altered and thus link to changes in the frequency of synaptic currents. Therefore, quantifying changes in synaptic function and neuronal function should provide insight into the electrophysiological changes that are occurring at a single cell level at a phase where dendritic spine stability is decreased.

2.3 METHODS

2.3.1 Ethical approval

This study was approved by the University of Exeter Animal Welfare Ethical Review Board. All procedures, including Schedule 1 procedures, were performed in accordance with the UK Animal (Scientific Procedures) Act 1986 and its subsequent amendment in 2012 to align with European Directive 2010/63/EU on the protection of animals used for scientific purposes.

2.3.2 Animals

2.3.2.1 rTg4510 mice

Male rTg4510 (TG) mice and wildtype (WT) littermate controls were bred at ENVIGO (Oxon, UK) and provided by Eli Lilly & Company. These mice were kept on a 12:12 light/dark cycle, with *ad libitum* access to food and water. TG mice were carriers for both the tetracycline transactivator and P301L mutant tau, whereas WT mice were null for both transgenes. Animals were transferred to a vivarium at the University of Exeter and were habituated to the new environment for at least two weeks prior to experiments. At the University of Exeter, mice were single housed, kept on a 12:12

light/dark cycle, and granted *ad libitum* access to food and water. Experiments and analysis were performed blind with respect to genotype.

The TG mouse has specific synaptic deficits at 5-6 months which occurs just prior to neurodegeneration onset at 6-7 months (Jackson et al., 2017; Kopeikina et al., 2013a; Ramsden et al., 2005; SantaCruz et al., 2005). Therefore, the mice used in this chapter were at ~5.5 months of age (pre-neurodegeneration onset) and ~7.5 months of age (following neurodegeneration onset). Experiments were done in batches of littermate animals with details shown below (Table 2.1):

Table 2.1 Experimental batches of animals. Experiments were performed on three batches of animals. Each batch were composed of WT and TG littermates. The second and third column details the n numbers, and details about the age of the animals used in weeks.

Animal batch	*WT group details*	*TG group details*
Batch 1 (synaptic properties at ~5.5M)	N: 10 animals Range: 19.6 – 24.4 weeks Mean: 22.4 weeks	N: 10 animals Range: 19.9 – 25.1 weeks Mean: 22.5 weeks
Batch 2 (intrinsic neuronal properties at ~5.5M)	N: 5 animals Range: 21.7 – 26.4 weeks Mean: 24 weeks	N: 5 animals Range: 22.2 – 24.7 weeks Mean: 23.9 weeks
Batch 3 (synaptic properties at ~7.5M)	N: 5 animals Range: 31.4 – 33.9 weeks Mean: 33 weeks	N: 5 animals Range: 32.4 – 34 weeks Mean: 33.2 weeks

2.3.3 *In vitro* whole-cell patch clamp recordings

2.3.3.1 Slice preparation

All experiments began approximately between 10:00 and 12:00 (3-5 hours post lights on) to reduce experimental variation due to circadian effects (Bridi et al., 2020). Mice were sacrificed using cervical dislocation. The brain was then quickly removed with care and placed into an ice cold sucrose solution containing (in mM): 189 Sucrose, 10 D-Glucose, 26 $NaHCO_3$, 3 KCl, 5 $MgSO_4.7H_2O$, 0.1 $CaCl_2$ and 1.25 NaH_2PO_4 bubbled in carbogen (95% O_2, 5% CO_2).

The brain was dissected to produce thalamocortical slices as described by Agmon & Connors, 1991 (Figure 2.1 A) with slices prepared on a Leica VT1200 vibratome. To produce slices, the brain was removed from sucrose solution and placed on a custom block (Figure 2.1 B) with a 10° slope, with the rostral end pointing down the slope (Figure 2.1 A). The midline of the brain was aligned to be parallel with the edges of the slope. A cut was made at an angle of 55° from the midline as close to the olfactory bulbs as possible and the rostral tissue was discarded. The cerebellum was cut off and discarded and the brain was superglued with the rostral side face down onto the specimen holder (Figure 2.1 A). Slices of ~800 µm were cut and discarded until one hippocampal hemisphere was visible at ~-2.7 mm anterior-posterior from bregma. Cutting speed was then reduced to 0.09 mm/s and cutting thickness was reduced to 300 µm. Approximately 5 thalamocortical slices were cut to a thickness of 300 µm with ~4 of these slices containing the region of interest (visible barrel fields in layer IV of somatosensory cortex; Figure 2.1 C). Slices were removed from the chamber and placed into room temperature (~20°C) artificial cerebrospinal fluid (aCSF) composed of (in mM): 124 NaCl, 3 KCl, 24 $NaHCO_3$, 2 $CaCl_2$, 1.25 NaH_2PO_4, 1 $MgSO_4$, 10 D-Glucose bubbled in carbogen (95% O_2, 5% CO_2). Slices were left to recover in room temperature aCSF for at least 1 hour before experimentation.

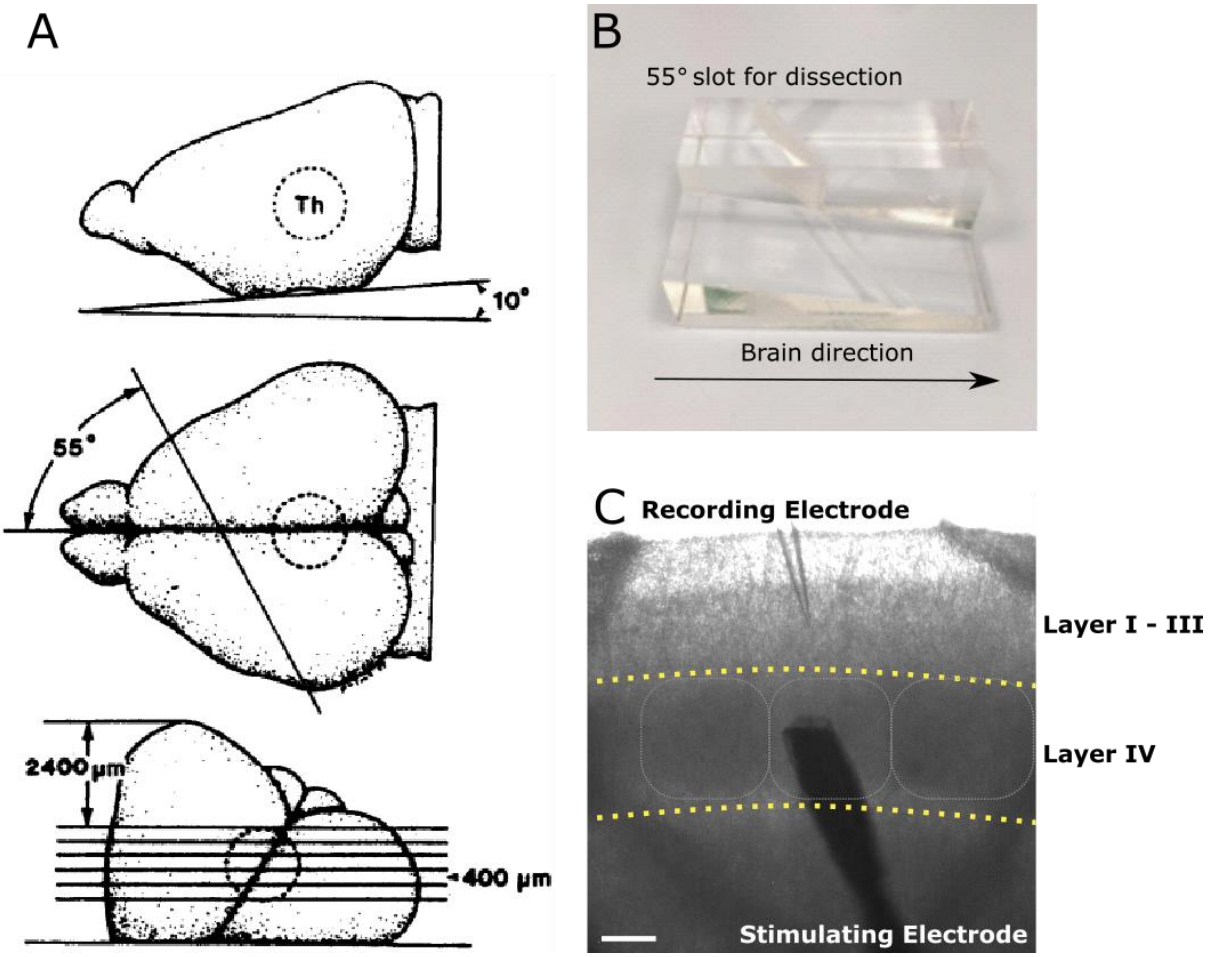

Figure 2.1 Thalamocortical slice preparation based on Agmon & Connors, (1991). An overview schematic of the preparation of thalamocortical slices (**A**), adapted from Agmon & Connors, (1991). A photograph of the cutting block used to make thalamocortical slices with annotations (used with permission from Michael T. Craig; **B**). An example image of a slice with barrel fields (highlighted with a yellow dotted line) showing the typical positioning of the recording and stimulating electrode under a 4x objective (**C**). Scale bar = 0.15 mm

2.3.3.2 Electrophysiological recordings

2.3.3.2.1 Recording solutions

A slice was placed in the recording chamber, held using a small metal harp, and was continuously perfused with oxygenated aCSF (flow rate ~2 ml/min) maintained at a temperature of ~33 °C. Drugs applied during *in vitro* recordings were bath applied with details shown in Table 2.2. All slice recordings were performed with bath applied Gabazine, a $GABA_A$ receptor antagonist, in the aCSF to allow isolation of excitatory responses by blocking feed-forward inhibition following electrical stimulation.

Recording electrodes were fabricated on a P-97 Flaming Brown micropipette puller (Sutter Instrument Co.) to a resistance of 3-7 MΩ. Electrodes were then filled with an intracellular solution (made as specified in Table 2.3).

Table 2.2 Drugs applied to the aCSF during neurophysiological recordings. A table showing details of the drugs applied to the extracellular solution (aCSF) for recordings. Drugs were added into the aCSF to produce the concentrations listed from stock solutions.

Drug	*Property*	*Catalogue no.*	*Company*	*Concentration in aCSF*
Gabazine	$GABA_A$ receptor antagonist	AB120042	Abcam, UK	5 µM (stock solution in dH_2O)
L689560	NMDA receptor antagonist	0742	Tocris, UK	5 µM (stock solution in DMSO)

Table 2.3 Intracellular solution compositions. A table showing the composition of the intracellular solutions used with concentrations in mM. All intracellular solutions were adjusted to pH 7.3 using CsOH for solution 1 and KOH for solution 2. The osmolarity of all solutions were ~295 mOsm.

Concentrations in mM	*Solution 1: $CsMeSO_4$*	*Solution 2: KGluconate*
$CsMeSO_4$	120	-
K-Gluconate	-	135
NaCl	6	5
QX314-Cl	5	-
HEPES free acid	10	10
EGTA	-	0.2
BAPTA	10	-
GTP-2Na salt	0.3	-
GTP-Na salt	-	0.3
ATP-Mg Salt	4	4
Biocytin	13.4	13.4

Recording voltages were corrected for a liquid junction potential error (JPE) of -15 mV for solution 1 and -10 mV for solution 2, based on a theoretical value calculated from the solution compositions, which arose due to the different concentrations of electrolytes between the aCSF and the intracellular electrode solution.

2.3.3.2.2 Barrel visualisation – region of interest identification

The somatosensory cortex contains discrete regions in layer IV known as barrel fields. These are darker elliptical fields which can be seen in Figure 2.1 C, with visual changes in darkness between the layers used to identify layer IV for stimulation electrode placement. Layer IV axons primarily innervate layer II/III neurons within the same cortical column, as part of the lemniscal whisker-sensing pathway, and so stimulation in layer IV should evoke synaptically-driven responses in layer II/III (Lefort et al., 2009).

Slices were visualised using a monochrome camera (Thorlabs, USA, Cat# DCC1545M) under either a 4x or 40x objective. A twisted wire stimulating electrode

(Scientifica, UK) connected to a constant-current isolated stimulator box (Digitimer, UK) was placed as close as possible to the centre of the barrel under 4x magnification. The stimulating electrode was then found under 40x magnification, and whole-cell patch clamp recordings were made from neurons located between the stimulating electrode and the edge of the brain slice (pia). This ensured that neurons were recorded in the same cortical column as the barrel, targeting putative pyramidal neurons in layer II/III specifically. Following recordings, coordinates of the cell in relation to the slice orientation and distance from the hippocampus were noted to allow for subsequent histological identification of recorded neurons.

2.3.3.2.3 Recording protocols: Characterisation of in vitro synaptic function

All recording protocols were optimised in pilot experiments using C57Bl/6J mice aged between 3-8 months (data not shown).

These recording protocols were performed using animals in Batch 1 (~5.5M) and 3 (~7.5M; Table 2.1). Recordings of *in vitro* synaptic function were performed in voltage clamp (VC) using intracellular recording solution 1 ($CsMeSO_4$ based; Table 2.3). Raw signals were lowpass filtered at 5 or 10 kHz, with 10x output gain and sampled at a rate of 20 kHz.

Signals were amplified using either an Axopatch 200B (Molecular Devices, USA) or a Multiclamp 700A (Molecular Devices). All were digitised using an Axon Digidata 1550 analogue-to-digital converter (Molecular Devices) and recorded on a PC using pClamp v10.4 (Molecular Devices).

Following recordings, brain slices were transferred into 4% PFA in 0.1 M PBS and fixed overnight. Slices were then stored in 0.1 M PB until needed.

2.3.3.2.3.1 Characterisation of in vitro synaptic function: Spontaneous excitatory postsynaptic currents (sEPSC)

sEPSCs were measured during the second minute post break-in, with the cell being held at fixed voltage of -70 mV. An example recording trace is shown in Figure 2.7 A.

2.3.3.2.3.2 Characterisation of in vitro synaptic function: NMDA:AMPA receptor response ratios

For recording NMDA:AMPA receptor response ratios, an electrical stimulus was applied using the stimulating electrode placed in layer IV. The duration was set at 1

ms and the intensity was changed to evoke a consistent EPSC response approximately between 50-150 pA in amplitude (range 10 pA-180 pA, with a mean response of 58 pA and a mean electrical stimulation intensity of 129 mA (range 10-900 mA)), based on the protocol described in (Booth et al., 2014). This stimulus intensity was kept constant throughout the rest of the recording protocols.

NMDA:AMPA receptor response ratios were measured by recording the response of the cell to a single stimulus at -70 mV, then at +40 mV, to get the AMPAR and NMDAR response values respectively. The response at +40 mV was composed of both AMPAR and NMDAR activity, and so 50 ms was chosen as a time point post stimulus to quantify the NMDAR-mediated component of the response. This time point was deemed to be past the end of the fast AMPAR-mediated activity, whilst still including NMDAR activity (assessed in pilot studies – data not included). The NMDAR antagonist, L689560 (5µm, Abcam; Table 2.2), was added to the extracellular aCSF in a subset of experiments to confirm that the recorded NMDA value was composed of NMDAR activity (Figure 2.2). The drug was washed on the slice continuously for at least 10 minutes prior to recordings (a reduction in the NMDAR evoked response leading to a corresponding reduction in the NMDA:AMPA ratio was seen after 5 minutes in pilot experiments - data not shown).

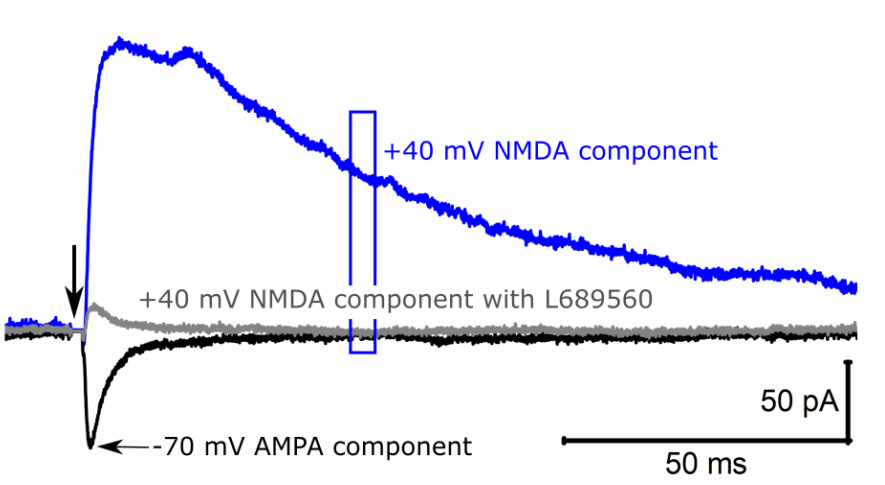

Figure 2.2 Measures of synaptic function: NMDA:AMPA receptor response ratios. Traces showing an example NMDAR and AMPAR response profile. The AMPAR component was taken as the peak amplitude at -70 mV, labelled and shown in black. The NMDAR component (blue line) was taken at +40 mV, as the recorded response value at exactly 50 ms post stimulus, with this time point highlighted on the trace in a blue box. This box also highlights the AMPAR-mediated response trace, showing that there is little contribution of AMPARs to the +40 mV response at this time point. This is emphasised by the response recorded following the application of the NMDAR antagonist, L689560 (5 µM; grey line). In this, and in all subsequent figures, stimulus artifacts were removed from the trace for clarity. The black downward arrow denotes stimulus onset.

2.3.3.2.3.3Characterisation of in vitro synaptic function: evoked excitatory postsynaptic currents

To record evoked EPSCs (eEPSCs), the cell was held at -70 mV and electrical stimulation was applied to layer IV with the same settings mentioned above for recording NMDA:AMPA ratios. Six stimuli were delivered at 5 Hz every 18 seconds (15 second recording sweep, 3 seconds between sweeps) for 10 sweeps and responses were recorded. This was then repeated at 10 Hz and 30 Hz frequencies. Example responses are shown in Figure 2.3.

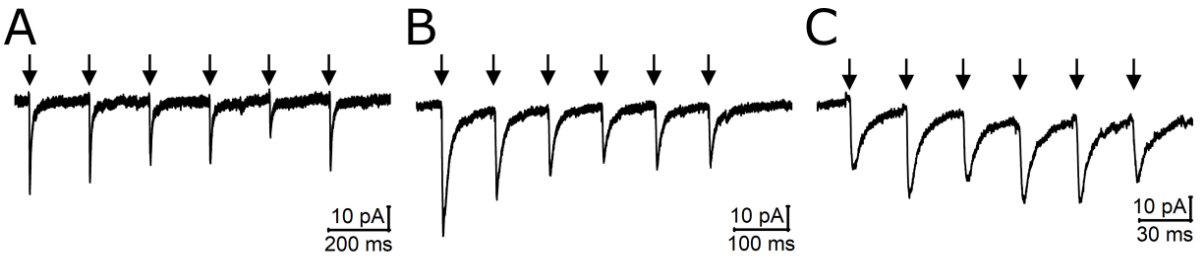

Figure 2.3 Example traces of eEPSCs. Representative traces showing eEPSC responses stimulated at 5 Hz (**A**), 10 Hz (**B**) and 30 Hz (**C**) in VC. Arrows denote stimulus onset.

2.3.3.2.4 *Recording protocols: Characterisation of in vitro intrinsic neuronal properties*

Recordings of intrinsic neuronal properties were performed in current clamp (CC) using intracellular recording solution 2 (KGluconate; Table 2.3). These recordings were performed using animals from Batch 2 (~5.5M; Table 2.1). Recordings were lowpass filtered at 10 kHz, with an output gain of 50x and sampled at a rate of 100 kHz. The bridge circuit of the amplifier was balanced at the start of each neuronal recording to give a more accurate measure of the membrane potential. Recordings were performed either at rest or the membrane potential was clamped at -70 mV (JPE corrected).

2.3.3.2.4.1 Characterisation of in vitro intrinsic neuronal properties: Passive and active electrical properties

A series of increasing current steps were injected for 500 ms, starting at -100 pA, increasing in 50 pA increments to + 300 pA. This was done at rest and at -70 mV (JPE corrected), and was used to determine passive electrical membrane properties from sweep 1 and excitability across all sweeps (Figure 2.4 A.).

Rheobase, the minimum amount of current needed to evoke an AP, was found by injecting a square pulse of increasing amplitude in 2 pA increments (200 ms pulse) at both rest and -70 mV (JPE corrected; Figure 2.4 B). The current step that evoked the first AP was taken as the rheobase, and AP properties were measured from this evoked AP.

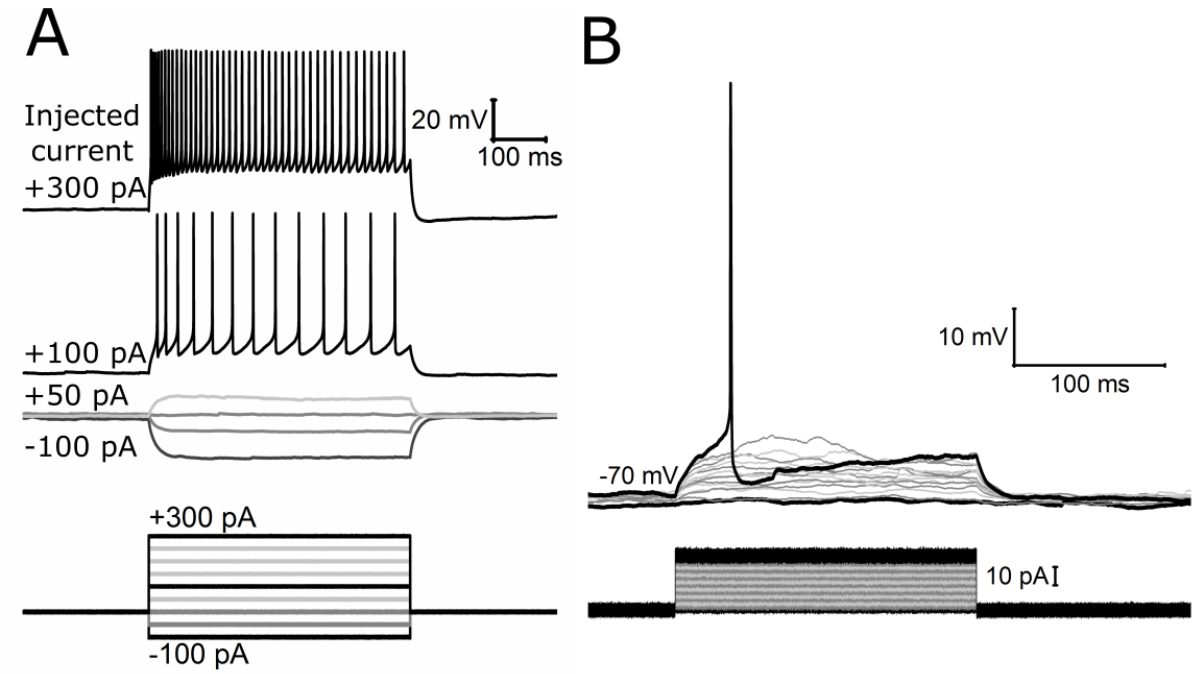

Figure 2.4 Passive and active electrical properties determined by square current injection. Current injections of increasing amplitude (sweeps) to evoke APs in cells with example responses to increasing current injection shown (**A**). An example rheobase protocol, where the minimum amount of current needed to evoke an AP was determined by injections of increasing current (**B**).

2.3.3.3 Analysis

2.3.3.3.1 Exclusion criteria

Cells were excluded based on the calculated series resistance at the start of recordings. To calculate series resistance, the cell was voltage clamped at -70 mV, and briefly depolarised to -65 mV using a square current injection. At the onset of this current injection, there was a large and fast capacitive transient, the amplitude of which is determined solely by the flow of charge through the recording electrode (the series resistance). The transient peak amplitude was quantified and by using Ohm's law (voltage = current x resistance), the series resistance was calculated by dividing the voltage step amplitude (5 mV) by the transient peak amplitude (pA). Cells with a series resistance greater than 40 MΩ were excluded from all *in vitro* data sets as this was greater than the 95th percentile distribution for the first batch of experiments (Batch 1, ~5.5M synaptic activity recordings).

Epileptiform activity was occasionally seen in recordings (~20% of recording sweeps excluded) when stimulating slices, due to the lack of $GABA_a$ receptor-mediated inhibition from bath application of Gabazine during recordings (Figure 2.5 B). This activity was considerably larger than the typical evoked response (typical evoked response was typically within the range of 50-150 pA, epileptiform activity was >400 pA; Figure 2.5 B). Any sweeps that appeared to have this activity were excluded from analysis, determined by visual inspection.

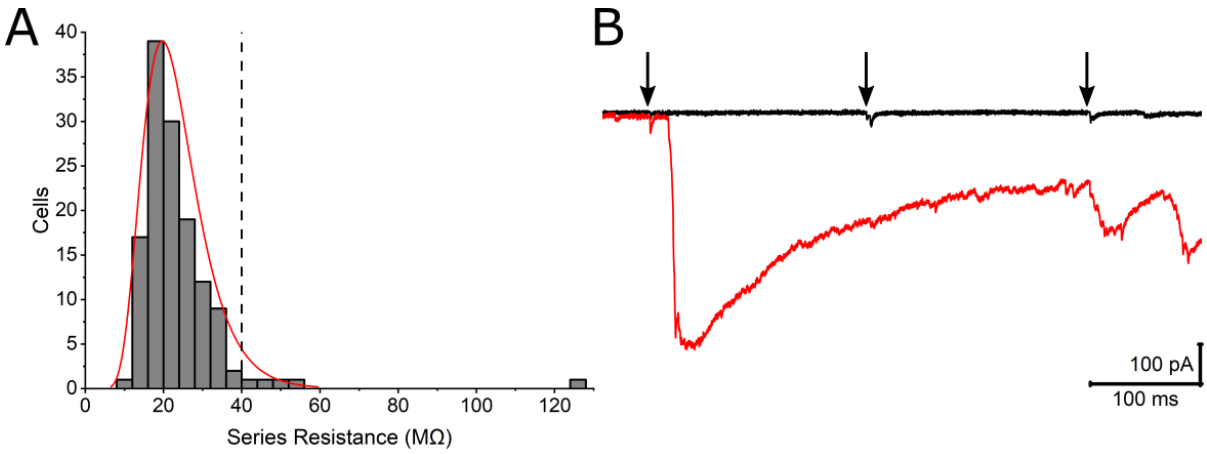

Figure 2.5 Exclusions criteria for in vitro recordings. A distribution plot of the recorded series resistance measurements per cell from Batch 1 (**A**), with the cut off criteria (determined as the 95th percentile of all series resistance measurements) shown as a dashed black line. An example of a typical evoked response to electrical stimulation (shown in black; **B**) and an epileptiform response to electrical stimulation shown in red from the same cell. Arrows denote electrical stimulations in **B**.

The experiments for the ~5.5M synaptic recordings (Batch 1) and the ~7.5M synaptic recordings (Batch 3) were performed 10 months apart, and between these batches the skill of the experimenter to record neurons improved significantly. This is reflected by a significant decrease in series resistance (generalised linear mixed model: genotype effect (p=0.97), batch(age) effect ($\chi^2_{(1, 227)}$ = 17.4, p<0.005***), interaction (p=0.37); Figure 2.6). An increased series resistance generally reflects poorer quality recordings, reducing the accuracy of recorded event kinetics. This would likely reduce the number of detected events as a function of increased noise, comparative to

recordings with lower series resistance. Due to this, these experimental batches were compared within age groups but not between age groups.

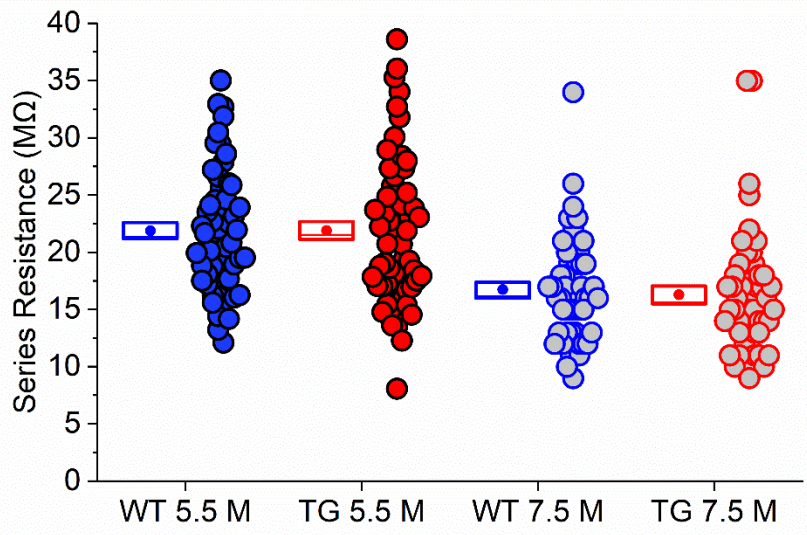

Figure 2.6 Series resistance of recordings from Batch 1 and Batch 3. A box and dot plot showing a significant decrease in series resistance in neuronal recordings between the ~5.5M and ~7.5M experiments. This and all subsequent box plots will show the mean represented by a filled circle within the box plot, the median as a line within the box, and the standard error of the mean (SEM) as the edges of the box. Individual cells are shown as filled circles to the right of the box plot.

2.3.3.3.2 sEPSCs

Analysis of sEPSCs was performed using a custom MATLAB code, with a sliding template fitting algorithm which scanned traces using a scaled template looking for matches (based on Clements & Bekkers, 1997). The framework for this code was provided by Michael C Ashby. Raw traces were filtered using a moving average filter with a window-size of 0.5 ms. The sum of squared error (SSE) between the filtered trace and a scaled EPSC waveform template (based on an idealized synaptic event consisting of an exponential rise and decay function) was calculated. A threshold of typically <20 SSE was used to detect sEPSCs. An overview of this is shown in Figure 2.7 C. sEPCS amplitude (peak height of sEPSC) and inter-event interval (time between sEPSC events) were calculated based on all extracted events. Rise time (10-90% time taken to reach peak from baseline) and decay T (10-90% time taken to decay

to baseline from a fitted exponential decay) were analysed based on the average waveform of the recording. An example of this is shown in Figure 2.7 B.

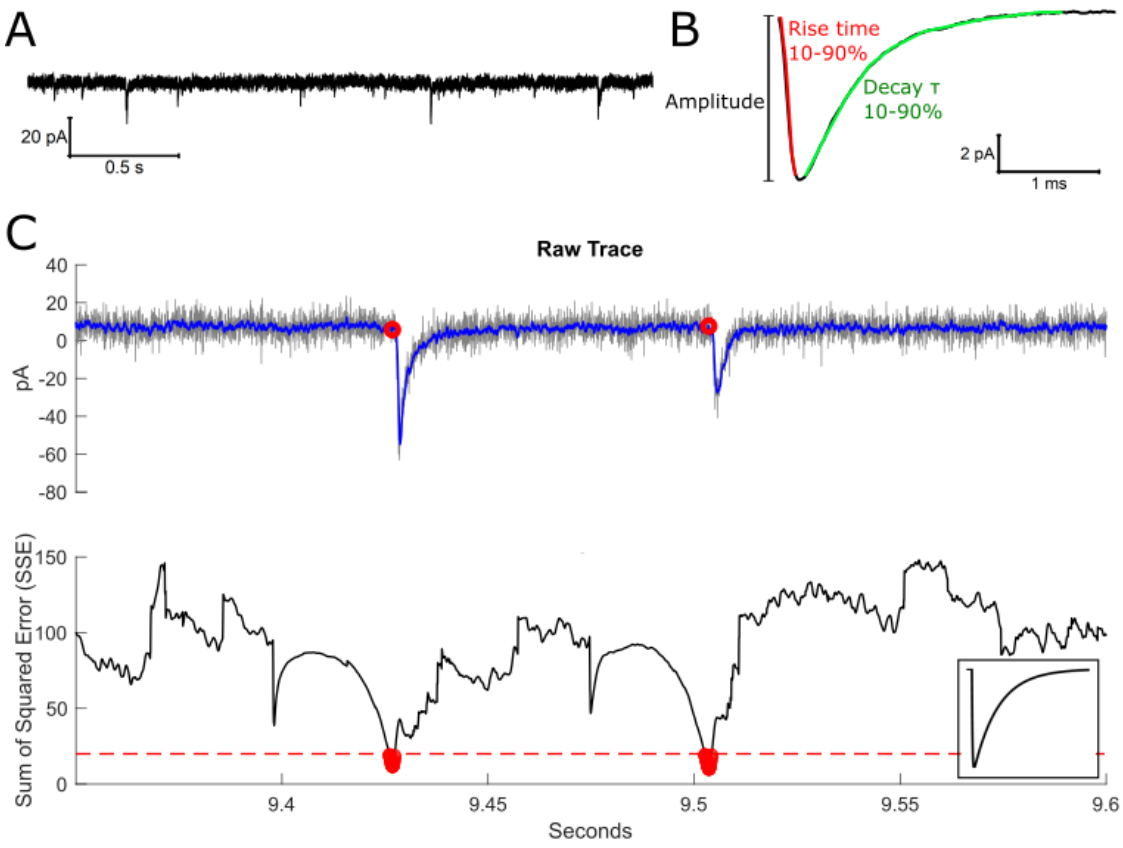

Figure 2.7 Measures of synaptic function: spontaneous activity. A representative trace showing spontaneous activity (**A**) with an average event waveform from one recording shown in **B**. Amplitude, rise time (in red) and decay T (in green) are labelled. Template scanning and analysis of spontaneous activity is shown in **C**. The top axis plots the unfiltered (grey) and filtered (blue) trace, with red circles highlighting detected events. The bottom axis plots the SSE when scanning the filtered recorded trace with a scaled waveform template (shown in inset). The detection threshold is shown as a dashed red line with red circles highlighting points past the threshold.

2.3.3.3.3 NMDA:AMPA ratios

For the NMDA:AMPA receptor ratio, the amplitude from baseline was measured at +50 ms post stimulus for the NMDAR-mediated component. This was divided by the peak amplitude of the AMPAR-mediated component (absolute peak at -70 mV) to produce an NMDA:AMPA ratio (Figure 2.2.). This was measured using custom MATLAB code, or manually analysed using Clampfit v10.4.

2.3.3.3.4 eEPSCs

For evoked EPSCs, peak amplitude was calculated using the baseline just prior to the evoked peak shown in Figure 2.8. This was performed per sweep for each evoked response.

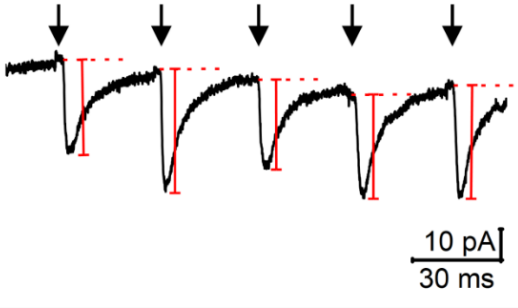

Figure 2.8 Quantification of eEPSCs. A representative trace showing evoked EPSCs (**A**) with a red dotted line showing the baseline value and the solid red line showing the quantified amplitude. Arrows denote stimulus onset.

The average response for each stimulation was then normalised to the first stimulus response amplitude using the following equation:

$$\text{Normalised eEPSC} = \text{eEPSC amplitude}_{(n)} / \text{eEPSC amplitude}_{(1)}$$

This measure was displayed per stimulus number as eESPC summation (changes in normalised response). The sum normalised area under the curve (i.e. the normalised change overall), was also measured to determine the overall facilitation or depression of the response and was calculated as the sum normalised response divided by 6. These analyses were completed using custom MATLAB code or manually using Clampfit v10.4.

2.3.3.3.5 Passive properties

Custom MATLAB code was used to analyse passive properties, with the framework provided by Jon T Brown. The resting membrane potential (RMP) was taken as the average membrane voltage prior to any current injection on the first sweep. Passive properties were taken from the first current injection step (-100 pA) which evoked a negative voltage deflection (Figure 2.9 A.). Input resistance (R_i) was calculated using Ohm's law, by calculating the mean voltage change at the steady state of the voltage

deflection, divided by the amplitude of the negative current injection (100 pA). An exponential curve was fitted to the response at the start of the current step, with the time constant T calculated from 10-90% of this curve. Another way of measuring R_i (extrapolated) was calculated from the exponential fit, extrapolated to a steady state response. This assesses R_i independently of I_h current (sag) activation. Similarly, sag was calculated using two methods. One measure of sag ("fit") was based on the exponential fit, calculating the difference between the change in voltage deflection at steady state compared to the extrapolated exponential curve at steady state. The other ("sub") was taken as the difference between the peak hyperpolarisation to the current step compared to the mean voltage change at steady state. An approximation of capacitance was calculated as T/input resistance.

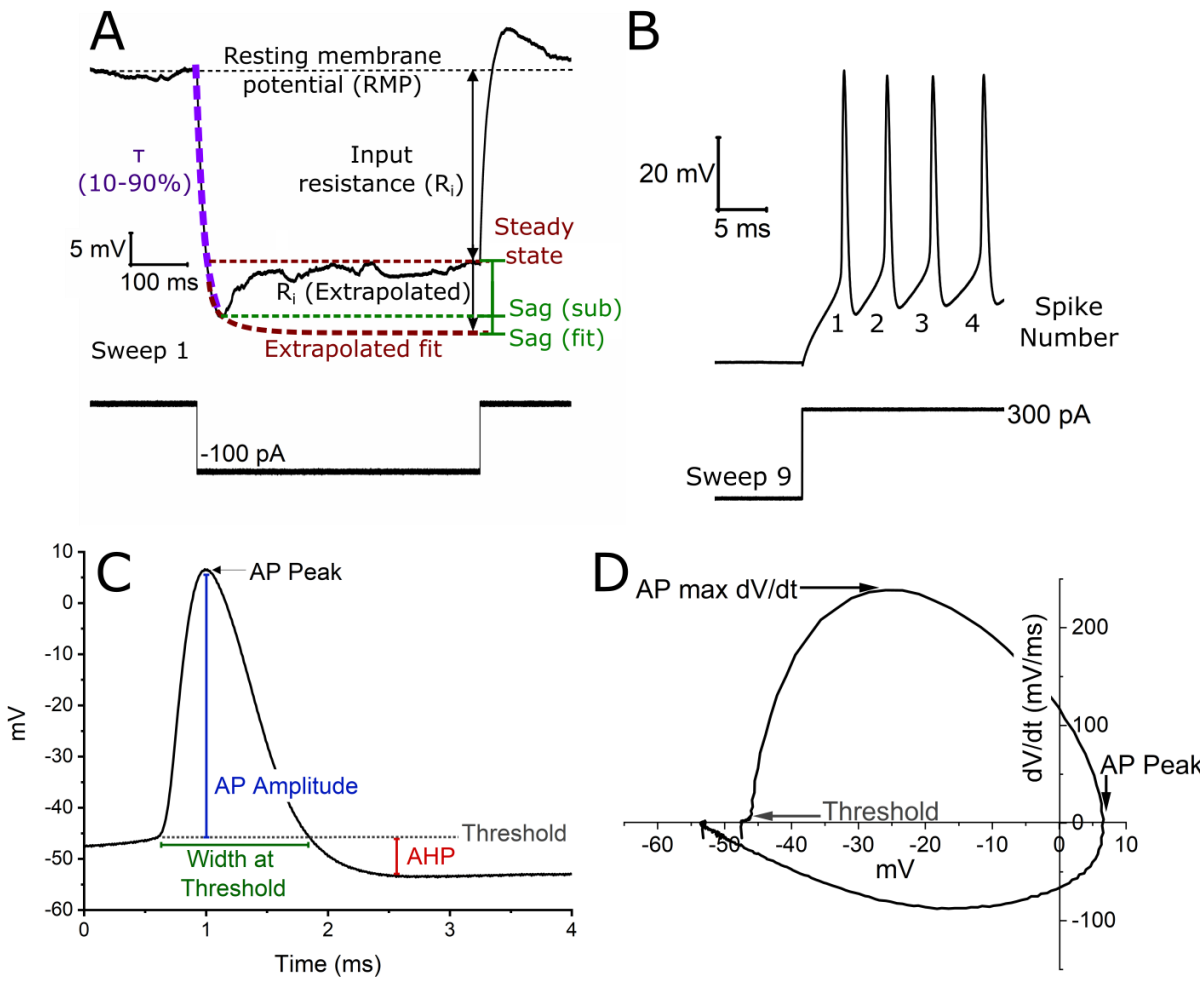

Figure 2.9 Passive and active electrical properties determined by square current injection. Sweep 1 showing a hyperpolarising response of the cell (shown in black) and the different properties analysed from this sweep (**A**). An extrapolated exponential fit was fitted to the start of the hyperpolarising response, shown in maroon. The point of steady state of the neuronal response is also labelled on in maroon. T was quantified as shown in purple from the exponential fit. RMP was taken as the measure just before the current injection, with the difference between RMP and neuronal steady state used to calculate one measure of R_i, indicated with black arrows. R_i extrapolated was calculated from RMP to the extrapolated fit steady state, also shown in black arrows. The sag current measures are labelled in green, with sag sub calculated from the peak hyperpolarising response and sag fit from the extrapolated fit. Sweep 9 showing a depolarising active neuronal response with spike number quantified (**B**). An AP waveform showing quantification of width at threshold (highlighted in green), AP amplitude (shown in blue), AP peak (labelled in black) and AP threshold (shown in grey) (**C**). The afterhyperpolarisation (AHP) is also labelled on in red. A phase-plane plot of the AP showing membrane potential (Vm) plotted against the rate of change (dV/dt) (**D**). Highlighted are AP peak, threshold (in grey) and the maximum rate of change (AP max dV/dt).

2.3.3.3.6 Active properties

Custom MATLAB code was used to analyse AP properties, with the framework provided by Jon T Brown. Excitability was explored by measuring the number of APs evoked in response to increasing amounts of injected current (Figure 2.9 B), with sweeps excluded if APs were deemed to be part of epileptiform activity (determined by visual inspection) as the recorded properties could be different in this scenario (Figure 2.5 B). Excess excitation under sustained input currents of increasing strength also led to depolarisation block, where neurons stop eliciting APs (Bianchi et al., 2012; Dovzhenok and Kuznetsov, 2012). This was observed in some recordings with higher current injections. These traces were manually quantified and excluded if not showing accurate AP waveforms, determined by visual inspection.

Rheobase was calculated as the minimum amount of current needed to elicit an AP. AP properties were analysed from this elicited AP (Figure 2.9 C). AP threshold was calculated from phase-plane plots, where dV/dt surpassed 30 $mV.ms^{-1}$ (Naundorf et al., 2006; Tamagnini et al., 2017; Figure 2.9 D). The AP peak was taken as the maximal voltage (mV) response with AP amplitude calculated as the difference between AP peak and AP threshold. AP width was measured as the width of the waveform at threshold and at -15 mV. Peak afterhyperpolarisation (AHP) was measured as the difference between AP threshold and the peak hyperpolarisation following the AP.

2.3.3.4 Statistics

Statistical tests were performed using R software (v3.5.1) with the RStudio (v1.1.456) integrated development environment.

The datasets were split into three experimental batches: Batch 1 (synaptic properties at ~5.5M), Batch 2 (intrinsic neuronal properties at ~5.5M), Batch 3 (synaptic properties at ~7.5M). Whilst Batch 1 and 3 have similar experimental conditions, there was a significant difference in the series resistance in these recordings (Figure 2.6 B). Therefore, for these results statistics were calculated per batch and not compared between batches.

The experimental unit for this work was individual cells, with the data presented and compared as such. Each cell may respond differently, with pathology potentially having differential effects per cell (Crimins et al., 2012). I specifically wanted to explore

how each individual cell behaved in the brain in pathological conditions. However, by the nature of the experimental design, multiple cells were sometimes recorded from single animals (nested variable) and cells from within one animal may be more similar compared to cells from other animals (pseudo-replication). Therefore, I used generalised linear mixed models (GLMM) to help statistically account for this to avoid pseudo-replication (Figure 2.10; Lazic, 2010; Moen et al., 2016). GLMMs are an extension of linear models such as analysis of variance tests (ANOVAs), that can account for sources of random variability from sampling (such as sampling multiple cells from the same animal) (McCullagh, 2018; Nelder and Wedderburn, 1972). It can also model data that has a non-linear distribution.

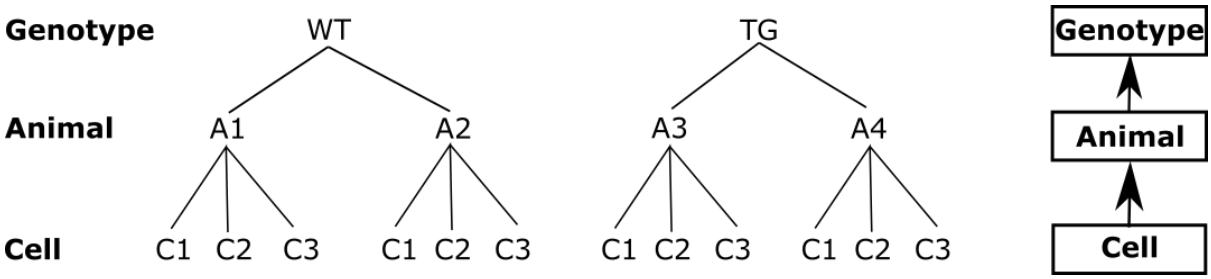

Figure 2.10 Diagram to show nesting of cells within animals for the two genotypes. A figure showing the hierarchy and clustering of cells to animals within genotypes. There were two genotypes in the study (WT and TG; fixed factor). Multiple cells could be recorded from a single animal (nested variable), and there could be an infinite number of animals and cells, which made animal number a random factor.

For this work, genotype was considered as a fixed factor and animal number was included as a random factor (Figure 2.10). Whilst slice number from animals could also be considered as a random effect, adding extra random variables with a low sample size would increase the dimensionality of the model whilst decreasing the modelling power (overly complex modelling for a low n number). In addition, slices from the same animal were handled in the same way, likely minimising variance between slices. Therefore, slice was not considered as a random factor in the statistical modelling.

Before modelling the data, the distribution was visualised using a histogram and quartile-quartile-plot and factored into the model when necessary (i.e. normal distribution, gamma distribution).

For results with single data points (i.e. where there was one measure from the cell such as mean Vm), the GLMM had the following structure:

$$Variable \sim Genotype + (1 \backslash AnimalNumber)$$

Variable of interest | Fixed factor (main effect) | Random factor (possible "random" effect on variable)

The main effect tested was the effect of genotype on the variable of interest. Random factors were included as 1\random factor using the R syntax for GLMM testing.

For results with repeated measures (i.e. multiple responses to a stimulus or paired measures within the same cell), the GLMM used had the following structure:

$$Variable \sim Genotype * RepeatedMeasure + (1 \backslash AnimalNumber | CellNumber)$$

Variable of interest | Fixed factor (main effect) | Modelled as a fixed factor (main effect) Repeated measures of the same variable | Interaction | Random factor (possible "random" effect on variable)

Similar to the first GLMM, the main effect of genotype on the variable of interest was statistically modelled. However, when repeated measures were taken, these were accounted for by factoring in the repeated measure (i.e. stimulus number) as a fixed interacting factor (interaction denoted by the asterisk). The repeated measure was modelled as a fixed effect, and cell number was factored in as a random effect as multiple measures were taken from the same cell.

The best model for the data was chosen based on the lowest Akaike information criterion (AIC) value along with other measures of fit from the model such as assessment of the residuals for normality and heteroscedasticity. The intraclass coefficient (ICC) was measured to determine whether animal number had a significant effect on the data variability (values greater than 0.1 were included, quantified on a scale of 0 to 1). If so, then a GLMM was used to examine the data. For ICC values of <0.1, t-tests were used to help reduce the dimensionality of the model and avoid an overly complex model with lower statistical power as t-tests are specifically recommended to test this type of data (Fiero, 2016).

For GLMMs, goodness of fit chi squared (χ^2) tests were used to evaluate the fit of each factor included within the model to determine the statistical significance within the model. Significant results were described as ($\chi^2_{(df, n)}$ = a, p=b*). This lists the degrees of freedom within the χ^2 test (df) and the number of observations within this linear model (n). The χ^2 value was then listed (a) along with the corresponding p value (b) with asterisks denoting significance when alpha <0.05. Non-significant results were listed with a p value only. Results were sometimes also stated as the estimate of change with standard error in brackets as part of the reported output from the GLMM to help signify the amount and direction of the effect. A Tukey-Kramer multiple comparison adjustment was used for *post hoc* testing whilst controlling for multiple comparisons.

If animal number was shown to have no effect on the variance (i.e. an ICC value of <0.1), then the data was tested for normality using a Shapiro-Wilk test. If the data was not normally distributed (i.e. non-parametric), then a Mann-Whitney U non-parametric t-test was run. If the data was normally distributed with equal variances, then a Student's t-test was run. If the variances were unequal, then a Welch t-test was run. Significant results were described as ($t_{(df, n)}$ = a, p=b*), where a was the t-test statistic (t), df was the degrees of freedom, n was the total n number, and the p value was b. Significance was denoted with asterisks: p<0.05*, p<0.01**, p<0.005***. Non-significant results were listed as a p value only.

Two-sample Kolmogorov-Smirnov tests were used on cumulative distribution plots to determine if the samples came from different populations. Significant results were described as ($D_{(df)}$ = a, p =b*). A was the Kolmogorov-Smirnov test statistic (D), df was the degrees of freedom, and the p value was b. Significance was denoted with asterisks: p<0.05*, p<0.01**, p<0.005***. Non-significant results were listed as a p value only.

Unless stated otherwise, data was presented as mean ± standard error of the mean (SEM). Box plots show mean (square), median (line) ± SEM (box). Significance was denoted with asterisks: p<0.05 *, p<0.01 **, p<0.005 ***.

2.4 RESULTS

2.4.1 Spontaneous synaptic activity was reduced in frequency following neurodegeneration onset in the rTg4510 mice

A total of 46 cells across 20 animals (10 animals per genotype, n = 23 cells per genotype, ~5.5M of age, Batch 1) were recorded and analysed for spontaneous synaptic activity. There was no significant difference in series resistance between genotypes (WT 21.89 ± 0.72 MΩ, TG 21.91 ± 0.78 MΩ, GLMM, p=0.98).

Amplitude (WT 12.19 ± 0.89 pA; TG 13.86 ± 0.89 pA, GLMM, p=0.24) and inter-event interval (WT 807 ± 171 ms; TG 653 ± 122 ms, GLMM, p=0.91) of sEPSCs were not statistically different between genotypes (Figure 2.11 A & B). Whilst the average responses were similar, the distribution of events may have been different (i.e. proportion of different event amplitudes). However, the cumulative frequency distribution of amplitude (KS test, p=0.65) and inter-event interval (KS test, p=0.99) were also not statistically different between genotypes (Figure 2.11 C & D).

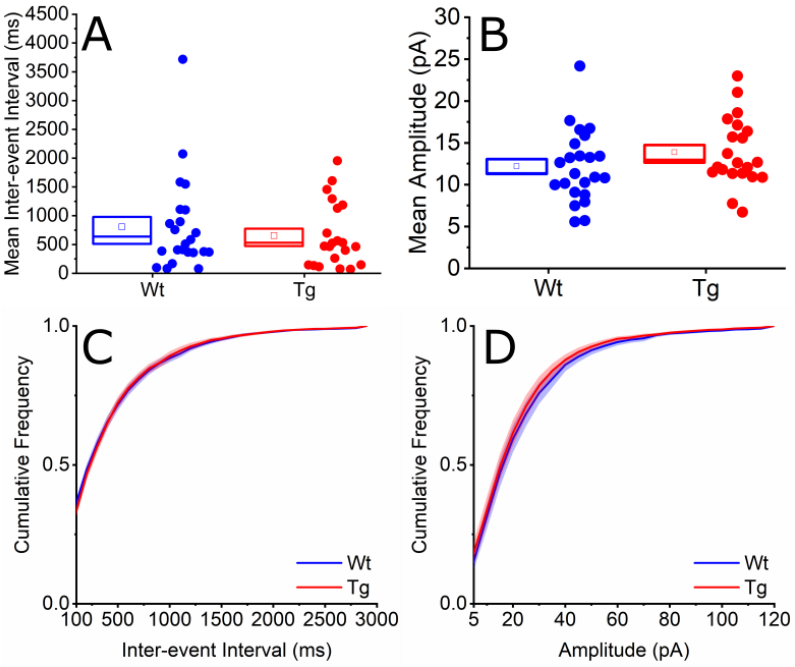

Figure 2.11 sEPSC properties in ~5.5 M old TG and WT mice were not statistically different between genotypes. Mean inter-event interval (**A**) and amplitude (**B**) are shown as box and dot plots. Cumulative frequency plots of inter-event interval (**C**) and amplitude (**D**) are shown below. For **C** & **D**, the line plots the average, and the shading represents the SEM.

In addition, the kinetics of the average sEPSC waveform were analysed and rise time (WT 0.8 ± 0.05 ms; TG 0.8 ± 0.06 ms, GLMM, p=0.63) and decay T (WT 3.11 ± 0.22 ms; TG 2.70 ± 0.22 ms, GLMM, p=0.34), were not statistically different between genotypes (Figure 2.12).

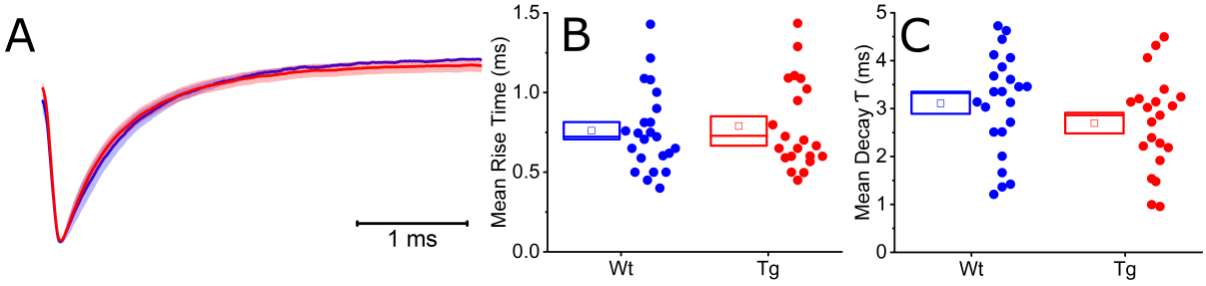

Figure 2.12 sEPSC waveform kinetics in ~5.5M old TG and WT mice were not statistically different between genotypes. The average waveform (line) of all recorded neurons, based on the average waveform per neuron per genotype, scaled to values between 0 and 1 with SEM (shaded) (**A**). Box plots of average rise time (**B**) and decay T (**C**) are also shown.

A total of 43 cells were analysed across 10 animals to assess differences following neurodegeneration onset (5 animals per genotype, n=20 WT & 23 TG cells, ~ 7.5M of age, Batch 3). There was no differences in series resistance between genotypes within the batch (WT 15.56 ± 0.73 MΩ, TG 15.57 ± 1.24 MΩ, GLMM, p=0.2, Figure 2.6). As mentioned in the methods, there was a significant reduction in series resistance between Batch 1 and 3 (Figure 2.6). This change would alter the ability to faithfully record the kinetics of the synaptic currents recorded, producing artificial differences between the two batches. Therefore, statistical comparisons were restricted to within-age group comparisons, and not used to compare across age groups.

sEPSC inter-event interval was significantly increased in the TGs following neurodegeneration onset (WT 1273 ± 389 ms; TG 1740 ± 289, $U_{(1,43)}$=145, p=0.04*, Mann-Whitney U t-test; Figure 2.13 A). Amplitude was not statistically different between genotypes (WT 18.71 ± 1.23 pA; TG 16.85 ± 0.83, p=0.22, students t-test) (Figure 2.13 B). Cumulative frequency plots of inter-event intervals revealed a right-ward shift in the distribution of all interval sizes (KS test, $D_{(31)}$=0.42, p=0.03*, Figure 2.13 C), implying a reduction in the overall number of events. The cumulative

frequency plot of amplitude was not statistically different between genotypes (KS test, p=0.52, Figure 2.13 D). Rise time (WT 0.6 ± 0.04 ms; TG 0.6 ± 0.03 ms, GLMM, p=0.38) and decay T (WT 3.12 ± 0.29 ms; TG 2.52 ± 0.16 ms, GLMM, p=0.28) were also not statistically different between genotypes (Figure 2.14).

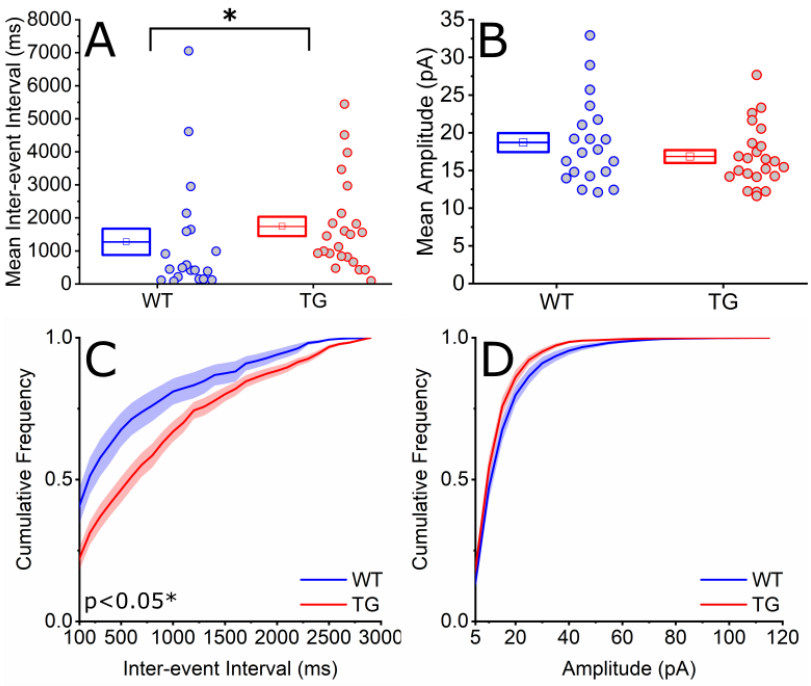

Figure 2.13 A significant increase in inter-event interval was observed in ~7.5M old TG mice compared to WT mice when assessing sEPSC properties. Mean inter-event interval (**A**) and amplitude (**B**) were shown as box and dot plots with cumulative frequency plots of inter-event interval (**C**) and amplitude (**D**). Significance denoted with asterisks: p<0.05*.

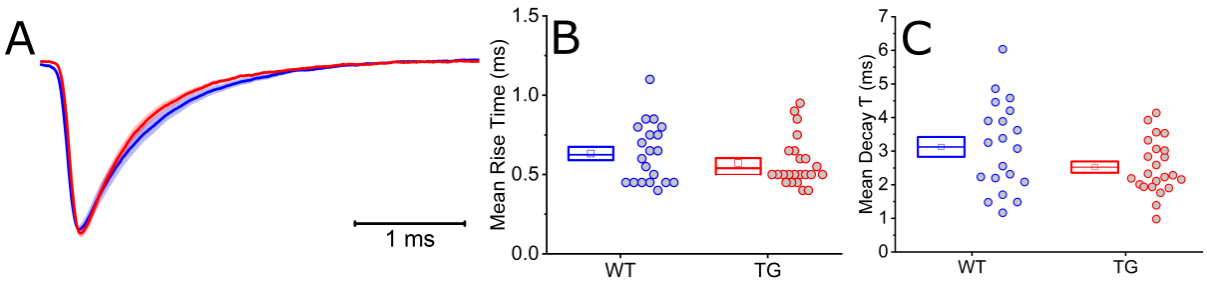

Figure 2.14 sEPSC waveform kinetics were not statistically different in ~7.5M old TG and WT mice. The traces plot the average sEPSC waveform (**A**) from each genotype normalised between 0 to 1 with SEM (shaded) of all recorded neurons based on the average waveform per neuron. Box plots of rise time (**B**) and decay T (**C**) are also shown.

2.4.2 Observed reductions in the NMDA:AMPA receptor ratio in TG mice at early but not progressed neurodegenerative phases of tauopathy

At the ~5.5M age point (Batch 1), a total of 39 and 33 cells in 10 WT and 10 TG animals respectively, were recorded for synaptically-evoked NMDA:AMPA receptor ratios. The stimulation electrode was positioned within layer IV, in the same cortical column as the recorded cell. This ratio was significantly lower (WT 0.79 ± 0.1; TG 0.53 ± 0.1, Mann-Whitney U t-test, $U_{(1,72)}$=755, p=0.05*), in the TGs compared to WTs (Figure 2.15 A & B). This ratio was reduced to near 0 (mean=0.1, range=0.01 – 0.43) with application of L689560 (an NMDAR antagonist) in both genotypes, reflecting a block of recorded NMDAR responses which confirms the specificity of the recorded NMDAR current.

At the ~7.5M age point (Batch 3), a total of 42 WT and 30 TG cells were measured in 10 animals (5 animals per genotype). There were no significant differences in the NMDA:AMPA receptor ratio between genotypes (WT 0.71 ± 0.13; TG 0.65 ± 0.16, Mann-Whitney U t-test, p=0.78; Figure 2.15 C & D).

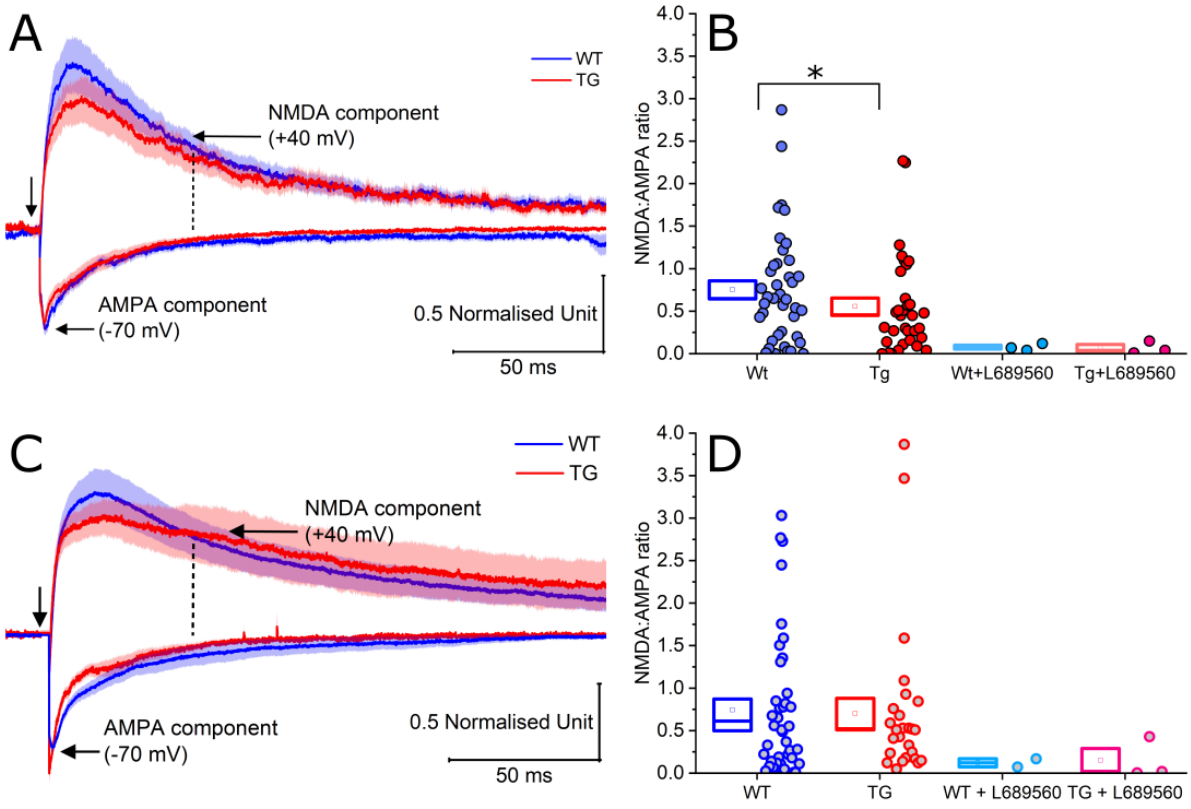

Figure 2.15 NMDA:AMPA receptor ratio responses in TG mice were reduced at ~5.5M. The average normalised waveforms (normalised to AMPAR peak, plotted as thick lines) from all recorded cells at ~5.5M (**A**) and ~7.5M (**C**). The vertical arrow indicates stimulus onset and shading represents SEM. Box and dot plots of the NMDA:AMPA receptor response ratio in dark blue and red which were reduced with the application of L689560 (shown in lighter blue and pink) at ~5.5M (**B**) and ~7.5M (**D**). Significance denoted with asterisks: p<0.05*.

2.4.3 Evoked synaptic transmission was not altered in the TG mice at either early or progressed phases of tauopathy-mediated neurodegeneration

Six stimuli were applied at 5, 10 and 30 Hz frequencies, to investigate the short-term plasticity of evoked synaptic transmission in 29 WT and 27 TG cells (8 and 9 animals respectively) at ~5.5M (Batch 1). The number of sweeps excluded for epileptiform activity did not change between genotypes across all frequencies (WT 1.18 ± 0.16 sweeps ,11% of total sweeps; TG 1.51 ± 0.2 sweeps, 15% of total sweeps). For all stimulation frequencies, a large proportion of the variance was accounted for by the animal and cell number (as seen by high ICC values). This suggested that although different cells exhibited different short-term synaptic plasticity profiles, any single cell likely responded in the same manner across all stimuli (i.e. facilitating cells will facilitate for the whole of the response).

For all three stimulation frequencies (5 Hz, 10 Hz, 30 Hz), there was a significant effect of stimulation number in altering the response when normalised to the first eEPSC (5 Hz: $\chi^2_{(5, 336)} = 33.8$, p<0.005***; Figure 2.16 A), (10 Hz: $\chi^2_{(5, 312)} = 36.23$, p<0.005***; Figure 2.16 C), (30 Hz: $\chi^2_{(5, 276)} = 16.56$, p<0.005***; Figure 2.16 E). There was no significant effect of genotype (5 Hz p=0.78, 10 Hz p=0.67, 30 Hz p=0.67) or interaction (5 Hz p=0.94, 10 Hz p=0.88, 30 Hz p=0.56) between repeated stimulation and genotype (i.e. the cells responded in a similar manner per evoked response) at any of the stimulation frequencies.

At the lower stimulation frequencies (5 Hz and 10 Hz), the mean cellular response was reduced in response to subsequent stimuli (depressing) (paired pulse ratio of 0.85 ± 0.05 WT cells and 0.9 ± 0.09 TG cells at 5 Hz, Figure 2.16 B; 0.94 ± 0.08 WT cells and 0.92 ± 0.09 TG cells at 10 Hz, Figure 2.16 D). At 30 Hz, the mean response showed an increasing (facilitating) response to subsequent stimuli (paired pulse ratio of 1.26 ± 0.17 WT cells and 1.28 ± 0.26 TG cells, Figure 2.16 F). Overall, there was no significant effect of genotype on any short-term plasticity measures at ~5.5M.

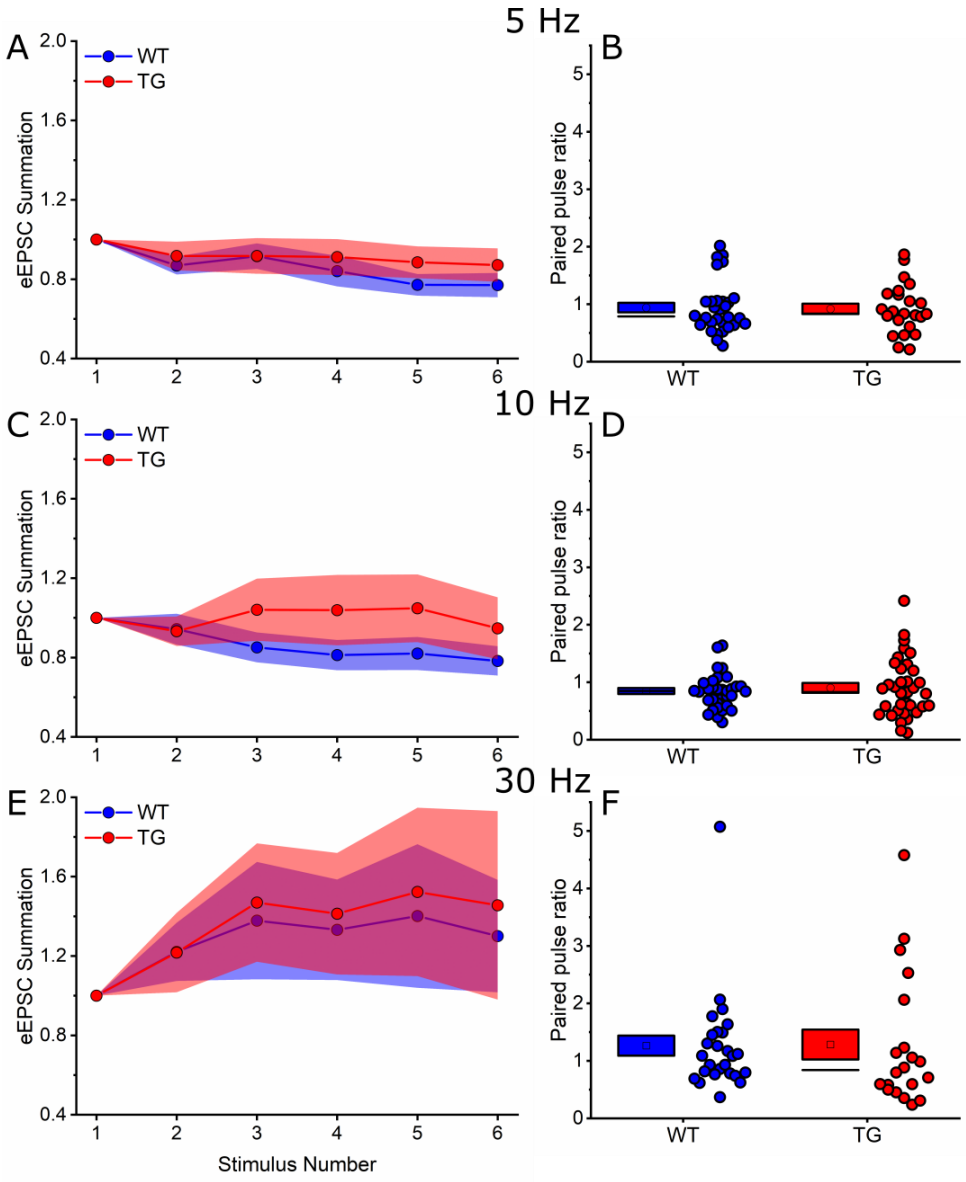

Figure 2.16 Serial evoked responses at ~5.5M of age in WT and TG mice were not statistically different. Normalised response summation from 6 stimuli given at a frequency of 5 Hz (**A**), 10 Hz (**C**) and 30 Hz (**E**) are shown as joined dot plots representing normalised responses (area under the curve normalised to the first evoked response amplitude) to stimulations, with the mean normalised response summation shown in a coloured line (WT shown in blue and TG in red) and shading representing SEM. The right-hand panels (**B**, **D**, **F**) show the paired pulse ratio (the second response normalised to the first response). Values above 1 suggest an overall facilitation of the response and values below 1 suggest a depression.

Post-neurodegeneration onset (Batch 3, ~7.5M), 38 WT and 19 TG cells were recorded for eEPSC analysis (from 5 animals per genotype). The number of sweeps excluded for epileptiform activity did not change between genotypes across all frequencies (WT 2 ± 0.02 sweeps, 20% of total sweeps; TG 1.8 ± 0.03 sweeps, 18% of total sweeps).

At ~7.5M, the results mirror those seen at the earlier age point. For all three stimulation frequencies (5 Hz, 10 Hz, 30 Hz), there was a significant effect of stimulation number in altering the response when normalised to the first eEPSC (5 Hz: $\chi^2_{(5, 342)} = 113$, p<0.005***; Figure 2.17 A), (10 Hz: $\chi^2_{(5, 324)} = 36.95$, p<0.005***; Figure 2.17 C), (30 Hz: $\chi^2_{(5, 294)} = 22.75$, p<0.005***; Figure 2.17 E). There was no significant effect of genotype (5 Hz p=0.77, 10 Hz p=0.8, 30 Hz p=0.92) or interaction (5 Hz p=0.34, 10 Hz p=0.77, 30 Hz p=0.41) between repeated stimulation and genotype (i.e. the cells responded in a similar manner per evoked response) at any of the stimulation frequencies.

At the lower stimulation frequencies (5 Hz and 10 Hz), the majority of cells displayed a reduced response to subsequent stimuli (depressing) (mean paired pulse ratio in WT of 0.9 ± 0.14 and in TG of 0.63 ± 0.08 at 5 Hz, p=0.21; Figure 2.17 B; mean paired pulse ratio in WT of 0.9 ± 0.09 and TG of 1.05 ± 0.17 at 10 Hz, p=0.89 ; Figure 2.17 D). At 30 Hz, the mean cellular response was facilitating in response to subsequent stimuli (mean paired pulse ratio in WT of 1.16 ± 0.16 and TG of 1.26 ± 0.2 at 30 Hz, p=0.95; Figure 2.17 F). Similar to the ~5.5M age group, there was no significant effect of genotype on any short-term plasticity measures at ~7.5M.

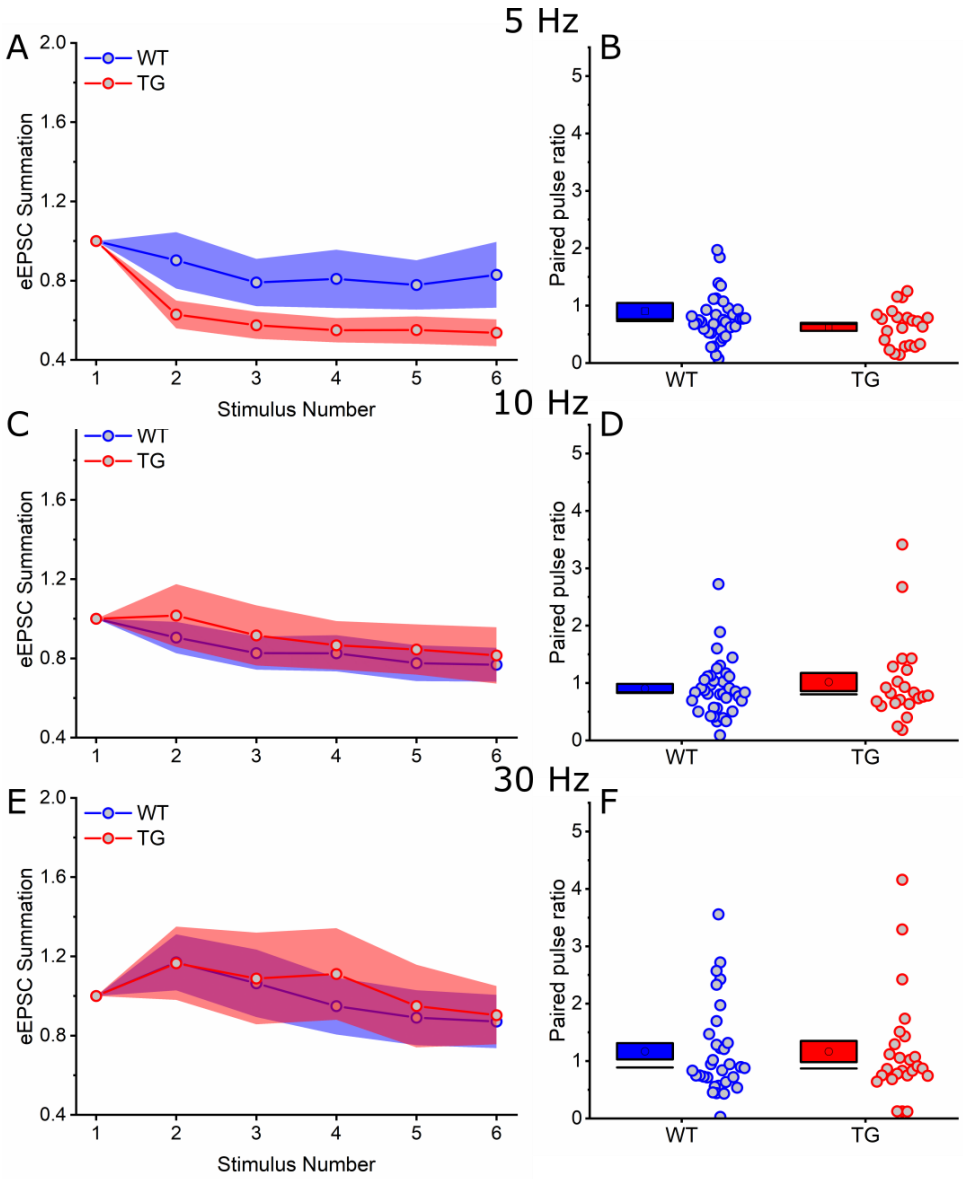

Figure 2.17 Serial evoked responses from ~7.5M old TG and WT mice were not statistically different. Normalised response summation from 6 stimuli given at a frequency of 5 Hz (**A**), 10 Hz (**C**) and 30 Hz (**E**) are shown as joined dot plots representing normalised responses (area under the curve normalised to the first evoked response amplitude) to stimulations, with the mean normalised response summation shown in a coloured line (WT shown in blue and TG in red) and shading representing SEM. The right-hand panels (**B**, **D**, **F**) show the paired pulse ratio (the second response normalised to the first response). Values above 1 suggest an overall facilitation of the response and values below 1 suggest a depression.

2.4.4 TG neurons from ~5.5M mice were significantly depolarised with a decreased capacitance when recorded at RMP

18 WT and 44 TG cells were recorded from 4 and 5 animals respectively (Batch 2 ~5.5M). A series of current injection protocols were run in CC recording mode to determine the passive and active electrical membrane properties at both RMP and a held membrane potential of -70 mV. Passive properties such as R_i, T, capacitance, and sag were measured using a -100 pA square-wave current injection at RMP or when RMP was held at -70 mV.

With no current injection, the RMP of TG neurons (measured at the fourth minute following break-in) was significantly depolarised compared to WTs (WT -74.57 ± 3.41 mV; TG -67.47 ± 2.12 mV; Mann-Whitney U t-test, $U_{(1,44)}$=261, p=0.04*; Figure 2.18 A).

At RMP (WT -75 mV, TG -67 mV), membrane capacitance was significantly lower in TG cells (63.67 ± 7.84 pF, 50.71 ± 4.82 pF, Mann-Whitney U t-test, $U_{(1,44)}$=474, p=0.05*; Figure 2.18 E). R_i measured by steady-state difference (WT 145.52 ± 17.94 MΩ; TG 236.31 ± 25.94 MΩ, Mann-Whitney U t-test, p=0.08; Figure 2.18 B) and by extrapolation of exponential fit (WT 155.67 ± 22.31 MΩ; TG 262.07 ± 32.36 MΩ, Mann-Whitney U t-test, p=0.09; Figure 2.18 C) was not significantly different between genotypes. The membrane time constant (T, students t-test, p=0.69; Figure 2.18 D) and sag (students t-test, p=0.9; Figure 2.18 F) were also not statistically different between genotypes.

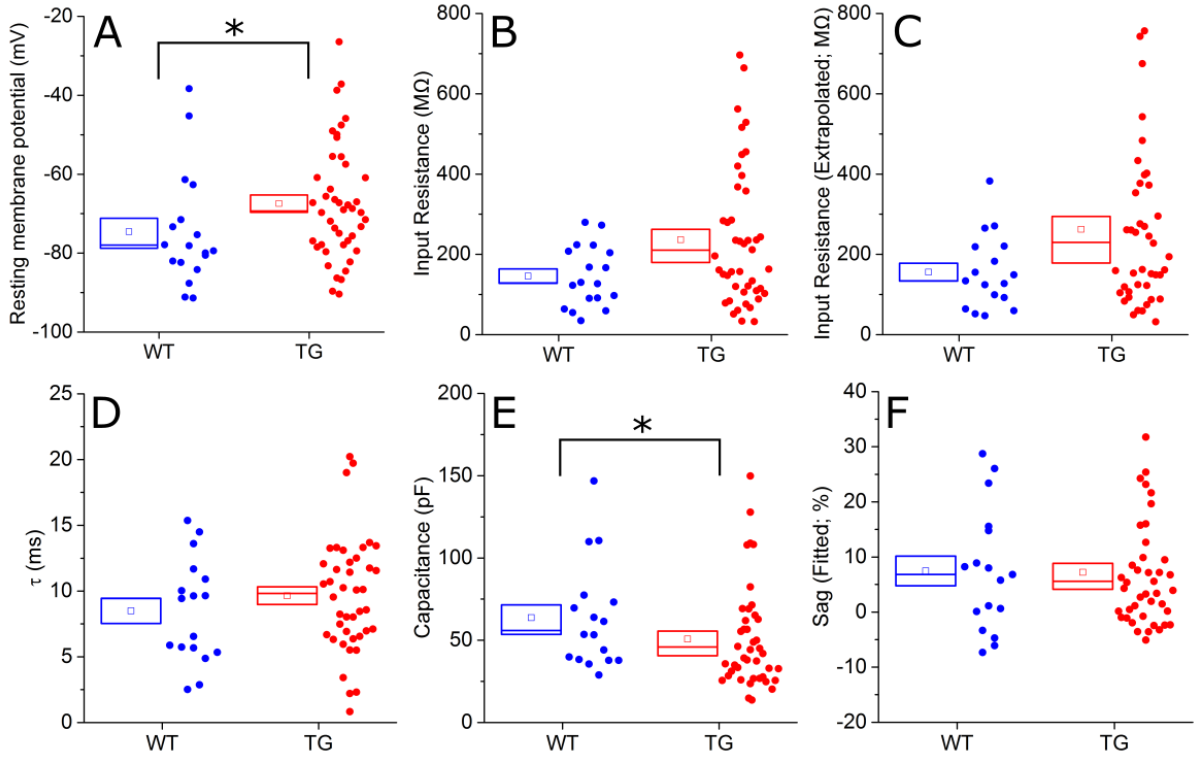

Figure 2.18 Depolarised RMP and decreased capacitance when measured at RMP in ~5.5M old TG mice. Passive electrical membrane properties measured in response to a -100 pA current injection. RMP (**A**), input resistance (**B** & **C**), T (**D**), capacitance (**E**) and sag (**F**) are shown. Significance denoted with asterisks: p<0.05*.

2.4.5 Decreased capacitance in TG neurons at ~5.5M at a held membrane potential of -70 mV

Under conditions in which the membrane potential was held at -70 mV, capacitance was significantly decreased in TG cells compared to WTs (WT 73.18 ± 10.26 pF; TG 53.80 ± 5.06 pF; Mann-Whitney U t-test, $U_{(1,50)}$=513, p=0.05*; Figure 2.19 D). R_i calculated from steady state (WT 155.69 ± 20.45 MΩ; TG 224.72 ± 23.07 MΩ; Mann-Whitney U t-test, p=0.07; Figure 2.19 A) and by extrapolation from exponential fit (WT 169.93 ± 26.57 MΩ; TG 240.19 ± 26.57 MΩ; Mann-Whitney U t-test, p=0.07; Figure 2.19 B), although not significantly different trended towards an increase, which may reflect the change in capacitance. T (Mann-Whitney U t-test, p=0.96; Figure 2.19 C) and sag (Mann-Whitney U t-test, p=0.38; Figure 2.19 E) were not statistically different between genotypes.

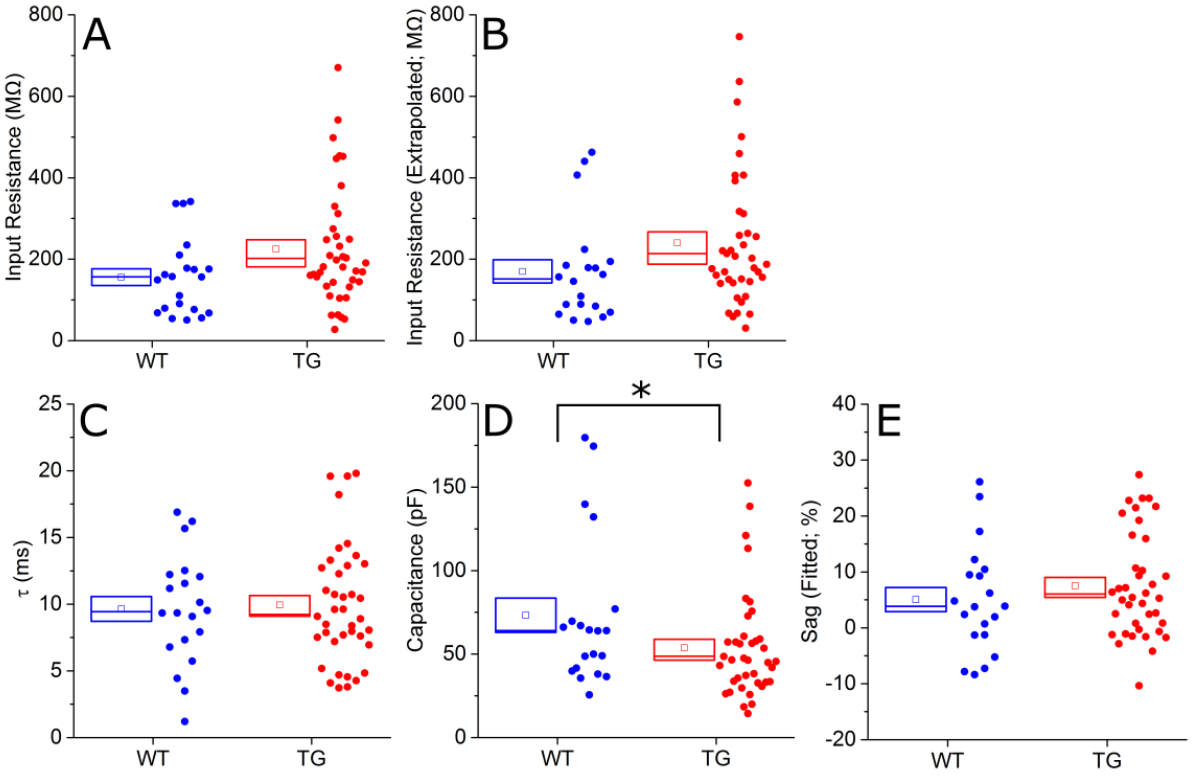

Figure 2.19 Decreased capacitance at -70 mV in ~5.5M old TG mice. Passive electrical membrane properties in response to a -100 pA hyperpolarising square current injection when the RMP was held at -70 mV. R_i (**A** & **B**), T (**C**), capacitance (**D**) and sag (**E**) are shown. Significance denoted with asterisks: p<0.05*.

2.4.6 Neuronal excitability: significant interaction effects of genotype in response to increasing current injections in ~5.5M old WT and TG cells

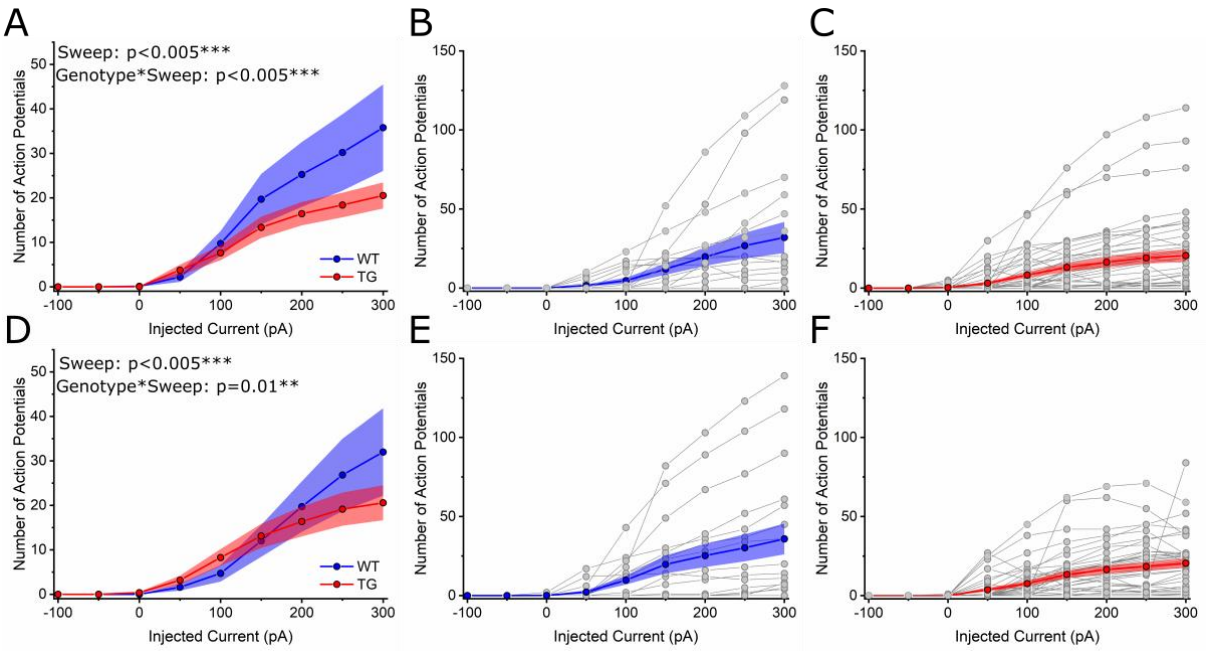

Figure 2.20 AP firing in response to a series of progressively increasing current injections in WT and TG cells from ~5.5M old animals. The average number of APs in response to increasing amounts of injected current at rest (**A**) and at -70 mV (**D**). The line plots the average response, and the shaded error bars plot the SEM. Individual input output plots shown for WT and TG cells at rest (**B** & **C** respectively) and at -70 mV (**E** & **F** respectively). Significant effects written with significance denoted with asterisk: p<0.01**, p<0.005***.

Square current injections were applied starting at -100 pA to 300 pA in increasing steps of 50 pA in order to measure cellular excitability. At rest and when RMP was held at -70 mV, depolarising current injections of 100 pA or larger led to significantly more firing as expected (RMP: $\chi^2_{(8, 486)} = 1011$, p<0.005***; Figure 2.20 A; -70 mV: $\chi^2_{(8, 504)} = 1141$, p<0.005***; Figure 2.20 B). There was no significant effect of genotype at rest (p=0.94) or when the cell was held at -70 mV (p=0.47). There was a significant interaction of genotype with stimulus at rest ($\chi^2_{(8, 486)} = 19.75$, p<0.01**) and when the cell was held at -70 mV ($\chi^2_{(8, 504)} = 39.35$, p<0.005***). However, *post hoc* comparisons showed no significant differences between genotypes per sweep.

2.4.7 Neuronal excitability: rheobase was not statistically different between genotypes in ~5.5M TG and WT cells

The rheobase was determined as the minimum current injection needed to elicit an AP from incremental 2 pA current injections. At both -70 mV and at RMP, rheobase was not statistically different between genotypes (Mann-Whitney U t-test, RMP: p=0.18, -70 mV: p=0.3; Figure 2.21 A & B). For both genotypes, there was a significant negative correlation between RMP and rheobase with more depolarised cells needing less current to elicit an AP (Pearson's rank test; WT $F_{1,15}$ 4.5, r=-0.49, p=0.05*; TG $F_{1,30}$ 64.3, r=-0.83, p<0.005***; Figure 2.21 C).

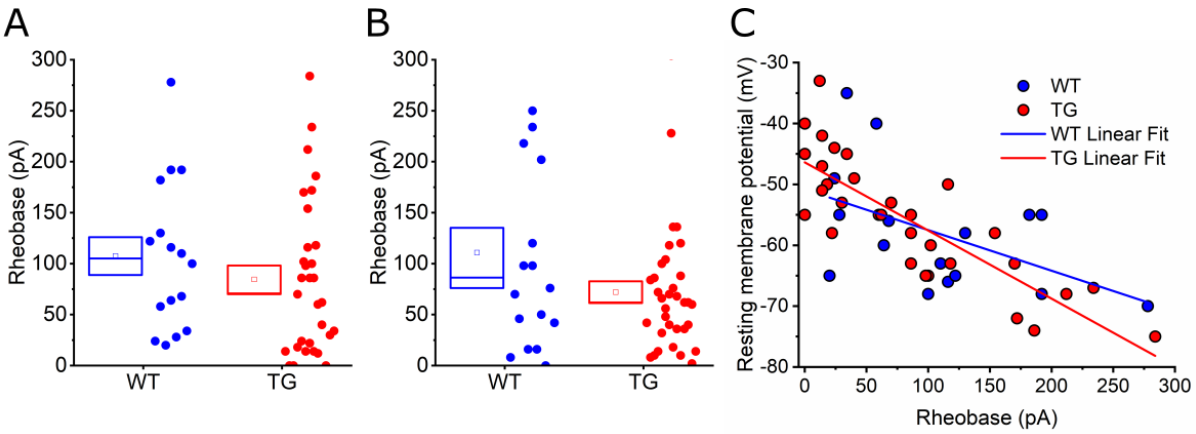

Figure 2.21 Rheobase at rest and at -70 mV. Rheobase value (pA) at RMP (**A**; rest) and when the RMP was held at -70 mV (**B**; -70 mV). Resting membrane potential values correlated against rheobase values, with linear fits per genotype drawn on the plot (**C**).

2.4.8 AP-related properties revealed an increased peak AHP at RMP and increased AP width at -70 mV in ~5.5M rTg4510 mice

AP properties were calculated from the rheobase evoked AP. At RMP, AP peak (students t-test, p=0.89), AP maximum dV/dt (students t-test, p=0.17), AP width at -15 mV (students t-test, p=0.11), AP width at AP threshold (Mann-Whitney U t-test, p=0.08), and AP amplitude (Mann-Whitney U t-test, p=0.22) were not statistically different between genotypes. Peak AHP was significantly increased (WT 12.40 ± 0.79 mV; TG 15.11 ± 1.08 mV; Welch t-test, $t_{(1,42)}$=-2.02, p=0.05*), and AP threshold trended towards an increase, although this was not significantly different (WT -50.49 ± 1.55 mV; TG -47.25 ± 0.95 mV; Student's t-test, p=0.07). This data is summarised in Figure 2.22.

At -70 mV, AP peak (students t-test, p=0.63), maximum dV/dt (students t-test, p=0.17), AP amplitude (students t-test, p=0.53), and peak AHP (students t-test, p=0.89) were not significantly different between genotypes. AP threshold showed a trend towards a more depolarised threshold in the TG cells, although this was not significantly different (WT -52.29 ± 1.55 mV; TG -48.71 ± 1.09 mV; Students t-test, p=0.06). AP width at -15 mV (WT 0.40 ± 0.05 ms; TG 0.57 ± 0.04 ms; Mann-Whitney U t-test, $U_{(1,42)}$=142, p=0.03*) and at threshold (WT 1.35 ± 0.24 ms; TG 1.47 ± 0.09 ms; Mann-Whitney U t-test, $U_{(1,42)}$=160, p=0.05*) was significantly larger. This data is summarised in Figure 2.23.

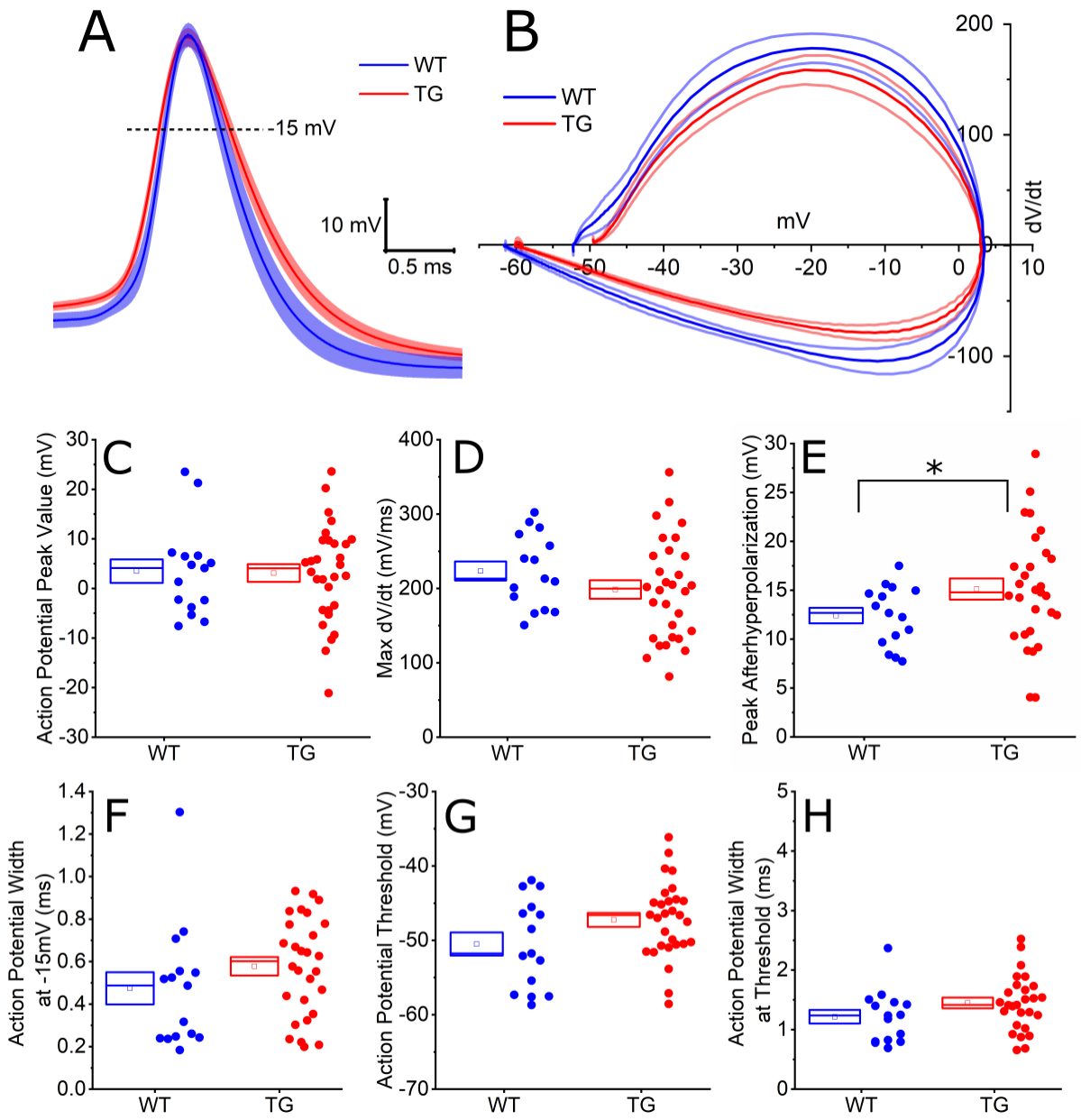

Figure 2.22 Increased AHP at RMP in ~5.5M old TG mice. AP-related properties calculated on APs evoked from rheobase at RMP, with average AP waveforms (**A**) and average phase plots (**B**) shown with WT in blue and TG in red (shading & outline denotes SEM). Box plots showing AP peak value (**C**), maximal dV/dt (**D**), peak AHP (**E**), AP width at -15 mV (**F**), AP threshold (**G**) and AP width at threshold (**H**). Significance denoted with asterisks: p<0.05*.

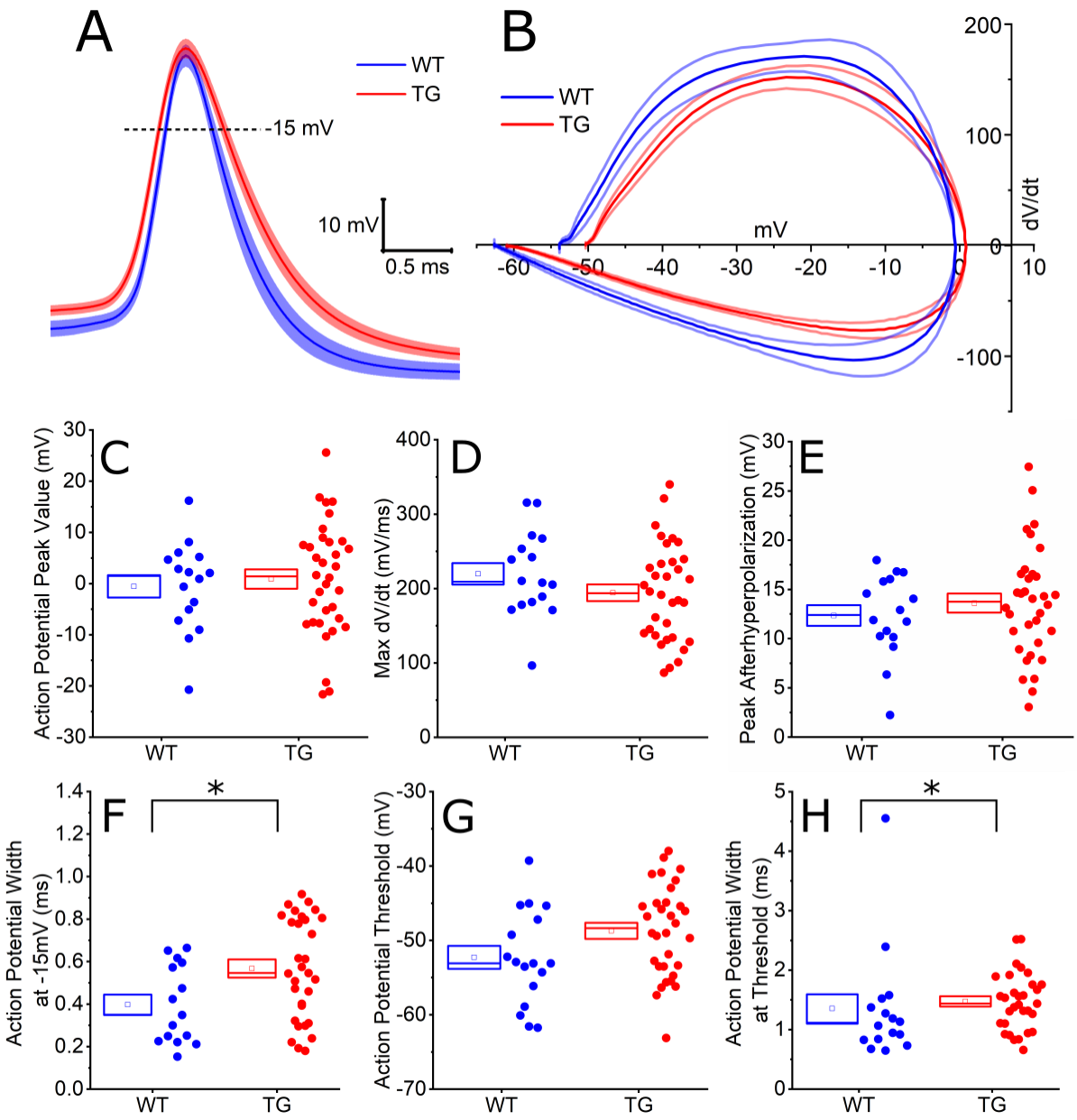

Figure 2.23 Increased AP width at a held membrane potential of -70 mV in ~5.5M old TG mice. AP average waveforms (**A**) and average phase plots (**B**) are shown with WT in blue and TG in red (shading and outlines denote SEM). Box plots showing AP peak value (**C**), maximal dV/dt (**D**), peak AHP (**E**), AP width at -15 mV (**F**), AP threshold (**G**) and AP width at threshold (**H**). Significance denoted with asterisks: p<0.05*.

2.5 DISCUSSION

This chapter presents a functional assessment of the somatosensory cortex in the rTg4510 model at early neurodegenerative phases of tauopathy (~5.5M). These data showed a significant decrease in the NMDA:AMPA receptor ratio, suggesting a subtle alteration in the synaptic function of layer II/III somatosensory neurons at this age point. Following neurodegeneration onset, the sEPSC inter-event interval was decreased whilst the NMDA:AMPA receptor ratio was balanced in contrast with the younger age point, with other measures of synaptic function similar between genotypes. Alterations in some intrinsic neuronal properties were observed at ~5.5M of age in the rTg4510 cells (change in capacitance, AP width, peak AHP), with some of these changes being voltage dependent.

2.5.1 Subtle synaptic dysfunction was observed in the rTg4510 model that differed at early and progressed neurodegenerative phases of tauopathy

In early neurodegenerative phases of tauopathy (~5.5M age point), there was no observed difference in the inter-event interval of spontaneous synaptic activity (Figure 2.11). Previous studies suggest that synapse density was unchanged (Kopeikina et al., 2013a) and spine turnover was increased at this age point (Jackson et al., 2017), which could help to maintain function in the face of synaptic degeneration by increasing the formation of new synapses to replace degenerating ones. However, increases in sEPSC inter-event interval were measured post-neurodegeneration onset (~7.5M; Figure 2.13). Large reductions in synapse density and spontaneous AP-related Ca^{2+} transients have been observed in the rTg4510 model post-neurodegeneration onset (Crimins et al., 2011, 2012; Jackson et al., 2017; Kopeikina et al., 2013a), which would likely have an impact on spontaneous synaptic currents. This result was in contrast with Crimins et al., 2012 who detected an increased sEPSC frequency post neurodegeneration onset (9M). There may be further compensatory mechanisms and dynamic reshaping of synaptic activity such as synaptic scaling or local homeostatic plasticity that come into play at more aged points such as 9M that could explain the discrepancy between this study and Crimins et al., 2012. There may also be differences in the overall excitability of neurons in the slices, with sEPSCs but not miniature EPSCs recorded in both pieces of work which would incorporate

neuronal excitability into the measured events (Johnston and Wu, 1994). These recordings were also performed in different brain regions which have different timelines of pathological tau accumulation and neurodegeneration (Harrison et al., 2020). There were no changes in sEPSC waveform properties and kinetics such as amplitude, rise time or decay T at either age point (Figure 2.12 & Figure 2.14). Overall, a reduction in sEPSCs following neurodegeneration onset could be mediated by decreased spontaneous pre-synaptic activity, supported by lowered neuronal activity seen at this age (Jackson et al., 2017). It could also be due to a reduction in AMPAR receptor containing synapses, with no change in existing AMPAR function related to subunit composition, following neurodegeneration onset (Grosskreutz et al., 2003; Lomeli et al., 1994; Mosbacher et al., 1994; Vicini et al., 1998). These recordings could be further complimented by recordings of miniature EPSCs to confirm whether changes in sEPSC frequency were related to changes in excitability.

The ratio between NMDAR to AMPAR responses is thought to be important in governing synapse plasticity and excitatory synaptic integration (Rao and Finkbeiner, 2007; Watt et al., 2000). The reduction in the NMDA:AMPA receptor ratio observed in this study at ~5.5M within the rTg4510 mice (Figure 2.15) potentially highlights dysfunctional synapses or neurons prior to synaptic or neuronal degeneration. Following neurodegeneration onset, this difference appears to be rebalanced (Figure 2.15), which could relate to a loss of these imbalanced synapses. Alterations in NMDA:AMPA receptor ratios can affect the ability of the neuron to entrain with oscillations (Wolf et al., 2005) and a reduced NMDA:AMPA receptor ratio has been associated with reduced LTP in a model of AD (Tozzi et al., 2015). This altered ratio may therefore impact LTP and oscillatory entrainment, and so work to investigate these two measures in this neuronal population could reveal further deficits.

It is not possible to tell from the NMDA:AMPA receptor ratio specifically which receptor function is altered. However, in consideration with the other measures examining putative AMPAR function (sEPSCs and eEPSCs at -70 mV; Figure 2.11 & Figure 2.16), it is more likely to be NMDAR dysfunction or a reduction in NMDAR expression. This could be clarified by recording and quantifying spontaneous NMDAR-mediated currents at +40 mV. It is likely that there is a shift in NMDAR expression towards silent synapses (Moldavski et al., 2019), when considered together with the observed shift in spine distrubtion towards immature filopodia, increased spine turnover, and

preserved total spine density at ~5.5M in the rTg4510 mice (Crimins et al., 2011; Jackson et al., 2017; Kopeikina et al., 2013a). The NMDA:AMPA receptor ratio would also be affected by a change in receptor expression. Expression of glutamatergic receptor subunits (NR1 & GluR1) were decreased in the rTg4510 model at 12M (Kopeikina et al., 2013a), but whether these changes in expression occur simultaneously with the changes in function observed here is unknown.

Short term plasticity measures in the barrel cortex showed depression at lower frequency simulation patterns and facilitation at higher ones (Lefort and Petersen, 2017). This was replicated in the present study, albeit with some subtle discrepancies in the facilitation pattern between the two age points in this study (Figure 2.16 & Figure 2.17). Changes in short term plasticity likely reflect a change in the pre-synapse, either in release probability, vesicle depletion or calcium dependent mechanisms (Fioravante and Regehr, 2011). Overall, there was no change in short-term plasticity between genotypes at either age (Figure 2.16 & Figure 2.17). In consideration with the other measures of synaptic function (sEPSCs and NMDA:AMPA receptor ratio), it is likely that there was a change in post-synaptic activity with no observable changes at the pre-synapse. Interestingly, abnormal tau pathology can be found at both the pre- and post-synapse, and has also been shown to influence pre-synaptic physiology by binding to pre synaptic vesicles (McInnes et al., 2018; Zhou et al., 2017). This is implied to be another early mechanism of synaptic dysfunction, and so is perhaps occurring in other vulnerable synaptic pathways or degeneration may have already occurred within these pre-synaptic partners. Altered synaptic plasticity has been observed in recordings with acute application of oligomeric tau via the intracellular recording solution and in an inducible overexpression model of pro-aggregant tau (Hill et al., 2019; Sydow et al., 2011). These changes in synaptic plasticity may therefore occur early in the rTg4510 model development in acute exposure to more soluble tau isoforms, but perhaps not to chronic tau exposure that would be in a more fibrillar form.

One limitation of the present study is that there was a change of series resistance between different batches of recordings which precluded direct comparison of measures of synaptic function between batches (Figure 2.6). An increased series resistance reduces the recording accuracy of certain waveform parameters such as rise time, decay Ƭ and event amplitude (Johnston and Wu, 1994). As there were no differences between sEPSC dynamics between genotypes per age group this is likely

not an issue. However, it would be interesting to see if these properties are changed across aging within genotype.

Another limitation of this study relates to the whole-cell patch clamp methodology, measuring synaptic currents using the voltage clamp configuration. Voltage clamp recordings are inaccurate in recording synaptic currents in neurons with complex structures, as the voltage clamp is not uniformly controlled throughout the dendritic tree and decays across the length of dendrites (space-clamp issues; Williams and Mitchell, 2008). Changes in dendritic structure, which have been previously reported in the rTg4510 mice, may also compound this effect skewing the proportion of detected synaptic currents (Crimins et al., 2012; Rocher et al., 2010). Compartmentalisation of electrical signals in the heads of dendritic spines has also been shown to prevent voltage clamping of spines, reducing the accuracy of recording synaptic activity (Beaulieu-Laroche and Harnett, 2018; Yuste, 2013). Again, changes in the shape and size of dendritic spines have also been reported within the rTg4510 model, which would skew recordings of synaptic currents between genotypes (Crimins et al., 2011; Jackson et al., 2017). Although this may be considered as a limitation of the study, whole-cell patch clamp electrophysiology remains the pre-eminent method for recording synaptic physiology.

2.5.2 Neurophysiological function was altered in early neurodegenerative phases of tauopathy in the rTg4510 model

The intrinsic properties of wildtype neurons in this study were similar to other recordings made from layer II/III cells in the barrel cortex (Lefort et al., 2009). A depolarised RMP and a decreased capacitance were seen in this study in rTg4510 mice (Figure 2.18 & Figure 2.19). A depolarised RMP has been seen in the rTg4510 model (Crimins et al., 2011, 2012; Rocher et al., 2010) and also with the acute application of intracellular tau oligomers (Hill et al., 2019). This could be caused by a number of different alterations including changes in the maintenance of transmembrane ionic currents such as Na^+ and K^+ currents, tau-mediated blockages of ion channels such as K^+ channels, or by changes in overall excitatory or inhibitory synaptic tone (Shimojo et al., 2020). Changes in capacitance could reflect a change in the structure of these neurons, and therefore a change in ion channel expression. A change in capacitance was modelled in the rTg4510 mice in the hippocampus at 7-

8 M, and suggested that a 30% change in capacitance would have an effect on sag, T, AHP and resonance (Booth et al., 2016a). In this study, there was alterations in AHP and capacitance, without effects on sag and T, and so it would be interesting to see if resonance was also altered in this population of neurons at this earlier age point in comparison to Booth et al., 2016a. Further investigation of neuronal structure and ion channel expression is needed to pinpoint the mechanisms related to the observed change in capacitance. A decreased capacitance would produce larger and quicker responses to a given voltage, and in consideration with the depolarised RMP, would suggest neurons would need less depolarisation to reach AP threshold and therefore be more excitable. However, rheobase showed no difference between genotypes and increasing current injection spiking outputs trended towards lowered spiking outputs in the rTg4510 cells. There is research to suggest that the axon initial segment is mislocated further down the axon within the rTg4510 model, which could also reduce excitability by depolarising the threshold for AP initiation (Hatch et al., 2017; Kaphzan et al., 2011; Sohn et al., 2016). Other models of tauopathy have shown changes in excitability and other AP properties (Tamagnini et al., 2017) and so it is surprising to not observe altered excitability in this study.

This study showed that layer II/III somatosensory cortex neurons exhibited a wider AP waveform and increased AHP in ~5.5M rTg4510 mice (Figure 2.22 & Figure 2.23). In the hippocampus, decreased AP amplitude, depolarised AP threshold and reduced firing to increasing current was seen prior to neurodegeneration (Hatch et al., 2017). Oligomeric, but not monomeric, tau application has also been shown to affect the AP waveform (Hill et al., 2019). It is therefore likely that at least some of the changes observed are due to localised increases in soluble tau expression from transsynaptic spread within the rTg4510 mice, and not to the more progressed tau pathology accumulation and neurodegeneration. Doing a time course characterisation in the somatosensory cortex would confirm this, as the deposition of tau pathology has been suggested to be heterogeneous across the cortex in this model (Harrison et al., 2020). There are observable alterations in the firing pattern and network dynamics in the rTg4510 model, and this could be related to changes in the AP waveform by altering ion flow dynamics across the neuronal membrane (Booth et al., 2016b; Busche et al., 2019; Jackson et al., 2017; Witton et al., 2016).

Some of these properties (increased AHP at rest and increased AP width at -70 mV) appear to be altered in a voltage dependent manner (Figure 2.22 & Figure 2.23). Alterations in properties based on the voltage of the neuron would suggest there was an involvement of voltage gated ion channels. Inhibition of voltage sensitive potassium channels such as Kv2 and BK, have been shown to increase AP width and alter AHP currents without affecting excitability (Kimm et al., 2015; Palacio et al., 2017). Blockage of Kv2 channels also showed an increased propensity to enter depolarization block (Palacio et al., 2017), which was also seen in this study (data not shown). Other voltage sensitive channels, such as HCN channels, could also be implicated. However, HCN channels are unlikely to be playing a role as sag was similar between genotypes. Functional characterisation or quantification of expression of these voltage sensitive potassium channels in this model may reveal a mechanism behind the changes in AP properties observed.

As this analysis was blinded, exclusion criteria were based on non-physiological properties such as the series resistance of the recordings. The population of neurons recorded in the rTg4510s may be dying or changing their intrinsic properties including Vm. Therefore, neurons with non-typical properties such as a depolarised Vm were included as to not bias the results. By not excluding cells in both groups that were depolarised, we may have a more complete picture of the physiology of these neurons in the rTg4510s. Neuronal recovery would increase the confidence of the recordings, both by revealing if neuronal structure looked abnormal or whether the recordings are from the correct cell type which could explain these property changes.

2.6 CONCLUSIONS

At earlier neurodegenerative phases of tauopathy, there was a subtle synaptic deficit, observed as reductions in evoked NMDA:AMPA receptor ratios with other measures of synaptic activity unchanged. Glutamatergic receptor function imbalance could be an early change that could link to changes in synapse stability as seen in Jackson et al., 2017. Following neurodegeneration onset, there was an increase in sEPSC inter-event interval which could be mediated by a decrease in synapse density, as has been observed in the cortex of rTg4510 mice at >7M (Crimins et al., 2011; Kopeikina et al., 2013b). The presence of a subtle synaptic phenotype implies homeostatic mechanisms are in play to attempt to maintain network stability. Some subtle changes

in intrinsic function, which have been seen in other tauopathy models, were also seen in this study such as a depolarised RMP and changes in the AP waveform. These changes would likely lead to aberrant encoding and integration of incoming sensory information at earlier neurodegenerative phases of tauopathy, mediated by imbalanced glutamatergic receptor responses.

3 NEURONAL RESHAPING AND REDUCTIONS IN THE EXPRESSION OF SYNAPTIC PROTEINS IN RTG4510 MICE IN THE SOMATOSENSORY CORTEX IN PRODROMAL AND PROGRESSED TAUOPATHY

3.1 INTRODUCTION

In tauopathies, progressive brain atrophy occurs, with degeneration of both neurons and synapses occurring in parallel (Braak et al., 1994; Merino-Serrais et al., 2013; Scheff et al., 2006, 2007). Changes in dendritic architecture prior to neurodegeneration is thought to occur, potentially as a homeostatic mechanism to compensate for loss of synaptic connections (Dickstein et al., 2010; Rocher et al., 2010). The process of synaptic dysfunction and degeneration is also thought to be an early change, that may happen separately to neurodegeneration (Crimins et al., 2013; Hoover et al., 2010; Jackson et al., 2019). An important mediator of synaptic dysfunction in tauopathies is likely to be changes in the expression of synaptic proteins, such as alterations in glutamatergic receptor expression (Crimins et al., 2013).

Results presented in Chapter 2 demonstrated changes in membrane capacitance in layer II/III somatosensory cortex neurons in ~5.5 month (5.5M) old rTg4510 mice. This result may correspond to a change in dendritic architecture. To investigate this, dendritic morphology was analysed within a subset of neurons from which electrophysiological recordings were made. In addition, electrophysiological measurements of synaptic function revealed alterations in glutamatergic signalling in both ~5.5M and ~7.5M rTg4510 mice, which could reflect changes in glutamate receptor expression. This was further investigated by measuring protein expression in isolated synaptosomes from the somatosensory cortex (compared to control tissue from the cerebellum) at both 5.5M and 7.5M age points in rTg4510 and wildtype littermate mice.

3.1.1 Tau pathology alters neuronal structure

Alzheimer's disease (AD) patients with advanced tau pathology (e.g. neurofibrillary tangles) have dendritic atrophy and a loss of dendritic spines (Braak et al., 1994; Merino-Serrais et al., 2013) with similar changes also observed in mouse models of

tauopathy (Crimins et al., 2011, 2012; Jaworski et al., 2011). Within tauopathy models, dendritic structure progressively changes with the development of pathology, with neurons displaying either increased complexity in their dendritic arbours in mice that overexpress human tau (Dickstein et al., 2010), or atrophy and reduced dendritic complexity in mice that overexpress mutant human tau (Crimins et al., 2012; Rocher et al., 2010). These conflicting results suggest that these changes may reflect different pathological disease stages in response to different tau isoforms. Changes in dendritic structure would be sufficient to alter input resistance and capacitance, as these measures both relate to total membrane area, and could explain the decreased neuronal excitability that has been observed in tauopathy models, including in rTg4510 mice (Booth et al., 2016a). Changes in dendritic structure could therefore provide a mechanistic explanation for some of the changes in the intrinsic membrane properties and synaptic function in rTg4510 neurons reported in Chapter 2**.**

3.1.2 Tau-mediated dysfunction and degeneration of synapses

Abnormal tau pathology is thought to mislocate and accumulate in synapses. Tau pathology has been detected in synapses in post-mortem AD brain tissue (Fein et al., 2008; Perez-Nievas et al., 2013; Tai et al., 2014) and in tauopathy mouse models (Hoover et al., 2010; Xia et al., 2015). This process is suggested to then lead to tau-mediated synaptic dysfunction and degeneration (Eckermann et al., 2007; Kopeikina et al., 2013b; Rocher et al., 2010). Within the rTg4510 model of tauopathy, there has also been observed reductions in the expression of synaptic genes and proteins (Castanho et al., 2019; Kopeikina et al., 2013a). Synaptic structure and structural plasticity were also altered in other models of tauopathy, with changes in spine shape, volume and turnover observed (Hoffmann et al., 2014; Jackson et al., 2017).

Overall, tauopathy has been implicated in the physiological alteration of synapses, but few studies have investigated how these changes relate to the progression of neurodegeneration. Investigating changes in synaptic protein expression at early and progressed neurodegenerative phases of tauopathy in the rTg4510 model will generate a pathological timeline of synaptic protein expression, that can be cross-referenced to the emergence of changes in synaptic function.

3.1.3 The role of tau pathology in excitatory receptor dysfunction

Glutamate receptor dysfunction has been a long-standing hypothesis for symptomatic changes observed in tauopathies (Benussi et al., 2019). NMDA receptors (NMDARs) are a likely candidate to play a role in the dysfunction and degeneration observed in tauopathies (Liu et al., 2019). NMDAR activity can modulate excitotoxicity of neurons, by the overactivation of extrasynaptic NMDARs (Hardingham and Bading, 2010; Léveillé et al., 2008; Wang and Reddy, 2017). NMDAR subunit expression (GluN1, GluN2A and GluN2B) was also reduced in models of tauopathy (Kopeikina et al., 2013a). Recently, it has been suggested that tau interacts with NMDARs and fyn kinase to regulate NMDAR excitotoxicity via GluN2B phosphorylation (Ittner et al., 2010; Miyamoto et al., 2017; Mondragón-Rodríguez et al., 2012). In support of this, the A152T variant of tau, which increases the risk for tauopathies, has also been identified as increasing the risk of NMDAR-mediated excitotoxicity (via the GluN2B subunit) (Decker et al., 2016; Maeda et al., 2016).

The importance of other ionotropic glutamate receptors, such as AMPA receptors (AMPARs), in tauopathies has been less extensively studied. In AD post-mortem brain tissue, AMPAR binding sites were decreased in the hippocampus (Dewar et al., 1991) and AMPAR subunit expression was decreased in the hippocampus (Yasuda et al., 1995). Downregulation of genes that express AMPAR subunits (Alldred et al., 2012) and reductions in AMPAR subunit expression (Hoover et al., 2010; Kopeikina et al., 2013a) have been observed in chronic tau overexpression models. Also, phosphorylation of tau at different sites can differentially reduce AMPAR activity in cultured neurons (Teravskis et al., 2019), suggesting that tauopathies are associated with reduced AMPAR expression and hypoactivity. Conversely, AMPAR-mediated activity was increased in the rTg4510 model in the hippocampus and frontal cortex following neurodegeneration onset (Crimins et al., 2011, 2012; Dalby et al., 2014). Interestingly, AMPAR activity, but not NMDAR activity, also facilitates the release of tau from neurons, which would suggest a mechanism for trans-synaptic spread of pathological tau that may involve AMPAR activity (Pooler et al., 2013).

Results presented in Chapter 2 showed alterations in glutamate receptor function in early (~5.5M) and progressed (~7.5M) neurodegenerative phases of tauopathy in rTg4510 mice. It would be prudent to determine whether these changes were related

to changes in the expression of NMDARs and AMPARs, whether that be overall receptor expression or subunit expression.

3.2 AIMS

This work aimed to address whether there were changes in dendritic morphology which may account for some of the changes observed in neuronal properties, such as a reduced capacitance, at 5.5M of age in rTg4510 mice in Chapter 2. To do this, changes in morphology was assessed by reconstructing dendritic morphology from previous recorded neurons in Chapter 2.

In addition, at 5.5M of age in the rTg4510 mice, there was an observed reduction of the NMDA:AMPA receptor ratio which could be linked to altered expression of AMPA and NMDA receptors. Therefore, synaptosomes were isolated from the somatosensory cortex of 5.5M and 7.5M rTg4510 and wildtype littermate mice to quantify glutamate receptor and synaptic protein expression.

3.3 METHODS

3.3.1 Histology

3.3.1.1 Samples

Whole-cell patch clamp recordings were made from neurons in layer II/III of the somatosensory cortex in thalamocortical brain slices. Protocol details and electrophysiological data from this population of cells was presented in Chapter 2. These recordings were performed in three experimental batches (Batch 1, 2, 3): Batch 1 and 2 from ~5.5M old rTg4510 (TG) mice and wildtype (WT) littermate controls, Batch 3 from ~7.5M old TG mice and WT littermate controls. During these recordings, neurons were simultaneously filled with biocytin that was dissolved in the intracellular solution. This labelling procedure allowed recorded neurons to be detected and morphological reconstructed *post hoc*.

Following whole-cell patch clamp recordings, brain slices were fixed overnight in 4% paraformaldehyde (in 0.1M phosphate buffered saline (PBS)) at 4°C. Slices were then transferred to 0.1M phosphate buffer (PB) at 4°C until immunofluorescence staining.

3.3.1.2 Immunofluorescence staining

Two different immunofluorescence protocols were used. The first protocol used no antigen retrieval techniques or blocking of background signal (Protocol 1). This

protocol was used on brain slices from Batch 1, which measured synaptic physiology. In this first protocol, no recorded neurons colocalised with tau pathology. It was thought that this may be due to antigen masking during the fixation process. Following this, heating was used to help increase the recovery of the tau signal. In addition, this second protocol also included an extra blocking step in glycine to help reduce non-specific background signal seen in the first protocol (Figure 3.1). This protocol was used on the brain slices from Batch 2 (Protocol 2), which assessed intrinsic neuronal properties.

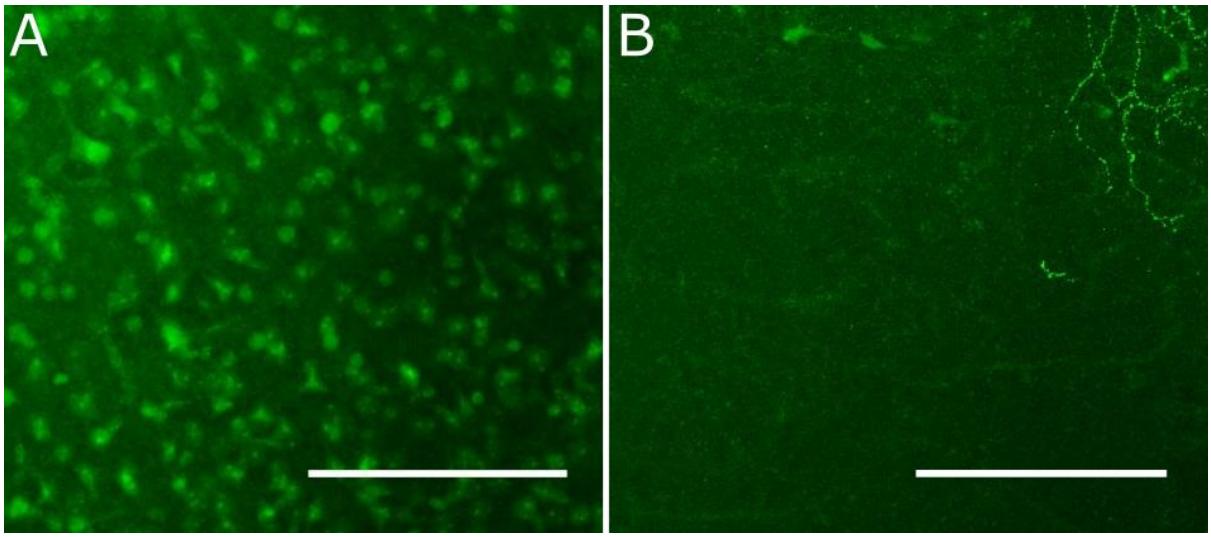

Figure 3.1 Non-specific background signal observed in brain slices following neuronal recovery. The left-hand image (**A**) is from Protocol 1, with large amounts of non-specific background signal. The right-hand image (**B**) shows a large reduction in non-specific background signal using Protocol 2. Dendrites from a filled cell are clearly visible in the top right-hand corner of this image. Scale bars: 100 µm.

3.3.1.2.1 Immunofluorescence protocols: Protocol 1 used on Batch 1

Brain slices were rinsed 3 times for 5 minutes in 0.1M PB, followed by 3 lots of 5 minute washes in 0.1M PBS. Slices were blocked for 1 hour at room temperature using Normal Goat Serum (Vector Labs, UK, Cat#S-1000) diluted 1:200 in 0.1M PBS with 0.3% Triton-X and 0.05% Sodium Azide. Slices were then incubated in the primary antibody (MC-1 IgG1, 1:1000, specific for conformationally changed tau epitopes (kindly provided by Peter Davies)) diluted in 0.1M PBS with 0.3% Triton-X and 0.05% Sodium Azide at 4°C for 3 days. Following this, slices were rinsed 3 times for 5 minutes in 0.1M PBS. Slices were then incubated in “secondary” antibodies (1:1000 goat anti-

mouse AlexaFluor 594 IgG (Cat#A11005, ThermoFisher, USA) & anti-avidin Alexafluor 488 conjugate (Cat#A21370, ThermoFisher)) in 0.1M PBS with 0.3% Triton-X and 0.05% Sodium Azide at 4°C overnight. Following this, slices were rinsed in dH_2O for at least 5 minutes and then were mounted using VectaShield Mounting Medium for Fluorescence (Cat#H-1000, Vector Labs) and coverslipped.

3.3.1.2.2 Immunofluorescence protocols: Protocol 2 used on Batch 2

The additional steps from Protocol 2 are shown in italics and underlined.

Brain slices in PB storage solution were placed in wells in dH_2O and incubated within a waterbath until at 78°C for 25 minutes (for increased antigen retrieval). The brain slices were then left to cool in wells for 35 minutes. Brain slices were rinsed 3 times for 5 minutes in 0.1M PB, followed by 3 times 5 minutes washes in 0.1M PBS. *Slices were then incubated in glycine (100 mM diluted in PBS with 0.3% Triton-X and 0.05% Sodium Azide, Sigma-Aldrich Cat#G7126) for 30 minutes.* Following this step, slices were treated the same as per Protocol 1 from the Normal Goat Serum blocking step.

3.3.1.3 Imaging

Slices were imaged using a two-photon microscope (Scientifica, UK) equipped with a tuneable Ti:Sapphire pulsed laser (Coherent, Chameleon Discovery NX, USA) or a confocal microscope (SP8; Leica, Germany). Slices were imaged using two-photon microscopy, with the laser wavelength set to 790 nm to excite both AlexaFluor 488 and 594, with 0.5 µm optical slices taken with an average of 8 frames per slice at a 512x512 pixel resolution using a 20x objective. For the confocal microscope, pre-set dye bandwidth filter settings for AlexaFluors 488 and 594 were picked with 0.5 µm optical slices taken with a line average of 2 at a 512x512 pixel resolution using a 20x objective. Images were acquired using ScanImage (Vidrio, USA) and Leica application suite X (Leica) acquisition software for the two-photon microscope and the confocal microscope, respectively.

3.3.1.4 Analysis

Image stacks were analysed using the Fiji distribution of ImageJ software (Schindelin et al., 2012). The two imaging channels were split from the acquired image stack and the green channel (AlexaFluor 488) was used for cell tracing to ensure blinding to genotype. Cells were morphologically traced using the Simple Neurite Tracer plugin (Longair et al., 2011). Cells were selected for analysis based on the quality of recovery

(soma and dendrites visible). Traced neurons were than analysed by Sholl analysis (Ferreira et al., 2014) with radii binning occurring every five µm (Figure 3.2).

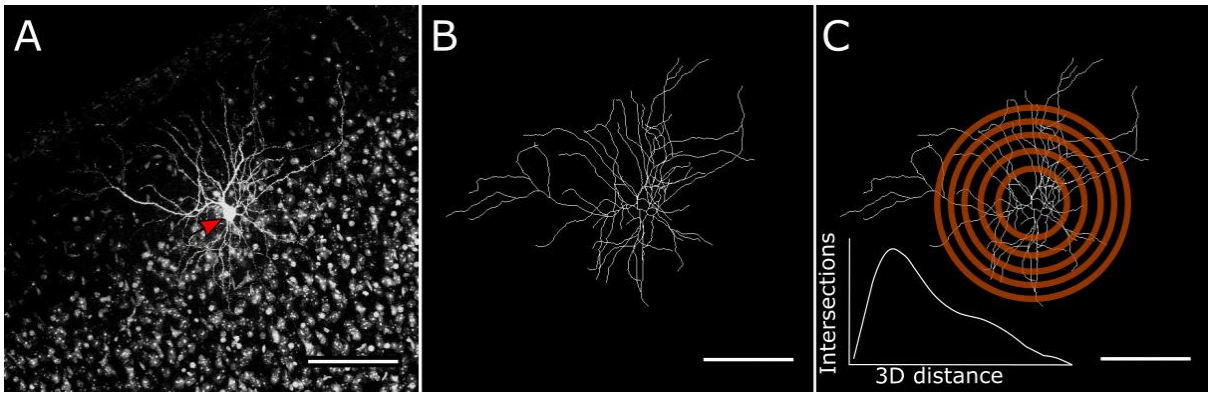

Figure 3.2 Sholl analysis of a traced neuron. A max projection image of a biocytin labelled neuron (soma highlighted with an arrowhead) (**A**), and a max projection image of its' skeleton following morphological tracing (**B**). Sholl analysis was used to analyse the dendritic structure (**C**), where intersections are measured at radii of increasing size. This generates a Sholl plot (inset), which plots the number of intersections against the radial distance. Scale bar: 100 µm.

3.3.1.5 Statistics

Statistical tests were performed using R software (v3.5.1) with the integrated development environment RStudio (v1.1.456).

Consistent with statistical analyses presented in Chapter 2, the experimental unit considered was the 'cell'. Yet again, by nature of the experimental design, multiple cells may have come from a single animal. Cell from the same animal may therefore be more similar when compared to cells that came from another animal. Therefore, a generalised linear mixed model (GLMM) was used to estimate the contribution of animal to the spread of the individual datasets.

The following GLMM was used to model results with single data points (i.e. when there was a single point measure):

$$Variable \sim genotype + (1|animal\ number)$$

The variable was the experimental measure being tested, with genotype as the main tested effect of interest. Animal number was integrated into the model as a random

variable, denoted as 1|animal number to conform with standard notation. The interclass correlation coefficient (ICC) measured the effect of animal variability on the measured outcomes. If the ICC value was >0.1, then a GLMM was used to determine significance (Fiero, 2016). The best model for the data was chosen based on lowest Akaike information criterion (AIC) value along with other measures of fit from the model such as assessment of the residuals for normality and heteroscedasticity. The data distribution was visualised using a histogram and quartile-quartile-plot and factored into the model when necessary (i.e. normal, tweedie, gamma distribution).

For GLMMs, goodness of fit chi squared (χ^2) tests were used to evaluate the fit for each main effect to determine significance of factors in the model. Significant results were described as ($\chi^2_{(df,\ n)}$ = a, p=b*). The degrees of freedom were listed for the χ^2 test (df) with the number of observations within this linear model (n). The χ^2 value was then listed (a) along with the corresponding p value (b) with asterisks denoting significance when alpha <0.05. Non-significant results were listed with a p value only. Results were sometimes also stated as an estimate of change with standard error in brackets to help signify the amount and direction of the effect. A Tukey-Kramer multiple comparison adjustment was used for *post hoc* testing whilst controlling for multiple comparisons.

If the ICC value <0.1, then t-tests were used for statistical comparisons between genotypes (Fiero, 2016). If the data was not normally distributed (i.e. non-parametric), then a Mann-Whitney U non-parametric t-test was run. If the data was normally distributed with equal variances, then a Student's t-test was run. If the variances were unequal, then a Welch's t-test was run. Significant results were described as ($t_{(df,\ n)}$ = a, p=b*), where a was the t-test statistic (t), df was the degrees of freedom, n was the total n number, and the p value was b. Significance was denoted with asterisks: p<0.05*, p<0.01**, p<0.005***. Non-significant results were listed as a p value only.

The sholl plot analysis was a repeated measure, quantifying number of intersections over increasing radii. Therefore, the GLMM used was changed to account for repeated measurements within the same cell.

Therefore, for the Sholl plot analysis, the following GLMM used was:

$$Intersections \sim radius * genotype + (1|animal\ number/cell\ number)$$

Within this model, the number of intersections was the tested variable of interest, to test whether there was a difference in intersections at different radii between genotypes. Radius, genotype and the interaction between these two effects (denoted as an asterisk) were modelled in as the main effects for statistical testing. Because these repeated measures came from a single cell, this was included in the random variable to account for nesting of measures. This was denoted as (1|animal number/cell number), which means cell number was a nested variable that came from an animal number.

Unless stated otherwise, data is stated as mean ± standard error of the mean (SEM). Box plots show the mean (square shape), median (line), and SEM (box). Significance was denoted with asterisks: $p<0.05$ *, $p<0.01$ **, $p<0.005$ ***. For line plots, the line represents the mean and the shaded area is the SEM.

3.3.2 Synaptosome preparations

3.3.2.1 Animals: P301S mice

Aged P301S mice (over 5 months of age) and WT littermate controls were used to optimise the synaptosome protocol and to determine suitable antibody concentrations for protein detection. The P301S model is a mouse model of tauopathy which overexpresses human tau with the P301S mutation. Mature tau pathology is detectable at around 5-6 months of age (Allen et al., 2002).

3.3.2.2 Samples

Whole brains were used to optimise and compare different protocols for synaptosome isolation. This was done using whole brains from aged P301S mice and WT littermates (>5M).

The TG brain tissue dissections for synaptosome preparations were kindly performed by Tracey K Murray and Lukasz Jankowski (Eli Lilly, Surrey, UK). For these samples, mouse body weight was recorded and mice were then culled using a Schedule 1 procedure. The whole brain was removed, and brain weight was recorded. The brains were placed in a mouse brain matrix to create 2.3mm thick coronal slices between Bregma 0.38 - -1.94 (Figure 3.3). The somatosensory cortex was dissected, weighed and snap frozen on dry ice. The cerebellum was dissected, weighed and snap frozen on dry ice (Figure 3.3). Samples were collected in RNAase free vials. Cerebellar tissues were collected as a negative control since expression of P301L human tau

was restricted to the forebrain in TG mice (Ramsden et al., 2005; SantaCruz et al., 2005).

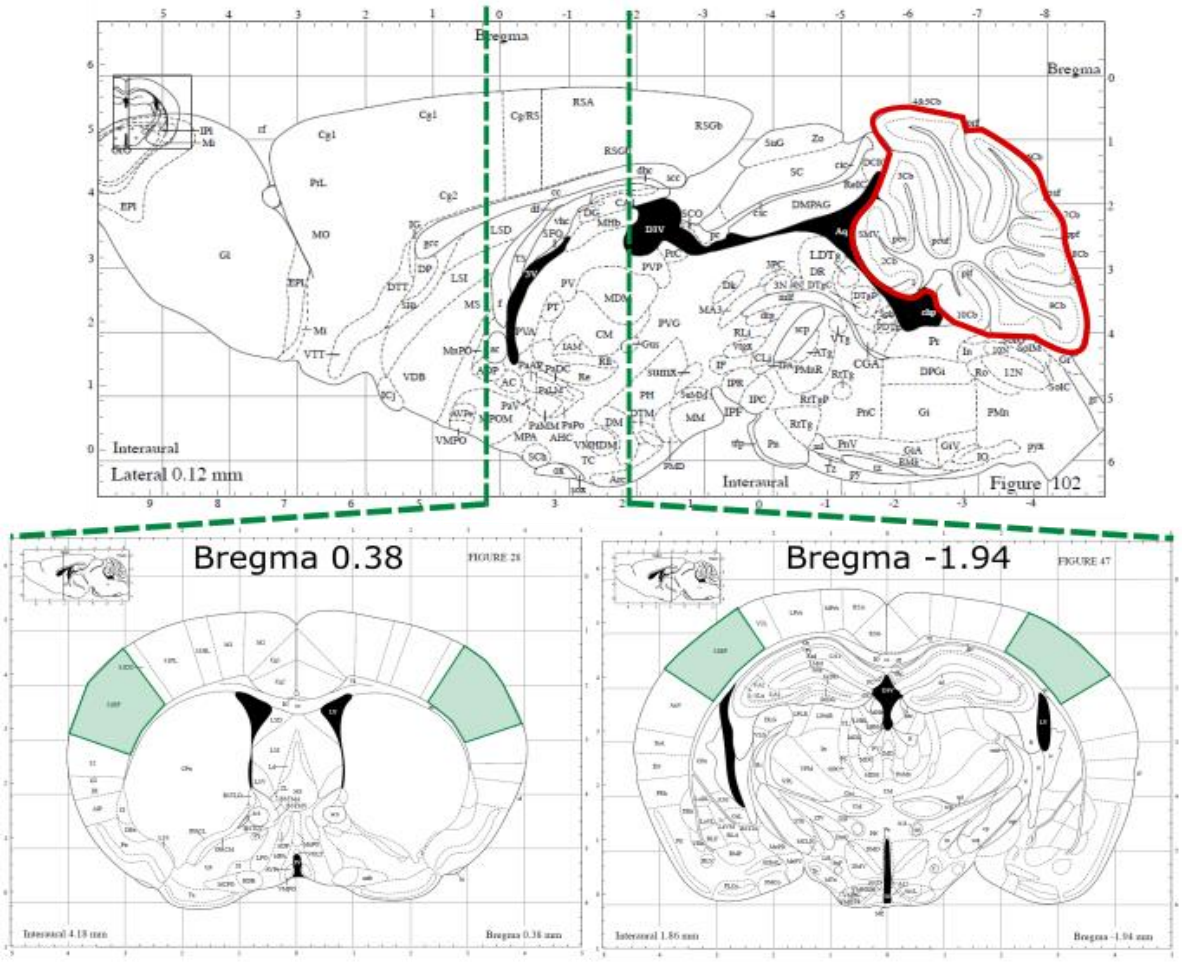

Figure 3.3 Isolation of the somatosensory cortex and cerebellum. The cerebellum (shown in red) was dissected, and somatosensory cortex (shown in green) was isolated between stereotaxic coordinates (from Bregma): 0.38 - 1.94 mm.

3.3.2.3 Synaptosome preparations: overview

To study synaptic proteins, synaptosomes were isolated from TG and WT controls. Synaptosomes are sealed nerve terminal ends which encompass and preserve the synaptic environment including vesicles and synaptic bound receptors (Evans, 2015; Whittaker, 1993). Three methods were compared in this chapter (pellet 2 (P2), lysed pellet (LP), and a discontinuous sucrose gradient) to measure the total output protein concentration (i.e. synaptosome concentration) and to confirm the enrichment of synaptic markers by each of the methods (Dunkley et al., 1986; Gray and Whittaker,

1962; Huttner et al., 1983; Nagy and Delgado-Escueta, 1984; Tenreiro et al., 2017). An overview of the three protocols is shown in Figure 3.4, with buffer composition for the protocols listed in Table 3.1. Protocols were based specifically on methods described by Mazzo et al., 2016 & Sahara et al., 2014.

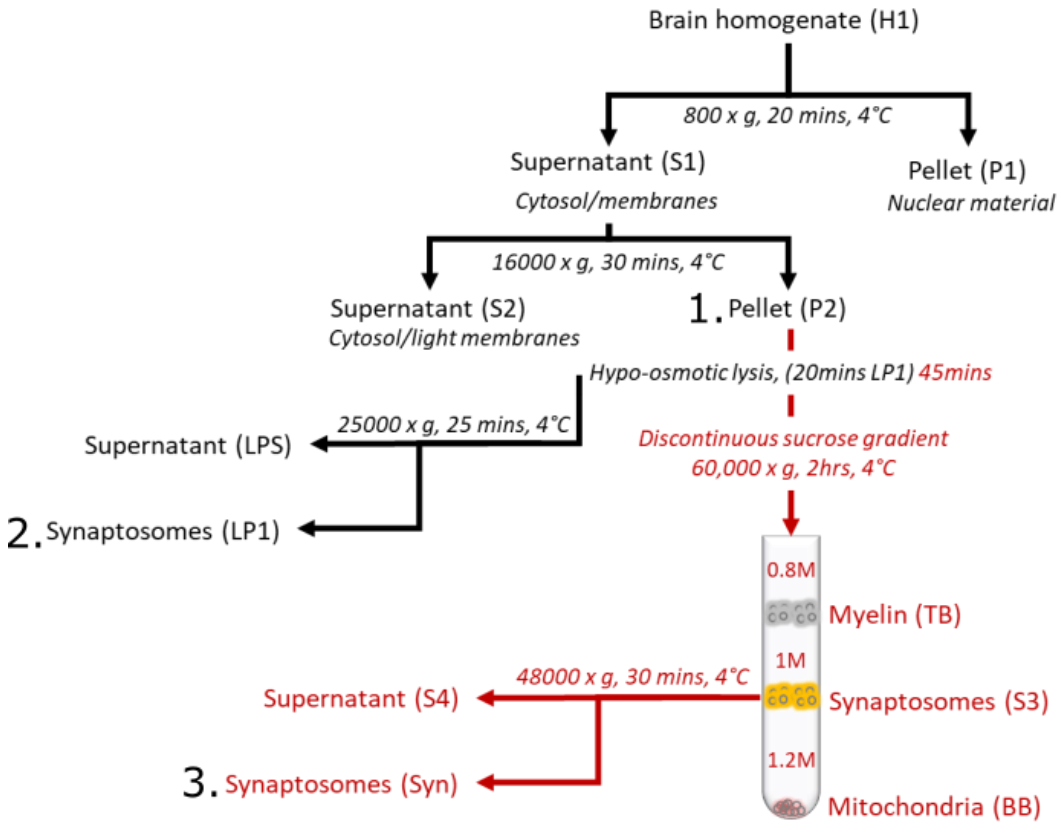

Figure 3.4 Synaptosome preparation overview. A schematic overview of the three methods used for synaptosome preparations (**1.** P2, **2.** LP1 and **3.** Discontinuous sucrose gradient purified synaptosomes (highlighted in red)). Acronyms: H = homogenate, S = supernatant, P = pellet, LP = lysed pellet, LPS = lysed pellet supernatant, TB = top band, BB = bottom band, Syn = synaptic fraction.

Table 3.1 Formulation of buffers used for isolated synaptosome preparations. Buffer formulations used for the three protocols (P2, LP1 and discontinuous sucrose gradient purified).

	Sonicating/ homogenisation buffer	***Buffer A***	***Buffer B***	***Buffer C***	***Tris (50 mM)***
cOmplete mini (Roche, Switzerland, Cat# 11836153001)	1 tablet	1 tablet	1 tablet	1 tablet	1 tablet
Phosphatase inhibitor cocktail #2 (Sigma, USA, Cat# P5726)	1:100 dilution	1:100 dilution	1:100 dilution	1:100 dilution	1:100 dilution
Phosphatase inhibitor cocktail #3 (Sigma, Cat# P0044)	1:100 dilution	1:100 dilution	1:100 dilution	1:100 dilution	1:100 dilution
Tris-HCl, pH 7.4	50 mM	/	50 mM	50 mM	50 mM
Tris-HCl, pH 8.0	/	5 mM	/	/	/
Sucrose	0.3 M	/	1.2 M	0.85 M	/
EDTA, pH 7.4	50 mM	/	/	/	/
EGTA, pH 8	50 mM	0.5 mM	0.5 mM	0.5 mM	/

3.3.2.3.1 Sample preparation (H1)

All samples were sonicated in an ice cold sonicating buffer (see Table 3.1) using a QSonica sonicator (CL-18) set to 40% amplitude pulses on 1 second, off 1 second for ~10 seconds. A subset of experiments also used a homogeniser (Ultra-Turrex T10 with S10N-8G metal tip – 12 strokes) to homogenise, rather than sonicate the samples.

3.3.2.3.2 Crude synaptosome (P2) preparation

TG and WT littermate samples underwent synaptosome preparation up to P2. P301S WT littermate control samples were further purified to explore synaptosome concentration and purification (Figure 3.4).

Sonicated tissue samples (H1) were centrifuged in a Sigma 4-16KS centrifuge (rotor: 12130) for 20 minutes at 800 x g at 4°C to separate the nuclei (P1) from the homogenate (H1). The supernatant (S1) was transferred to a new centrifuge vial and centrifuged for 30 minutes at 16,000 x g at 4°C to separate microsomes and other soluble enzymes (S2) from the crude synaptosomal preparation (P2). If crude synaptosomes (P2) were required, then this 2nd pellet was resuspended in 100 µl of 50 mM Tris (Table 3.1) and the protein concentration was calculated using a Bicinchoninic acid (BCA) assay. The P2 fraction was then diluted to 1 mg/ml in 50mM Tris (Table 3.1) and stored at -80°C until needed.

If further purifying the P2 fraction, P2 was then resuspended in a solution specific for the LP1 or discontinuous sucrose gradient protocol.

3.3.2.3.3 Purified synaptosomes (LP1)

The P2 pellet underwent further purification (LP1 protocol) as highlighted on Figure 3.4 (protocol 2).

The P2 pellet was resuspended in Buffer A in falcon tubes. Samples were left on ice for 30 mins to lyse out internal organelles such as mitochondria from synaptosomes, known as hypo-osmotic shock. The samples were then centrifuged for 25 minutes at 25,000 x g to get LP1 (“Synaptosome membranes”). The supernatant was discarded (LPS) and the pellet (LP1) was resuspended in 50 mM Tris (Table 3.1). The protein concentration was calculated using a BCA assay.

3.3.2.3.4 Purified synaptosomes (Syn)

The P2 pellet underwent further purification using a discontinuous sucrose gradient as highlighted in red on Figure 3.4 (protocol 3).

The P2 pellet was resuspended in 2.04 mL of buffer B (Table 3.1) in 15 ml falcon tubes. The tube was left on ice for 45 mins to lyse out internal organelles such as mitochondria from synaptosomes, known as hypo-osmotic shock. Following hypo-osmotic shock, the sample was mixed well by pipetting. 0.96 ml of 1 M sucrose solution was added to the lysed solution to take the total volume up to ~ 3 ml and the sucrose concentration to ~0.3 M. The solution was then mixed well with a pipette. A discontinuous sucrose gradient with equal volumes of liquid was made in a 13.4 mL Beckman Coulter Ultra Clear tube (Cat#344059). From the bottom to the top of the tube, solutions were carefully layered in the following order: 1.2M sucrose-based

solution (buffer B, Table 3.1), 0.85M sucrose-based solution (buffer C, Table 3.1), prepared sample (~0.3M sucrose-based solution; Figure 3.4). This tube was added to the Sorvall TH-641 swing bucket rotor (rotor: SW41Ti) with appropriate counterbalances as necessary. Samples were spun at 60,000 x g for 2 hours at 4°C on a Beckman Coulter Optima XPN-80 Ultracentrifuge. During centrifugation, separation of three different layers occurred. From top to bottom of gradient, there was the top band (TB) (myelin) fraction, the synaptosome fraction in middle (S3), and the bottom band (BB) fraction (mitochondrial). Each fraction was removed carefully with a pipette and put into individual eppendorf's. The S3 fraction was diluted with 50 mM Tris (Table 3.1) to 10% sucrose (assuming the band collected contained ~30% sucrose concentration, so 2 volumes of 50 mM Tris was added to one volume of band sample collected (~1ml recovered: 2ml added)). The S3 fraction was spun at 48,000 x g for 30 mins at 4°C (Rotor: 45TI, Centrifuge: Beckman Coulter Optima XPN-80 Ultracentrifuge). The supernatant S4 was discarded and the pellet (Syn) was resuspended in 50 mM Tris (Table 3.1). The protein concentration was calculated using a BCA assay.

3.3.2.3.5 Bicinchoninic acid (BCA) assay: protein concentration

A BCA protein concentration assay was performed on all samples using a BCA Protein Assay Kit (#23227; ThermoFisher). Manufacturer guidance was followed for the protocol. In brief, an albumin standard (within the kit) was used as the assay standard. Samples and standards were serial diluted using Tris 50 mM (Table 3.1). Samples and standards were plated in duplicate on 96-well plates. The BCA working reagent was formulated and added to all samples, and was left to incubate for 30 minutes at 37 °C. Following this, well plates were imaged on a spectrophotometer (Precision microplate reader, Molecular devices) and sample values were compared to a calculated standard curve from the standard measures.

For the TG samples, all P2 purified cerebellum samples had a protein concentration above 1mg/ml. Therefore, they were normalised to 1 mg/ml stocks using 50 mM Tris buffer (Table 3.1). The majority of the P2 purified somatosensory cortex samples were above 1mg/ml in concentration. These samples were normalised to 1mg/ml stocks using 50 mM Tris (Table 3.1). However, some samples were below 1mg/ml, likely due to the low starting sample weight prior to purification (Table 3.2). These samples were used at the P2 measured concentration, i.e. used as neat.

Table 3.2 Protein concentration of somatosensory cortex P2 samples from TG mice. Rows contain data for individual TG mice samples. Columns contain the mouse ID number, genotype (wildtype homozygous, W:W; transgenic homozygous, CC), age, extracted tissue weight and calculated P2 concentration (plate concentration). Highlighted rows were samples that were run at below 1mg/ml concentration.

ID	Genotype	Age	Somatosensory Cortex extracted weight (mg)	Plate Concentration (µg/ml)
1	W:W	5.5M	10.7	1043
2	W:W	5.5M	9.1	1226
3	W:W	5.5M	7.9	1510
4	W:W	5.5M	13.4	1918
5	W:W	5.5M	8.5	1088
6	W:W	5.5M	8.8	1828
7	W:W	5.5M	9.7	1441
8	W:W	5.5M	9.4	1313
9	W:W	5.5M	10.2	1340
10	W:W	5.5M	7.6	1184
11	C:C	5.5M	8.3	1041
12	C:C	5.5M	9.2	992
13	C:C	5.5M	7.7	980
14	C:C	5.5M	8.9	1162
15	C:C	5.5M	8.0	1972
16	C:C	5.5M	6.5	692
17	C:C	5.5M	8.4	993
18	C:C	5.5M	5.6	779
19	C:C	5.5M	9.6	1194
20	C:C	5.5M	8.0	1175
21	C:C	5.5M	8.9	1149
22	W:W	7.5M	13.1	1938
23	W:W	7.5M	8.9	1177
24	W:W	7.5M	8.9	1082
25	W:W	7.5M	9.5	1937
26	W:W	7.5M	9.3	1300
27	W:W	7.5M	12.5	1332
28	W:W	7.5M	10.1	1383
29	W:W	7.5M	13.3	1677
30	W:W	7.5M	11.2	1382
31	W:W	7.5M	11.1	1556
32	C:C	7.5M	8.6	1051
33	C:C	7.5M	8.5	1238
34	C:C	7.5M	5.8	735
35	C:C	7.5M	4.4	424
36	C:C	7.5M	3.0	223
37	C:C	7.5M	5.8	957
38	C:C	7.5M	5.8	694
39	C:C	7.5M	6.2	849
40	C:C	7.5M	6.4	805
41	C:C	7.5M	7.1	931
42	C:C	7.5M	7.9	1179

3.3.2.4 Protein Detection

3.3.2.4.1 SDS-Page

Antibody concentrations were optimised for ideal detection of proteins of interest on crude P2 synaptosomes prepared from P301S whole brains (data not shown). Therefore, P301S P2 synaptosomes was ran as a positive control alongside samples from the TG and WT samples.

Samples were diluted into 2x Laemmli Sample Buffer (BioRad, Cat#161-0737), or 4x NuPage LDS Sample Buffer (Novex, NP0008), diluted with Mercaptoethanol (1:20 and 1:10 respectively, Cat#161-0710, Bio-Rad). Samples were then heated at 95°C for 5 minutes using a Grant QBD2 heating block. Samples were loaded, 20 µl (~10 µg) per lane (Figure 3.5), into an Invitrogen NuPAGE 8% Bis-Tris Midi Gel (Cat#WG1002BX10) with 1x MOPS SDS Running Buffer (diluted from 20x to 1x, Novex, Cat#NP0001) and ran at 150 V for 75 minutes (or until the protein band reached the bottom of the gel) using a PowerEase 300W (Life Technologies). SeeBlue Plus 2 Prestained Standard (Invitrogen, Cat#LC5925) was used as the molecular weight ladder.

Gel 1

L	P301S	Blank	SCTX	SCTX	SCTX	Blank	SCTX	SCTX	SCTX	SCTX	Blank	SCTX	SCTX	SCTX	Blank	SCTX	SCTX	SCTX	SCTX
L	Ctrl	B	1	11	22	32	B	2	12	23	B	33	3	13	24	B	34	14	35
1	2	3	4	5	6	7	8	9	10	11	12	13	14	15	16	17	18	19	20

Gel 2

L	P301S	Blank	SCTX	SCTX	SCTX	Blank	SCTX	SCTX	SCTX	SCTX	Blank	SCTX	SCTX	SCTX	SCTX	Blank	SCTX	SCTX	SCTX
L	Ctrl	B	4	15	25	B	36	5	16	26	B	6	17	37	B	18	27	38	28
1	2	3	4	5	6	7	8	9	10	11	12	13	14	15	16	17	18	19	20

Gel 3

L	P301S	Blank	SCTX	SCTX	SCTX	SCTX	Blank	SCTX	SCTX	SCTX	Blank	SCTX	SCTX	SCTX	Blank	SCTX	SCTX	SCTX	SCTX
L	Ctrl	B	7	19	29	39	B	20	40	8	B	30	9	41	B	10	21	42	31
1	2	3	4	5	6	7	8	9	10	11	12	13	14	15	16	17	18	19	20

Figure 3.5 SDS-Page gel loading map. Three gels were run per antibody per brain region (this example shows the somatosensory cortex (SCTX)). Blue samples are WT 5.5M, orange TG 5.5M, green WT 7.5M and grey TG 7.5M. Samples were randomly spread across the three gels to reduce confounding variability due to gels. The first row per gel is the sample description, the second row specifies sample ID number and the third row is the lane number. L = ladder, Ctrl = P301S samples, B = blank.

3.3.2.4.2 Western Blotting

Proteins were transferred onto a nitrocellulose membrane (Amersham Protran Premium 0.4 µm Nitrocellulose, Cat#10600003) soaked in a transfer buffer (NuPage Transfer Buffer, Novex, Cat#NP0006-1, diluted to 1x concentration with 20% methanol), using a BioRad PowerPac Universal which was ran at 25 V for 80 minutes. Following protein transfer, Ponceau S (Sigma-Aldrich) staining was used to ensure protein transfer and to confirm where to cut blots if required. Following this, membranes were incubated for an hour in PBS containing 0.05% tween (PBS-T) and 5% milk (Marvel, Original Dried Semi Skimmed Milk). Next, membranes were incubated overnight at 4°C in primary antibodies (targeted at either tau, synaptic proteins, AMPARs or NMDARs; Figure 3.6) diluted to the optimised concentrations (Table 3.3) in PBS-T with 5% milk. The next day, membranes were washed 3 times for 10 minutes with PBS-T. Corresponding secondary antibodies were used at either 1:20,000 for anti-mouse, 1:10,000 for anti-rabbit (Table 3.3) and incubated for one hour at room temperature in PBS-T with 5% milk. Membranes were washed again 3 times for 10 minutes with PBS-T. Membranes were then incubated using Dura or Femto detection substrates depending on signal strength (SuperSignal West Dura Extended Substrate, Cat#34075, ThermoScientific; SuperSignal West Femto Maximum Sensitivity Substrate Cat#34095, ThermoScientific) for 5 minutes, and following this membrane images were taken using an Amersham Imager 600. If required, membranes were stripped by incubation in Restore PLUS Western Blot Stripping Buffer (ThermoScientific, Cat#46430) for 10 minutes. Membranes were then rinsed with PBS-T. Membranes then underwent the blocking step and the protocol continued as before (i.e. block, primary antibody incubation, etc). Stripping was only done once per membrane as this removes some of the protein on the membrane which can bias results.

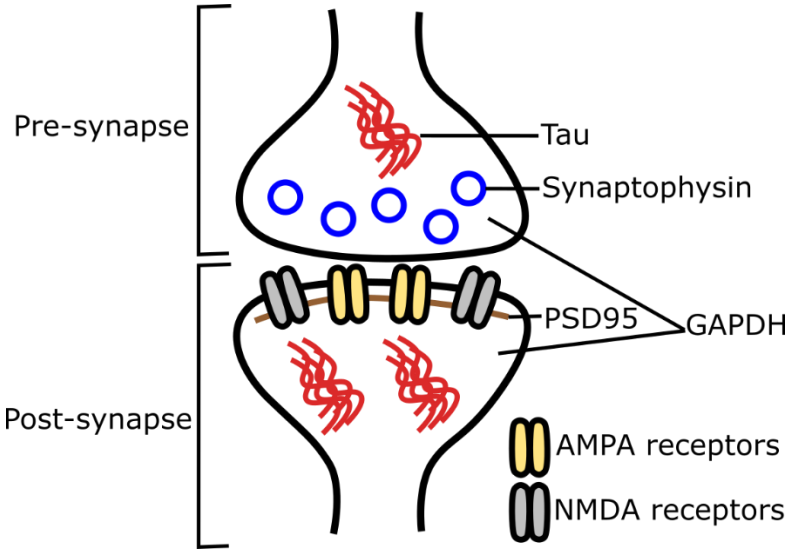

Figure 3.6 Synapse schematic. An overview of a synapse to highlight antibody targets at the pre- and post-synapse. *Note: GAPDH is mainly localised to the cytosol (as indicated by the lines) but is also found at plasma membranes, nuclear membranes and vesicles (Tristan et al., 2011).*

Table 3.3 Antibodies used for protein detection on western blots. A table showing all primary and secondary antibodies used for protein detection within synaptosomes preparations. Secondary antibodies are highlighted in yellow and antibodies that did not work (deemed as no visible detection in optimisation samples) in this assay are highlighted in green.

Antibody	***Target***	***Species***	***Dilution used***	***Supplier***	***Catalogue No.***	***Lot No.***
GAPDH	Housekeeping protein (localised mainly to cytosol)	Mouse	1:6000	Invitrogen, USA	AM4300	Multiple
AT-8	Tau	Mouse	1:1000	Peter Davies	-	-
CP27	Tau	Mouse	1:1000	Peter Davies	-	-
PSD95	PSD95	Mouse	1:1000	BD, USA	610495	8128742
Synaptophysin	Synaptic vesicles	Mouse	1:1000	Abcam, UK	Ab8049 (SY38)	GR3280108-1

GluR1 (AMPA) [EPR5479]	AMPA receptor, subunit 1	Rabbit	1:1000	Abcam, UK	Ab109450	GR3241245-1
Anti-GluA2/GluR2 Glutamate Receptor Clone L21/32	AMPA receptor, subunit 2	Mouse	1:1000	NeuroMab, USA	75-002	472-IJU-17
GluR3	AMPA receptor, subunit 3	Mouse	1:1000	Invitrogen, USA	32-0400	RH240594
NMDAR1 Monoclonal Antibody (54.1)	NMDA receptor, subunit 1	Mouse	1:1000	Invitrogen, USA	32-0500	UH286597
Anti-NR2A, M264-10ug	NMDA receptor, subunit 2A	Rabbit	1:1000	Sigma, USA	1002457527	MKCC8197
NMDAR2B	NMDA receptor, subunit 2B	Mouse	1:1000	BD, USA	610416	8159860
GluN2C clone N422/18	NMDA receptor, subunit 2C	Mouse	1:1000	NeuroMab, USA	75-411	455-6JD-37
NR2D	NMDA receptor, subunit 2D	Rabbit	1:1000	Abcam, UK	Ab35448	851239
HRP linked anti-mouse IgG	Mouse raised immunogens	-	1:20000	Cell Signallng, USA	7076S	Multiple
ECL anti-rabbit IgG HRP linked	Rabbit raised immunogens	-	1:10000	GE, USA	NA934V	Multiple
Anti-NR1, CT (Not working in assay)	NMDA receptor, subunit 1	Mouse	1:500	Millipore, USA	05-432	3046782
Anti-NR1 glutamate receptor, clone N308/48 (Not	NMDA receptor, subunit 1	Mouse	1:500	NeuroMab, USA	75-272	455-10JD-76

working in assay)						
NMDA receptor 1 (GluN1) (D65B7) (Not working in assay)	NMDA receptor, subunit 1	Rabbit	1:1000	Cell Signaling, USA	5704	N/A
Anti-NMDAR (NR2C) (Not working in assay)	NMDA receptor, subunit 2C	Rabbit	1:500	R&D Biosystems, USA	PPS033	1509151

3.3.2.5 Analysis

Images were analysed using ImageQuantTL (v8.2.0 GE). Bands of interest were highlighted and the background signal was subtracted using a rolling ball filter. This gave a raw value for protein expression. This was then normalised to the raw protein expression value for the housekeeper protein (GAPDH), to account for loaded sample differences, particularly important for those samples below 1mg/ml.

3.3.2.6 Statistics

Samples were excluded if the detected bands were incomplete (e.g. a bubble in the middle of the detected band) or if significantly faint compared to the rest of the gel (determined by visual inspection). Randomised block allocation of sample groups across each of the gels and normalisation of protein expression to GAPDH controlled for regional variation in signal intensity within areas of the gel. If the GAPDH band was excluded, then any samples that were normalised to that band were also excluded.

Statistical tests were performed using R (v3.5.1) with RStudio (v1.1.456). GLMMs were used on the normalised expression data to assess statistical significance.

The following formula was used to statistically model the data:

$$Normalised\ protein\ expression \sim genotype * age + (1|gel\ number)$$

Normalised protein expression was the tested variable of interest, genotype and age were the main effects with interactions between the two effects tested (indicated by the asterisk in the formula). As the experiment was performed using a randomised

block design, gel was built into the model as a random variable (as there were an infinite number of gels that could have been run). This was written into the formula as 1|gel number to conform with R syntax. An overview of the different tested effects and the subgroupings that were part of the experimental design are shown in Figure 3.7.

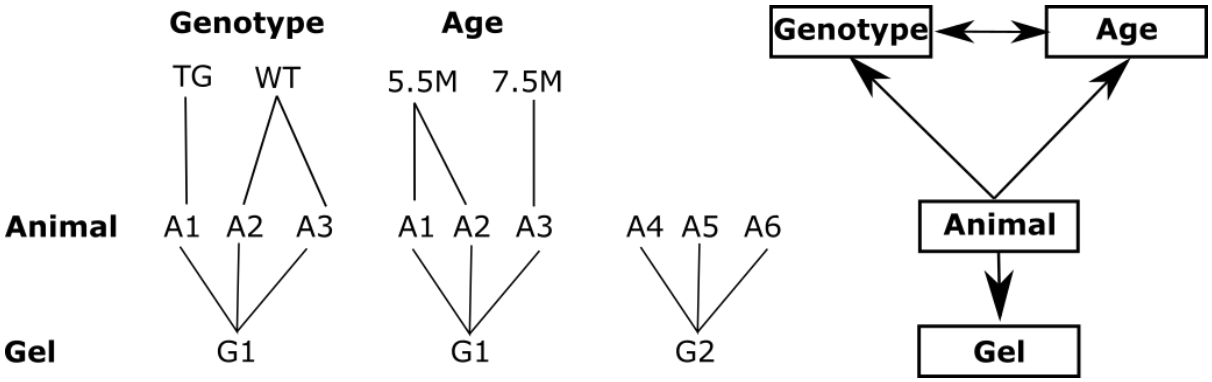

Figure 3.7 Overview of effect subgroups in the synaptosome assay. Each sample (animal; A1-A6), was run on a gel (gel; G1-G2). Different gels had different detection levels unrelated to age or genotype and so were a random grouping factor. Each animal belonged to a genotype (TG & WT) and an age group (5.5M & 7.5M) which were the main effects of interest. These factors may also have an interaction effect, which was also explored in the model.

Consistent with other statistical modelling described in this chapter, the best model was chosen based on AIC along with other measures of fit. The ICC value was listed, which describes the effect the different gel numbers had on the total variance on a scale of 0-1. Values close to 0 were deemed non-influential on the variance of the data, whereas values closer to 1 suggested that different gels had an influential value on the clustering of the data. This may be due to labelling variability per gel for example. Significant results were described as ($\chi^2_{(df,\ n)}$ = a, p=b*). Non-significant results were listed with a p value only. Least squares means with Tukey-adjusted comparisons were used to analyse main effects between groups by performing *post hoc* comparisons. Asterisks were used to denote significance with p<0.05 *, p<0.01 ** and p<0.005 ***.

3.4 RESULTS

3.4.1 Tau pathology was only detectable in TG brain tissue

Tau pathology was detected using the MC-1 antibody, specific for pathogenic conformationally changed tau epitopes. MC-1 antibody staining was present in all tissue samples from TG mice and absent from WT controls (Figure 3.8). Colocalisation between MC-1 staining and recovered neurons was not observed in any of the samples with either staining protocol.

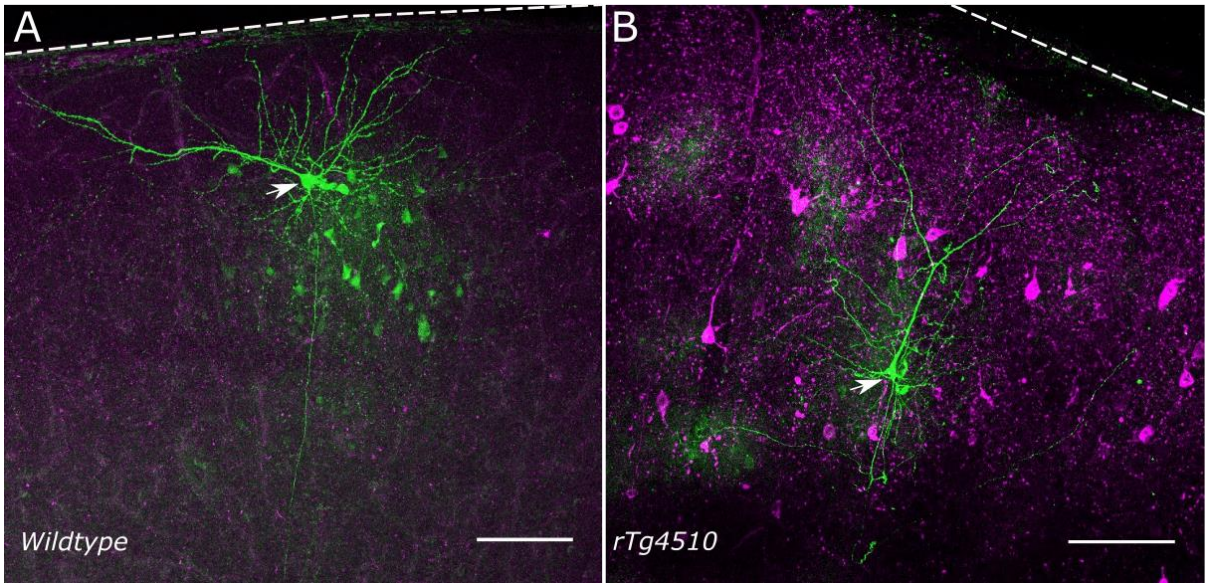

Figure 3.8 WT and TG neurons from ~5.5M old mice with and without MC-1 positive staining. Two example filled neurons labelled in green (AlexaFluor-488, highlighted with white arrowheads), with MC-1 staining in magenta. The neuron in **A** was from a WT animal, and the tissue section does not contain any MC-1 positive inclusions. There was some cellular staining surrounding the neuron in green, which was detected non-specific biocytin recovery from electrophysiological recordings. The neuron in **B** was from a TG animal. Note the large amount of MC-1 positive pathology, including neuronal inclusions (magenta). The pia is denoted with a dashed white line. Scale bars: 100 µm.

3.4.2 Increased dendritic complexity proximal to the soma at ~5.5M in TG mice compared to WT mice

Biocytin labelled neurons from the two recorded batches were grouped together (similarly aged animals) and morphologically traced. 21 WT neurons (10 animals) and 26 TG neurons (13 animals) were successfully recovered and deemed of sufficient

quality for analysis for changes in dendritic structure. Sholl analysis quantified how many times the traced neuron intersected radii of increasing size until there were no more intersections. From this analysis, the complexity of the dendritic structure can be quantified. There was a significant main effect of radius ($\chi^2_{(119,5520)}$ = 5715, p<0.005***), but not genotype (p=0.89) on the sholl analysis. However, there was a significant interaction effect between genotype and radius ($\chi^2_{(119,5520)}$ = 310.4, p<0.005***). This analysis revealed a significant increase in the number of intersections between 35-95 and 105-110 µm from the soma (GLMM; p<0.05; See Figure 3.9 for individual p values) in the TG neurons compared to WT neurons.

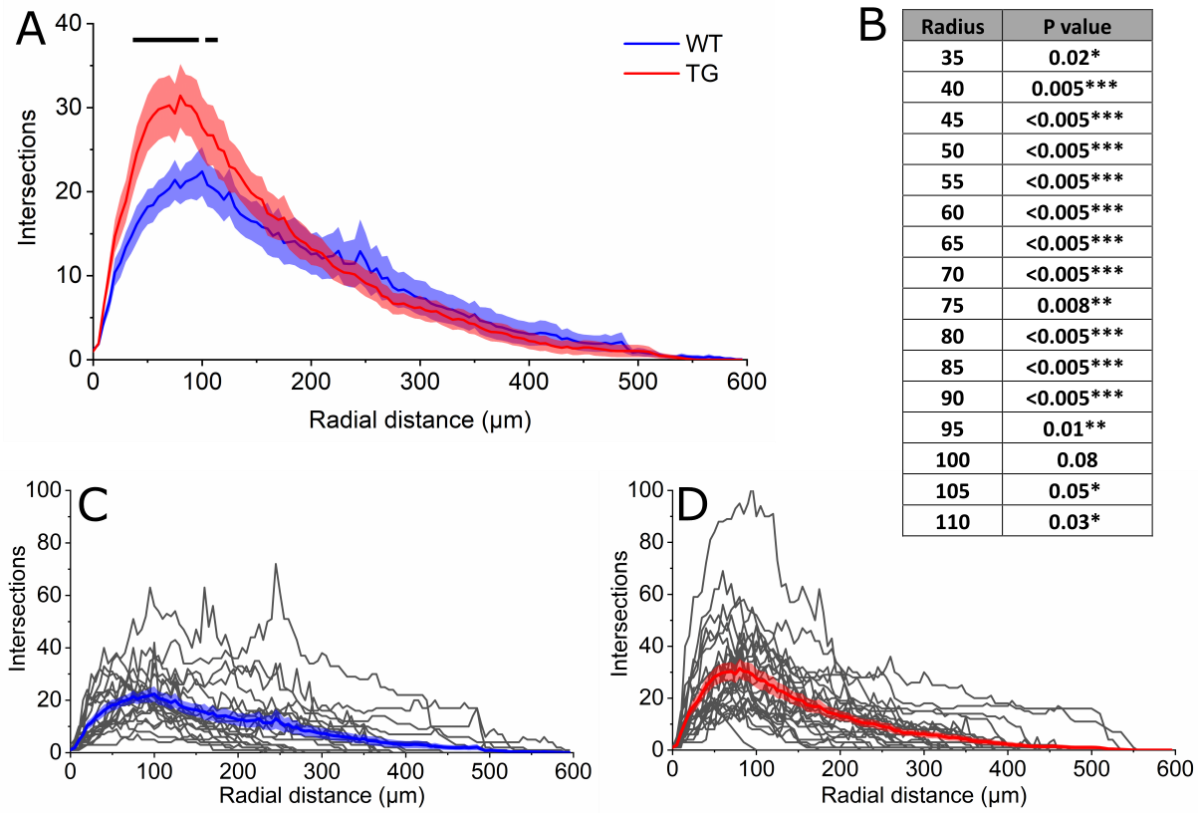

Figure 3.9 Sholl plots of morphologically traced TG and WT neurons. A Sholl plot of the average distribution of dendritic intersections per radial distance from the soma for WT neurons (blue) and TG neurons (red) (**A**). The black line denotes a significant difference of p<0.05, with the p values for the Sholl plot between the highlighted range listed in a table (**B**). Sholl plots for each individual neuron are shown in grey for WT (**C**) and TG (**D**), with the average distribution plotted in blue and red respectively. Lines represent the mean and shaded areas represents SEM.

The maximum intersections value and maximum intersecting radius determines the maximum intersections that occurred at one radius. A change in the maximum intersections and which radius this occurred in would suggest a change in the shape of the neuron, but perhaps not a change in the complexity. The maximum intersecting radius was not significantly different between genotypes (p=0.32, Figure 3.10 A). However, the maximum number of intersections was significantly increased for TG neurons (WT 30.52 ± 3.32 intersections, TG 40 ± 3.56 intersections; Mann-Whitney U t-test, $U_{(1,47)}$ = 175, p<0.04*; Figure 3.10 B).

The enclosing radius is the largest radius that encloses the whole structure (i.e. the last radius to have at least one dendritic intersection). This value can be used as a proxy for the size or area covered by the neuron. The enclosing radii was not statistically different between genotypes (WT 374 ± 25 µm, TG 353 ± 22 µm; p=0.55; Figure 3.10 D).

The sum intersections value was the total number of intersections detected across all measured radii. The mean intersections value was this value divided by the total number of measured radii. Any of these variables changing would represent a change in the complexity of the dendritic arbour. Higher mean intersections for example would suggest a more complex arbour across the whole dendritic structure. However, neither the sum (WT 982 ± 141 intersections, TG 1146 ± 144 intersections; p=0.4, Figure 3.10 E), median (WT 12.14 ± 1.35 intersections, TG 12.33 ± 0.93 intersections, p=0.41; Figure 3.10 C) or the mean number of intersections (WT 12.70 ± 1.30 intersections, TG 15.19 ± 1.22 intersections; p=0.13; Figure 3.10 F) were statistically different between genotypes.

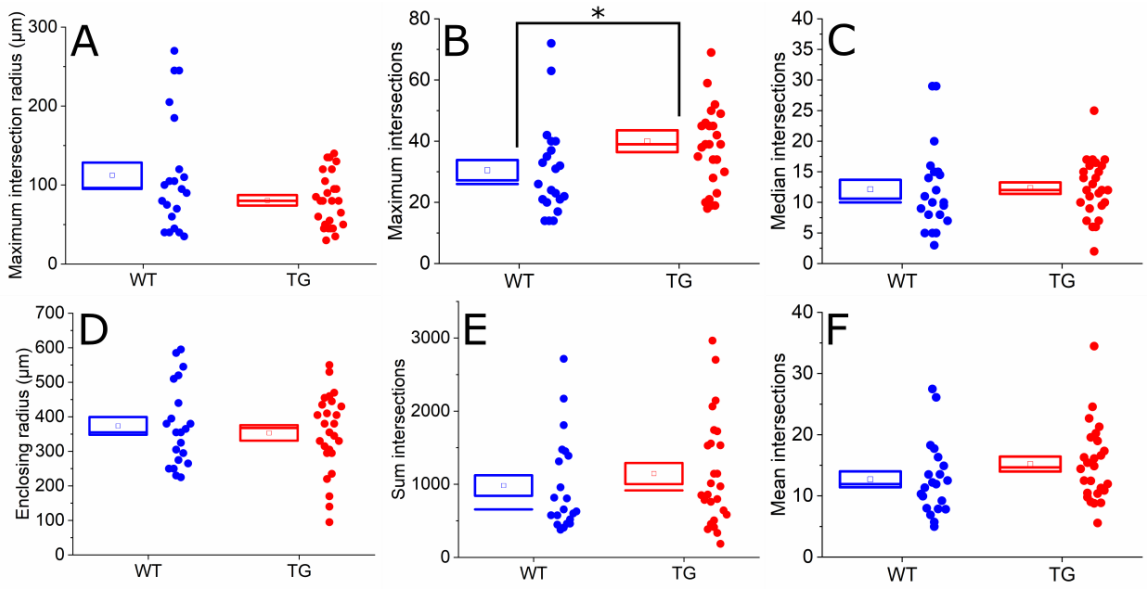

Figure 3.10 Measures of dendritic structure and complexity from Sholl analysis. Box and dot plots of the maximum intersections radius (**A**), maximum intersections (**B**), median intersections (**C**), enclosing radius (**D**), sum intersections (**E**) and mean intersections (**F**) with WT in blue and TG in red. Statistical significance is denoted as $p<0.05$ *.

The traced skeleton was also analysed using Simple Neurite Tracer to extract total branch length, mean branch length, number of junctions, number of branches and number of end points. The total branch length was the total length of all traced branches. Mean branch length was the mean length of each dendrite branch. Number of branches was the total number of skeleton branches, with the number of junctions being a proxy measure of neuronal branching. The number of end points was the number of ending points of the skeleton (i.e. no more branches following that point).

Looking at the overall dendritic skeleton in the traced cells, total dendritic length was significantly increased for TG neurons (WT 5750.33 ± 802.70 µm, TG 9258.53 ± 1063.74 µm; GLMM, $\chi^2_{(1,47)} = 5715$, p=0.02*, ICC 0.19; Figure 3.11 A), with an increase in the number of dendritic branches (WT 86.52 ± 15.73 branches, TG 151.58 ± 24.83 branches; Mann-Whitney U t-test, $U_{(1,47)} = 158$, p=0.01**; Figure 3.11 E), junctions (WT 39.24 ± 7.40 junctions, TG 72.54 ± 12.91 junctions; Mann-Whitney U t-test, $U_{(1,47)} = 161$, p=0.02*; Figure 3.11 D) and end points (WT 49.48 ± 8.07 end points, TG 70.85 ± 7.67 end points; Mann-Whitney U t-test, $U_{(1,47)} = 154$, p=0.01**; Figure 3.11 F). Together with the results of the Sholl analysis, this suggests that there was an increase in the complexity of lower order dendrites within close proximity (<110 µm) of the soma in TG neurons.

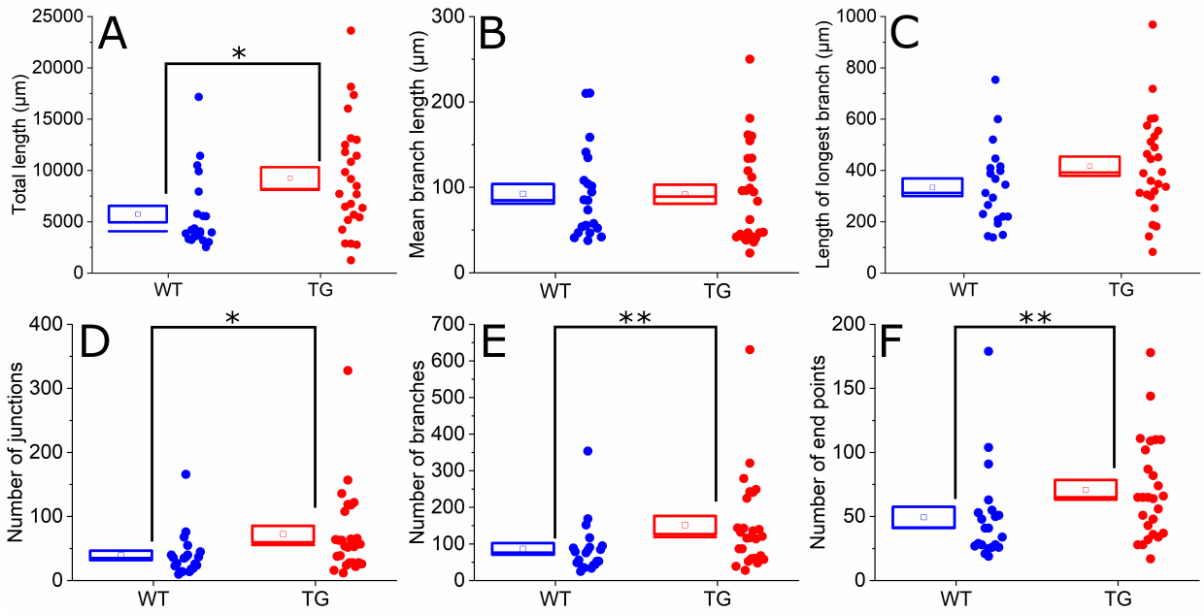

Figure 3.11 Properties measured from the dendritic skeleton. Measures of total length (**A**), mean branch length (**B**), length of the longest branch (**C**), number of junctions (**D**), number of branches (**E**) and the number of end points (**F**) with WT in blue and TG in red. Statistical significance is denoted as $p<0.05$ *; $p<0.01$ **.

3.4.3 Synaptosomes: purification methods

Methods of synaptosome purification were compared to find the optimum method to be used for TG and WT samples.

Shear force is required to tear nerve terminals from axons and dendrites, which then reseal to form synaptosomes. Homogenisation is the typical method of cellular disruption used for synaptosome preparations to produce the H1 fraction (Dunkley and Robinson, 2018). Homogenisation was compared to sonication, which is another common method of cellular disruption which uses ultrasonic soundwaves rather than physical force. Sonication provides a gentler disruption of cell membranes compared to homogenisation (Burden, 2012). Sonication was therefore tested to determine whether it yielded increased recovery of synaptosomes.

Protein concentration was examined at a number of points throughout the P2 protocol to determine whether there was a difference in protein concentration (i.e. recovery of synaptosomes) between the two methods of cellular disruption. Two brains per technique (sonication and homogenisation) were compared for a difference in protein

concentration. The average concentration of protein in the H1 fraction using homogenisation was 2139 mg/ml (range: 2130 - 2148 mg/ml) and using sonication was 2829 mg/ml (range: 2375 - 3282 mg/ml). The average P2 concentration using homogenisation was 7339 mg/ml (range: 3971 – 10706 mg/ml) and sonication was 10215 mg/ml (range: 7995 – 12434 mg/ml). From this, sonication was deemed to be the optimal method for cellular disruption as it produced a higher protein concentration output and therefore a higher putative synaptosome output.

The P2 protocol was then compared to the LP and sucrose gradient protocols to measure protein concentration and synaptosome enrichment (by quantification of synaptosome markers), with sonication used as the method of cellular disruption. The synaptosome fractions were P2 for the P2 protocol, LP1 for the LP protocol and Syn for the sucrose gradient protocol. The average protein concentration at the end of the P2 protocol was 10215 mg/ml (range: 7995 – 12434 mg/ml), compared to 9344 mg/ml for the LP1 protocol (range: 8059 – 10628 mg/ml) and 2246 mg/ml (range: 1150 – 3341 mg/ml) for the sucrose gradient protocol. The P2 protocol was therefore deemed to yield the highest “synaptosome output”.

Each of the methods were also compared for protein expression to ensure that synaptosomes were present and being enriched per fraction. P2, Syn and LP1 all showed synaptosome enrichment when compared to H1 (as measured by synaptophysin and PSD95 detection) (Figure 3.12). Syn and LP1 showed larger enrichment compared to H1 than the P2 fraction.

The P2 protocol was therefore selected to isolate synaptosomes from the TG samples, due to its higher protein concentration per volume yield compared to the sucrose gradient and LP methods.

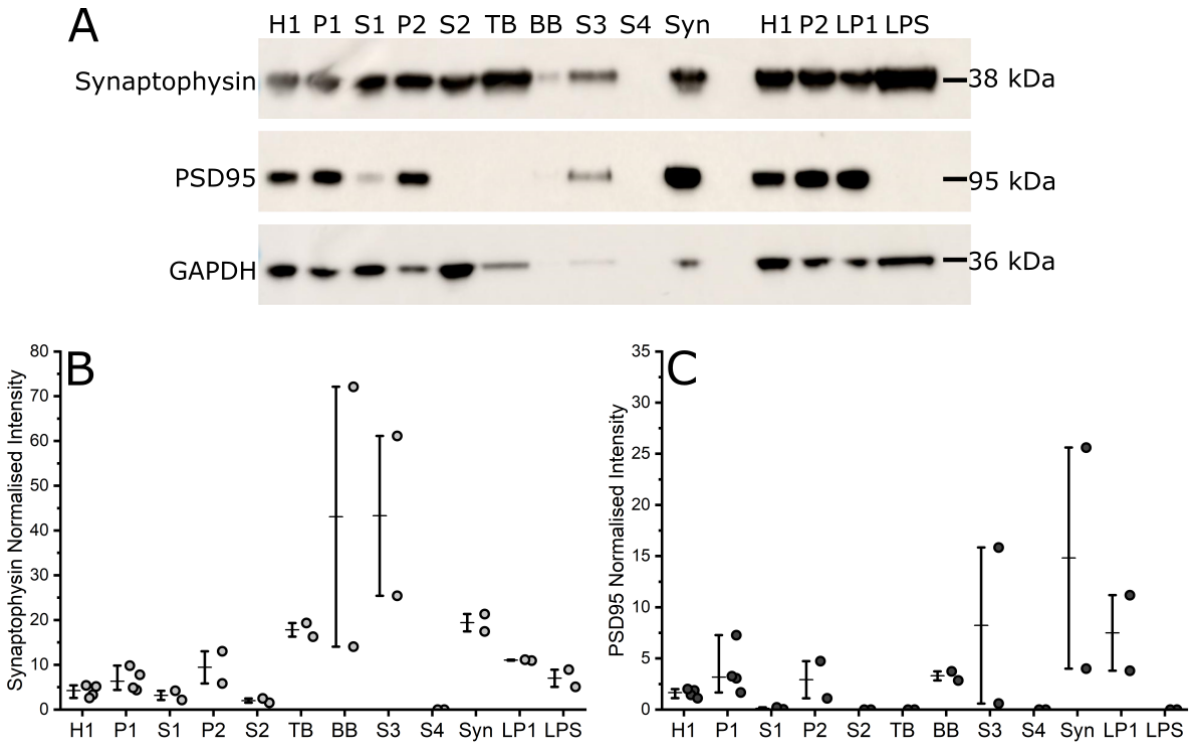

Figure 3.12 Synaptosome enrichment of synaptophysin and PSD95 using the three synaptosome protocols. A western blot with the corresponding fraction listed above each lane (**A**). P2 was the synaptosome fraction compared from the crude synaptosome protocol, Syn was the synaptosome fraction from the sucrose gradient protocol, and LP1 was the synaptosome faction from the LP protocol. Synaptophysin detection, PSD95 detection and the corresponding GAPDH detected band is shown with the corresponding molecular weight on the right-hand side. The intensity of antibody labelling was normalised to the GAPDH expression band. The normalised intensity of synaptophysin (**B**) is shown with light grey filled circles and PSD95 (**C**) with dark grey filled circles. Each synaptosome fraction is listed underneath on the x axis, the error bars illustrate the range with the line representing the mean.

3.4.4 Synaptosomes in TG and WT mice

Synaptosomes were isolated using the P2 fraction method (with sonication) which produced crude synaptosomes. The somatosensory cortex and cerebellum synaptosome preparations from 42 animals across two different age points, 5.5M (10 WT; 11 TG) and 7.5M (10 WT; 11 TG) were probed for synaptic proteins.

3.4.5 Synaptic markers were lower in 5.5M old TG mice

In the somatosensory cortex, there was a significant effect of genotype on synaptophysin expression (GLMM, $\chi^2_{(1,42)} = 4.73$, p=0.02*, ICC 0.53; Figure 2.1 B). There was no age effect (p=0.64) or interaction (p=0.58) between the two factors. There was also a significant effect of genotype on PSD95 expression in the somatosensory cortex (GLMM, $\chi^2_{(1,40)} = 14.13$, p<0.005***, ICC 0.39; Figure 2.1 C). In addition, there was a significant age effect (GLMM, $\chi^2_{(1,40)} = 3.75$, p=0.05*, ICC 0.39), with no interaction between the two factors (p=0.31). Overall, synaptic marker expression was altered with genotype in the somatosensory cortex.

Unlike the somatosensory cortex, there was no effect of genotype (p=0.08) on synaptophysin expression in the cerebellum (Figure 2.1 E). However, there was a significant age effect (GLMM, $\chi^2_{(1,42)} = 4.84$, p=0.03*, ICC 0.45). There was also a significant interaction between age and genotype (GLMM, $\chi^2_{(1,42)} = 5.7$, p=0.02*, ICC 0.45). In contrast to the somatosensory cortex, there was no effect of genotype (p=0.22), age (p=0.73) or interaction (p=0.25) between the two factors on expression of PSD95 in the cerebellum (Figure 2.1 F).

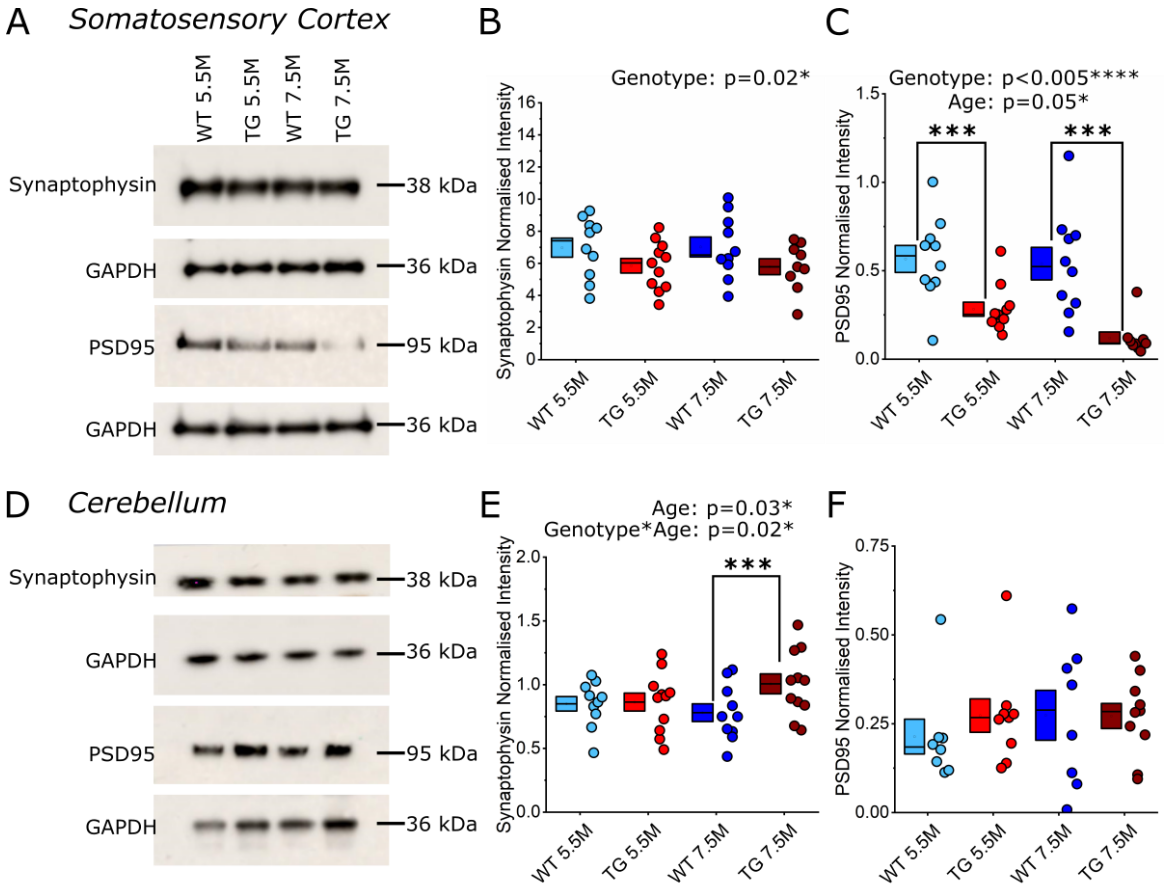

Figure 3.13 Synaptic marker expression was significantly reduced in the somatosensory cortex in TG mice throughout tauopathy. Representative western blots of synaptophysin and PSD95 protein expression in the somatosensory cortex (**A**) and cerebellum (**D**) from WT and TG animals at 5.5 and 7.5M (labelled along the top). Along the left-hand side are the detect proteins of interest with the corresponding GAPDH band below. Along the right-hand side is the molecular weight of the detected protein. Each detected protein band was normalised to the corresponding GAPDH band as a control. Quantification of normalised synaptophysin (**B** & **E**) and PSD95 (**C** & **F**) protein expression. Statistics: GLMM, main significant effects written on the graph, *post hoc* significant denoted by lines and asterisks, p<0.005 ***.

3.4.6 AMPAR expression was lower in TG mice in the somatosensory cortex

There was no effect of genotype (p=0.26), age (p=0.11) or interaction (p=0.44) on GluA1 expression in the somatosensory cortex (Figure 3.14 B). Interestingly, there was a significant effect of genotype on GluA2 (GLMM, $\chi^2_{(1,42)} = 29.1$, p<0.005***, ICC 0.06; Figure 3.14 C) and GluA3 (GLMM, $\chi^2_{(1,41)} = 9$, p<0.005***, ICC 0.25; Figure 3.14 D) expression in the somatosensory cortex. There was also a significant age effect on GluA2 expression (GLMM, $\chi^2_{(1,42)} = 4.33$, p=0.04*, ICC 0.06), but not for GluA3 (p=0.15). There was no interaction (p=0.43) between the two factors for either GluA2 (p=0.43) or GluA3 (p=0.5) expression.

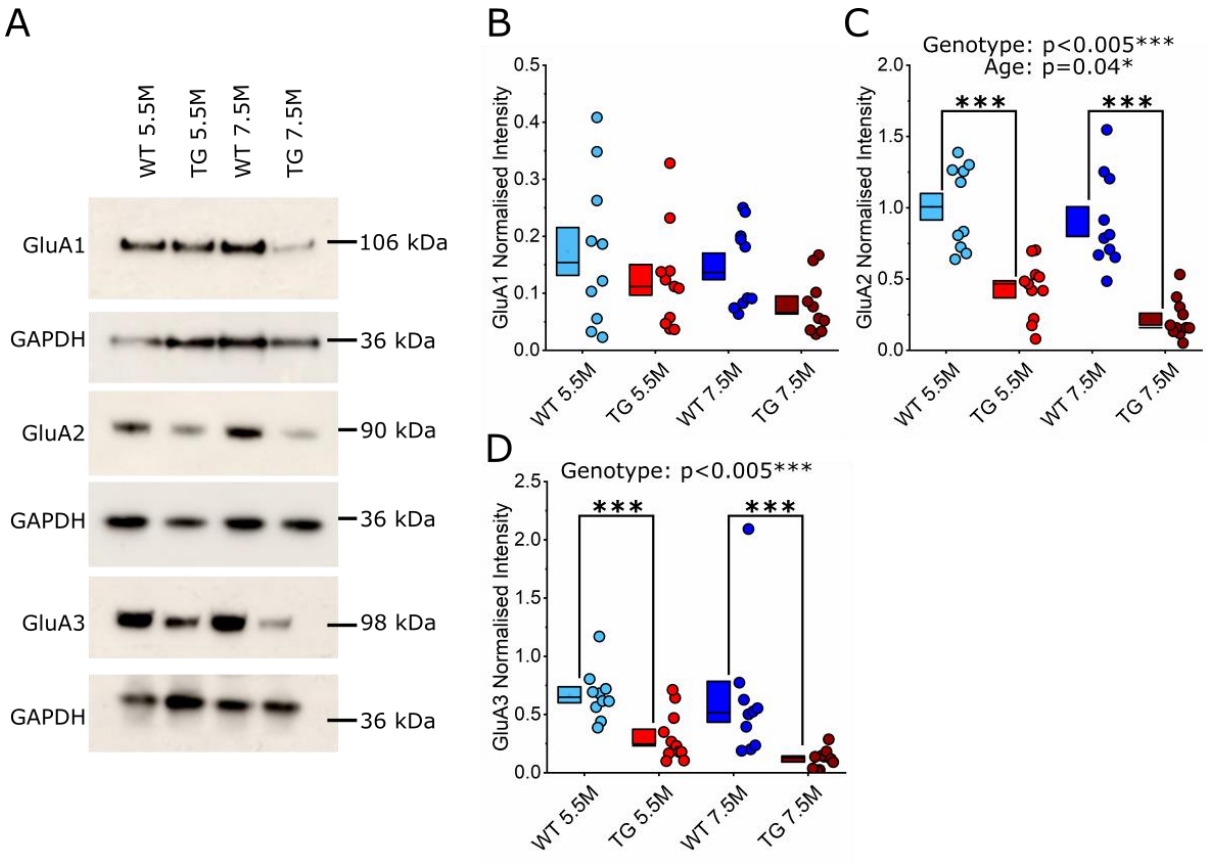

Figure 3.14 AMPAR subunit expression in the somatosensory cortex was significantly decreased in TG mice throughout tauopathy. Representative western blots of AMPAR subunit expression (GluA1-3) from the somatosensory cortex of WT and TG animals at 5.5 and 7.5M (groups labelled along the top) shown in panel **A**. Along the left-hand side of the western blots is the detect protein expression, with the corresponding quantified housekeeping protein GAPDH band below. The expression of each protein of interest was normalised to the corresponding GAPDH expression. Along the right-hand side of the western blots is the molecular weight of each protein band. Quantification of normalised GluA1 (**B**), GluA2 (**C**), and GluA3 (**D**) expression. Statistics: GLMM, main significant effects written on the graph, *post hoc* significance labelled with lines and denoted by asterisk, p<0.005 ***.

For cerebellar expression of AMPAR subunits, there was no significant effect of any factor on expression. Specifically, there was no effect of genotype (p=0.86), age (p=0.27) or interaction (p=0.29) between the two factors on expression of GluA1 in the cerebellum (Figure 3.15 B). There was no effect of genotype (p=0.3), age (p=0.78) or interaction (p=0.35) between the two factors on expression of GluA2 in the cerebellum (Figure 3.15 C). There was also no effect of genotype (p=0.76), age (p=0.53) or interaction (p=0.26) between the two factors on expression of GluA3 in the cerebellum (Figure 3.15 D).

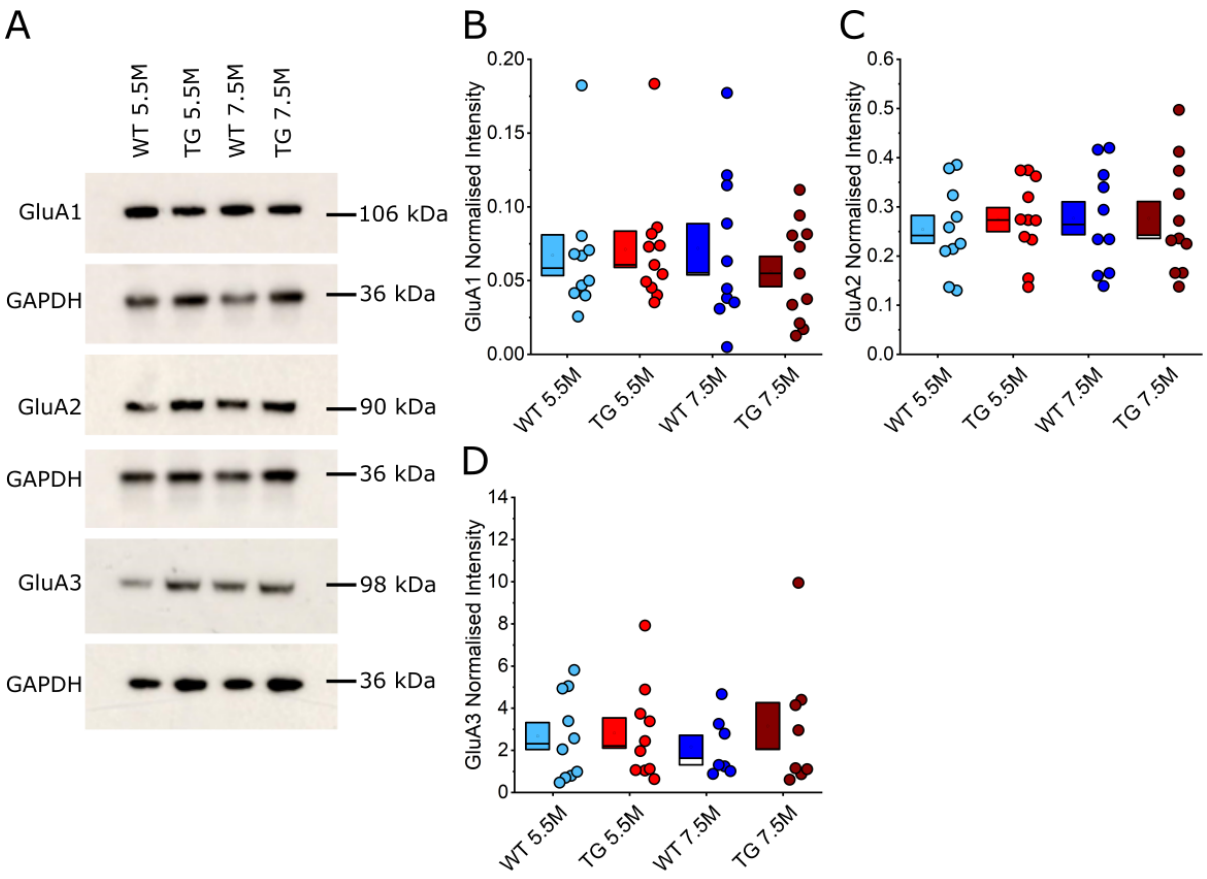

Figure 3.15 AMPAR expression in the cerebellum was not significantly different between genotypes at either age point. Representative western blots of AMPAR subunit expression (GluA1-3) in the cerebellum from WT and TG animals at 5.5 and 7.5M (labelled along the top) shown in panel **A**. Along the left-hand side of the western blots are the detected proteins, with corresponding molecular weight listed on the right. Protein expression was normalised to the corresponding GAPDH band shown below. Quantification of normalised GluA1 (**B**), GluA2 (**C**), and GluA3 (**D**) expression in the cerebellum. Statistics: GLMM, no significant differences between ages or genotypes.

3.4.7 NMDA receptor expression was lower in TG mice in the somatosensory cortex

There was a significant effect of genotype on GluN1 expression in the somatosensory cortex (GLMM, $\chi^2_{(1,42)} = 6.27$, p=0.01**, ICC 0.27; Figure 3.16 B). There was also a significant effect of age (GLMM, $\chi^2_{(1,42)} = 5.72$, p=0.02*, ICC 0.27), which suggests GluN1 expression was decreased with genotype and with age. There was no interaction (p=0.62) between the two factors. For GluN2A expression, there was no effect of genotype (p=0.27), age (p=0.38) or interaction (p=0.34) between the two factors (Figure 3.16 C). There was also no effect of genotype (p=0.1), age (p=0.16) or interaction (p=0.89) between the two factors on sum GluN2B expression (Figure 3.16 D). GluN2C was not detectable in the somatosensory cortex, as expected based on NMDAR subunit expression data (Monyer et al., 1992). Surprisingly, there was a significant effect of genotype on GluN2D expression in the somatosensory cortex (GLMM, $\chi^2_{(1,41)} = 8$, p<0.005***, ICC 0.14; Figure 3.16 E). There was no effect of age (p=0.51), or interaction (p=0.11) between the two factors.

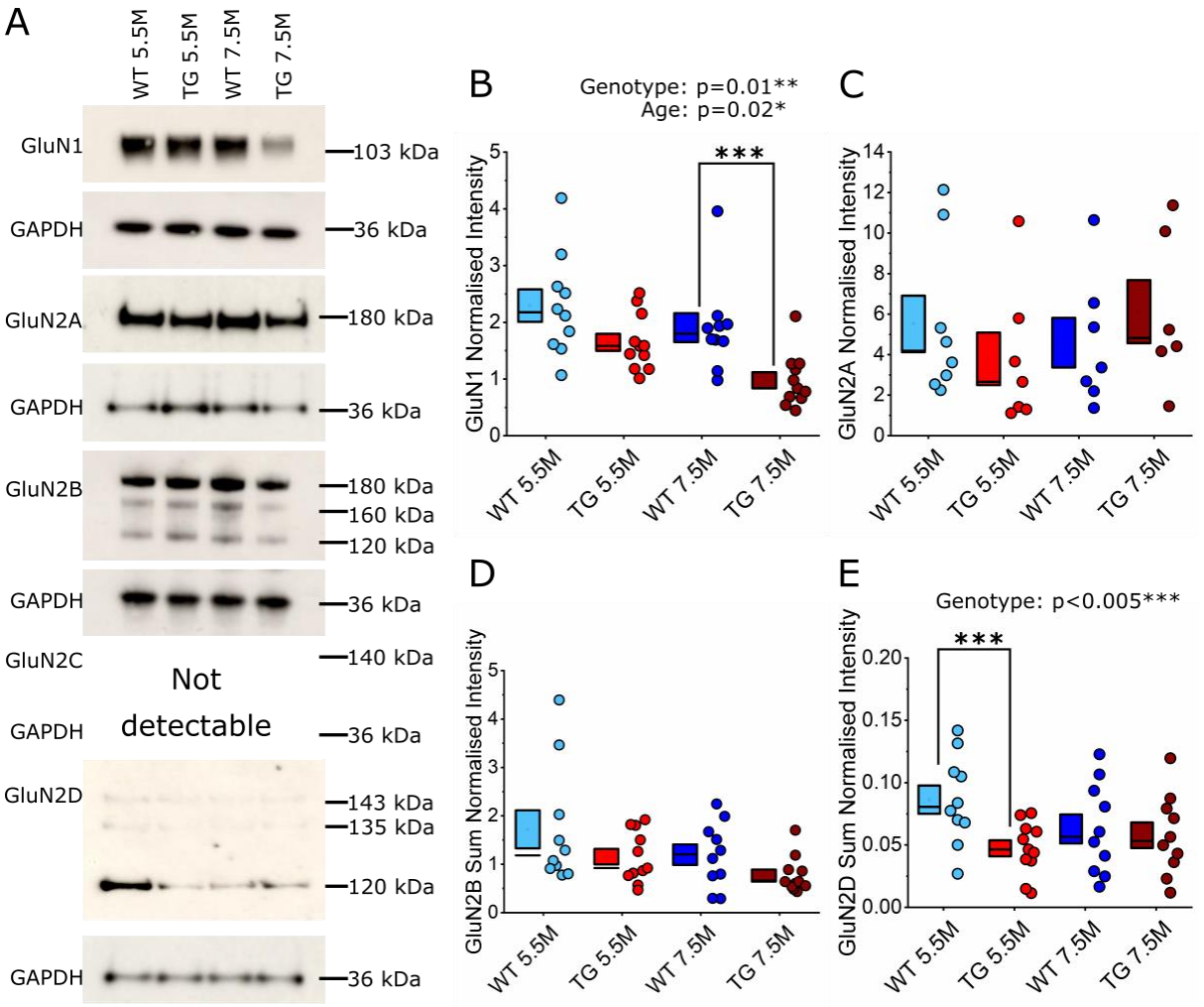

Figure 3.16 NMDAR expression was decreased in progressed tauopathy in the somatosensory cortex. Representative western blots of NMDAR subunit expression (GluN1, GluN2A, GluN2B, GluN2D) in the somatosensory cortex from WT and TG animals at 5.5 and 7.5M (labelled along the top) shown in panel **A**. Along the left-hand side of the western blots are the detected protein, with corresponding molecular weight listed on the right. Where there were multiple detected bands, all detected band expression was summed and the total value was normalised to GAPDH expression. Protein expression was normalised to the corresponding GAPDH band shown below. Quantification of normalised GluN1 (**B**), GluN2A (**C**), and sum GluNB (**D**) and sum GluN2D (**E**) expression in the somatosensory cortex. Statistics: GLMM, main effects were stated on the graphs, with *post hoc* significance denoted by asterisks between ages or genotypes, p<0.05*, p<0.01**, p<0.005***.

Within the cerebellar samples, there was no effect of genotype (p=0.43), age (p=0.24) or interaction (p=0.7) between the two factors on expression of GluN1 (Figure 3.17 B). There was no effect of genotype (p=0.46), age (p=0.5) or interaction (p=0.59) between the two factors on expression of GluN2A in the cerebellum (Figure 3.17 C). GluN2B was not detectable in the cerebellum, as expected based on NMDAR subunit expression data (Monyer et al., 1994). Surprisingly, there was a significant effect of genotype on GluN2C expression (GLMM, $\chi^2_{(1,28)} = 3.86$, p=0.05*, ICC 0.36; Figure 3.17 D). There was no effect of age (p=0.95) or interaction (p=0.49) between the two factors on expression of GluN2C in the cerebellum. There was no effect of genotype (p=0.13), age (p=0.61) or interaction (p=0.95) between the two factors on expression of GluN2D in the cerebellum (Figure 3.17 E).

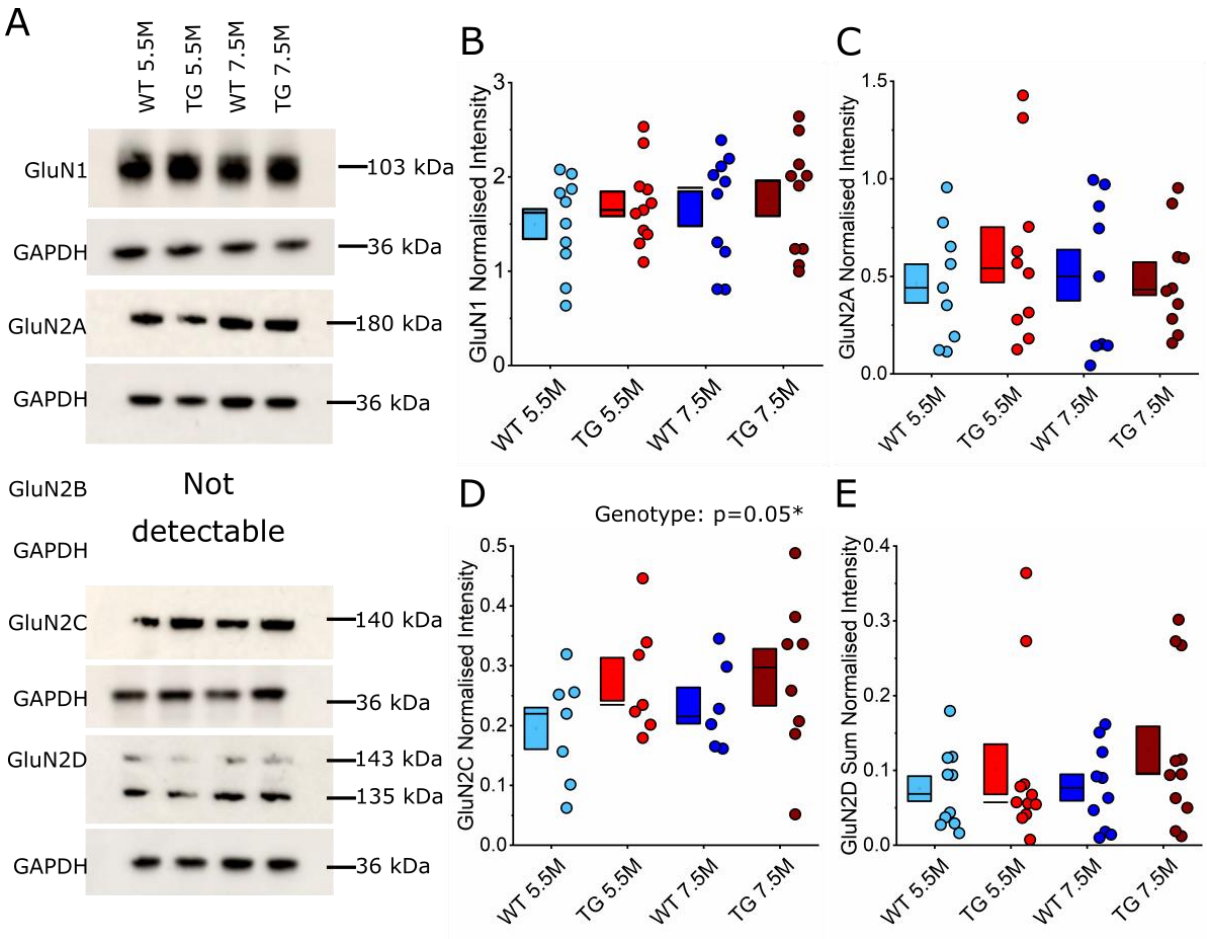

Figure 3.17 NMDAR expression in the cerebellum. Representative western blots of NMDAR subunit expression (GluN1, GluN2A, GluN2B, GluN2D) in the cerebellum from WT and TG animals at 5.5 and 7.5M (labelled along the top) shown in panel **A**. Along the left-hand side of the western blots are the detected protein, with corresponding molecular weight listed on the right. Where there were multiple detected bands, all detected band expression was summed and the total value was normalised to GAPDH expression. Protein expression was normalised to the corresponding GAPDH band shown below. Quantification of normalised GluN1 (**B**), GluN2A (**C**), GluN2C (**D**), and sum GluN2D (**E**) expression in the cerebellum. Statistics: GLMM, main effects were stated on the graphs, $p<0.05$*, no *post hoc* significance observed.

The HUman synapse proteome integrity ratio (HUSPIR) (Bayés et al., 2014) was also calculated based on the GluN2B detected degradation product from the somatosensory cortex synaptosome preparations (Figure 3.18 A).

The ratio was calculated by:

$$HUSPIR = High\ molecular\ weight\ GluN2B\ band \Big/ \frac{degredation\ products\ of\ GluN2B}{(lower\ molecular\ weight\ bands)}$$

This ratio gives a measure of synaptosome quality: ratios higher than 1 are thought to be of good quality, typically indicating a low post-mortem delay. This is mostly used for human synaptosome preparations where there can be long delays between death and tissue isolation, but there may be faster degradation in the TG samples for example due to being structurally compromised and vulnerable to damage. Therefore, this was checked within all the samples. There was no effect of genotype (p=0.9), age (p=0.24) or interaction (p=0.3) between the two factors on HUSPIR (Figure 3.18 B). There were two samples in the WT 7.5M group that had a HUSPIR lower than 1. These samples were in a region of weaker detection on one of the gels and so all bands detected in this area were lower compared to other gels. Therefore, it is likely that the ratio is low in these two samples due to a technical issue and not because these samples are outliers. GluN2B was not detectable in the cerebellum, and so this was not performed on the cerebellar samples.

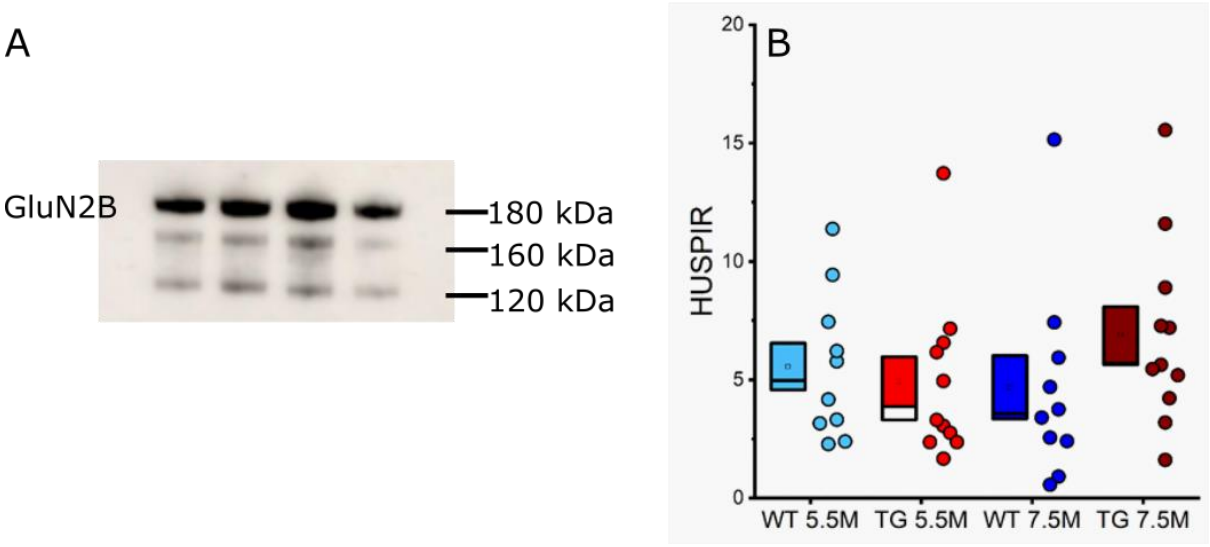

Figure 3.18 HUSPIR measurement in synaptosomes. GluN2B detection by western blot in the somatosensory cortex (**A**). The HUSPIR is calculated as the 180 kDa band divided by the sum of the other lower molecular weight bands, which represents the degradation products of the GluN2B protein. Quantified HUSPIR values across all somatosensory cortex samples shown as a box and dot plot for WT and TG samples at both ages (**B**).

3.4.8 Total tau and hyperphosphorylated tau were increased in the TG mice

CP27 is a marker for total human tau, and AT8 is a marker for hyperphosphorylated tau (Goedert et al., 1995; Jicha et al., 1999). Tau expression (using these two makers) was not detectable in any WT sample from any brain region or age (Figure 3.19 A & D). AT8 positive tau was not detectable in the cerebellum. Multiple bands between 50-60 kDA were detected using CP27 in TG mice at both 5.5M and 7.5M of age (Figure 3.19 A & D). Higher molecular weight bands (i.e. 60 kDa band) are thought to be representative of tau which has large amounts of post-translation modifications such as hyperphosphorylation, with these species only detectable in tauopathies (Zhou et al., 2018). In the somatosensory cortex, this higher molecular weight band was also detected using AT8 confirming that this was indeed hyperphosphorylated tau (Goedert et al., 1995). This higher molecular weight band was not present in the cerebellum, and AT8 labelling was also undetectable. This confirms the absence of tau aggregate pathology in the cerebellum, consistent with previous reports in the TG model (Ramsden et al., 2005; Spires et al., 2006).

There was a significant effect of genotype on CP27 expression in the somatosensory cortex (GLMM, $\chi^2_{(1,42)} = 421.88$, p<0.005***, ICC=0.15; Figure 3.19 B). There was also a significant age effect (GLMM, $\chi^2_{(1,42)} = 15.54$, p=0.005***, ICC=0.15) with expression decreased with age, and a significant interaction (GLMM, $\chi^2_{(1,42)} = 7.57$, p<0.005***, ICC=0.15) between the two factors. There was a significant effect of genotype on sum AT8 expression in the somatosensory cortex (GLMM, $\chi^2_{(1,42)} = 47.03$, p<0.005 ***, ICC=0; Figure 3.19 C). There was no age effect (p=0.55) or interaction (p=0.16) between the two factors.

There was a significant effect of genotype (GLMM, $\chi^2_{(1,38)} = 91.74$, p<0.005***) and age (GLMM, $\chi^2_{(1,38)} = 19.66$, p=0.007**) on CP27 detected expression in the cerebellum (Figure 3.19 E). There was no interaction (p=0.95) between the two factors on expression of CP27 in the cerebellum.

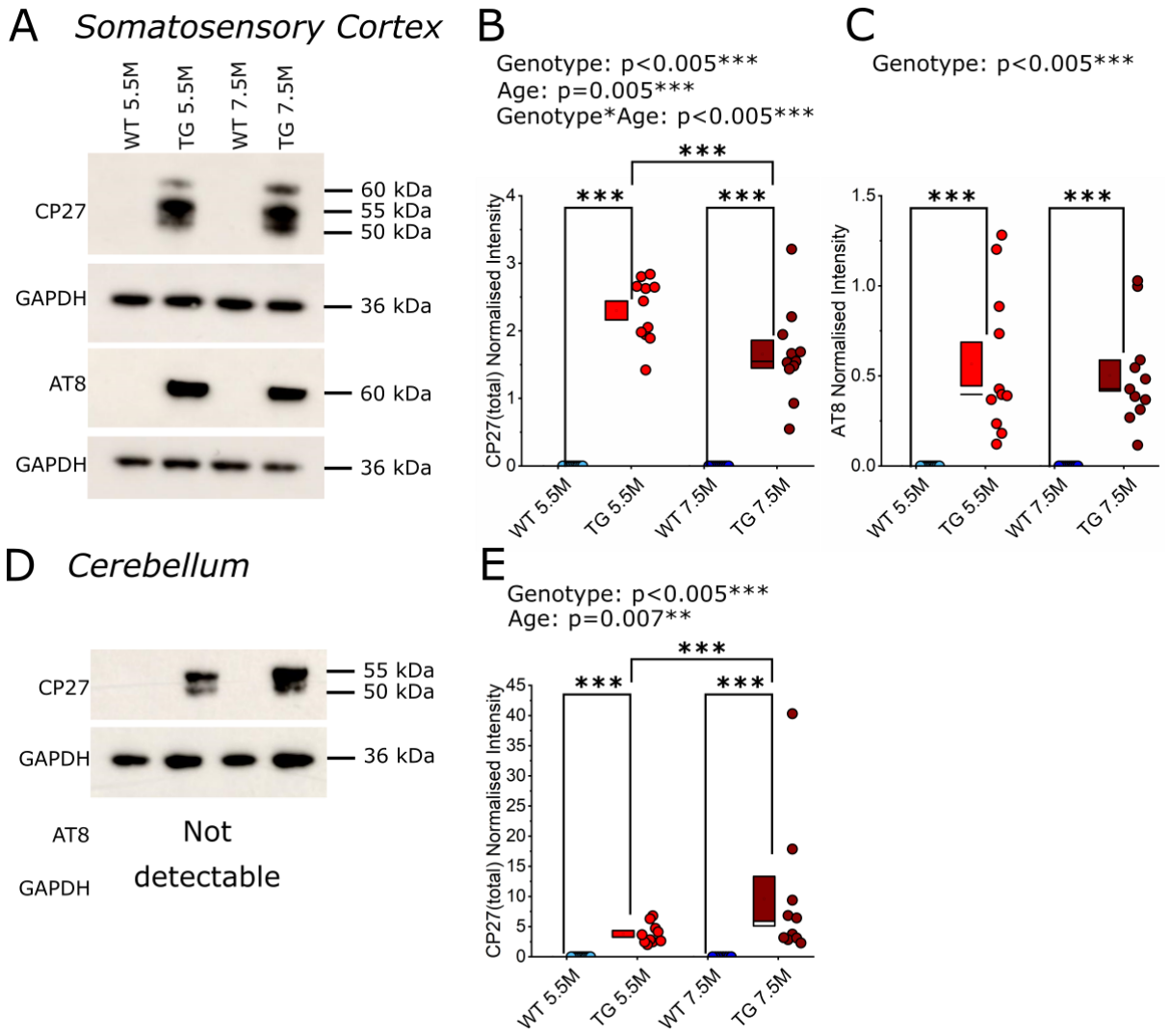

Figure 3.19 Tau expression in the somatosensory cortex and cerebellum. Representative western blots of human (CP27) and hyperphosphorylated (AT8) tau expression in the somatosensory cortex (**A**) and cerebellum (**D**) from WT and TG animals at 5.5 and 7.5M (labelled along the top). Along the left-hand side of the western blots are the detected protein, with corresponding molecular weight listed on the right. For CP27, all detected bands that were expressed were summed and the total value was normalised to GAPDH expression. Protein expression was normalised to the corresponding GAPDH band shown below. Quantification of normalised sum CP27 (**B**) and AT8 (**C**) expression in the somatosensory cortex is shown as dot and box plots. Quantified normalised CP27 expression for the cerebellum is shown in (**E**) Statistics: GLMM, main effects were stated on the graphs, with *post hoc* significance denoted by asterisks between ages or genotypes, p<0.05*, p<0.01**, p<0.005***.

3.5 DISCUSSION

The results in this chapter demonstrate a role of tauopathy in the early neurodegenerative phase of tauopathy in altering dendritic structure and synaptic protein expression. There was increased dendritic complexity closer to the soma of neurons and a reduction in synaptic markers and glutamatergic receptor expression. Following neurodegeneration onset, further decreases were observed in glutamatergic receptor expression.

3.5.1 Dendritic structure was changed with tauopathy

rTg4510 neurons had an increased overall branch length with increased branching proximal to the soma, without changes in total area covered by the dendrites in this study (Figure 3.9, Figure 3.10 & Figure 3.11). Dendritic proliferation in apical dendritic branches was observed in a subset of pyramidal neurons in aged rTg4510 mice (~10M) (Crimins et al., 2012). Similar changes in dendritic complexity was also observed in 12M hTau mice, which was suggested to be a compensatory mechanism of neurons in response to loss of dendritic spines (Dickstein et al., 2010). This is in contrast to other work suggesting significant atrophy of neurons in tauopathy (Jaworski et al., 2011; Rocher et al., 2010). Increased dendritic branching could be in response to deprivation or loss in inhibitory tone, alterations in synaptic connectivity, or aberrant neuroplasticity which is known to occur in tauopathy (Jackson et al., 2017, 2020; Shimojo et al., 2020). This could also reflect subsampling of a specific neuronal phenotype, whilst other neurons are showing significant atrophy (Crimins et al., 2012).

Early in neurodegeneration, there could be a change in synaptic inputs from neighbouring neurons, suggested by the increased structural synaptic plasticity observed in the rTg4510 mice (5-6M) (Jackson et al., 2017). A decrease in the frequency and/or efficacy of synaptic inputs that target the proximal dendrite may lead to increased dendritic growth to compensate for these changes. It is likely that these same connections may also increase in strength leading to an amplification of the signal to compensate for reduced efficacy of other synaptic inputs. In either case, this would likely skew signal processing towards proximal inputs. Within layer II/III, neurons receive differential inputs to different parts of the dendrite. For example, the distal apical tuft of layer II/III pyramidal neurons extends into layer I and typically receives long range and higher order inputs from distal sensory areas and the thalamus,

whereas proximal dendrites receive local excitatory inputs from layer IV and neighbouring layer II/III neurons (Cauller, 1995; Cauller and Connors, 1994; Feldmeyer et al., 2002, 2006; Lübke et al., 2000; Waters et al., 2003; Zhang and Bruno, 2019). Increased dendritic branching proximal to the soma in the rTg4510 model may therefore skew signal processing to local bottom-up signals. Overall, an increase in dendritic complexity is likely to alter dendritic filtering and signal integration, leading to altered processing of incoming synaptic information by the neuron.

Capacitance was lower in rTg4510 mice compared to wildtypes at this time point (Chapter 2). Capacitance is a measure of how well the membrane can separate electrical charge and impacts how much charge is needed to cause a change in voltage. Capacitance is related to total membrane area, with larger cells typically having a higher capacitance as there is more membrane to separate and store the charge (Henderson and Miller, 2002). Whilst the increased structural complexity observed in this chapter may contradict the decreased capacitance observed in Chapter 2, voltage clamp recordings from the soma are limited in their ability to uniformly control and record voltages across the dendritic tree (space-clamp issues; Williams and Mitchell, 2008). Therefore, capacitance is only a crude measure of cell surface area and by extension dendritic complexity.

One limitation to note is that none of these cells colocalised with tau pathology markers (Figure 3.8). This may be due to wash out of the detectable tau isoform during recordings, or potentially a preferential skew towards healthy cells during recordings. I would think that it is more likely the former, as it is highly unlikely that all of the cells recorded from were negative for tau pathology, especially when some cells were in regions with a high tau pathology burden. However, if these recordings are from healthier cells, this may suggest that this phenotype is only seen in cells that have a lower pathological burden.

3.5.2 Synaptic marker expression was reduced in the somatosensory cortex in rTg4510 mice

In the somatosensory cortex, there was a significant effect of genotype on both synaptophysin and PSD95 expression (Figure 2.1). Bouton (pre-synapse) and dendritic spine (post-synapse) density and structural plasticity in the rTg4510 model prior to neurodegeneration are conversely affected. Boutons showed decreased

turnover rates and increased stability, compared to spines which showed increased turnover with decreased stability (Jackson et al., 2017). There was a subtle but significant genotype effect on synaptophysin expression which does not change following neurodegeneration, which would link to a lower but stabilised bouton presence. There was a dramatic reduction in PSD95 expression in the somatosensory cortex in 5.5M rTg4510 mice compared to controls, which progressively decreased with age. This could be a consequence of a generalised loss of dendritic spines from rTg4510 neurons, but may also reflect the increased turnover of dendritic spines observed by Jackson et al., 2017, with an observed increase in the proportion of smaller immature dendritic spines expressed by rTg4510 neurons (Crimins et al., 2011). PSD95 help anchor AMPARs and NMDARs to the synaptic membrane and stabilises synapses (Cane et al., 2014; Chen et al., 2015b). Therefore, lower PSD95 expression would likely lead to reductions in glutamatergic receptor expression and decreased spine size, which have been observed in the rTg4510 model (Crimins et al., 2011, 2012; Kopeikina et al., 2013a).

3.5.3 Glutamatergic receptor expression was reduced in the somatosensory cortex of rTg4510 mice

Expression of the AMPAR subunit GluA1 was similar to wildtype levels at both ages (Figure 3.14). However, GluA2 and GluA3 expression in rTg4510 mice was significantly lower compared to wildtypes (Figure 3.14). This would suggest a reduction in AMPAR expression at the synapse. AMPARs are highly mobile, with AMPAR localisation and stabilisation to the synapse regulated in part by PSD95 (Anggono and Huganir, 2012; Henley and Wilkinson, 2013). As there was a significant decrease in PSD95 expression in rTg4510 neurons, GluA2/3 containing AMPARs may not be able to stabilise at the synapse leading to a detected reduction in synaptosomes. In fact, PSD95 knockdown leads to redistribution of AMPARs to the extrasynaptic space (Elias et al., 2006). However, PSD95 knockout mice do not show this redistribution, with other membrane-associated guanylate kinases performing a compensatory role (Elias et al., 2006). Therefore, measuring the expression of other membrane-associated guanylate kinases in the rTg4510 model may provide further insight into whether this is the case at early and post-neurodegenerative phases of tauopathy.

Whilst there were large reductions in subunit expression, there was no change in AMPAR-mediated function at ~5.5M in the rTg4510 mice (Chapter 2). GluA1 containing AMPARs may be functionally compensating for the lack of GluA2/GluA3 containing AMPARs at synapses. GluA2 containing receptors can compensate for GluA1 knockdown by redistributing to the synapse (Terashima et al., 2019), and so it is possible that the inverse could also be true. GluA3 containing AMPARs have low conductance in basal states and therefore contribute little to synaptic currents such as sEPSCs (Renner et al., 2017). This may also explain why no difference in function was observed at ~5.5M.

Following neurodegeneration onset, there was a reduction in AMPAR-mediated function (Chapter 2) and a progressive age effect on GluA2 expression (Figure 3.14). The most common subunit compositions of AMPARs are GluA1/2 and GluA2/3 (Wenthold et al., 1996), with GluA1/2 heteromers accounting for the majority of AMPARs at synapses (Lu et al., 2009). Therefore, this decrease in AMPAR-mediated activity following neurodegeneration may be underpinned by a reduction in GluA2 expression reducing GluA1/2 containing AMPARs at the synapse. In addition, GluA2/3 containing AMPARs are thought to replace GluA1 containing AMPARs in long-term potentiation and other forms of plasticity. The reduction in GluA2/3 expression would suggest alterations in the long-term stability of synaptic plasticity at early neurodegenerative phases of tauopathy. This would also align with the increased turnover of dendritic spines observed at this age point (Jackson et al., 2017).

The constitutive NMDAR subunit, GluN1 was significantly lower in the rTg4510 model (Figure 3.16). This would suggest a reduction in overall NMDAR expression. Results presented in Chapter 2 demonstrated a reduction in the NMDA:AMPA receptor ratio in rTg4510 neurons at 5.5M of age. A reduction in NMDARs would lead to a lowering of NMDAR -mediated synaptic transmission, which would reduce the NMDA:AMPA ratio. GluN1 expression was also reduced with age. The NMDA:AMPA ratio following neurodegeneration onset was similar between genotypes, suggesting that there was a large reduction in AMPA function or expression by this age to balance out the ratio. Interestingly, the changes in AMPAR expression do not suggest that this is the case.

Subunits of the NMDAR change with development and control many aspects of NMDAR function including voltage and agonist sensitivity (Furukawa et al., 2005;

Hansen et al., 2018; Traynelis et al., 2010). GluN2A and GluN2B subunits are involved in plasticity processes such as long-term potentiation and long-term depression, and GluN2B is thought to mediate NMDAR excitotoxicity, one of the hypothesised mechanisms of neurodegeneration in neurodegenerative diseases (Hardingham and Bading, 2010; Léveillé et al., 2008; Liu et al., 2007; Wang and Reddy, 2017). Interestingly, the expression of these two subunits were similar between genotypes. However, as overall NMDAR expression was reduced (GluN1 expression decreased), it was unusual that the GluN2 subunits were not reduced in a similar pattern. It is possible that there was subunit switching or upregulation of certain NMDAR subtypes compared to other subtypes. GluN2D expression was lower in the rTg4510 model at 5.5M, so perhaps NMDARs containing GluN2D subunits are preferentially lost first in the neurodegeneration process. GluN2D containing NMDARs have low voltage and agonist sensitivity with a slow deactivation curve and are thought to be involved in tonic NMDAR activity (Hansen et al., 2018; Traynelis et al., 2010). This reduction of GluN2D expression would therefore not be measured in the NMDA:AMPA receptor ratio, so measuring tonic NMDAR activity may show differences in the rTg4510 model.

Different glutamatergic receptor subunits are also expressed in different populations of cells in different brain regions. Results presented in Chapter 2, characterised the synaptic function of putative excitatory neurons. However, glutamatergic receptors are also expressed by glia and interneurons (Akgül and Mcbain, 2016; Lee et al., 2010; Verkhratsky and Kirchhoff, 2007). For example, GluN2D containing receptors are mostly expressed in interneurons (Küppenbender et al., 2000; Standaert et al., 1996), and glial cells also express both NMDARs and AMPARs (although GluA2 expression is low in glial cells) (Burnashev et al., 1992). Directly comparing the results of receptor subunit expression analyses presented here with electrophysiology analyses presented in Chapter 2 may therefore be confounded by the fact that receptor expression was determined from a crude synaptosome preparation, and not from an isolated subpopulation of neurons.

3.5.4 Tau overexpression did not alter protein expression in the cerebellum at 5.5M

The cerebellum in the rTg4510 model does not develop aggregate pathology, nor does it overexpress tau or undergo neurodegeneration and so was used as a control region

(SantaCruz et al., 2005; Spires et al., 2006). The cerebellum in this study showed very few changes in receptor expression or synaptic marker expression. Human tau was significantly higher in this region than in wildtype mice, as detected by increased CP27 labelling in western blot analysis of isolated synaptic proteins (Figure 3.19). AT8 was undetectable, and there was also a lack of the higher molecular weight species in the CP27 labelling that were seen in the somatosensory cortex, which suggests a lack of aggregate pathology.

Interestingly, synaptophysin was increased in the cerebellar synaptosome fraction in 7.5M old rTg4510 mice (Figure 2.1). There was also a genotype effect observed in GluN2C expression, with expression being higher in the rTg4510 mice. GluN2C expression is largely restricted to cerebellum granule cells (Thompson et al., 2000) and GluN2C expression is increased in granule cells following dendritic growth (Iijima et al., 2008). This could also lead to increases in synaptophysin expression via increased synapses. Therefore, perhaps there is some form of dendritic growth that occurs with longitudinal soluble tau incubation, with support for this seen in a model of human tau overexpression which developed increased dendritic complexity in neurons (Dickstein et al., 2010). Alternatively, GluN2C expression is also detected within glia cells (Karavanova et al., 2007), which play a role in synapse function. Therefore, perhaps there is increased glial proliferation and/or recruitment following neurodegeneration onset, leading to an upregulation in synapses. Nevertheless, this result was surprising and therefore more work would need to be done to determine what changes were occurring in the cerebellum following neurodegeneration onset.

Overall, whilst there were two changes in markers at 7.5M in the rTg4510 mice within the cerebellum, there were no changes at 5.5M. Therefore, if the changes observed in the somatosensory cortex were solely due to soluble tau overexpression, we would expect to see similar changes in the cerebellum. As this was not the case, there is added confidence that the changes observed in the somatosensory cortex are related to expression of progressed tauopathy in the rTg4510 mice.

3.6 CONCLUSIONS

Synaptic and structural dysregulation occur within the early neurodegenerative phase of tauopathy in the rTg4510 model. Dendritic complexity was altered, and synaptic and glutamatergic receptor expression was decreased, suggesting large scale

compensation to changes in synaptic inputs in the local environment. Following neurodegeneration onset, synaptic and glutamatergic protein expression decreased, suggesting these processes occurred in parallel to the progression of neurodegeneration. The cerebellum showed no changes in protein expression at 5.5M as expected. This suggests that the disruption in the somatosensory cortex was related to expression of progressed tau pathology. Overall, this provides evidence of subunit selective synaptic vulnerability and structural alterations in response to increasing tau pathology concentrations and changes in synaptic connections in the local neuronal environment. It is likely that there may be a degree of homeostatic compensation within the network, which when past a threshold leads to widescale network alterations and symptomatic changes. Deconstructing this mechanism in the brain in neurodegenerative diseases will shed light on how to delay symptomatic onset in tauopathies.

4 IMPLEMENTATION AND OPTIMISATION OF *IN VIVO* TWO-PHOTON TARGETED WHOLE-CELL PATCH CLAMP ELECTROPHYSIOLOGY IN THE SOMATOSENSORY CORTEX OF ADULT MICE

5.1 INTRODUCTION

This chapter will summarise a series of experiments to set-up and validate the use of *in vivo* two-photon targeted whole-cell patch clamp electrophysiology in the mouse somatosensory cortex. This was done as a necessary precursor to using this method to examine the physiological function of somatosensory neurons in the rTg4510 model at ~5.5 months (5.5M; see Chapter 5). Recordings were performed under urethane anaesthesia to help isolate spontaneous and synaptically-evoked activity without the contamination of other local and global activity seen in awake states. The majority of *in vivo* recordings in the literature are performed in juvenile mice (<1M), and so adult mice of >3M were used for recordings to ensure comparability with the age of the mice that will be used for the rTg4510 experiment as electrophysiological properties can change with age (Cheng and Lin, 2013; Luebke et al., 2015; Randall et al., 2012).

Whole-cell properties were recorded *in vivo* from layer II/III of the somatosensory cortex to establish typical electrophysiological properties under urethane anaesthesia. In addition, in light of the glutamatergic deficits identified in Chapter 2 and 3 in the rTg4510 model (i.e. reduced NMDA:AMPA ratio and reduced AMPA receptor (AMPAR) and NMDA receptor (NMDAR) expression in the rTg4510 mice at 5.5M), part of the work discussed in this chapter aimed to develop a protocol to quantify how this alteration manifested *in vivo*.

4.1.1 The value of in vivo whole-cell patch clamp recordings

Whole-cell recordings are highly versatile and can provide information on subthreshold membrane potential dynamics, intrinsic properties, and can be combined with *post hoc* recovery of recorded neurons allowing for cellular identification. The ability to record in the intact brain as a physiological system provides invaluable information about how a single cell behaves within the network. Some properties such as input resistance, action potential (AP) threshold and neuronal spike output can also differ significantly *in vivo* when compared to *ex vivo* recordings made from brain slices (Bourne and

Rosa, 2006; Fernandez et al., 2018; Tsuno et al., 2015). Therefore, the ability to perform this technique can fully characterise how a neuron behaves in a physiologically relevant environment.

4.1.2 In vivo whole-cell recordings in the somatosensory cortex under urethane anaesthesia

Recordings made under urethane anaesthesia induce a slow wave oscillation (<1 Hz), known as up and down states, which are also observed during other physiological states such as slow wave sleep (Steriade et al., 1993c; Wilson and Groves, 1981). Up and down states are thought to be representative of the local network activity, with down states representing periods of reduced synaptic input, and up states periods of increased synaptic input, arising from a balanced excitatory and inhibitory dynamic system (Arieli et al., 1995; Haider et al., 2006; Lampl et al., 1999; Okun et al., 2010; Renart et al., 2010). Measuring up and down state activity seems to be a reasonable model of cortical network dynamics, and can also inform on how that neuron behaves within the network.

Up state initiation within the cortical column is thought to be driven from layer V pyramidal neurons, likely when a critical amount of synchronised synaptic drive is provided onto these cells (Beltramo et al., 2013; Chauvette et al., 2010; Lőrincz et al., 2015; Sanchez-Vives and McCormick, 2000; Timofeev et al., 2000). Up states then persist for periods of up to a few seconds, maintained by a combination of recurrent excitatory synaptic activity with contribution of intrinsic mechanisms that maintain bistable cellular states (Egorov et al., 2002; Palmer et al., 2014; Sanchez-Vives and McCormick, 2000). *In vitro* and early *in vivo* characterisation of up states suggests a paramount role of ionotropic glutamate receptors in up state maintenance (Sanchez-Vives and McCormick, 2000; Steriade et al., 1993a). However, *in vivo* characterisation with bath or intracellular application of NMDAR antagonists shows conflicting results in comparison, suggesting no effect of NMDARs on up state frequency or maintenance (Chen et al., 2013; Palmer et al., 2014; Smith et al., 2013). Synaptic inhibition also helps sustain up states, as a consequence of balanced synaptic excitation and inhibition at these more depolarised potentials (Haider et al., 2006; Waters and Helmchen, 2006). Up state termination occurs from a likely combination of increased inhibitory drive and the activation of hyperpolarizing conductances (Haider et al., 2006;

Sanchez-Vives and McCormick, 2000; Steriade et al., 1993a). Down states are said to be stable periods of synaptic quiescence, facilitated by the network refractory period (Neske, 2016; Wilson, 2008). Overall, this activity reflects local synchronous synaptic activity with balanced inhibition and excitation during state maintenance.

The somatosensory cortex in the rodent has been used extensively as a classical model system, due to its stereotypical and somatotopic architecture, experimental accessibility, and the ease of evoking a defined response using a behavioural stimulus (whisker stimulation) (Adibi, 2019; Petersen, 2007). Unsurprisingly, some of the earliest two-photon targeted whole-cell recordings *in vivo* were made in the somatosensory cortex, with almost all recordings performed in juvenile animals (Kitamura et al., 2008; Margrie et al., 2003). Intracellular recordings have confirmed neurons in the somatosensory cortex respond to whisker stimulation with an evoked post-synaptic potential (PSP) and that this response is modulated by up and down states (Ferrarese et al., 2018; Gambino and Holtmaat, 2012; Petersen et al., 2003; Sachdev et al., 2004). This response is thought to be glutamatergic with a short latency non-NMDAR component and a slower component which is NMDAR-mediated (Armstrong-James et al., 1993; Gambino and Holtmaat, 2012; Gambino et al., 2014). Therefore, evoked responses could be used to determine glutamatergic function, and help isolate NMDAR-mediated responses *in vivo*.

4.2 AIMS

This chapter aimed to identify typical neuronal properties *in vivo* in ~5M old mice in the somatosensory cortex under urethane anaesthesia, as age can alter neurophysiological properties and typical *in vivo* whole cell recordings are performed in adolescent mice (<1M). Following on from the results in Chapter 2 and 3, there was altered glutamatergic receptor expression and function, which may manifest in different ways *in vivo*, and so a protocol to explore this *in vivo* was also established. In addition, the local field potential (LFP) was recorded to characterise how neuronal properties link to the LFP and whether this would be altered with MK801 application (an NMDAR antagonist).

Therefore, this work characterised typical neuronal properties in ~5M old mice in the somatosensory cortex under urethane anaesthesia *in vivo.* In addition, different sensory stimulation protocols were investigated which evoked a glutamatergic PSP,

to establish a protocol that could explore glutamatergic receptor function, particularly NMDAR-mediated activity. Extracellular recordings of the LFP were made to gain an understanding of wider scale dynamics and were compared to whole-cell recordings which helped determine and confirm how responses of the single cell related to the network.

4.3 METHODOLOGY

4.3.1 Ethical approval

All procedures including sacrifice by schedule 1 methods were performed in accordance with the UK Animal (Scientific Procedures) Act 1986 and its subsequent amendment in 2012 to align with European Directive 2010/63/EU on the protection of animals used for scientific purposes. Mice were kept on a 12:12 light/dark cycle and granted *ad libitum* access to food and water.

4.3.2 Animals

Mouse lines used to establish *in vivo* whole-cell patch clamp electrophysiology were from a mixture of genotypes including C57BL/6J, Ai95, vGluT2-IRES-cre & TdTomato. C57BL/6J mice were supplied by Charles River, with the rest bred in house. These mice were aged between 3-12 months. All animals were held in a vivarium at the University of Bristol and if supplied externally, animals were habituated to their new environment for at least two weeks prior to experiments.

4.3.3 Surgery Preparation

All surgical procedures were done using sterile and aseptic conditions where possible. Animals were weighed before surgery began to ensure the correct urethane anaesthetic doses were given. Experiments were acute, non-recovery procedures. At the end of experiments, the animal was sacrificed using cervical dislocation.

4.3.4 Surgical Procedure

Animals were anaesthetised under isoflurane (3-4% in O_2) in an induction chamber. Once anaesthetised, the fur was shaved from the scalp above the skull using hair trimmers (Wella). Animals were then transferred and placed into an anaesthetic mask on a customised stereotaxic frame (Figure 4.1). Isoflurane flowed through the mask at a rate of ~0.4L/min, with isoflurane concentration adjusted to give sufficient anaesthetic depth (judged by lack of toe pinch reflex and rhythmic slow breathing).

This was also adjusted throughout the procedure to maintain appropriate anaesthetic depth based on breathing rate and signs of wakefulness such as twitching. Internal body temperature was monitored using a rectal temperature probe and controlled thermostatically via a heat pad underneath the animal set to 37°C. Lacri-lube (Allergan, Ireland) was applied to the animals' eyes to prevent drying. The mouse was fixed within the frame using ear bars and a bite bar.

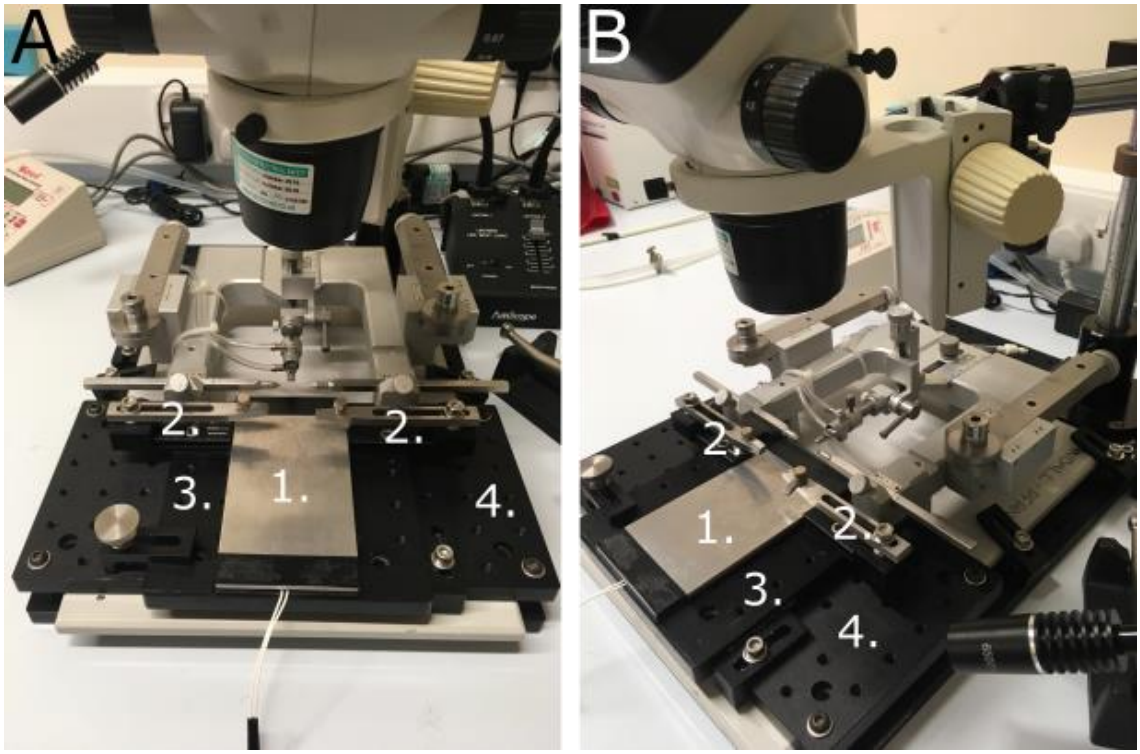

Figure 4.1 Overview of customised stereotaxic frame. Face-on (**A**) and side-on (**B**) views of the stereotaxic frame which was customised to have a Thorlabs metal breadboard (**4**) fixed to it. A removable smaller breadboard (**3**) was placed on top and held down with a thumbscrew and clamp. This allowed for easy transfer between surgery and experimental recordings. Attached to this was removable head bar clamps (**2**) and a custom-made heat pad (**1**).

The scalp was washed with iodine (Videne, Ecolab), and lidocaine (Aspen, South Africa) was applied. An incision was made in the scalp and stretched to expose the top of the skull, which was then cleaned with cortical buffer soaked cotton buds (aCSF, buffer composed of (in mM) 135 NaCl, 5 KCl, 5 HEPES (Free Acid), 1.8 $CaCl_2$ and 1 $MgCl_2$) and dried with cotton buds. The coordinates for the somatosensory cortex

(anterior-posterior +1.3 mm, medial-lateral -3.4 mm from bregma; Paxinos & Franklin, 2001) were marked on the skull with a permanent marker. The skull was then scored with a microlance needle (BD, USA) to provide extra surface area for the super glue to affix to, to increase grip. A thin layer of super glue was then applied over the whole skull avoiding the area marked for the craniotomy. A custom-made linear head bar was then attached to the posterior of the skull (on the interparietal bone) using superglue and left to set (ensuring it was flat and level; Figure 4.2). The head bar was further covered with super glue to ensure that it was firmly secured and to increase the water tightness of the well. As the head bar was metal, this needed to be completely covered in areas which would contain extracellular solution which could break the electrical circuit during whole-cell recordings. The whole area that was covered with super glue was then covered with a thin layer of dental cement (Kemdent, UK; Figure 4.2). Once this was dried, a well was built up out of dental cement around the edge of the skull. The well needed to hold in the aCSF and so had high walls, but was also wide enough for the objective to image the craniotomy unimpeded (~1.5 cm x 1.5 cm).

A ~1mm craniotomy was made at the coordinates marked out (anterior-posterior +1.3 mm, medial-lateral -3.4 mm from Bregma), corresponding to the somatosensory cortex. This was done by drilling slowly in a circle until the skull became thin. At this point, the well was filled with aCSF and the thin bone was pricked with a microlance needle (BD) to reduce damage to the cortical surface. Once the drilled skull fragment was loose and unattached from the surrounding skull, the fragment was removed using a hooked needle (BD Microlance Needle, bent to make a hook). Once the skull fragment was removed, the buffer was refreshed and maintained at a high level in the well for the rest of the procedure including experimental recordings.

The dura was then carefully removed in this area using a hooked syringe needle (BD Micro-Fine U-100 Insulin Needle, bent to a 45° angle) which was carefully dragged over the brain surface to make a hole in the dura. The dura was then removed from the surface of the brain. A schematic showing an overview of the finished surgical procedure is shown in Figure 4.2.

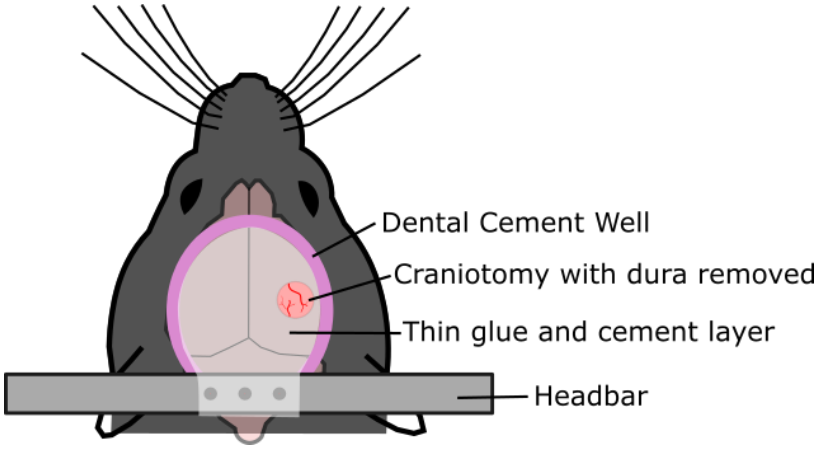

Figure 4.2 Surgical overview schematic. A schematic showing an overview of a finished surgical preparation with the dental cement well labelled in pink, the craniotomy with dura removed, a head bar attached and labelled at the back, with the glue and cement layer shown as a shaded area.

For a subset of experiments, an LFP electrode was fixed into place following the duratomy. A PlasticsOne (USA) wire electrode was bent to sit within the brain, perpendicular to the surface. This wire was inserted into the brain and fixed to the wall of the well with superglue (Figure 4.3).

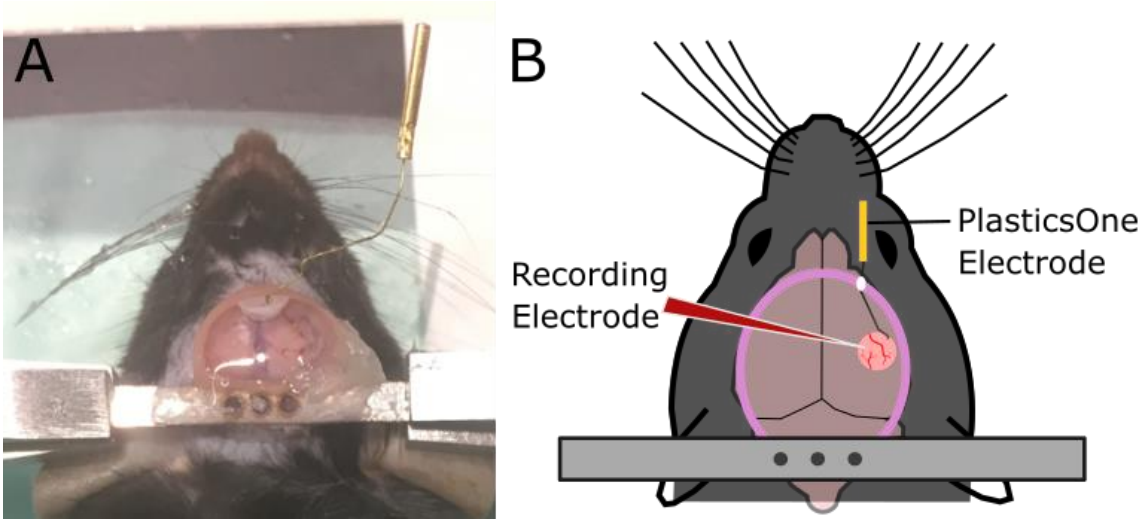

Figure 4.3 Overview of the surgical procedure with the addition of an LFP electrode. A photo following LFP electrode placement (**A**) with a cartoon schematic on the right (**B**) showing the location of the LFP electrode and the likely location of the recording electrode.

Following the procedure, mice were injected with urethane prior to transfer to the two-photon recording set up. Electrophysiology recordings were made solely under urethane anaesthesia. The dose varied between 1.5 - 2 mg/kg based on responsive depth from the mouse, with top up doses given throughout the recording periodically as required.

After confirming the anaesthetic depth of the mouse by checking toe pinch and corneal reflexes, the head bar fixation clamps were attached to the removable plate and the mouse was removed from the stereotaxic frame (i.e. ear bars and bite bar). The mouse was then fixed using the head bar to the removable plate (Figure 4.1). This plate was then transferred and fixed within the *in vivo* two-photon recording set up. The aCSF in the well was topped up if required, a rectal probe was placed and the heat mat was plugged into the recording set up, set to 37°C. A ground electrode was placed into the well (Figure 4.4). Whiskers were clumped together using Vaseline and the tips trimmed if required to form the bundle. Then two different whisker stimulation methods were used. A piezo wafer was placed near the whiskers with an attached metal tube to place the whiskers in, or an open-ended cone was placed next to the whiskers to allow air puff stimulation using a Pneumatic PicoPump (World precision instruments, UK, PV820).

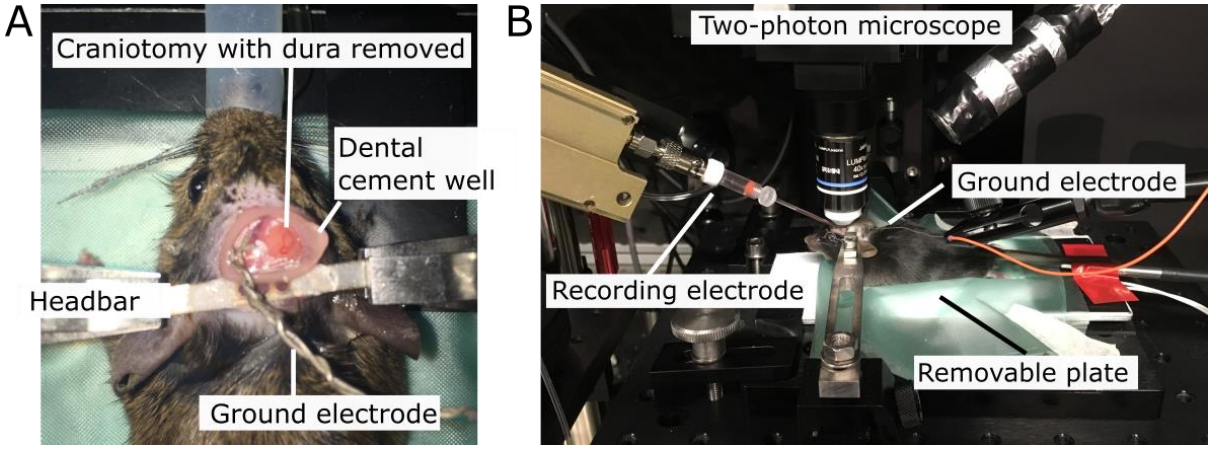

Figure 4.4 Overview of the mouse in the recording set up. A photo following the end of the surgical procedure, with the mouse in the recording set up. The mouse is head fixed via the attached head bar, with a dental cement well which encompassed the craniotomy (**A**). A ground electrode has been placed in the well away from the craniotomy. A side angle photo shows further components of the recording set up (**B**) including the position of the recording electrode, the surgical removable plate, the ground electrode, and the position of the two-photon microscope.

4.3.5 Recording equipment

The surgical plate was attached to a customised Scientifica (UK) microscope on a motorised stage. A camera was attached to the microscope allowing visualisation using Micromanager software (version 1.4.22; Edelstein et al., 2014) on the PC. A flexible gooseneck lamp was used to help illuminate the recording area. Brightfield imaging was used to visualise the craniotomy to determine the target region of interest and electrode placement.

For two-photon imaging, a MaiTai Ti-Sapphire tuneable laser (Spectra Physics, USA) was used at an 800 nm excitation wavelength. The power used was kept to the minimum necessary for accurate visualisation of cellular shadows when recording in the brain. Image acquisition was controlled using SciScan software (Ward et al., 2017).

For electrophysiology recordings, signals were amplified using a Multiclamp 700A (Molecular Devices, UK) and digitised using a CED Power 1401 data acquisition system (CED, UK). Recordings were made and stored on a PC using Signal v5.07 software (CED). Whole-cell recordings were low pass filtered at 10 kHz, with an output gain of 10x. LFP recordings were low pass filtered at 1 kHz and had an output gain of 100x. Both recordings were sampled at 50 kHz.

4.3.5.1 Intracellular recordings combined with local field potentials (LFP)

Recording simultaneous local field potentials (LFP) with whole-cell recordings provides insight into the local network activity and how that relates to the subthreshold dynamics of the single cell. Two different LFP methods were tried. One was a fixed wire electrode implanted during surgery (Figure 4.3). The second was a glass electrode attached to a separate headstage to the recording electrode, on a second micromanipulator (Scientfica PatchStar) that was in place on the electrophysiology recording set up.

The glass electrode had limited placement options as it was a rigid electrode and the curvature of the objective needed to be considered when placing it within the brain. However, as it was on a micromanipulator, it could be moved easily and replaced as needed.

The wire electrode provided a flexible solution that was flat to the skull which meant that it was out of the way of the objective path ensuring no damage to the brain during

recordings. This also reduced the time needed to place the LFP electrode during recordings. However, the electrode was difficult to place within the craniotomy without damaging the brain or spilling adhesive onto the exposed brain. Therefore, LFP recordings were done using the glass electrode as this led to the least amount of overall brain damage.

4.3.5.2 Recording electrode fabrication and recording solutions

Whole-cell and LFP electrodes were fabricated on a Narishige (UK) PC-10 puller with a resistance of 5-10 MΩs. The LFP electrode was filled with aCSF. The whole-cell recording electrode was filled with one of two intracellular solutions (Table 4.1).

Initial optimisation of the technique was performed using solution 1, before switching to solution 2 to maintain consistency with the rest of the work in this thesis. Both intracellular solutions were made up with the addition of 25 µM of AlexaFluor Hydrazide 594 (Invitrogen, UK). The inclusion of AlexaFluor dye allowed for neuronal visualisation in the brain when imaged using two-photon microscopy. MK801 (1 mM; HelloBio, UK) was also added to the intracellular solution for a subset of recordings, as is stated in the description of relevant results. The whole-cell recording electrode was connected to a pneumometer (AP-C30W; Keyence, UK) to measure the pressure at the electrode tip.

Table 4.1 Composition of intracellular solutions. Table of intracellular solution composition, with concentrations listed in mM.

Concentrations in mM	Solution 1: Sucrose	Solution 2: KGluconate
K-Gluconate	-	135
$KMeSO_4$	115	-
NaCl	8.5	5
QX314-Cl	-	-
HEPES free acid	5	10
EGTA	0.5	0.2
BAPTA	-	-
GTP- 2Na salt	-	-
GTP- Na salt	0.3	0.3
ATP- Mg Salt	4	4
Sucrose	31	-
Biocytin	-	6.7

4.3.6 Visualisation and targeting of neurons for recordings

Under a 4x objective (Olympus UPlanFl, 4x/0.13), an area within the craniotomy was identified for whole-cell recordings. This area was away from any surgical damage and had low amounts of blood vasculature as this could obscure imaging and could also get damaged during electrode placement.

Once an area was identified, the objective was changed to a 40x objective (Olympus LUMPlanFL N, 40x/0.80 W, UIS-2). For LFP recordings, the glass electrode was located under the 40x objective and then inserted into an area nearby to the region selected for recordings. This was done prior to the insertion of the whole-cell recording electrode. This was inserted to an estimated depth of 150 µm from the surface of the brain based on measurements from the PatchStar controller and micromanager software.

For whole-cell recordings, a glass electrode filled with an intracellular solution was placed under the 40x objective within the aCSF. The electrode and objective were

lowered to focus on the surface of the brain and ~300 mBar pressure was applied to the electrode. The electrode was inserted into the brain on the approach angle to a depth of ~50 µm from the pia. The objective was focussed approximately near the electrode tip and all lights were turned off, to switch to visualisation using two-photon imaging. Frames were scanned at 32 Hz using a resonant galvanometer.

The methodology used to visualise the electrode and cells within the brain is referred to as 'Shadow Patching', and was first described by Kitamura et al., 2008 (Figure 4.5). Perfusion of the AlexaFluor containing intracellular solution within the brain allowed for visualisation of the extracellular space. This solution was not taken up by the cells or blood vessels within the brain, leading to dark "shadows" of these structures (Figure 4.5 B). This technique can therefore be used to navigate the electrode through the brain with minimal damage and visualise cells to target for recordings. If shadows were not visible using two-photon imaging upon insertion of the electrode, the electrode was likely clogged and was removed from the brain and changed. If shadows of cells were visible, the pressure at the electrode was reduced to ~85 mBar. The electrode was progressed deeper into the brain to around 80-150 µm from the surface, avoiding blood vessels. Whilst progressing the electrode into the brain the electrode resistance was also observed, as deflections or a change in resistance would suggest a blockage of the tip. Layer II/III was targeted based on depth of the electrode and also by visualisation of the cell density. At layer II, there was a very noticeable increase in the number of cells in the visible area. Once at layer II, the pressure was reduced to ~45 mBar. Pyramidal neurons were targeted based on their shape (triangular). Once selected, whole-cell recordings were made based on the methodology in Margrie et al., 2002 (Figure 4.5 C). Pulsatile deflections were looked for alongside visualisation of the electrode approaching the cell. Once confirmed to be on the cell, suction (negative pressure) was applied to the electrode and the current was held at -70 mV to seal onto the cell ("cell-attached mode"), to then allow break in. Small suction pulses were applied to attempt to break into the cell. If successful, deflections were seen on the trace showing that whole-cell access had been established.

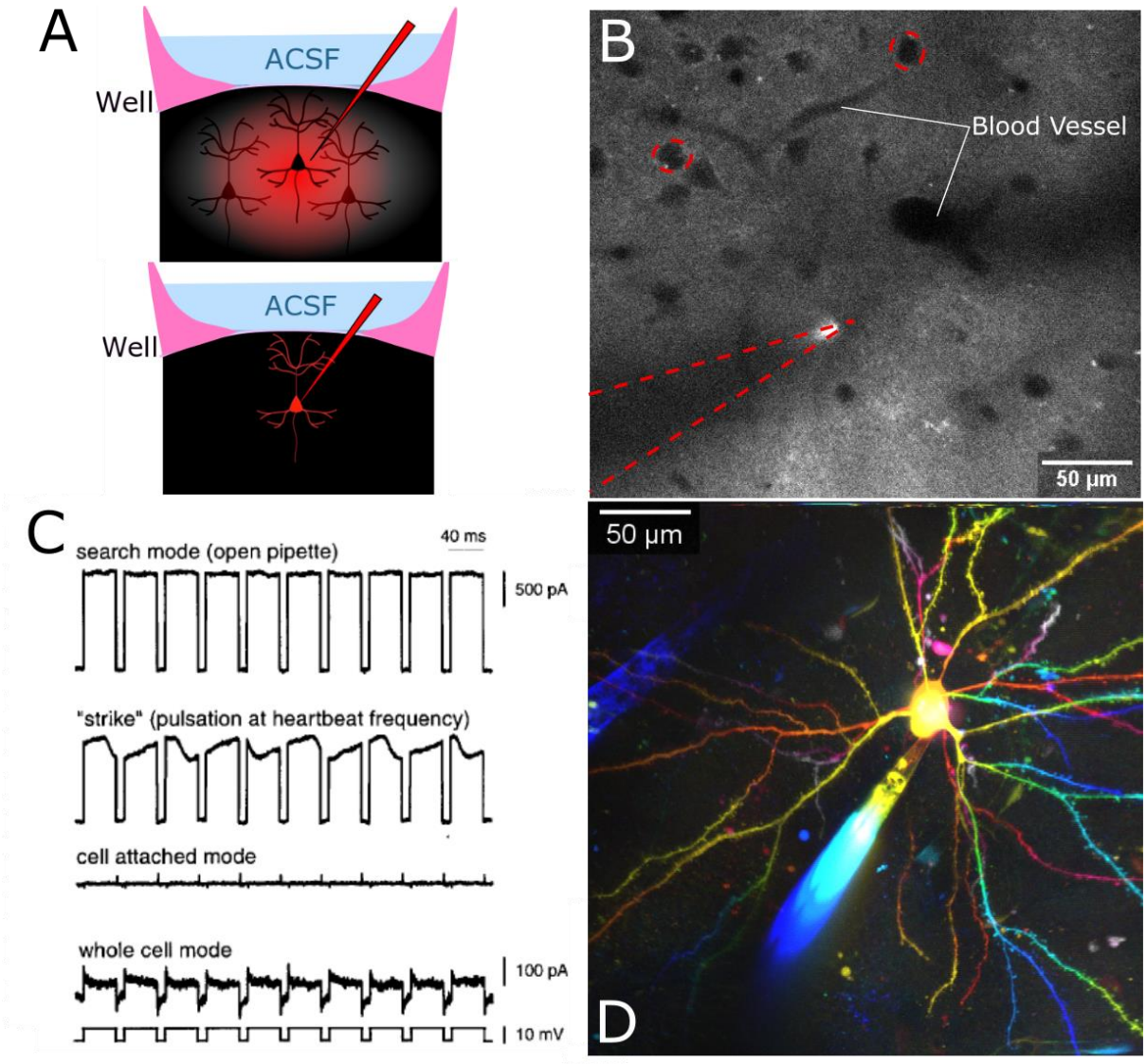

Figure 4.5 In vivo whole-cell "Shadow Patching" recording methodology. Shadow patching involves observation of the resistance changes of the electrode alongside visual neuronal identification. **A** shows a schematic of shadows of neurons being visualised via dye spreading into the extracellular space. Once the neuron is recorded, this dye clears from the extracellular space whilst the neuron simultaneously fills with the dye, leading to neuronal visualisation. **B** shows shadows of the electrode (in dashed red lines), an outline of some cellular shadows (in dashed red circles) and blood vessels (labelled in white). **C** shows the typical changes in electrode resistance throughout the process. When close to the surface of a cell, pulsations are observed ("strike") in the electrode resistance, shown in the second line of the schematic. A max projection of a z-stack of a filled neuron following recordings with the recording electrode still attached (**D**). The image is depth colour coded (hotter colours correspond to an increase in depth (86 µm depth range); pia - blue to bottom of neuron - red). **C** is adapted from Margrie et al., 2002.

During recordings, junction potential error (JPE) was not corrected for as the makeup of the external solution (i.e. the brain cerebrospinal fluid (CSF)) was not known. Bridge balance correction was also not applied as series resistance is thought to change more throughout *in vivo* recordings and therefore would be inappropriate (Kodandaramaiah et al., 2018; Schramm et al., 2014; Wang et al., 2016).

During recordings, cells filled with the AlexaFluor dye that was used for visualisation (Figure 4.5 A). This allowed for cell visualisation following recordings, imaged using two-photon microscopy (Figure 4.5 D). A z-stack from the pia to the depth of filled neuron visibility (32 frames per plane, 1 µm steps) was taken using a 40x objective, visualised using an excitation wavelength of 800 nm. This helped to confirm neuronal identity (putative pyramidal neurons) post recording by imaging the structure looking for a large dendritic arbour with the presence of dendritic spines.

Afterwards, mice were sacrificed using a schedule 1 method. Following this, the whole brain was extracted and drop fixed into 4% PFA in 0.1M PBS and fixed overnight. Brains were then stored in PBS (0.1M).

4.3.7 Technical considerations of note

A funded placement (an award from the MRC flexible funding supplement that I gratefully acknowledge in allowing this placement to occur) in Berlin in the laboratory of James Poulet with Jean-Seb Jouhanneau provided insight into what details are important for successful two-photon targeted *in vivo* patch clamp electrophysiology recordings. Therefore, some technical details are highlighted here as they were deemed important to experimental success.

4.3.7.1 Equipment

4.3.7.1.1 Removable surgical plate

An image of the surgical set up is shown in Figure 4.1. One crucial component of acute *in vivo* whole-cell patch clamp recordings is speed (as shorter surgery times typically equals longer recording time). Therefore, the surgical set up was optimised to facilitate this. A metal plate was designed with a fixed heat pad that was portable. This metal plate could be fixed and removed easily from the surgical set up. The fixed heat pad was small and electrical noise free, and so was suitable for recordings of this nature. Head bar clamps were also fitted to the metal plate so that the implanted head bars could be fixed whilst on the surgical set up prior to transferring the mouse to the

recording set up. The angle of the clamp and position of the head bar was optimised to ensure that imaging could occur straight away based on the location of the craniotomy.

4.3.7.1.2 Electrode placement

Following surgery, the mouse was transferred under the two-photon microscope for experimental recordings. The electrode angle and position were optimised to ensure appropriate visualisation and access to the craniotomy (Figure 4.6). A shallow electrode angle would not be able to access the craniotomy over the well and a deep angle was difficult to visualise under the microscope. In addition, the objective could push on the electrode if positioned wrong. An angle of ~38° was deemed optimal. The positioning of the whole-cell (headstage 1) and LFP electrode (headstage 2) were also chosen to allow recordings in close proximity to each other without collisions or contacts with the objective.

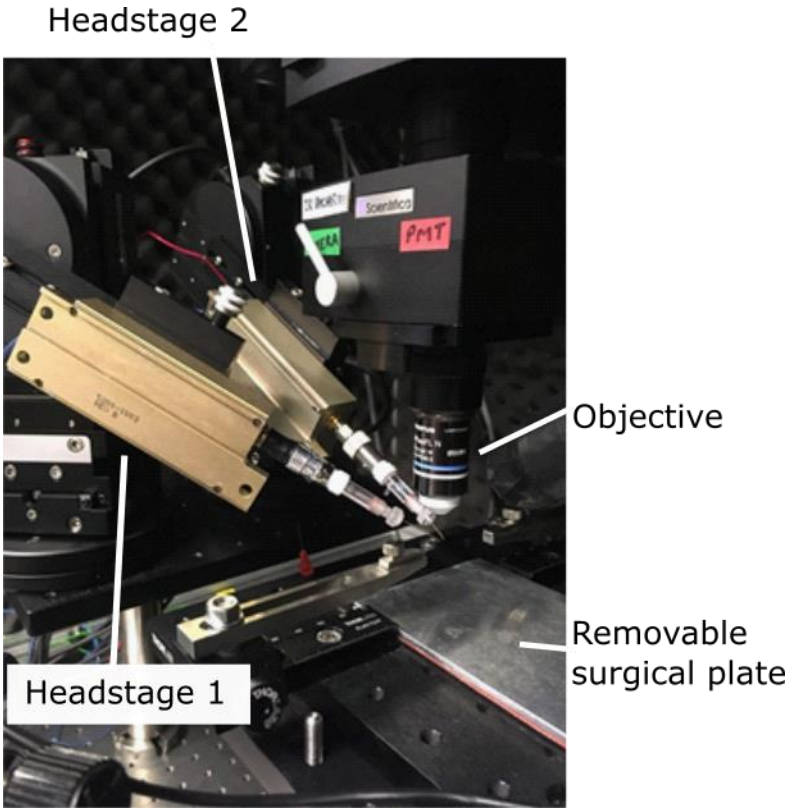

Figure 4.6 Electrode position and angle in relation to the objective. The position and angle of each headstage (with the electrode) were carefully considered. Angle was chosen based on objective angle and well dimensions. Spacing and approach position were spaced apart to allow recordings from nearby locations without collisions between electrodes.

4.3.7.2 Anaesthesia

Urethane was used as the recording anaesthesia for two reasons. Firstly, it has been shown to induce minimal disruption to normal network physiology, especially glutamatergic signalling, which was of specific interest for experimental recordings (Hara and Harris, 2002; Sceniak and Maciver, 2006). A second benefit was that it produced minimal pulsatile brain movements compared to other anaesthetics as it is not a vasodilator, and thus is commonly used for *in vivo* recordings (Masamoto and Kanno, 2012).

4.3.8 Experimental protocols

4.3.8.1 Series resistance

Series resistance was measured at the start of recordings following break in and was measured from the current deflection recorded in response to a voltage step of a defined size. This was converted to a resistance measure using Ohm's law.

4.3.8.2 Up and down states

This was recorded using "gap free" recording mode in current clamp, where no current was applied to the cell (i.e. at rest). The first three minutes were recorded using a "gap free" protocol following break in. Longer recordings were also made (up to 30 minutes) to observe other basal properties such as cyclic up and down state modulation.

4.3.8.3 Evoked activity

Whisker stimulation evoked a recordable synaptic response (PSP). Different stimulation methods and protocols were characterised, and will be described below. This was recorded in current clamp, with no current applied to the cell (i.e. at rest). For responses evoked on up and down states, the average was shown per cell from a stimulation period of at least 10 minutes. Comparisons of evoked responses were also made over time. The average response evoked on down states from the first and last 5 minutes of the recording protocol were compared. Whilst there was some variability within this, stimulation recording protocols were typically 10-15 minutes long, with recordings shorter than 10 minutes not included in comparisons made over time.

4.3.8.4 LFP recordings

LFPs were also recorded using a "gap free" protocol in current clamp. This activity was recorded simultaneously to spontaneous or evoked single cell activity as specified in the text.

4.3.9 Analysis

4.3.9.1 Up and down states

Up and down states display a network bistability, leading to voltages having a bimodal distribution (due to the relatively short amount of time spent between the two states). Therefore, a histogram of the membrane potential (Vm) typically has a bimodal distribution of two distinct states (up and down) which can be split. This method is used to define up and down states in this work and the features of these states.

A custom MATLAB script was used to analyse up and down state properties. APs were filtered out of the recorded trace, with APs present exclusively on up states in these recordings. To do this, the AP was identified by finding the point on the trace where dV/dt surpassed 10 $mV.ms^{-1}$. This identified possible APs, with the maximum mV then measured up to 1 ms after this point. If this value was larger than -50 mV, then it was classified as an AP. To filter out the AP, the AP threshold was identified (defined as the recorded mV on phase-plane plots where dV/dt surpassed 30 $mV.ms^{-1}$) and all points greater than this threshold on the identified AP waveform were changed to be equal to the AP mV threshold. Following AP filtering, the traces were down sampled to 1 kHz. A 10 s scanning window scanned the trace in 1 s increments, with a histogram of the Vm calculated within this window. A bimodal distribution was fitted to the histogram of Vm (using fitgmdist in MATLAB for two populations) to identify the thresholds for up and down state detection. Two distributions were detected (representing up and down states) and the minimum between the two distributions was found. Two thirds of the up or down state peak to the local minimum distance was used to create a threshold for up and down states (Menkes-Caspi et al., 2015; Stern et al., 1997; Figure 4.7). This created a moving threshold for the trace to account for changes in baseline stability or changes in up and down state shape. These thresholds were used to detect up and down states.

Changes past the up state threshold were counted as up states if the Vm was above the up state threshold for longer than 200 ms (González-Rueda et al., 2018; Menkes-Caspi et al., 2015), with the start and end of the up state counted as the point where the voltage depolarised and hyperpolarised past the down state threshold (Figure 4.7 & Figure 4.8).

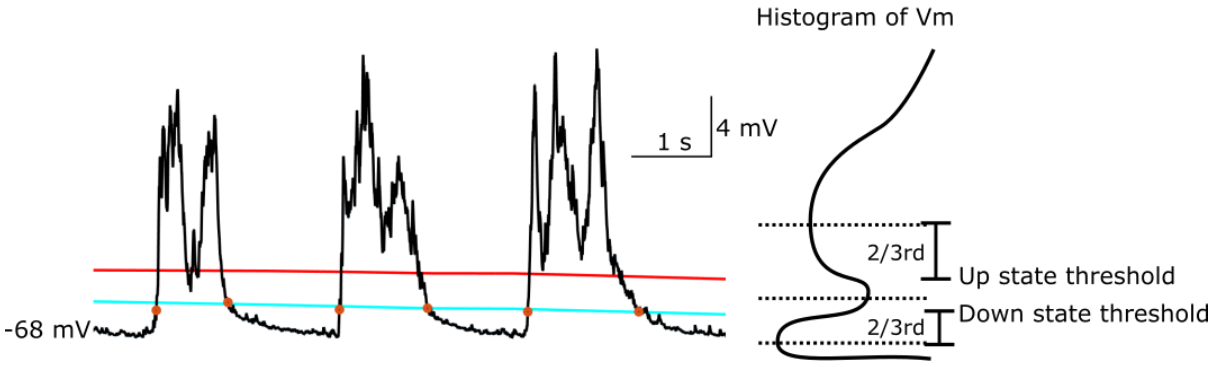

Figure 4.7 Thresholds for up and down state analysis. An example trace showing up and down states is shown on the left, with the starting Vm marked on. The determined up and down state thresholds are shown in red and cyan respectively. To the right is a histogram of Vm, with a bimodal distribution representing the mean up and down state Vm. Dashed lines mark the midpoint and 2/3rd points used for state threshold separation.

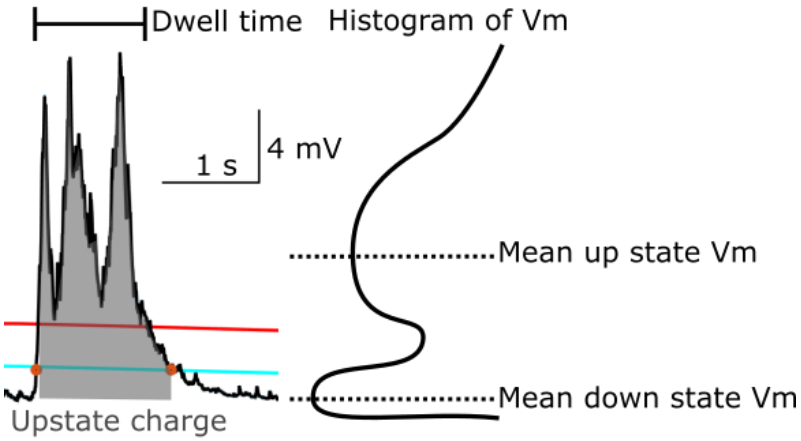

Figure 4.8 Quantification of up state properties. A schematic showing a detected up state with quantified properties. Up state charge is represented by the shaded area. Dwell time is shown as the amount of time above the down state threshold. Mean up state and down state Vm were taken as the mean Vm from the bimodal Vm histogram.

The mean Vm was taken as the average mV of the whole trace. The mean of up and down states was also calculated as the mean mV within each threshold band (Figure 4.8), with Δ up state:down state calculated as the range between these two values. The dwell time of up or down states was calculated as the average up or down state duration from all detected states (Figure 4.8). The variance of the trace was calculated as the standard deviation of the whole trace, indicative of the size and frequency of

the up and down states. The principal frequency (the frequency identified with the highest spectral power) was calculated using the periodgram function within MATLAB. The AP firing frequency was measured as the total APs over a minute, normalised to APs per second (Hz).

Cross and auto correlations between signals was performed using xcorr in MATLAB, used to evaluate the similarity (correlation) of two signals (cross) or the periodicity of one signal (auto) across time. This was done by shifting one signal across time and measuring the correlation at each time shift (lag) between the two signals. For auto correlations, this shifting was performed on a duplicate signal. The peak correlation and lags (s) were extracted from plots.

Data were presented as box and dot plots. The box represents standard error of the mean (SEM), and within the box the square represents the mean, and the line represents the median.

4.3.9.2 LFP recordings

LFP recordings were baseline normalised and the LFP traces were compared to the intracellular Vm either visually or using cross and auto correlations.

4.3.9.3 Cyclic modulation of up and down state activity

Slow cyclic modulation of up and down state activity was visible when examining 1 Hz power over time. This was therefore measured using the overall power in the 1 Hz frequency band which was z-score normalised. Troughs in the power oscillation were identified and used to quantify cyclic periodicity.

4.3.9.4 Evoked responses

Results were analysed using custom MATLAB scripts, developed in house. Evoked responses were plotted as mean waveforms with shaded SEM, unless specified otherwise. Responses evoked on up or down states were split into two respective groups, calculated as up state evoked if the range was >3 mV in the 50 ms preceding stimulus onset (Jouhanneau et al., 2014). These responses were baseline normalised to the Vm period 5 ms post first stimulus onset. This 5 ms period has been shown to be less than the latency of the evoked response in layer II/III neurons to whisker stimulation (Jouhanneau et al., 2014; Moore & Nelson, 1998).

The overall evoked response was averaged for comparisons. The overall evoked responses were quantified as total area under the curve (AUC; defined as the AUC of all points within the measured region, calculated using trapz in MATLAB). The evoked response to the first stimulus was also considered separately, to help identify individual response components without surround inhibition or excitation from neighbouring barrel stimulation (Gambino and Holtmaat, 2012). The response to the first stimulus was described in terms of peak and PSP, with peak referring to the rapid and large response at the start of the stimulation (maximum mV 0 – 40 ms following stimulus onset), and PSP referring to the slower and delayed depolarisation to the stimulation (mean mV 50 – 100 ms post stimulus onset; Figure 4.9).

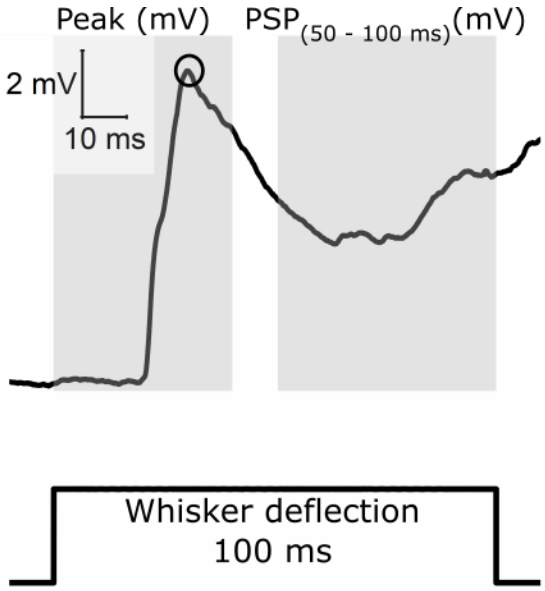

Figure 4.9 Peak and PSP components of evoked potentials. A schematic of the evoked response recorded in response to the first whisker stimulation. Labelled are the peak (fast, large amplitude response at the start of the deflection) and the PSP (slower after depolarisation).

Statistics were performed using R software (v3.5.1) with the integrated development environment RStudio (v1.1.456).

Similar to the previous results chapters, data was analysed using a generalised linear mixed model (GLMM). Animal number was not included due to the low number of animals per condition. As measures were compared between different states or drug

conditions, cell number was incorporated into the model as a random factor, to account for repeated measures from the same cell for each condition compared.

The following GLMM was used to model the data:

$$Variable \sim Drug * State + (1|cell\ number)$$

Variable was the experimental measure tested. Drug was compared as a main effect (either control or MK801 treated). State was also compared, which for this work was either up or down state, or “pre” or “post” (early or late in recordings).

Each main effect was evaluated using a goodness of fit chi squared test (χ^2). Significant results were described as ($\chi^2_{(df, n)}$ = a, p=b*). The χ^2 value was a, degrees of freedom was df, n was the number of recordings, and the corresponding p value (b) was listed with asterisks denoting level of significance when alpha <0.05. Non-significant results were listed as a p value only. A Tukey-Kramer multiple comparison adjustment was used for *post hoc* testing whilst controlling for multiple comparisons.

4.4 RESULTS: SPONTANEOUS PROPERTIES

4.4.1 Up and down state properties following break-in

Over the first few minutes of a cellular recording, there was an observable build-up of up state amplitude (Figure 4.10). This phenomenon seemed to plateau by ~2 minutes. This would suggest some relationship of up and down state transitions to the process of recording (e.g. excess K^+ perfusion in the region of recording leading to local network depression or dialysis of the intracellular solution).

Figure 4.10 Up state build up following whole-cell access. A recorded trace from a cell from the start of break in. A visible increase is seen in the size of the up states when comparing the start to the end of the trace.

Interestingly, this same signal build up was not seen in the LFP signal in comparison which would add further weight to the idea that there was some wash in effect of the recording solution at the start of recordings (Figure 4.11 A). This can be seen clearly by looking at the low frequency power of each of the signals in the spectrographs (Figure 4.11 B). However, whilst there was not a signal build up in the LFP, the first minute of the LFP signal was visually different to the later time points ("noisier" with a larger range of frequency activity) and so this would also suggest that the perfusion of the intracellular solution in the extracellular space prior to recordings did have some effects on the local network. The cross correlation between the LFP recordings and the intracellular signal showed a correlation between the two signals (peak value of ~0.2 for both; Figure 4.11 C & D; Doi et al., 2007). However, across the wash in period, this relationship between the two signals became more time locked, suggesting higher

intracellular synchrony with the network after the wash in period (lags 0.4 s to lags 0.03s; Figure 4.11 C & D).

Overall, it is likely that these changes in up state amplitude are due to intracellular dialysis of the intracellular solution, with some subtle changes in the local network from intracellular solution perfusion. This seems to have dissipated by the third minute of recordings. Therefore, it seemed appropriate to use the third minute following break in to quantify up and down state features where these alterations settle into a stable state.

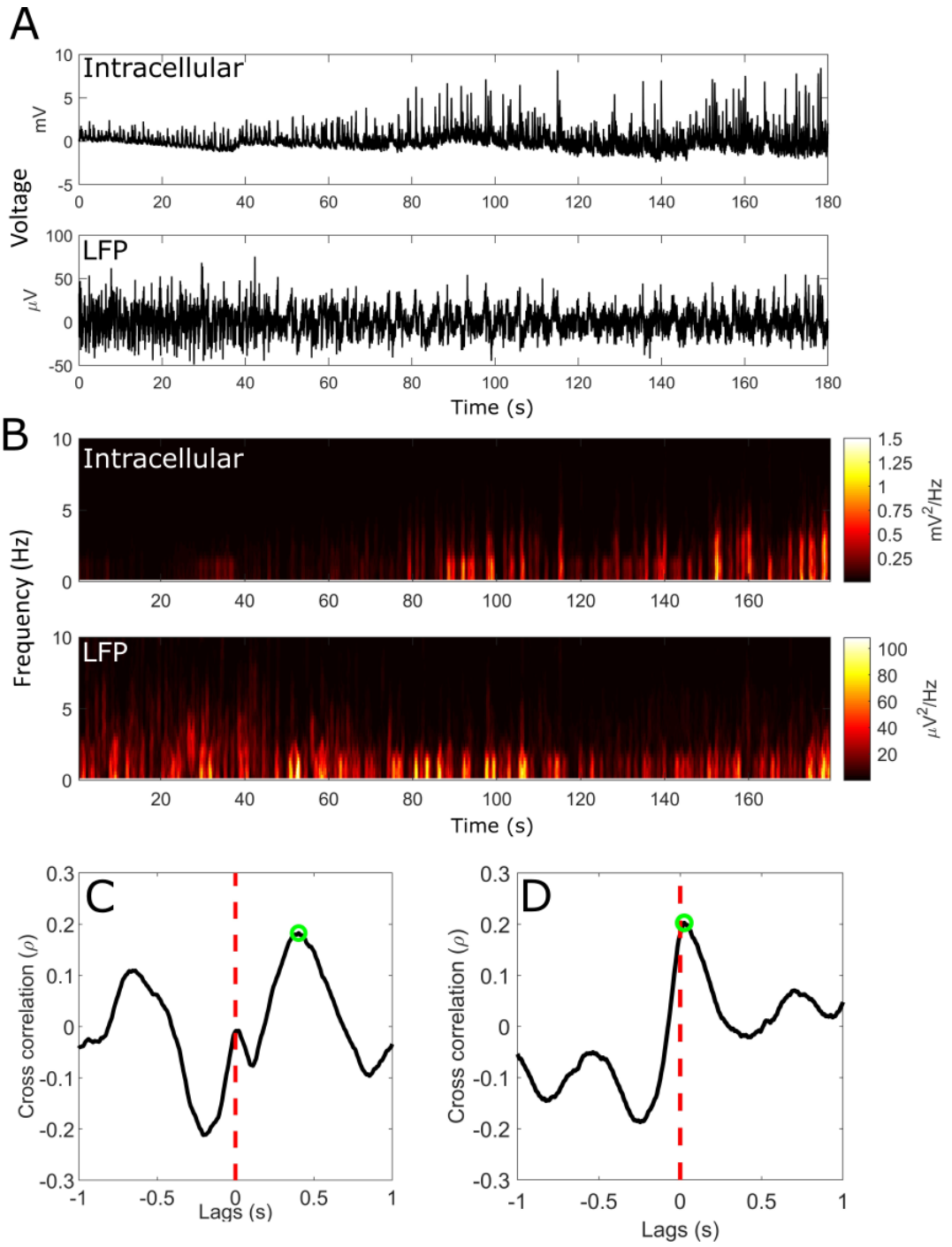

Figure 4.11 Up state size increases following break in in intracellular recordings only. A raw trace of intracellular Vm (top) and LFP (bottom) over the first three minutes following break in (**A**) (baseline normalised to 0 mV). Spectrographs of the intracellular Vm (top) and LFP (bottom) signals show an increase in power in low frequency bands in the intracellular Vm signal over time, but not in the LFP signal (**B**). Cross correlation between Vm and LFP at 1 minute (**C**) and 3 minutes (**D**) shows the peak correlation shift to 0 s lags by 3 minutes.

4.4.2 Up and down state properties of layer II/III neurons in the somatosensory cortex

19 neurons, recorded from 9 animals, were analysed for up and down state properties. The mice used were at a mean age of 215 days (range 187-232 days), in line with the target experimental age for the rTg4510 mice used in studies in other chapters (~5.5 M). The properties were analysed from the third minute following break in. 11/19 of the recordings were made with the use-dependent NMDAR antagonist MK801 (1 mM) in the intracellular solution. This has been shown to influence neuronal activity including up and down state properties after >5 minutes *in vivo* (Gambino et al., 2014; Lavzin et al., 2012; Smith et al., 2013).

The mean series resistance from these recordings was 38 ± 3 MΩ (range 11 – 100 MΩ). This was in line with similar studies, since series resistance is typically much larger for whole-cell recordings performed *in vivo* than *in vitro*. This is thought to be due to brain penetration depth, pipette contamination and physiological movement artifacts (Margrie et al., 2002). Recorded neurons had a mean Vm of -58 ± 2 mV, with a mean down state Vm -60 ± 2 mV of and a mean up state Vm of -55 ± 2 mV (Figure 4.12 A – C). The mean downstate Vm was more depolarised than expected from other literature values (~-80 mV) (Brecht et al., 2003; Waters and Helmchen, 2006). Δ up state:down state was 5 ± 1 mV (Figure 4.12 D) which was also slightly smaller than expected from the literature, which can be attributed to a more depolarised down state Vm in this work (Chen et al., 2013; Waters and Helmchen, 2006). Mean up state dwell time was 0.26 ± 0.02 s (Figure 4.12 E), similar to the literature (Haider et al., 2006; Waters and Helmchen, 2006). The principal frequency was 0.74 ± 0.12 Hz (Figure 4.12 F), which is a measure of the slow wave up and down state oscillation (Haider et al., 2006; Steriade et al., 1993c; Waters and Helmchen, 2006). The variance of the recordings was 8.3 ± 3.2 μV^2 (Figure 4.12 G) which is similar to literature values (Haider et al., 2006; Waters and Helmchen, 2006). There was a low firing rate (0.0009 ± 0.0009 Hz; Figure 4.12 H) as expected from literature (Barth and Poulet, 2012; Brecht et al., 2003), with only one neuron firing spontaneous APs. The discrepancies between some of the values in this chapter compared to the literature may be attributable to multiple aspects of the recording procedure, such as differences in age of the mice (typically juvenile animals (<1M) compared to ~5.5M in this work) (Margrie et al., 2002) or differences in recording solutions.

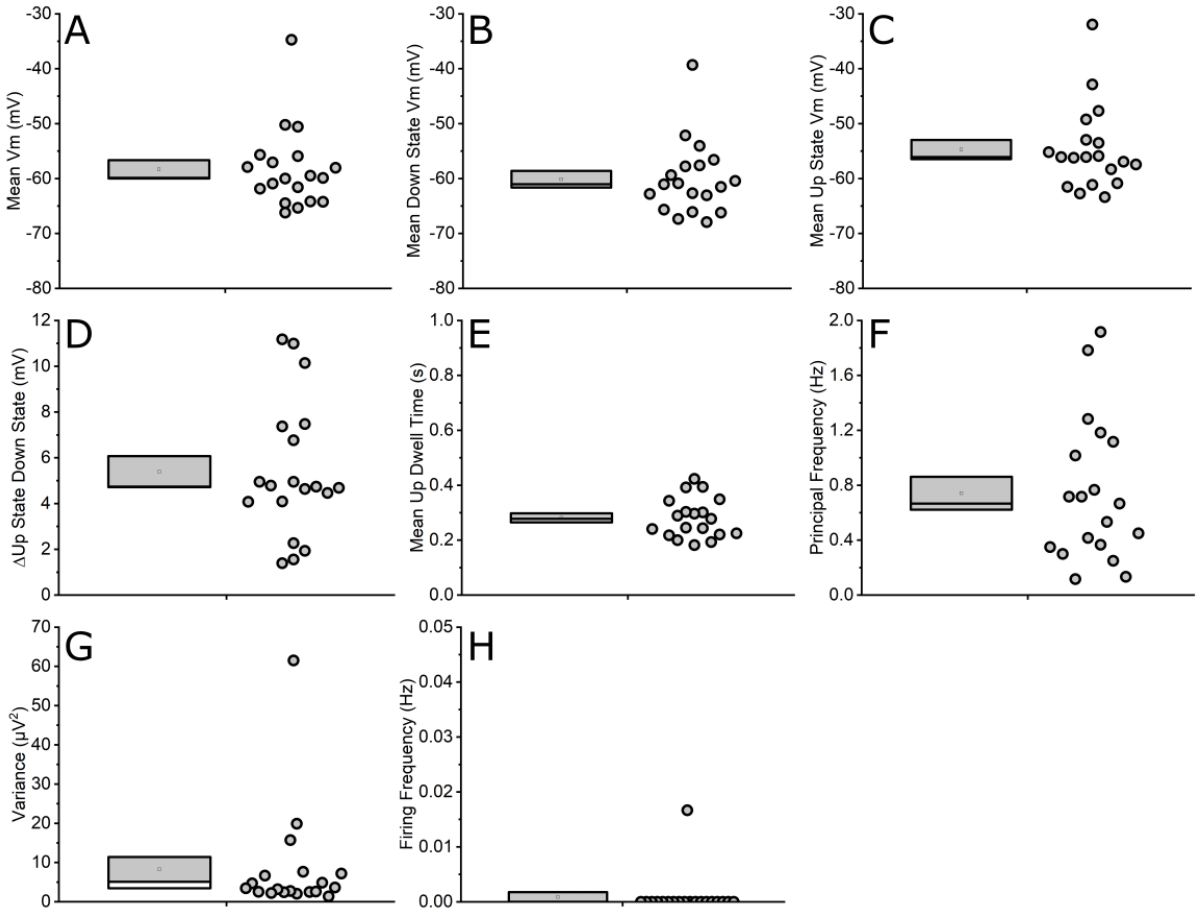

Figure 4.12 Spontaneous up and down state properties. Box and dot plots showing Vm properties (mean Vm (**A**), mean down state Vm (**B**), mean up state Vm (**C**), Δ up state:down state (**D**)), up state dwell time (**E**), the principal frequency of the up down state oscillation (**F**), the variance of the signal (**G**) and the firing frequency at rest (**H**).

4.4.3 Cyclic modulation of up and down state activity

Cyclic modulation of up and down state power, akin to transitions between slow-wave sleep (SWS) and rapid eye movement (REM) sleep states, has been observed under urethane anaesthesia (Clement et al., 2008; González-Rueda et al., 2018; Pagliardini et al., 2012, 2013). The up and down state oscillation cycles between periods of lower (REM-like) and higher amplitude (SWS-like) oscillations, and this can be quantified by measuring the power in the 1 Hz frequency band over time (Figure 4.13). This

modulation has been shown to be correlated with other homeostatic process in the body such as breathing rate, and cycle lengths are different between mouse strains (Clement et al., 2008; Pagliardini et al., 2012, 2013).

This cyclic modulation can be seen by eye when looking at the raw intracellular and LFP recordings over time scales of several minutes, and also at the spectrographs when looking at lower frequency power over time (Figure 4.13 A & B). By isolating out the 1 Hz frequency band, this cyclic oscillation is visible occurring over a longer time scale of several minutes in both the intracellular and LFP recording signals (Figure 4.13 C). Autocorrelation of the power fluctuations from the 1 Hz z-scored signal shows a periodicity to this of approximately 310 seconds (range: 270 – 380 seconds), and that this is highly synchronous between the two signals with a cross correlation value of 0.7 (range: 0.52-0.81) close to 0 phase lag (range: -10 - -17 ms; Figure 4.13 D & E). There were only 3 cells that had recordings of a sufficient length with accompanying LFP recordings to measure this phenomenon. All 3 cells showed similar cyclic modulation behaviour.

Whilst the mechanism underlying this modulation is unknown, it is thought to be a feature of a network with balanced inhibition and excitation (Renart et al., 2010) and could be altered in dementia models where there is dysregulation of neural circuit dynamics (Harris et al., 2020). This cyclic phenomenon is also likely to have an impact on measured and evoked activity. For example, the amplitude of up states would be larger in periods of high 1 Hz power. Therefore, this feature will be quantified and compared when recording activity in the rTg4510 and wildtype mice.

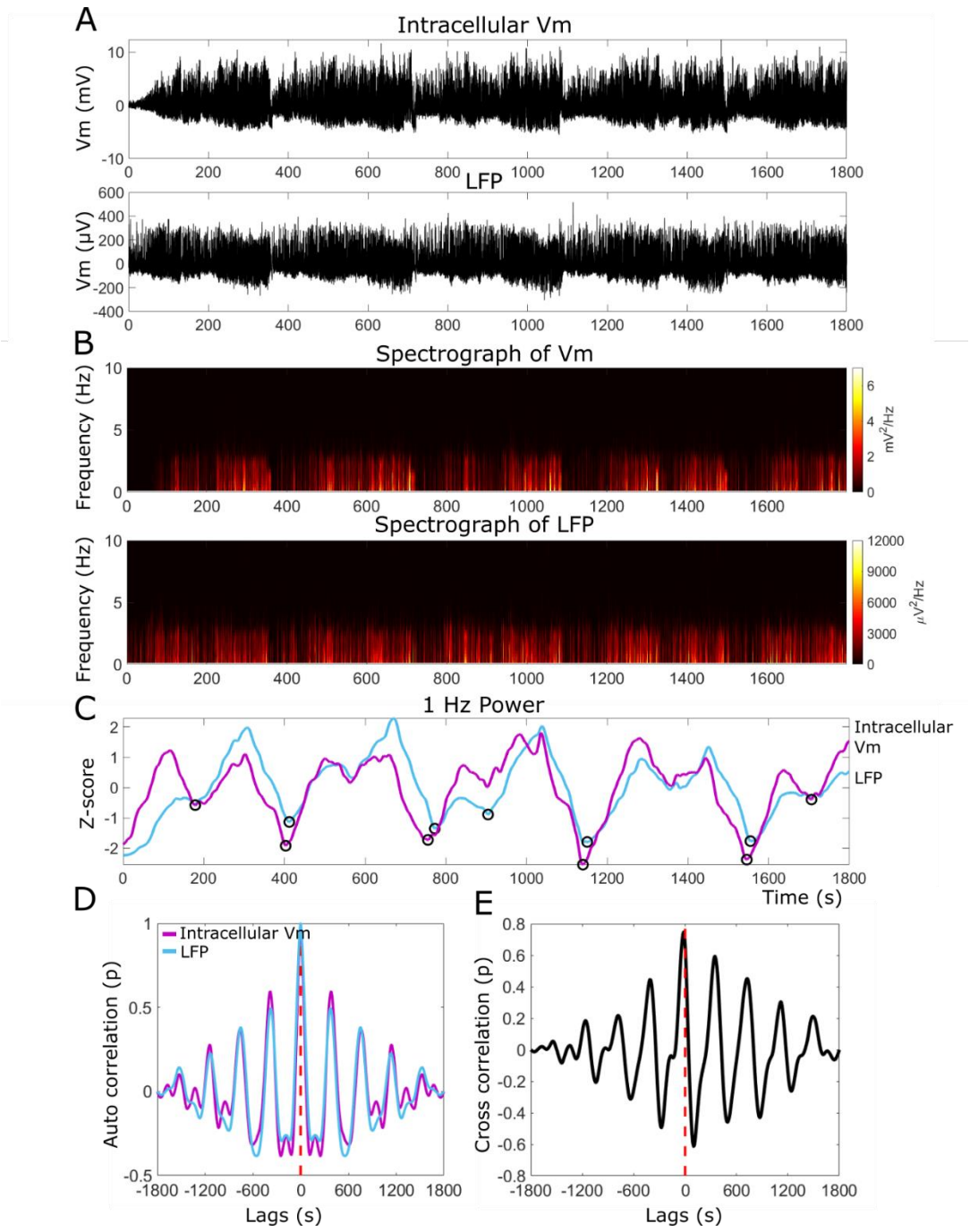

Figure 4.13 Intracellular cyclic modulation of up and down states. The top panel shows an intracellular recording of the Vm and an LFP recording over a period of 30 minutes (**A**). These recordings have been baseline normalised to 0 mV. Spectrographs of the two recordings are shown in the middle (**B**), with the power across low frequencies (0 – 10 Hz) shown across time. This shows observable fluctuations in the low frequency power (1 Hz). This fluctuation was quantified below (**C**), where 1 Hz power was measured and z-scored to normalise. Intracellular Vm is shown in pink and LFP in blue. The detected cyclic periods are denoted with black circles. Auto correlation of the 1 Hz power from the LFP (pink) and intracellular Vm (blue) are shown at the bottom (**D**), showing high rhythmicity of each of the signals. Cross correlation between the 1 Hz power of the two signals also shows a high degree of synchrony (**E**).

4.5 RESULTS: EXPERIMENTAL OPTIMISATIONS DEVELOPING A PROTOCOL TO MEASURE PUTATIVE NMDAR AND AMPAR FUNCTION

Findings presented in Chapter 2 indicate that glutamatergic receptor function may be altered in ~5.5M rTg4510 mice (e.g. reduced NMDA:AMPA receptor ratio). It was useful to try and assess this functional alteration *in vivo* using a behaviourally relevant stimulus. One benefit of the somatosensory cortex as a model system for this work is that whisker stimulation can be used to reliably evoke glutamatergic synaptic responses. Whisker stimulation would also stimulate the same layer IV to layer II/III synaptic pathway as the evoked responses generated in slices in Chapter 2. Therefore, whisker evoked activity could potentially be compared to the *in vitro* evoked activity. The whisker evoked response is a multicomponent response which can then be dissected for likely NMDAR and AMPAR activity based on the latency of the components (Armstrong-James et al., 1993; Gambino and Holtmaat, 2012; Gambino et al., 2014). This can be further quantified by using receptor antagonists to isolate the contribution of a specific receptor to the measured response. To this end, intracellular MK801 was used which is a use-dependent NMDA receptor antagonist.

4.5.1 Evoked responses to whisker stimulation: experimental design

4.5.1.1 How many whiskers to stimulate?

The first experimental consideration was whether to stimulate a single whisker compared to all the whiskers. Whilst stimulating a single whisker would provide a unitary evoked response within a barrel, this would add extra levels of technical complexity. The barrel field corresponding to the stimulated whisker would either need to be identified during surgery or multiple whiskers would need to be stimulated to identify the principal whisker corresponding to the recorded barrel field. Therefore, it was decided that all whiskers would be stimulated together, producing whisker evoked responses in whichever barrel field recordings were made from.

One thing to note, is that whilst it is technically easier to stimulate all whiskers, multi-whisker evoked responses can be significantly different from single whisker evoked responses (Brecht et al., 2003; Gambino and Holtmaat, 2012; Jouhanneau et al.,

2014). For example, the intracellular response to multi-whisker stimulation or surround whisker stimulation compared to principal whisker stimulation has a different overall response shape and a more variable onset (Brecht et al., 2003; Gambino and Holtmaat, 2012; Jouhanneau et al., 2014; Mirabella et al., 2001; Shimegi et al., 1999). However, multi whisker evoked responses also have a multicomponent response and so are still a viable means of interrogating AMPAR- and NMDAR-mediated synaptic function *in vivo*.

4.5.1.2 How to stimulate?

A second consideration was how to stimulate the whiskers, with airpuff stimulation compared to an electrically movable metal wafer (piezo wafer). A piezo wafer converts electrical energy into a mechanical stimulation. This allows for precise and consistent stimulation as long as the whiskers are placed on the wafer in the same way. Airpuff stimulation uses pressurised air to stimulate the whiskers (delivered by a PicoPump using Nitrogen at a pressure of 10 mBar). This method can be more variable but is comparable to piezo stimulation. Due to the nature of electrical piezo stimulation, this also produced an observable electrical artifact in the Vm signal (Figure 4.14). This artifact could potentially mask smaller or the quicker AMPAR component of the evoked responses and so it was decided to use airpuff stimulation for the experimental design.

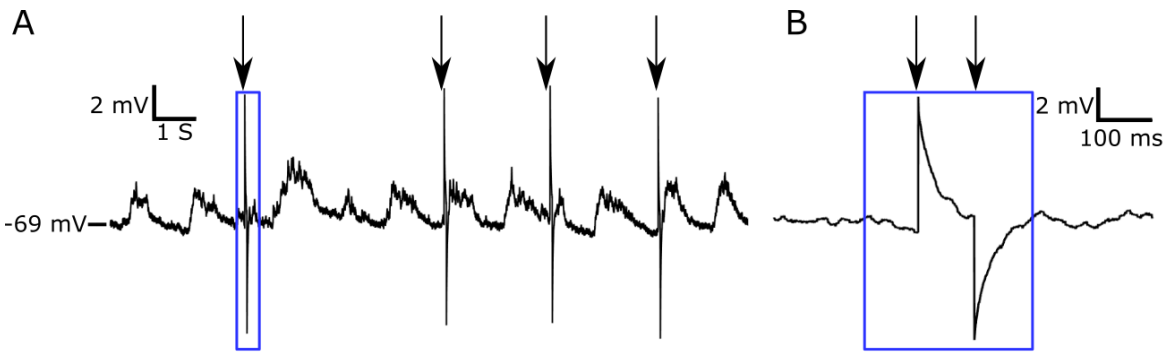

Figure 4.14 Stimulus artifacts from piezo wafer stimulation. Large and rapid change in the recorded electrical potential (stimulus artifacts) were measured when stimulating the whiskers using a piezo wafer (**A**) with stimulus onset denoted with arrows. A blue box highlights one stimulus which when examined at a higher time resolution, the onset and offset of the electrical trigger can be observed with the onset and offset denoted with arrowheads (**B**).

4.5.1.3 How often to stimulate?

Finally, a single evoked response was compared to repeated evoked responses by stimulating a whisker once compared to a repetitive stimulation train. A single stimulation should elicit a single evoked response with multiple components. However, the success rate of evoking a response can be variable from trial to trial (Kerr et al., 2007; Ranjbar-Slamloo and Arabzadeh, 2019). In comparison, repeated stimulation would more reliably evoke a synaptic response (Barros-Zulaica et al., 2019; Kheradpezhouh et al., 2017). Responses may facilitate producing a "response envelope" which could also be used to investigate the contribution of NDMAR activity to evoked responses. This could also allow for exploration of whether cell responses are different in their facilitation or depression to multiple stimuli. But multiple stimulations would recruit other surround and concurrent activity from neighbouring connected cortical columns which needs to be considered in this analysis. However, when applying multiple stimuli, the first response can still also be isolated and analysed separately. Therefore, a multiple stimulation protocol was chosen for protocols.

Different frequencies of stimulation were investigated and from the stimulation protocols tested (five stimulations at 2.5, 5 and 8 Hz), 5 Hz produced a clear synaptic response with slight overlap to allow for NMDAR activation whilst being able to identify individual responses (Figure 4.15). Therefore, five stimulations delivered at 5 Hz was chosen as the stimulation paradigm for future experimental protocols.

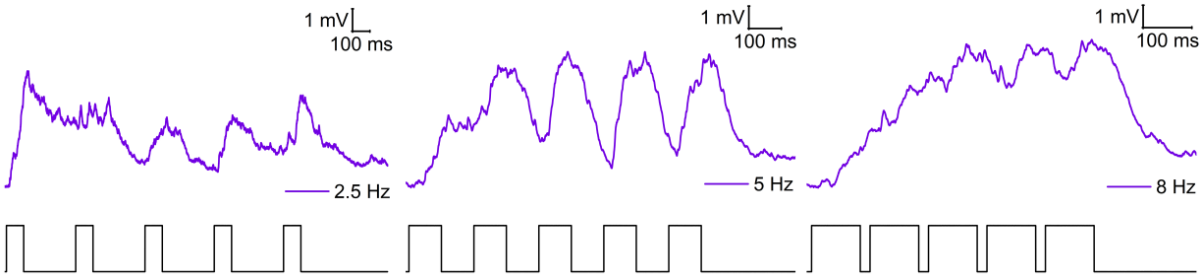

Figure 4.15 Different whisker stimulation frequencies. A single trace of responses to 5 whisker stimulations given at 2.5 Hz, 5 Hz and 8 Hz stimulation frequencies.

4.5.2 Evoked responses to whisker stimulation using the optimised protocol

It was concluded that the optimal whisker stimulation protocol to evoke a robust frequency-modulated train of glutamatergic synaptic responses would be multiple whiskers bunched together and stimulated using an air puff (five stimuli at 5 Hz (100 ms per stimulation)). Using this protocol, the evoked response was measured with or without 1 mM MK801 in the intracellular solution to characterise the effect of NMDAR antagonism on evoked synaptic responses. The average responses to all five stimulations and the first stimulation of the five were compared. For these protocols, whiskers were stimulated every 30 seconds, for recordings of a minimum length of 10 minutes (range: 10 – 30 minutes).

4.5.2.1 Evoked responses were modulated by up and down state activity and MK801 treatment

Responses evoked by whisker stimulation on up states are reduced in amplitude compared to responses on down states (Ferrarese et al., 2018; Gambino and Holtmaat, 2012; Petersen et al., 2003; Sachdev et al., 2004). This was also observed in the recordings presented within this chapter, as the total evoked response to all five stimuli, regardless of MK801 treatment, showed a larger depolarising response when stimulated in down states compared to up states ((Up or down state effect: $\chi^2_{(1, 20)} = 8.59$, $p<0.005$***; Figure 4.16 A, B, E). There was also a significant effect of MK801 treatment on the overall response ($\chi^2_{(1, 20)} = 6.55$, $p=0.01$**), but no interaction between the two effects ($p=0.24$; Figure 4.16 A, B, E). When focusing on the response evoked on the first stimulation out of five, the early peak component was not statistically different regardless of whether it was evoked on an up or down state ($p=0.65$), with or without MK801 treatment ($p=0.6$) and there was no interaction between these two effects ($p=0.68$; Figure 4.16 C, D, F). However, the PSP was significantly different when evoked on an up state compared to a down state ($\chi^2_{(1, 20)} = 7.7$, $p=0.006$**), but was not statistically different between MK801 treatment groups ($p=0.35$), and there was also no interaction effect ($p=0.52$; Figure 4.16 C, D, G). From this information, evoked responses will be split into those on up vs those on down states as they are inherently different responses.

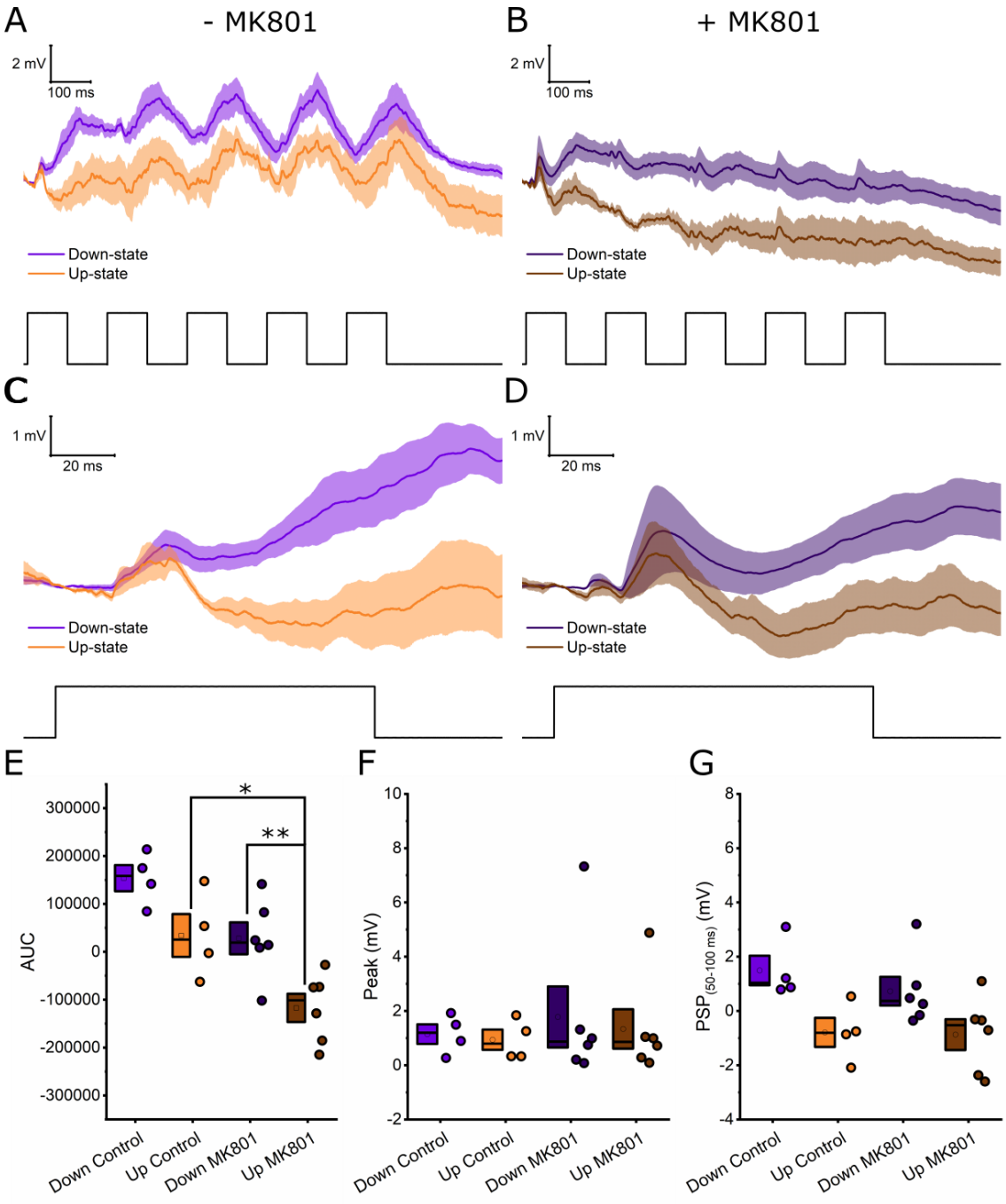

Figure 4.16 Up and down state evoked responses. The mean response to multiple whisker stimulations without MK801 (left-hand side; **A** & **C**) or with MK801 (right-hand side; **B** & **D**) in the intracellular solution. The coloured line represents the mean response, and the shaded area represents the SEM. The AUC value for these traces is shown in plot **E**. The first response of the train is highlighted in the bottom plots (**C** & **D**) for –MK801 and +MK801 conditions, respectively. The quantified peak (**F**) and PSP (**G**) components from these traces are shown below. The time-course of the whisker stimulation protocol is shown below each of the traces as a black line. Data shown is the average of 4 cells (1 animal) for the control condition and 6 cells (3 animals) for the MK801 condition. Significance is denoted as asterisks: $p<0.05$*, $p<0.01$**

4.5.2.2 Evoked responses were reduced over longer stimulation protocols, irrespective of MK801 treatment

Whiskers were stimulated every 30 seconds for at least 10 minutes. The data presented above in Figure 4.16 plotted the total average evoked response, but differences could appear when comparing the evoked responses across time in the stimulation protocol. Evoked responses may run down over time or there may be desensitisation to the stimulation. In addition, MK801 is a use-dependent NMDAR antagonist and therefore could require wash in time before becoming effective. Therefore, it was important to compare and acknowledge these effects, and at what time scale these effects occurred, in the experimental design. Due to its use-dependent actions, it would be expected that intracellular MK801 would have an increasing effect over time. This was measured on down state evoked responses only, where the effects of NMDAR antagonists have been highly characterised in comparison to up state responses.

Overall, responses did not significantly differ over time ($p=0.09$) or with MK801 treatment ($p=0.08$; Figure 4.17 A, B, E) in respect to the AUC measurement of the response. There was no significant effect of time on the peak ($p=0.33$) or PSP component ($p=0.22$), with or without MK801 treatment (peak: $p=0.59$, PSP: $p=0.85$), or interaction (peak: $p=0.95$, PSP: $p=0.99$) between the two effects; Figure 4.17 C, D, F, G).

Whilst the response was not significantly run down over time, it is still something that should be considered in the future experimental protocol (especially with marginal p values). From this pilot study, it was also deemed important to include both control and MK801 treated cells separately, as it seemed the drug may already be having an effect at the start of the recording. Another way to mitigate response run down is to include a second stimulation protocol after a break to measure and compare any differences from the start of the first protocol. Therefore, this will be included for the finalised protocol in case it is needed.

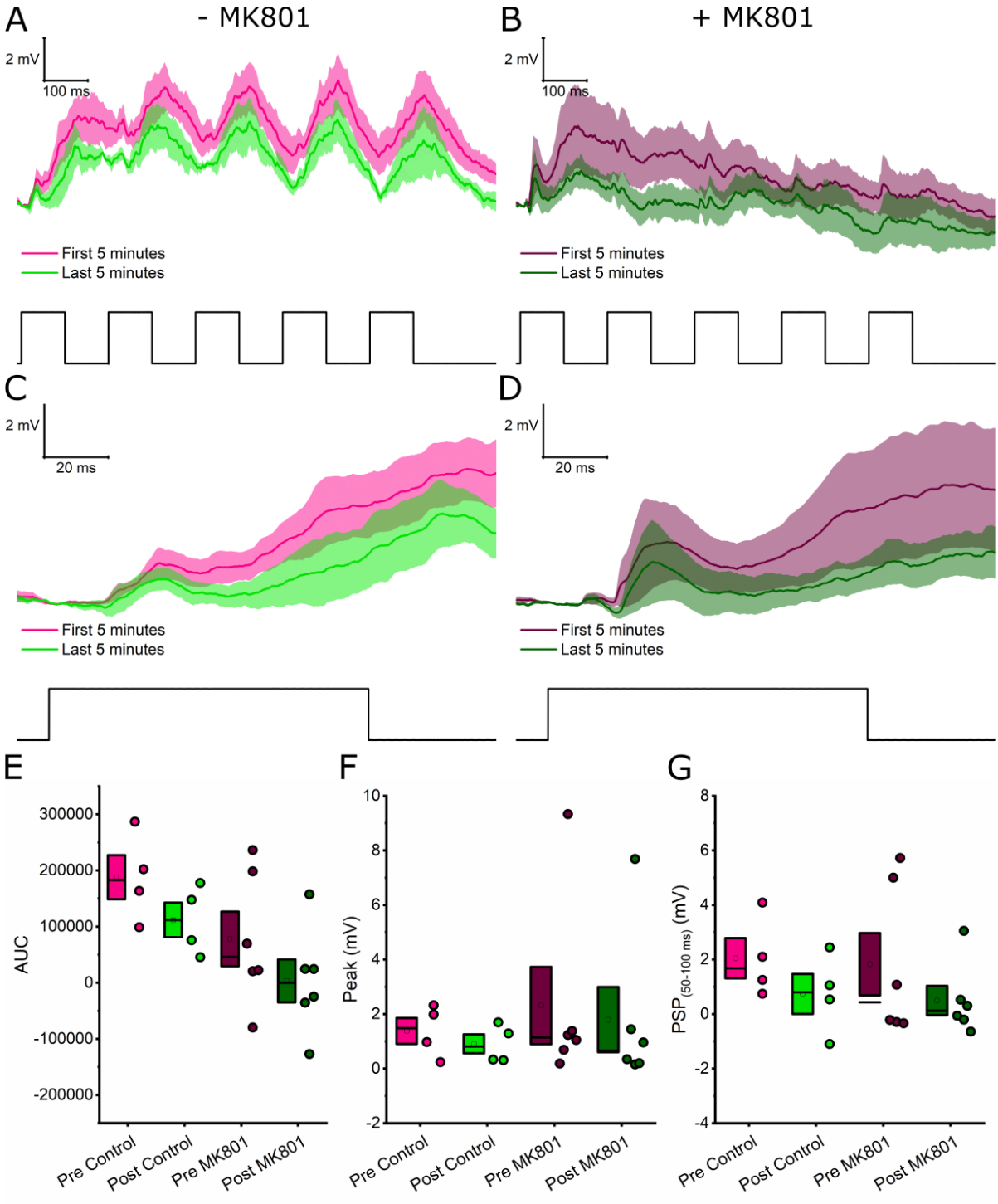

Figure 4.17 Evoked responses compared over time. Responses from the first 5 minutes of stimulation vs last 5 minutes shown in pink and green respectively. Cells recorded with MK801 in the intracellular solution are shown on the right-hand side (**B** & **D**), and cells without are shown on the left-hand side (**A** & **C**). The AUC value for these traces is shown in plot **E**. The first response of the train is highlighted in the bottom plots (**C** & **D**). The quantified peak (**F**) and PSP (**G**) components from these traces are shown below. The whisker stimulation protocol is shown below the average traces as a black line. Data shown is the average of 4 cells (1 animal) for the control condition and 6 cells (3 animals) for the MK801 condition.

4.5.2.3 Comparison of evoked responses measured using whole-cell recordings and LFP recordings with the application of MK801

Simultaneous LFP recordings were made to whole-cell recordings during whisker stimulation from 3 cells. These recordings were made with MK801 in the intracellular electrode, allowing comparisons of the effect of MK801 over time at the single cell level and how that compared to the LFP recordings. Evoked responses on down states were compared to the evoked responses detected in the LFP.

The LFP recordings showed detectable evoked responses (Figure 4.18 B, D, F), with 2 out of 3 of the recordings showing clear on and off responses to the whisker stimulation (Figure 4.18 B & F). These two recordings also did not appear to change across the ≥10 min stimulation protocol, suggesting no response run down of the global signal or spill over effects of MK801. The LFP recording from cell 2 showed variable whisker evoked responses during the first five minutes of recording (Figure 4.18 D). Later in recordings, this response only seems to be driven by the first stimulus and not subsequent ones. This change over time may be a genuine feature of the evoked response in this animal, or perhaps may be related to technical issues with the recording such as decline in mouse health, anaesthesia depth, or electrode placement and access.

When comparing the LFP recordings to the single cell recordings, the intracellular signal of cell 1 showed a clear whisker evoked potential which slightly reduced over time and the LFP recording also showed whisker evoked responses (Figure 4.18 A & B). Cell 2 showed a large evoked response to the first stimulation early in the recordings in the intracellular signal, but this is lost later in the recordings with a similar pattern seen in the LFP recording (Figure 4.18 C & D). The third cell showed a small evoked response to the first stimulus with a variable response afterward, whereas the LFP recordings showed a clear evoked response to whisker stimulation that does not change over time (Figure 4.18 E & F). Overall, this information suggests that whisker evoked responses can be variable both at the single cell and network level and emphasises the need to ensure whisker stimulation is consistent and even. From these 3 cells, it seems that excess MK801 in the extracellular space typically does not have an effect on the LFP. Although with only 2/3 LFP recordings showing no change over time, this data is not conclusive.

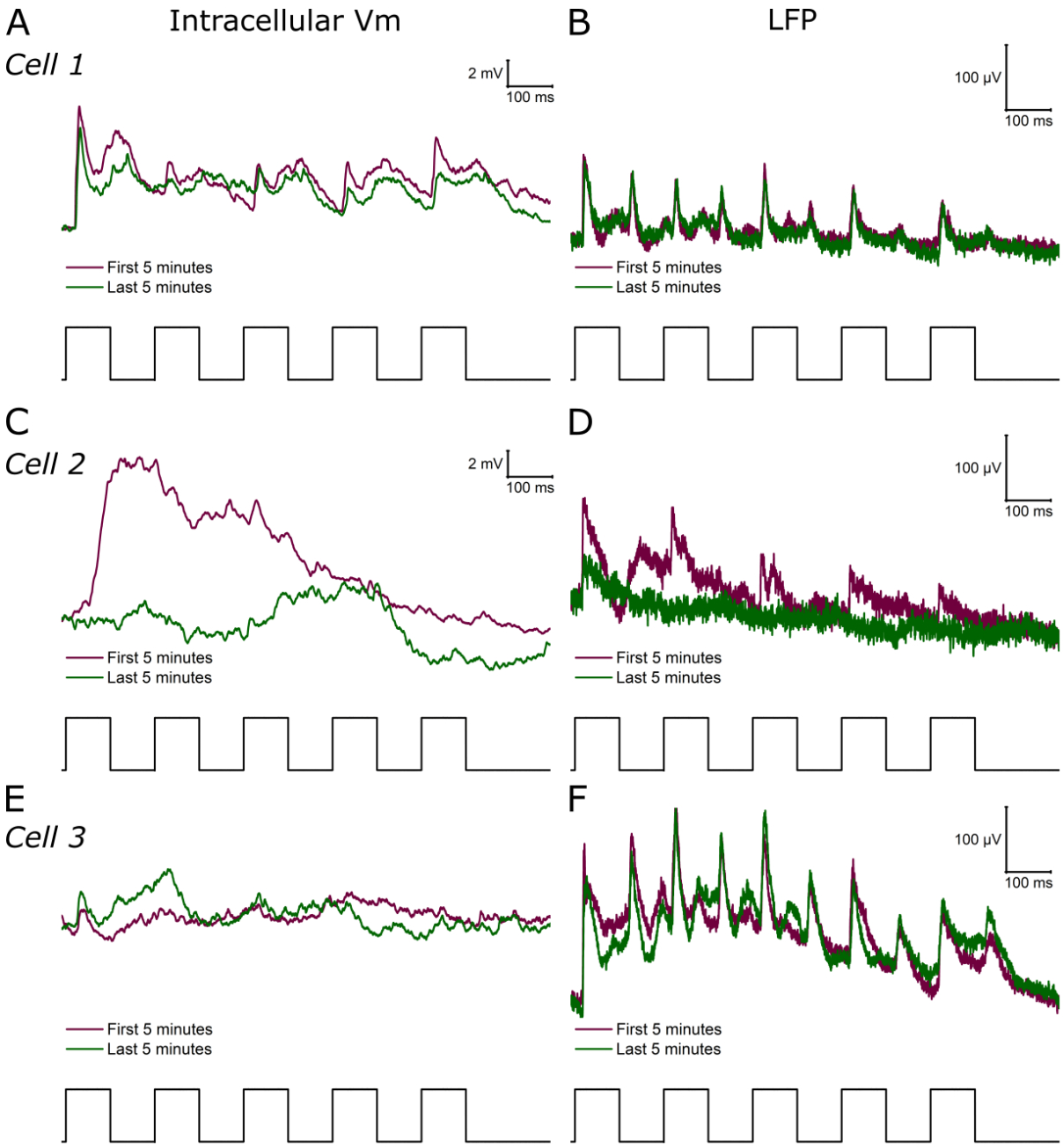

Figure 4.18 Different types of response to whisker stimulation with MK801 application. Comparison of whole cell evoked responses (**A, C, E**) and simultaneously recorded LFP responses (**B, D, F**) to whisker stimulation. Responses shown are average responses of individual cells or from the LFP from the first 5 minutes of the whisker stimulation protocol compared to the last 5 minutes. All three cells had the addition of the use dependent NMDAR antagonist MK801 to the intracellular solution.

4.6 FINALISED RECORDING PROTOCOL

From these pilot experiments, an experimental protocol was designed to measure *in vivo* properties of glutamatergic synaptic transmission in the rTg4510 model (Figure 4.19). A three minute "gap free" recording period at the start was used to allow for changes in up and down state properties following initial break-in and dialysis of the cell (Section 4.4.1). Following this, whisker stimulation would be delivered (five stimulations at 5 Hz) over a period of 15 minutes. Multiple whisker stimulations at a 5 Hz frequency appeared to produce an optimal response envelope to investigate NMDAR-mediated activity in this response (Section 4.5.1.3). Evoked responses would be analysed separately when evoked on an up or down state as this appeared to significantly alter the evoked response (Section 4.5.2.1). This work also showed a need to include a control recording dataset without MK801, even though MK801 is a use-dependent drug, as MK801 appeared to alter the evoked shape of responses from early on in recordings (Section 4.5.2.2 & 4.5.2.3). Further "gap free" and whisker stimulation periods were also included in the protocol to allow for a time course comparison to measure changes in spontaneous or evoked responses if needed (e.g. due to loss of access to the cell, plasticity induced changes from whisker stimulation, run down of the response, MK801 efficacy). Cyclic activity would also be included to examine genotype effects on this measure and determine whether this activity has an impact on evoked responses.

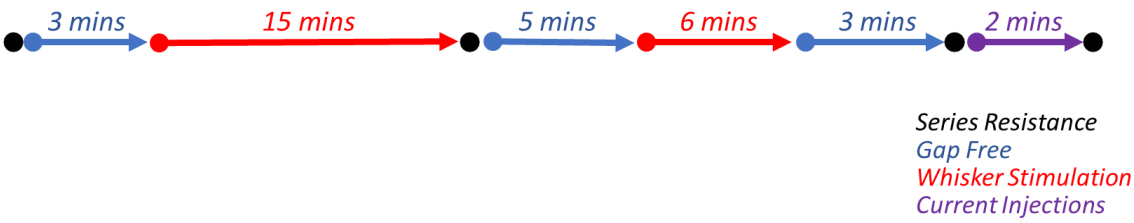

Figure 4.19 Optimised recording protocol. Spontaneous activity (no current injection or whisker stimulation, "gap free") is shown in blue. Whisker stimulation periods are shown in red. Current step injections is shown in purple, which could be used to measure excitability and AP properties. Series resistance (measured by current deflections and Ohm's law calculations) is shown in black.

Simultaneous LFP recordings provided valuable information about the spontaneous and evoked activity. However, these recordings were time consuming and increased the likelihood of damage to the craniotomy, reducing the number of cellular recordings that could be performed in a session. Therefore, LFP recordings were not included in the experimental design for the rTg4510 model.

4.7 CONCLUSIONS

In vivo two-photon targeted whole-cell recordings are a very powerful tool to dissect the *in vivo* whole-cell properties of single cells including subthreshold changes, and it can be combined with other techniques such as LFP recordings to provide a larger idea of the network state. The experimental protocol designed and optimised in this chapter was used in Chapter 5 to examine spontaneous and evoked properties in the rTg4510 mice and littermate controls.

5 *IN VIVO* TWO-PHOTON TARGETED WHOLE-CELL PATCH CLAMP ELECTROPHYSIOLOGY IN THE SOMATOSENSORY CORTEX OF ~5.5 MONTH OLD RTG4510 AND WILDTYPE MICE REVEALED ABNORMAL WHISKER-EVOKED RESPONSES

5.1 INTRODUCTION

It was established in Chapter 2 (*in vitro* functional synaptic assessment in the rTg4510 mice) that there was an imbalance in the NMDA:AMPA receptor ratio at ~5.5 months (5.5M) of age in the rTg4510 mice. In addition, work from Chapter 3 (synaptosome protein expression assay in the rTg4510 mice) found a significant reduction in NMDA receptor (NMDAR) and AMPA receptor (AMPAR) expression at ~5.5M of age in the rTg4510 mice. It is likely that these identified synaptic deficits could contribute to alterations of synaptic processing of neural information in the brain, for example in synaptically-driven responses (Lebedeva et al., 2019). To assess if this was the case, *in vivo* whole-cell patch clamp recordings were used to directly assess spontaneous synaptic function and synaptic responses to sensory stimulation in the rTg4510 mice at ~5.5M of age under urethane anaesthesia. This allowed direct quantification of subthreshold properties, alongside measurement of network activity. Whisker stimulation evokes a multi-component response that has been suggested to be mostly AMPAR- and NMDAR-mediated, providing a tool to investigate glutamatergic receptor function (Armstrong-James et al., 1993; Gambino et al., 2014; Lebedeva et al., 2019). To isolate the different receptor mediated components of synaptic responses, recordings were made with or without the NMDAR antagonist, MK801. All recordings were performed under urethane anaesthesia, which induced a synchronous slow wave oscillation (up and down states) which also provided a measure of network activity akin to that of slow wave sleep. The anaesthetised state helped to isolate evoked synaptic activity by reducing the highly variable barrage of other local and global activity associated with awake states.

5.1.1 Whole-cell in vivo alterations in tauopathy

There is currently only one paper that uses *in vivo* whole-cell patch clamp recordings to explore subthreshold neuronal function in tauopathy (Menkes-Caspi et al., 2015).

Specifically, Menkes-Caspi et al., 2015, investigated network oscillation dysfunction (specifically up and down state properties) in rTg4510 mice and wildtype littermate controls at 3.5 and 5.5M of age in the frontal cortex. In this study, 5.5M rTg4510 mice had a lower principal frequency than wildtype littermate controls, equating to fewer up states. Spontaneous firing was also reduced in the rTg4510 mice. However, these recordings were made under ketamine-xylazine anaesthesia, with ketamine being an NMDAR antagonist (Anis et al., 1983; MacDonald et al., 1987). *In vivo* administration of ketamine during up and down state recordings has been shown to reduce up state duration significantly (Steriade et al., 1993a).Therefore, it is possible that some of the changes observed by Menkes-Caspi et al., 2015, were related to a reduction in NMDAR function from the use of ketamine in combination with effects from tau overexpression. The work in this chapter should help substantiate the role of tauopathy in slow wave oscillation dysfunction.

5.1.2 The role of NMDAR function *in vivo*

NMDAR function is hypothesised to play a role in the generation and maintenance of slow wave oscillations and sensory-evoked responses in the somatosensory cortex. Therefore, the work presented in this chapter, in which neurons were recorded in the presence of an NMDAR antagonist, should detect alterations in oscillatory and evoked activity.

Slow wave oscillations (up and down states) are thought to be generated intrinsically, driven by dynamic fluctuations of excitation and inhibition. Antagonists targeting excitatory NMDARs, blocked the generation of up states in pyramidal neurons *in vitro* (Cossart et al., 2003; Woodward and Pava, 2009). However, whole-cell recordings *in vivo* with NMDAR antagonists have shown no change in up and down state properties. This includes, but is not limited to, up and down state frequency, amplitude, Δ up down state or up state dwell time (Chen et al., 2013; Palmer et al., 2014; Smith et al., 2013). However, other intrinsic properties were altered including a reduction in action potential (AP) frequency (Palmer et al., 2014; Smith et al., 2013).

In some of these studies, evoked activity was also altered, leading to neurophysiological dysfunction in sensory processing (Chen et al., 2013; Palmer et al., 2014; Smith et al., 2013). The evoked activity to whisker stimulation in the somatosensory cortex is comprised of a multi-component response with application of

NMDAR antagonists *in vivo* reducing the slower postsynaptic potential (PSP) component of this response (Gambino and Holtmaat, 2012; Gambino et al., 2014). From this, it is likely that application of MK801 (a use dependent NMDAR antagonist) during recordings alters whisker evoked responses but not up and down state properties. The work presented in this chapter clarifies tauopathy-mediated changes in the functional properties of single cells *in vivo* in the rTg4510 mice, specifically with and without the presence of NMDAR-mediated activity.

5.2 AIMS

Following the putative glutamatergic receptor dysfunction measured in Chapter 2, and the reduced glutamatergic receptor expression witnessed in Chapter 3, it was prudent to determine whether this dysfunction manifested itself *in vivo* in the rTg4510 model in both passive and stimulated conditions. Therefore, up and down state properties and slower cyclic modulation activity was measured in the rTg4510 and wildtype littermate mice in layer II/III neurons in the somatosensory cortex as a measure of spontaneous activity. These recordings were made in the same region used to measure glutamatergic receptor function in Chapter 2 and glutamatergic receptor expression in Chapter 3. This allowed for some comparisons to be made between the results of these chapters. In addition, the stimulation protocol established in Chapter 4 evoked glutamatergic receptor mediated responses and thus was used in this chapter to investigate glutamatergic receptor activity. The passive and stimulated properties were compared to responses with intracellular MK801 application, an NMDAR antagonist, allowing the isolation of NMDAR activity in the passive and stimulated activity. Together, this should help characterise glutamatergic receptor activity in passive and evoked activity and determine how the altered glutamatergic phenotype manifested in the intact network in the rTg4510 mice.

5.3 METHODS

5.3.1 Ethical Approval

Studies were approved by the University of Bristol Animal Welfare and Ethical Review Body. All procedures, including Schedule 1 procedures, were performed in accordance with the UK Animal (Scientific Procedures) Act 1986 and its subsequent amendment in 2012 to align with European Directive 2010/63/EU on the protection of

animals used for scientific purposes. All studies described are performed on adult mice, kept on a 12:12 light/dark cycle and granted *ad libitum* access to food and water.

5.3.2 Animals

5.3.2.1 rTg4510 mice

The experiments in this chapter used the rTg4510 (TG) mouse model of tauopathy with wildtype (WT) littermate controls, with or without the presence of both the tetracycline transactivator and the tau P301L transgene, respectively. Male TG mice and WT littermate controls of 4-5 months of age were bred at ENVIGO (Oxon, UK) and provided by Eli Lilly & Company. Animals were transferred to a vivarium at the University of Bristol and were habituated to their new environment for at least two weeks prior to experiments. Experiments were performed blind with respect to genotype.

5.3.3 Surgical details

In total, 15 WT animals (22 - 25 weeks of age, mean 23.5 weeks) and 15 TG animals (22 - 25 weeks, mean 23.5 weeks) underwent surgery for acute recordings. The surgical methodology is described in brief below. For further information on the surgical methods, refer to Chapter 4.

All surgeries began approximately between 12:00 and 13:30 hours with surgeries taking approximately 1:30-2:30 hours in length. Animals were weighed before surgery began to ensure correct urethane anaesthetic doses were given. Between genotypes, the mice were significantly different in weight (WT mean 34.1 g ± 0.7 g, TG mean 28.8 g ± 0.2 g; Mann-Whitney U t-test, $t_{2,29} = -6.43$, $p<0.005$***). This has been seen within the literature in the model (Yue et al., 2011), and did not impact the total normalised urethane dose given (1.5-2mg/kg).

At the start of the procedure, animals were anaesthetised using 3-4% gaseous isoflurane for induction. The head of the mouse was shaved, and the mouse was transferred to the stereotaxic frame (secured within the frame using stereotactic ear bars) under 1.5-2% gaseous isoflurane for anaesthetic maintenance. Eye drops, betadine and lidocaine was applied to the skin. Anaesthetic depth was checked by lack of toe pinch reflex and rhythmic slow breathing, and body temperature was monitored using a rectal temperature probe controlled thermostatically via a heat pad. An incision was made in the scalp, allowing access to the skull. Coordinates were

marked out for the somatosensory cortex (+1.3 mm anterior-posterior and -3.4 mm medial-lateral from Bregma), following which the skull was scored using a needle. The skull was covered with a thin layer of superglue and a custom-made linear head bar was glued to the posterior of the skull above the cerebellum using superglue. Once dried, a dental cement well was formed around the edge of the skull. A craniotomy was performed (approximately 1mm in diameter) at the marked reference point for the somatosensory cortex. The piece of skull covering the brain was removed under submersion with aCSF (composed of (in mM) 135 NaCl, 5 KCl, 5 HEPES (Free Acid), 1.8 $CaCl_2$ and 1 $MgCl_2$). The dura was then also removed from the area. Urethane was administered between 1.5-2mg/kg following surgery with isoflurane anaesthesia stopped, following which the animal was transferred to the recording set up.

5.3.4 Recording set up & equipment

Full details of the recording set up are specified in Chapter 4, including full methodology for targeting neurons for recordings. A brief overview of relevant protocol details is summarised below.

Once the animal was transferred to the recording set up, the whiskers contralateral to the craniotomy were clumped together using Vaseline and an open-ended cone was placed next to the bulk of the whiskers. This cone was connected via tubing to a Pneumatic PicoPump (WPI, PV820), to provide whisker stimulation at ~10 mBar pressure using Nitrogen.

Electrodes were fabricated using a Narishige PC-10 puller to a resistance of 4-10 MΩ with a long taper to limit damage when entering the brain. An intracellular solution composed of 135 mM K-Gluconate, 5 mM NaCl, 10 mM HEPES free acid, 0.2 mM EGTA, 0.3 mM GTP-Na salt, 4 mM ATP-Mg salt, 6.7 mM Biocytin, 25 µM 594 AlexaFluor Hydrazide, with or without 1mM MK801 (NMDAR antagonist; Hello Bio) was used to fill the electrodes for recordings. This solution used was comparable to the KGluconate solution used in Chapter 2 and 4, with the addition of the AlexaFluor dye and MK801. Solutions with and without MK801 were interleaved between cells so that there would be an even number of cells recorded from both conditions.

Cells were targeted using the shadow patch technique, visualised using two-photon microscopy (Kitamura et al., 2008). Layer II/III putative pyramidal neurons were targeted within the somatosensory cortex. Cells were targeted based on their shape

(triangular) at the right depth from the brain surface for layer II/III (~80 - 150 µm from pia), and were confirmed to be likely pyramidal neurons post recording by imaging the structure looking for a large dendritic arbour with the presence of dendritic spines.

Cells were recorded using whole-cell patch clamp electrophysiology. Signals were amplified using a Multiclamp 700A (Molecular Devices) and digitised using a CED Power 1401 data acquisition system (CED). Recordings were made and stored on a PC using Signal v5.07 software (CED). Recordings were low pass filtered at 10 kHz, with an output gain of 10x and sampled at 50 kHz. Liquid junction potentials were not compensated for (due to unknown extracellular ion concentrations), and the bridge was not balanced in these recordings (due to high and variable series resistance in these recordings to prevent extra artifacts).

5.3.5 Electrophysiology recording protocols

An overview of the full recording protocol is shown in Figure 4.1. In brief, following break in, series resistance was recorded in voltage clamp using a current step injection. Following this, recordings were made in current clamp “at rest” to measure spontaneous membrane potential properties (“gap free”; no current injection) for the first 3 minutes. Whisker stimulation was then delivered at 5 Hz (5 stimuli) every 30 seconds for 15 minutes with a hyperpolarising current step at the end to measure input resistance changes. A quick series resistance measurement was taken in voltage clamp following this protocol. After this, another 5 minutes were recorded “gap free” in current clamp to allow comparisons of the evoked responses at the start of the recordings. Another set of whisker stimulations were delivered (using the same parameters as before) for 6 minutes. This was followed by another “gap free” recording epoch of 3 minutes in length. Series resistance was then measured again. Finally, current steps were injected to examine action potential (AP) properties, followed by a final series resistance measurement. After recording, the electrode was withdrawn slowly to attempt to form a clean reseal of the recorded neuron. The recorded cells were filled simultaneously with the AlexaFluor dye whilst recording the electrical properties. Therefore, following recordings, cells were imaged using the two-photon microscope (z-stack from pia to depth of filled neuron visibility, 1 s per plane, 1 µm steps) using a 40x objective, visualised using an excitation wavelength of 800 nm. The coordinates were also noted (for depth and location in craniotomy, with respect to the

dorsal surface of the brain). This also helped to confirm neuronal recording depth (i.e. within layer II/III).

5.3.6 Analysis

Cells that depolarised above 0 mV for greater than 1 s during a protocol subsection (i.e. “gap free”), were excluded from that protocol but kept within previous protocols. Series resistance was measured at the start of recordings, recorded in voltage clamp, as the change in current deflection amplitude to a voltage step of 1 mV, converted to a resistance using Ohm’s law. Any recordings with a series resistance of over 100 MΩ was excluded. The series resistance exclusion criteria was much larger than that of *in vitro* recordings in Chapter 2. This was in line with similar *in vivo* studies, since series resistance is typically much greater *in vivo*, and this is thought to be due to brain penetration depth, pipette contamination and physiological movement artifacts (Margrie et al., 2002).

Series resistance itself was not statistically different between genotypes or between MK801 conditions following exclusions (27 WT control cells (13 animals), mean 48.6 MΩ ± 1.8 MΩ; 17 WT MK801 cells (9 animals), mean 49.8 MΩ ± 3.4 MΩ; 19 TG control cells (10 animals), mean 51.6 MΩ ± 3.7 MΩ; 17 TG MK801 cells (9 animals), mean 44.5 MΩ ± 3 MΩ) (GLMM, Genotype p=0.43, MK801 p=0.1, Genotype*MK801 p=0.16; Figure 5.1).

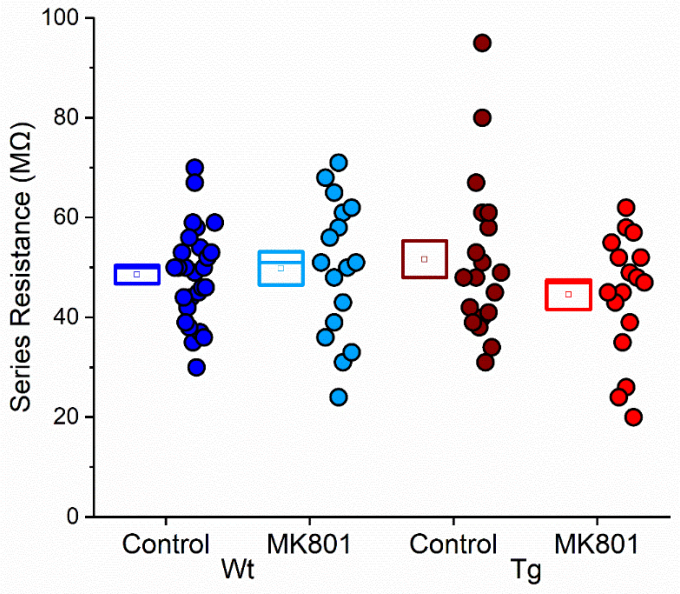

Figure 5.1 Series resistance from all recorded cells. Measured series resistance from the start of cell recordings with series resistance exclusions (1 cell excluded from the control TG group with 109 MΩ series resistance).

Recordings were analysed using custom MATLAB scripts, developed in house (see below for descriptions).

5.3.6.1 Up and down states

Up and down state analysis was performed on the third minute following break in for the starting analysis (due to wash in effects – see Chapter 4 for further details). Further comparisons were made to the later "gap free" period at 23 minutes to compare changes occurring across time. The analysis for up and down state extraction is described in brief, with further details presented in Chapter 4.

First, APs were filtered out of the trace. This was performed by finding points along the trace where dV/dt exceeded 10 $mV.ms^{-1}$, measuring the maximum mV 1 ms after this point. If this point was larger than -50 mV, then it was classified as an AP. The AP was then filtered out of the trace by finding the AP threshold (defined on phase-plane plots where dV/dt surpassed 30 $mV.ms^{-1}$) and changing the mV of the AP waveform past threshold to equal threshold (Figure 5.2 A). AP firing rate properties were analysed separately. Traces were then down sampled to 1 kHz. A 10 s scanning window was used to scan the trace in 1 s increments to find up and down state thresholds using the histogram of the membrane potential (Vm) in this window. This

was done by fitting a bimodal distribution to the histogram of Vm (using fitgmdist in MATLAB for two populations). The local minimum between the two distributions was found. Two thirds of the peak of each of the states to the local minimum distance was used to create a threshold for up and down states (Menkes-Caspi et al., 2015; Stern et al., 1997). This created a moving threshold for the trace to account for changes in baseline stability or changes in up and down state shape.

Up states were then counted if the Vm was above the up state threshold for longer than 200 ms (González-Rueda et al., 2018; Menkes-Caspi et al., 2015), with the start and end of the up state counted as the point where the voltage depolarised and hyperpolarised past the down state threshold.

Out of 77 recordings for “gap free” analysis, 25 recordings were excluded from a subset of “gap free” analysis when there was no clear split between the histogram distribution of the Vm, which prevented the analysis script from detecting up states. (Figure 5.2 C & D). This was determined by visual inspection of recordings during analysis, with approximately 50% detection rate as the cut off for exclusions. These recordings were not analysed for changes in up state properties (e.g. dwell time, mean Vm, Δ up state:down state, etc.) as up states could not be reliably detected. However, the recordings were analysed for other measures that did not require state separation (mean Vm, spectral analysis, variance and firing frequency). These cell recordings were likely to either be from a period of low 1 Hz cyclic power “rapid eye movement (REM)-like” or potentially other cell types (Clement et al., 2008; Pagliardini et al., 2013; Renart et al., 2010).

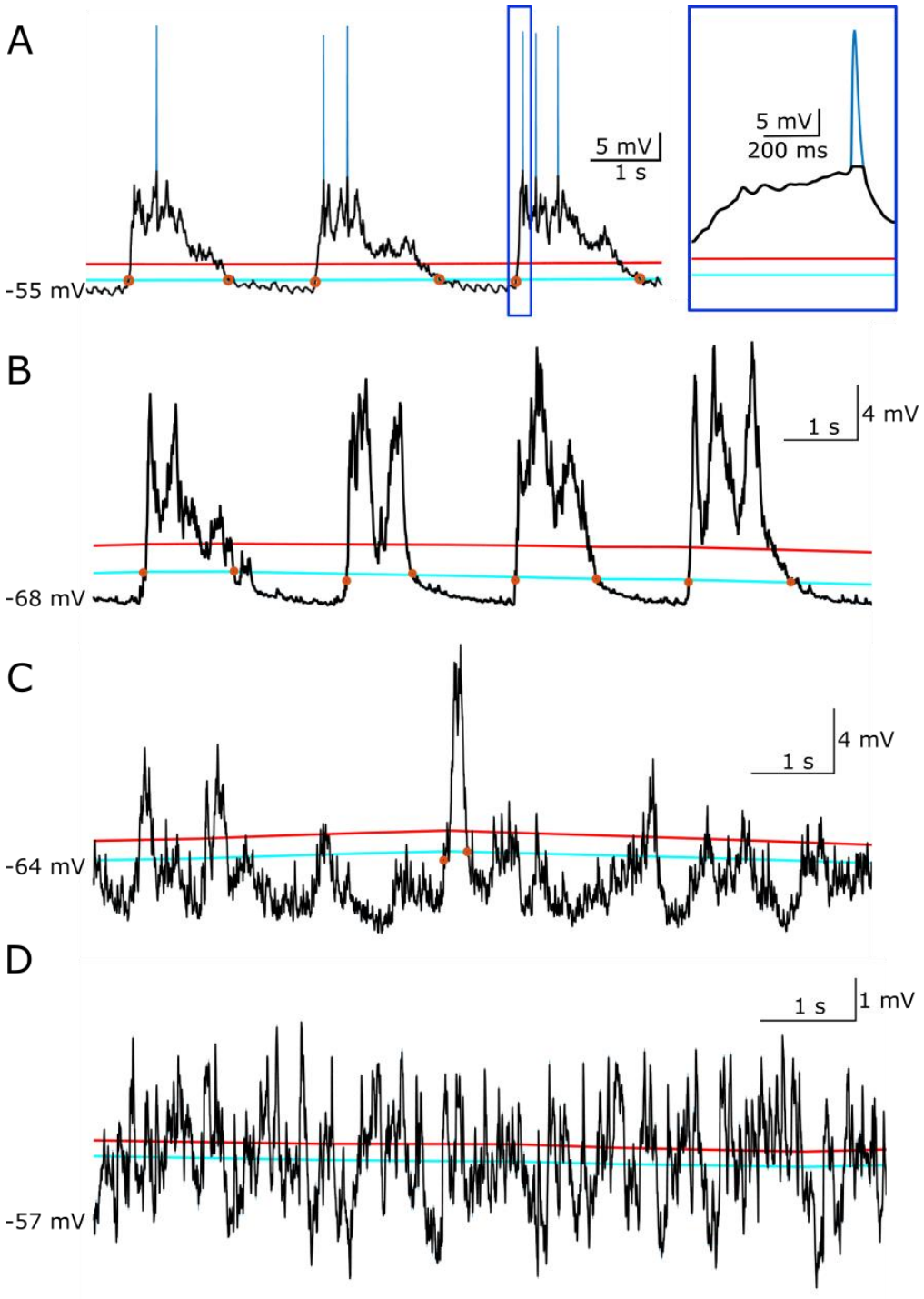

Figure 5.2 Detected up and down states in recordings with different up and down state properties. Examples of exclusion categories from up and down state recordings. Up and down state thresholds are marked as a red and cyan lines respectively. Orange circles denote the start and end of a detected up state. Clear up and down state detection is seen with (**A**) and without AP filtering (**B**), with an example of an AP filtered at AP threshold in the inset of **A**. Partial presence of clear up and down states but low detection rate is shown in **C**, and an example of a lack of clear up and down states and no detection shown in **D**.

The mean of the total Vm (regardless of up or down states) was measured, and the separate mean Vm of the up and down states within each threshold band was also measured. Δ up state:down state was calculated as the range between the two values calculated for mean up and down state Vm. Mean dwell time was taken as the average duration for up or down states. Firing frequency was the number of APs detected over 1 minute, normalised to spikes per second (Hz). Variance was measured as the standard deviation (SD) of the whole Vm trace (a proxy for size and frequency of up and down state oscillations). Up state charge was quantified as the area under the curve (AUC) of all the points during an up state, baseline normalised to the Vm immediately preceding the up state, calculated using the trapz function in MATLAB.

Up state frequency was calculated as the number of quantified up states divided by the total recording length in seconds (Hz). The principal frequency was measured as the frequency with the highest power on a power spectral density plot, calculated using the periodgram function within MATLAB. Peak power was taken as the power at the principal frequency. Peak bandwidth power was taken as the average power within principal frequency ± 0.5 Hz.

5.3.6.2 Evoked responses to whisker stimulation

The first whisker stimulation period (the first 15 minutes) was used for analysis. Whiskers were stimulated at a 5 Hz (5 stimulations, 100 ms duration) using air puff stimulation. Recordings were included if there was at least 6 minutes worth of stimulation before the Vm depolarised above 0 mV. This was to ensure there was a possibility of comparisons of the response over time (within 5 minute time bins). Recording sweeps where a cell depolarised above 0 mV were excluded, with previous recording sweeps (1 sweep every 30 seconds) included for the cell when the Vm was below 0 mV.

The evoked responses were split into those occurring on up and those occurring on down states (calculated as an up state response if the range is >3 mV in the 50 ms preceding the stimulus, Jouhanneau et al., 2014). Evoked responses on down states are significantly different to those on up states, and so were compared separately (Gambino and Holtmaat, 2012; Gambino et al., 2014; Jouhanneau et al., 2014; Petersen et al., 2003). Stimulus responses were normalised to the Vm in the first 5 ms post stimulus (which is less than the latency of neuronal response in layer II/III to

whisker stimulation, Jouhanneau et al., 2014; Moore & Nelson, 1998). Occasionally, whisker stimulations evoked APs. In these cases, APs were quantified and then filtered out of the evoked responses at the AP threshold using the same method used for the “gap free” AP filtering.

The overall mean response on up and down states was examined over all 5 stimulations. This response was measured from stimulation onset to 200 ms post the end of the last stimulus. The SD of the total response period (which would give a proxy of the variation of the response) and AUC (total area under the curve of the points of the response period) of the responses were extracted.

The average evoked response to the first stimulus was also analysed separately, to measure specific components of the response whilst reducing the contamination of surround inhibition or excitation from other barrel field stimulation (Gambino and Holtmaat, 2012). Specifically, it has been suggested that the fast peak and slower PSP components of this response are putatively AMPAR-mediated and NMDAR-mediated respectively (Gambino et al., 2014). The peak was defined as the peak mV within 0 – 40 ms of stimulus onset (Figure 5.3). The PSP was defined as the mean mV at 50 – 100 ms post stimulus onset (Figure 5.3).

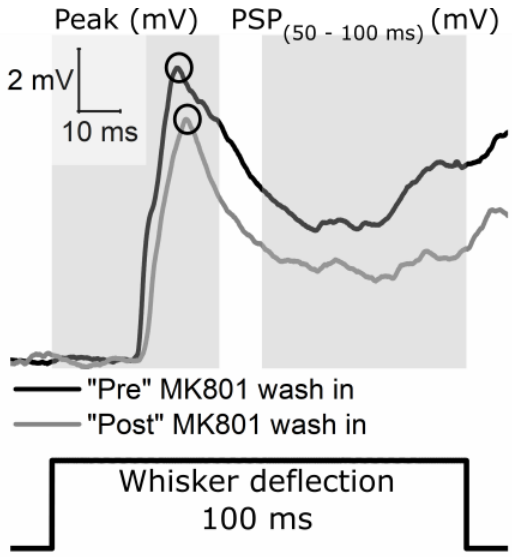

Figure 5.3 Peak and PSP quantification on evoked responses. Evoked responses from a single cell from 0-5 minutes and 5-10 minutes of recording with intracellular MK801 (NMDAR antagonist) application, defined as “pre” and “post” respectively. The peak response was calculated as the maximum response between 0 and 40 ms from stimulus onset (peaks shown in circles within the left shaded area). The PSP was the mean response between 50-100 ms from stimulus onset (within the right shaded area). There was a subtle reduction on both the peak and PSP response with MK801 application. The whisker stimulus waveform is shown below as a thick black line, and labelled whisker deflection.

SD, AUC, peak and PSP measures were also compared across all 5 stimuli to examine changes in facilitation or depression by the neuron in response to multiple stimulations. To calculate these measures, change was compared per stimulus by either normalising to the baseline prior to stimulus 1 or by normalising to the baseline prior to the stimulus that elicited each evoked response.

SD and AUC were also compared over time on down states within 5 minute bins. This was used to determine whether the recordings changed over time due to plasticity or evoked response rundown.

5.3.6.3 Cyclic modulation of up and down states

Slow cyclic modulation of up and down states was seen in recordings with changes in the amplitude of up and down states observable over time (Clement et al., 2008; Pagliardini et al., 2012, 2013; see Chapter 4 for characterisation). This was identifiable in longer continuous recordings such as during the whisker stimulation protocol. This

modulation was measured using the overall 1 Hz power z-scored over the recorded whisker stimulation period to determine cyclic activity length. For these analyses, cells were excluded if there was not a quantifiable cycle (either due to lack of large changes in 1 Hz power leading to misquantification from the analysis code or due to the recording length not being long enough to record a whole cycle).

This activity was examined during whisker stimulation to establish if the slow modulation might influence the size of evoked responses. The z-score 1 Hz power was compared to the evoked responses of the cell. All evoked responses of that neuron were split into up and down state responses, and all the evoked responses in either the up or down state were z-scored to normalise for changes in amplitude of response between cells.

5.3.7 Statistics

For this work, the effect of genotype on *in vivo* spontaneous and evoked Vm properties was measured with or without NMDAR antagonist application (MK801). Therefore, genotype (WT or TG) and MK801 treatment (Control or MK801 treated) were considered as fixed factors within statistical modelling. There may also be interactions between these two conditions, and so interaction effects were also considered (Figure 5.4).

The experimental unit was the “cell”, and sometimes more than one cell was recorded from a single animal (nested variable). Recorded cells from one animal may have a similar phenotype compared to cells from another animal (pseudoreplication). Therefore, generalised linear mixed models (GLMMs) were used to statistically model the main effects, including animal number as a random variable to account for this potential statistical bias (Figure 5.4).

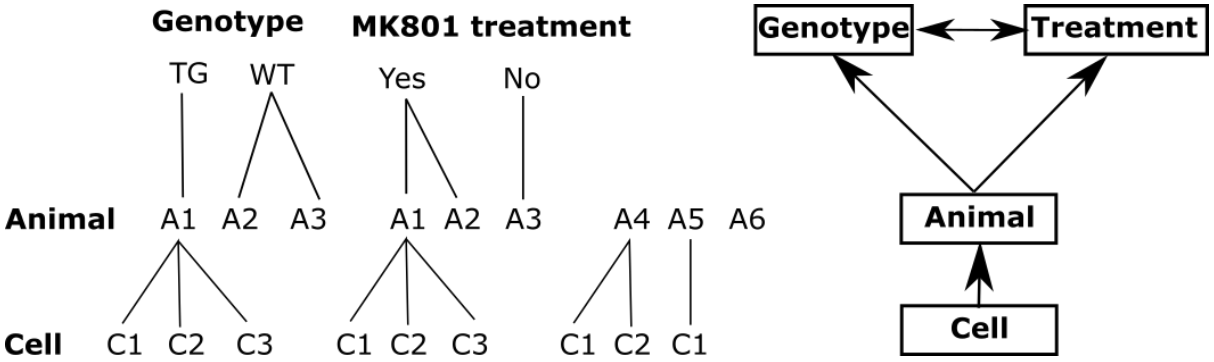

Figure 5.4 Overview of statistical effects and variable nesting. A schematic showing the two fixed effects included in analytical statistical models (genotype and treatment), and how animal number and cell number fit within that structure.

Before modelling the data, the distribution of the data was checked so this could be incorporated into the model. For example, data not normally distributed would either need a transformation (log transformed) or to be modelled using other data distributions (i.e. Poisson or Gamma distributions). Specific examples where the distribution would have been modelled as non-gaussian or transformed would include spike number (count data bound at 0, Poisson distribution), and power measures where the data underwent a log transformation.

For results with single data points (i.e. where there was one measure from the cell such as mean Vm), the GLMM had the following structure:

$$Variable \sim Genotype * MK801 + (1\backslash Animal\ Number)$$

Consistent with the formula for statistical methods used in the previous chapters, variable was the tested variable, genotype and MK801 application were the two main effects. The interaction between the two main effects was also tested, denoted by an asterisk. Animal number was modelled in as a random variable, denoted as 1\animal number.

For results with repeated measures (i.e. multiple responses to a stimulus or paired measures within the same cell), the GLMM used had the following structure:

$$Variable \sim Genotype * MK801 * Repeated\ Measure + (1\backslash Animal\ Number|Cell\ Number)$$

For repeated tests, the repeated measure was included as a main effect with its' interaction with the two other main effects. This investigated the effect the repeated measure had on the measured variable (i.e. does stimulation change the response). As the repeated measure was applied to a single cell, the cell number needed to be included to account for this. As a single cell would come from a single animal (nested variable), this was specified as 1\Animal number|Cell number, consistent with R syntax. This notation reflects the hierarchy of the variable nesting, i.e. the cell was from a single animal.

The interclass correlation coefficient (ICC) was measured to determine whether animal number had a significant effect on the data (values greater than 0.1 were included, quantified on a scale of 0 to 1). If not, animal number was dropped from the model. Values closer to 0 suggested a low effect of animal number on the measured variability, and values closer to 1 suggested a high effect. Similar statistical models were then evaluated and compared, with the model with the lowest Akaike information criterion (AIC) and best fit from assessment of the residuals for normality and heteroscedasticity chosen to model the results. Each main effect included in the GLMM was evaluated using goodness of fit chi (χ^2) squared tests to determine significance. Significant results were summarised as ($\chi^2_{(df, n)} = a$, p=b*). The χ^2 test is summarised as df (degrees of freedom), n (n number), test value (a), and the corresponding p value (b), with statistical significance denoted with asterisks when alpha <0.05. Results were sometimes also stated as an estimate of change with standard error in brackets to help signify the amount and direction of the effect. Non-significant factors were listed with a p value only. A Tukey-Kramer multiple comparison adjustment was used for *post hoc* testing whilst controlling for multiple comparisons.

The data was typically presented as box and dot plots, with a small square denoting the mean value, and the box defining ± standard error of the mean (SEM). The line across the box represents the median. Otherwise, data was also be presented as line graphs, with the mean shown as a line and the shaded area defining ± SEM.

5.4 RESULTS

5.4.1 Up and down state properties were not significantly different in TG mice, with subtle effects of NMDAR antagonism at 3 minutes post break in

Up and down state properties give a measure of local network activity in addition to intrinsic neuronal properties. Alterations in up and down states would suggest changes in network activity or changes in how the neuron could interact with the network, based on the intrinsic properties of the neuron. The up and down state properties were measured and compared from the third minute of recording following break in. The total number of animals and cells analysed for properties for mean Vm, variance, firing frequency, principal frequency and power and band power at principal frequency were: 25 WT control cells (13 animals), 17 WT MK801 treated cells (9 animals), 19 TG control cells (10 animals), 16 TG MK801 treated cells (9 animals). For the rest of the properties (where up and down states were split into further sub analysis with exclusions of cells that were not demonstrating clear up and down states), the total cell and animal numbers were: 13 WT control cells (7 animals), 11 WT MK801 treated cells (7 animals), 16 TG control cells (9 animals), 12 TG MK801 treated cells (9 animals).

The mean Vm of recorded neurons was approximately -50 mV, and was not significantly different between genotypes (p=0.74), between treatment groups (p=0.4) and there were no significant interactions between the two (p=0.77; ICC=0.11; Figure 5.5 A). This was also the case when split into up and down states, with no significant differences observed for mean down state (genotype p=0.18; MK801 p=0.93; interaction p=0.26; ICC=0; Figure 5.5 B) or up state Vm (genotype p=0.11; MK801 p=0.92; interaction p=0.3; ICC = 0; Figure 5.5 C). The difference between up and down state Vm (Δ up state:down state) was ~5 mV, and this was not significantly different between genotypes (p=0.43), between treatment groups (p=0.29) and there were no significant interactions between the two factors (p=0.26; Figure 5.5 D).

The variance of the recorded signal provided another measure of the up and down state properties. For example, increased frequency of up and down states with larger up state amplitude would increase the variability of the signal. Variance of the recorded signal (SD) was not significantly different between genotypes (p=0.41), between

treatment groups (p=0.77) and there was no significant interactions between the two (p=0.99; Figure 5.5 E).

AP firing frequency in layer II/III neurons of somatosensory cortex under anaesthesia has been reported as low in the literature, with a suggested range of 0 to 1 Hz (Petersen et al., 2003). The frequency of AP firing was also low in these recordings, with all conditions having a mean firing rate below 0.25 Hz, with many recorded cells not firing APs at all during the recordings. Firing frequency was not significantly different between genotypes (p=0.48), between treatment groups (p=0.27) and there was no significant interactions between the two (p=0.275) (Figure 5.5 F).

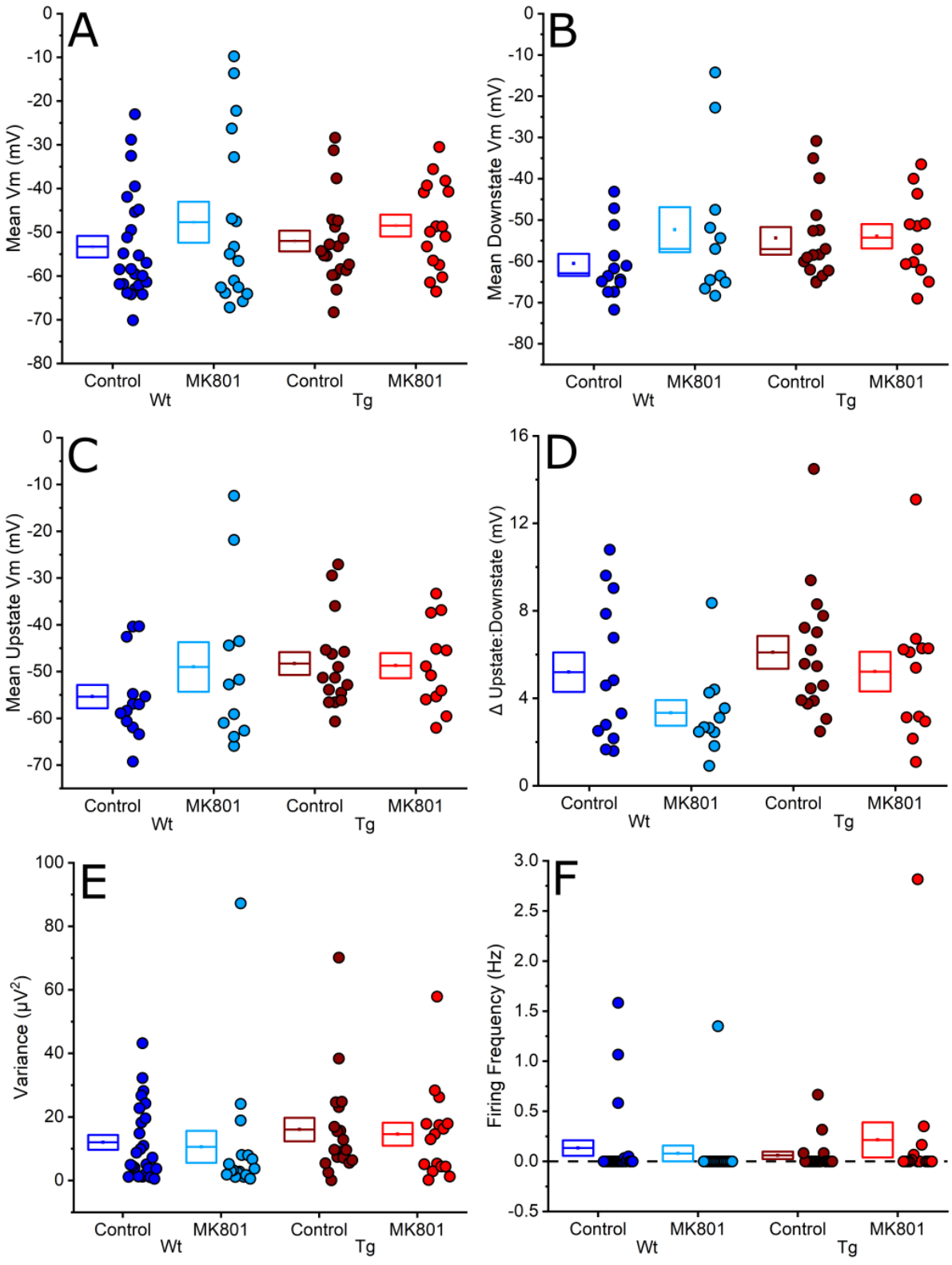

Figure 5.5 Properties related to Vm were not statistically different between genotype or with MK801 treatment. Properties based on Vm measures such as mean Vm of the whole trace (**A**) or the mean down state (**B**) or mean up state Vm (**C**) and the difference between the up state and down state Vm (Δ up state:down state) (**D**) are shown. Variance of the signal (**E**) and firing frequency (**F**) are also shown.

The amount of time spent in an up or down state may differ independently of changes in the frequency of these properties (i.e. a neuron that spends 1.25 s in up and down states equally would have a similar up state frequency as a neuron that spends 0.5 s in up states with 2 s in down states). However, mean down state dwell time was not significantly different between genotypes (p=0.82), between treatment groups (p=0.39) and there was no significant interactions between the two (p=0.5, ICC=0.12; Figure 5.6 A). Mean up state dwell time was ~1.25 s on average, and was also not significantly different between genotypes (p=0.48), between treatment groups (p=0.22) and there were no significant interactions between the two (p=0.38, ICC=0.1; Figure 5.6 B).

Mean up state charge (AUC of up states) was not significantly different between genotypes (p=0.17; Figure 5.6 C). However, there was a significant reduction of up state charge with MK801 treatment ($\chi^2_{(1, 52)}$ = 5.6, p=0.02*; ICC=0.12), even at this early time point in the recordings (3 minutes following break in). *Post hoc* statistical comparisons showed a significant reduction in up state charge in the WT cells from an average of 6244 mV.ms to 2997 mV.ms, which was not seen in the TG cells. There were no significant interactions between the genotype and treatment (p=0.76).

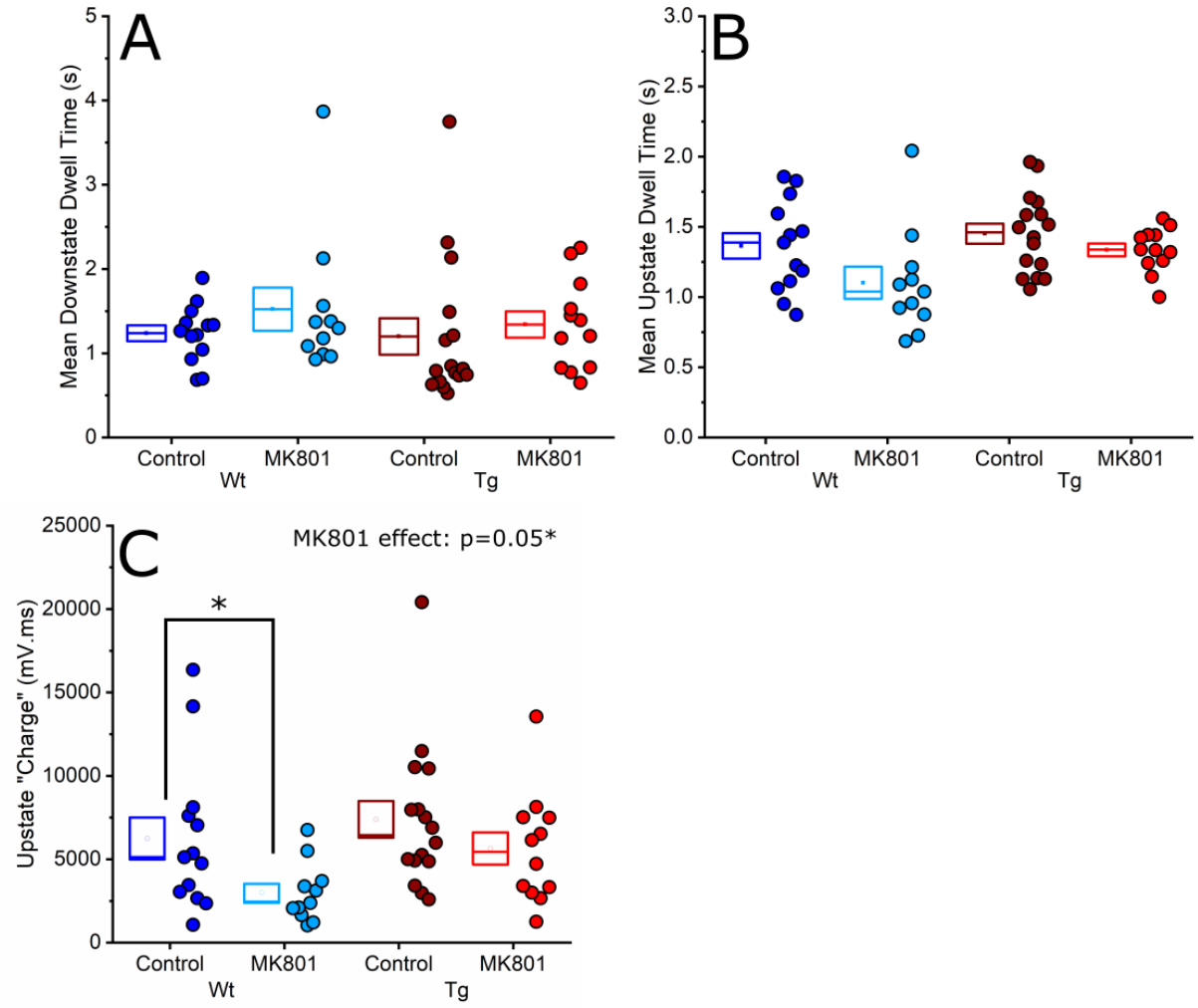

Figure 5.6 Dwell time and charge of up and down states. Dwell time of down (**A**) and up states (**B**), alongside normalised charge of up states (**C**). Statistical significant: GLMMs, main effects stated on the plot, with *post hoc* significance labelled and denoted with asterisks p<0.05*.

The principal frequency (calculated as the frequency peak on a power spectral density plot) and mean up state frequency (calculated as the number of quantified up states normalised to time) were similar, with the mean principal frequency being approximately 0.5 Hz compared to 0.4 Hz for up state frequency. This would suggest the main oscillation observed in the network was the slow wave up and down state oscillation, that oscillates between the up and down states at a frequency of between 0.4 - 0.5 Hz. Principal frequency was not significantly different between genotypes ($p=0.92$), between treatment groups ($p=0.14$) and there was no significant interactions between the two ($p=0.23$, ICC=0.18; Figure 5.7 C). Mean up state frequency was also not significantly different between genotypes ($p=0.78$), between treatment groups ($p=0.31$), and there were no significant interactions between the two ($p=0.71$, ICC=0.67; Figure 5.7 D).

Peak power (the power at the principal frequency) was not significantly different between genotypes ($p=0.35$), between treatment groups ($p=0.13$) and there was no significant interactions between the two ($p=0.8$, ICC=0.08; Figure 5.7 E). Peak band power within a 1 Hz frequency band at the principal frequency was also not significantly different between genotypes ($p=0.42$), between treatment groups ($p=0.22$) and there was no significant interactions between the two ($p=0.86$, ICC=0.1; Figure 5.7 F).

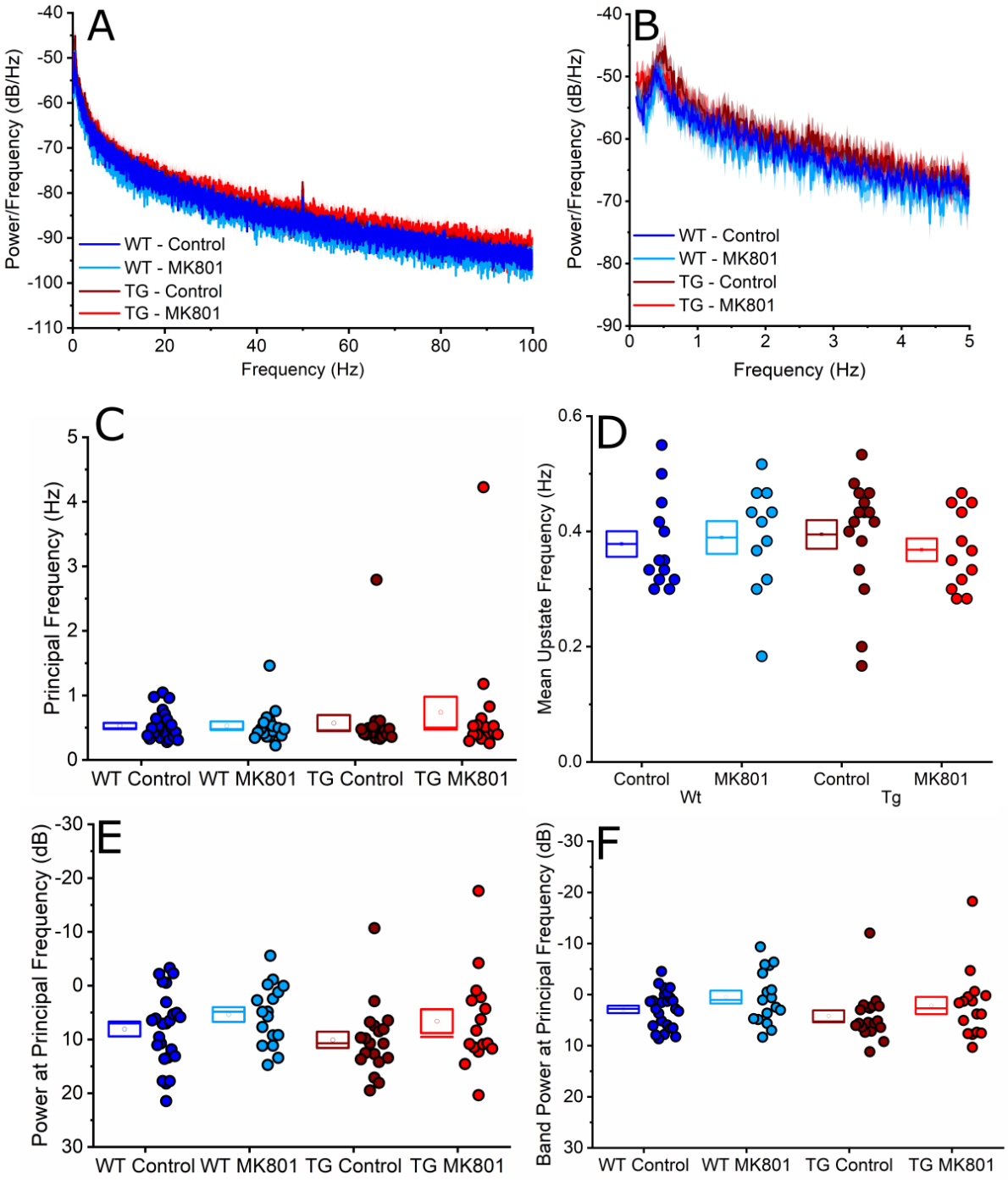

Figure 5.7 Vm spectral frequency and power properties during up and down states. A power spectral density plot of the first minute of "gap free" recording for 0-100 Hz (**A**) and 0 – 5 Hz (**B**) is shown. The line represents the mean, and shading represents the SEM. The principal spectral frequency (i.e. the peak of the power spectral density plot) (**C**) and the manual calculated frequency based on number of up states divided by length of recording time (**D**) are shown as box and dot plots. The power at the principal frequency (**E**) and the power within a 1 Hz band at that frequency (**F**) are also shown.

5.4.2 Comparisons of up and down state properties between early and late periods during experimental recordings suggests increased MK801 efficacy and decreasing recording quality

Paired comparisons of up and down state properties were made between the 3rd and 23rd minute of recordings to determine whether measures changed with recording length or with MK801 treatment. MK801 is a use dependent NMDAR antagonist, so whilst effects were observed from minute 3, it is possible that further alterations could be observed across longer recording epochs with further neuronal activity. Other work suggests an effect of MK801 treatment after at least 5 minutes (Gambino et al., 2014; Lavzin et al., 2012; Smith et al., 2013).

For this analysis, cells were only included in the analysis if there was a measure for the early (3 minutes) and late (23 minutes) time point. The total cells and animals compared were: 13 WT control cells (9 animals), 10 WT MK801 treated cells (7 animals), 11 TG control cells (7 animals), 9 TG MK801 treated cells (7 animals).

Mean Vm was significantly depolarised later in the recording session (depolarised by 11.39 mV (4.01), $\chi^2_{(1, 83)} = 8.1$, p <0.005***) and this was not specific to genotype (p=0.16) or treatment (p=0.76; Figure 5.8 A). Mean down state Vm was significantly depolarised later in the recording session (11.72 (4.74), $\chi^2_{(1, 56)} = 6.1$, p=0.01**) and this was not specific to genotype (p=0.27) or treatment (p=0.90; Figure 5.8 B). Mean up state Vm was also significantly depolarised later in the recording session (12.279 (4.13), $\chi^2_{(1, 56)} = 8.8$, p <0.005***) and this was not specific to genotype (p=0.16) or treatment (p=0.99; Figure 5.8 C). This suggests that there was a general (~10-20 mV) depolarisation of Vm over time during the recording that did not affect the size or shape of up and down states. Δ up state:down state was not affected by recording session as a main effect (p=0.51). However, there was a significant three-way interaction between genotype, treatment and recording session (p=0.05*; Figure 5.8 D).

Firing frequency was not significantly different with recording time as a main effect (p=0.43; Figure 5.8 E). Mean variance was not affected by recording time as a main effect (p=0.58). However, there was a significant two-way interaction of MK801 treatment with recording time ($\chi^2_{(1, 83)} = 11.4$, p<0.005***) and three-way interaction between genotype, treatment and recording time ($\chi^2_{(1, 83)} = 16.8$, p<0.005***; Figure 5.8 F), suggesting that MK801 treatment had a progressive effect over recording time.

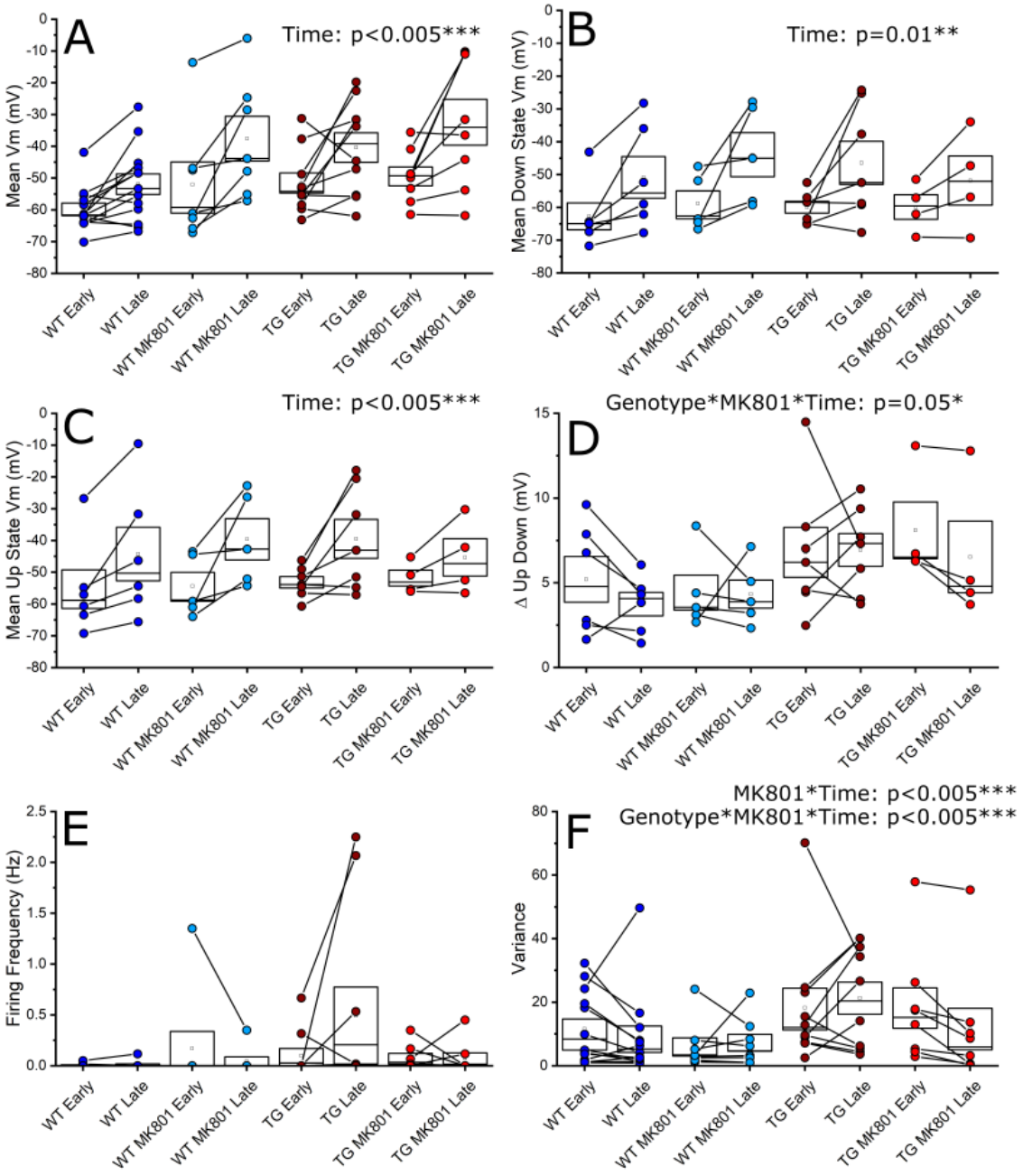

Figure 5.8 Repeated measures of up and down state properties over time. Properties measured from the same cell (paired) early (3 minutes) or late (23 minutes) during ”gap free” recordings. Properties based on Vm, either mean Vm of the whole trace (**A**) or the mean down state (**B**) or mean up state Vm (**C**) and the difference between the up state and down state Vm (Δ up state:down state) (**D**) is shown. Firing frequency (**E**) and variance of the signal (F) are also shown. Circles represent a data point from one cell, and a line joining the same cell together. Statistical significance: GLMM, main effects stated on model, asterisks denote significance, p<0.05*, p<0.01**, p<0.005***.

Mean up state or down state dwell time was not affected by recording duration (p=0.2 and p=0.56 respectively). Mean up state charge was not significantly different when looking at individual factors (genotype, p=0.47; MK801, p=0.5; recording time, p=0.77; Figure 5.9 C). However, there was a significant interaction between genotype and recording session ($\chi^2_{(1, 56)}$ = 5.4, p=0.02*). Overall, this would suggest that whilst the frequency of up and down states did not change, the charge of up states was larger in the TGs than the WTs.

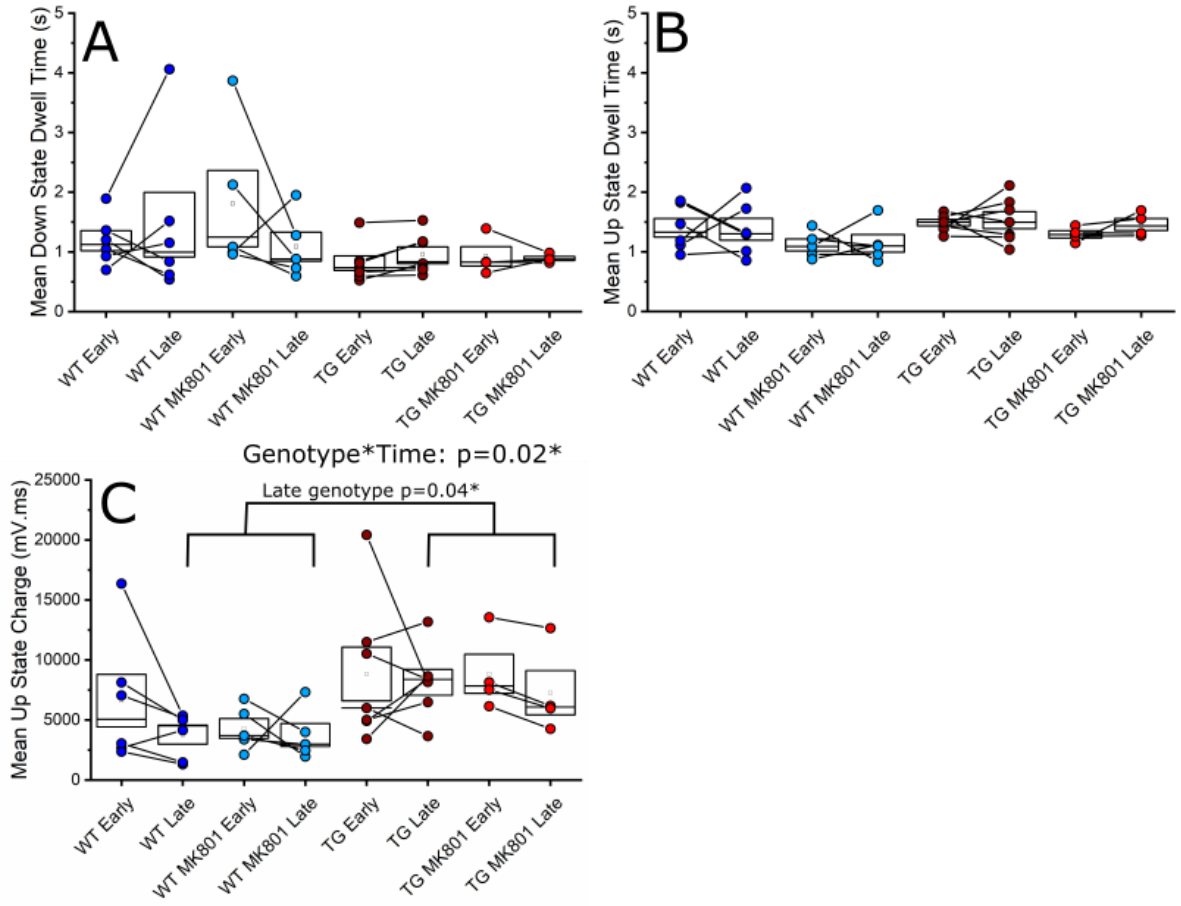

Figure 5.9 Repeated measures of up and down state dwell time and charge over time. Properties measured from the same cell (paired) early (3 minutes) or late (23 minutes) during "gap free" recording. Dwell time of down (**A**) and up states (**B**), alongside normalised charge of up states (**C**) is shown as box and dot plots with joined dots. There was a significant increase of up state charge at the late time point between genotypes as indicated on the figure. Circles represent a data point from one cell, and a line joins the same cell together. Statistical significance: GLMM, main effects stated on model, lines indicate *post hoc* significance with asterisks denoting significance, p<0.05*, p<0.01**, p<0.005***.

Mean up state frequency was not affected by recording time as a main effect (p=0.11; Figure 5.10 A). Principal frequency was not affected by recording time as a main effect (p=0.76; Figure 5.10 B). Principal frequency power was not significantly different with recording time as a main effect (p=0.7; Figure 5.10 C). Principal frequency band power was not significantly different with recording time as a main effect (p=0.41; Figure 5.10 D). There was a significant two-way interaction with MK801 treatment and recording time ($\chi^2_{(1, 82)}$ =9.66, p<0.005***) and a significant three-way interaction between genotype, treatment and recording time ($\chi^2_{(1, 82)}$ =6.1, p=0.01**). Specifically, band power was shown to be significantly lowered in the TG MK801 group between early and late conditions.

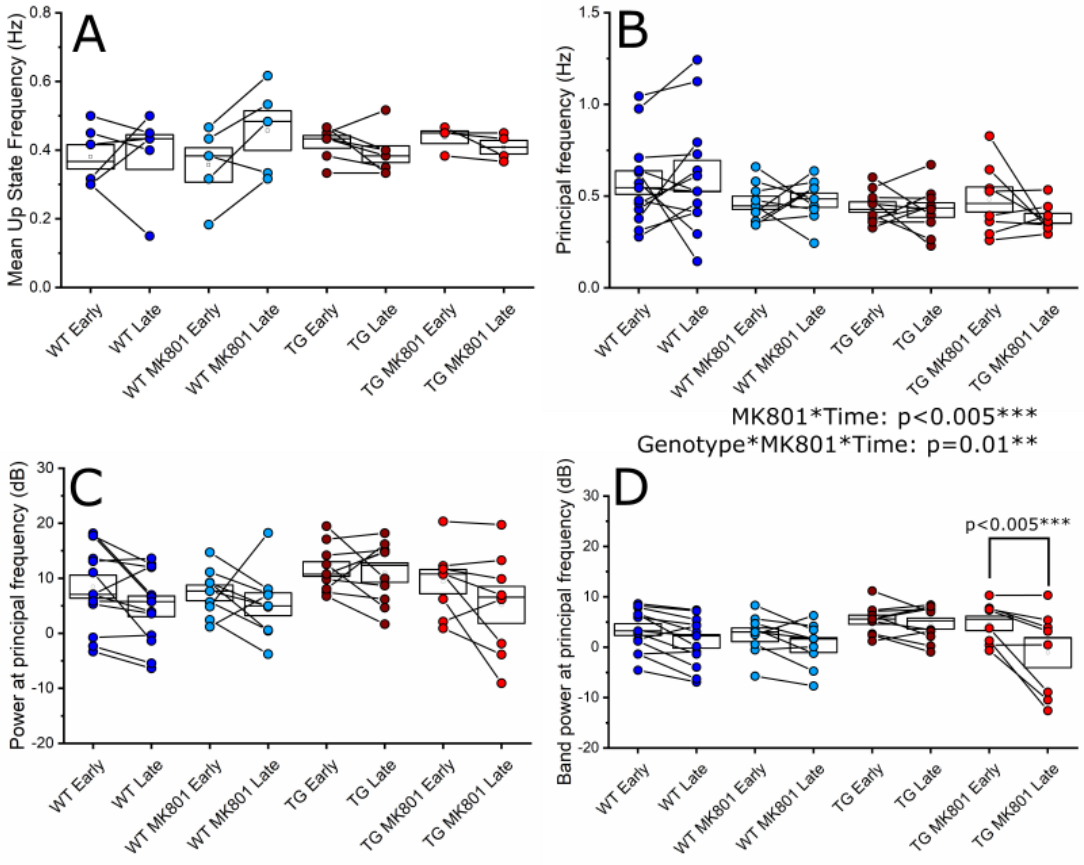

Figure 5.10 Repeated measures over time of frequency and power properties. Properties measured from the same cell (paired) early (3 minutes) or late (23 minutes) in "gap free". The manual calculated frequency based on number of up states divided by length of recording time (**A**) and the principal oscillating frequency (i.e. the peak frequency of the power spectral density plot) (**B**) with the power at the principal frequency (**C**) and the power within a 1 Hz band at that frequency (**D**) are shown. Circles represent a data point from one cell, and a line joins the same cell together. Statistical significance: GLMM, main effects stated on model, lines indicate *post hoc* significance with asterisks denoting significance, p<0.05*, p<0.01**, p<0.005***.

5.4.3 The overall evoked response to whisker stimulation was not significantly different with genotype or NMDAR antagonism

Evoked responses were measured by delivering a 5 Hz whisker stimulation (5 stimuli; 100 ms duration) to drive cellular responses in the somatosensory cortex. The total number of cells included in analyses of evoked responses, unless stated otherwise, was: WT control 19 cells (12 animals); WT MK801 treated 14 cells (8 animals); TG control 15 cells (10 animals); TG MK801 treated 14 cells (9 animals). Whisker stimulation generally caused a depolarisation, often clearly associated with each separate stimulation but responses also summated with subsequent stimuli. This response was also different when evoked on up or down states (see Chapter 4 for response characterisation). The response itself was a multi-component response, which can be split into fast and slow mediated components, which are thought to be AMPAR- and NMDAR- mediated respectively.

This evoked response for each cell was compared in several ways. Firstly, the overall evoked response envelope and shape was compared in response to the 5Hz stimulation. To do this, SD and AUC were compared as a measure of changes in the shape of the response, with this analysis performed on the average response from each cell. This was compared between treatment and genotype, split into responses that were evoked on an up or down state. The individual mean responses from each neuron and the mean response per condition are shown in Figure 5.11 and Figure 5.12 respectively.

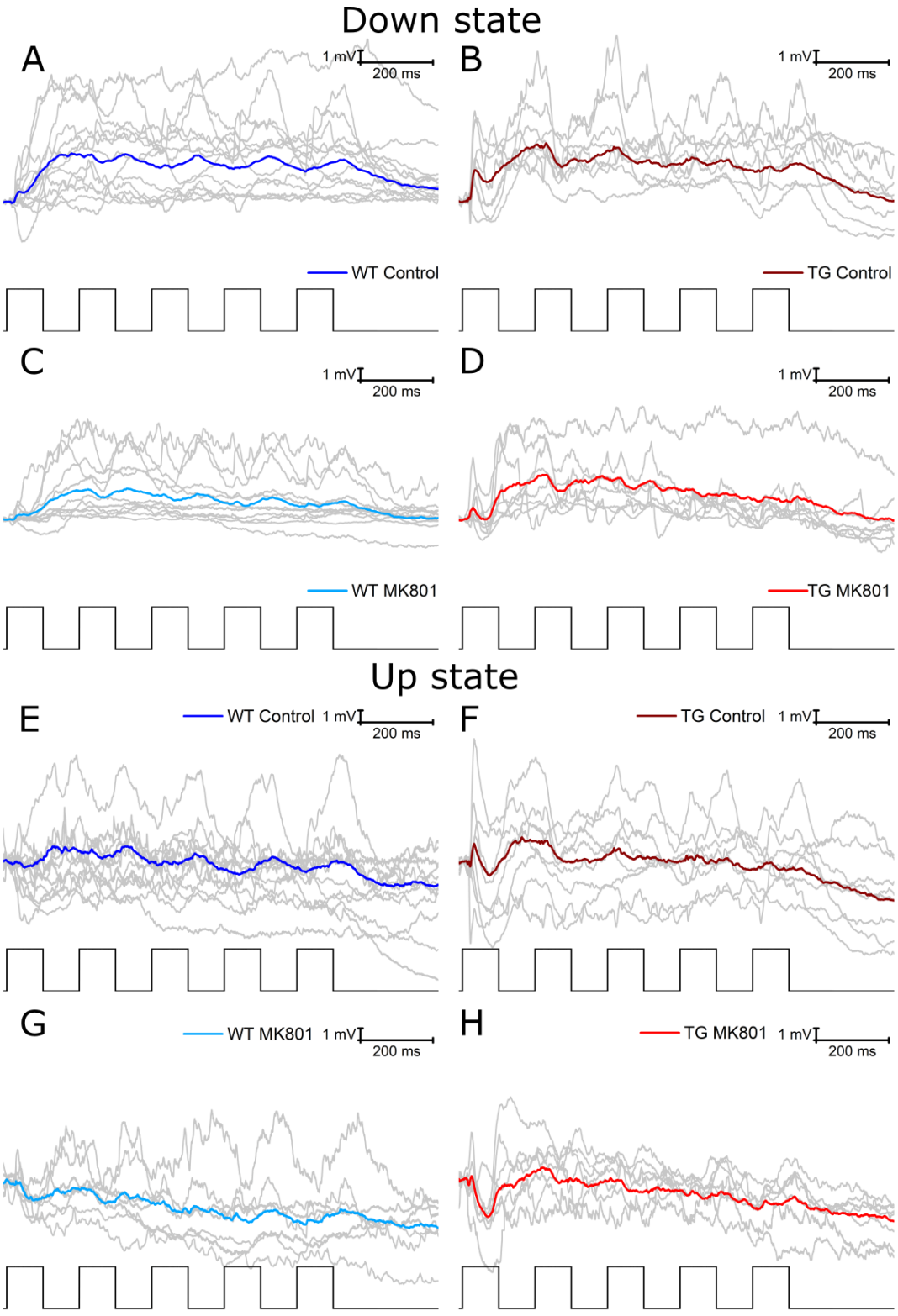

Figure 5.11 Individual evoked responses to whisker stimulation in up and down states. Line graphs showing the mean response in colour to whisker stimulation across all measured conditions evoked on down states (**A-D**) and up states (**E-H**). Mean evoked responses from individual cells are shown in grey. The stimulus waveform is shown beneath each trace in black, with upward square pulses denoting the application of airpuff stimulation.

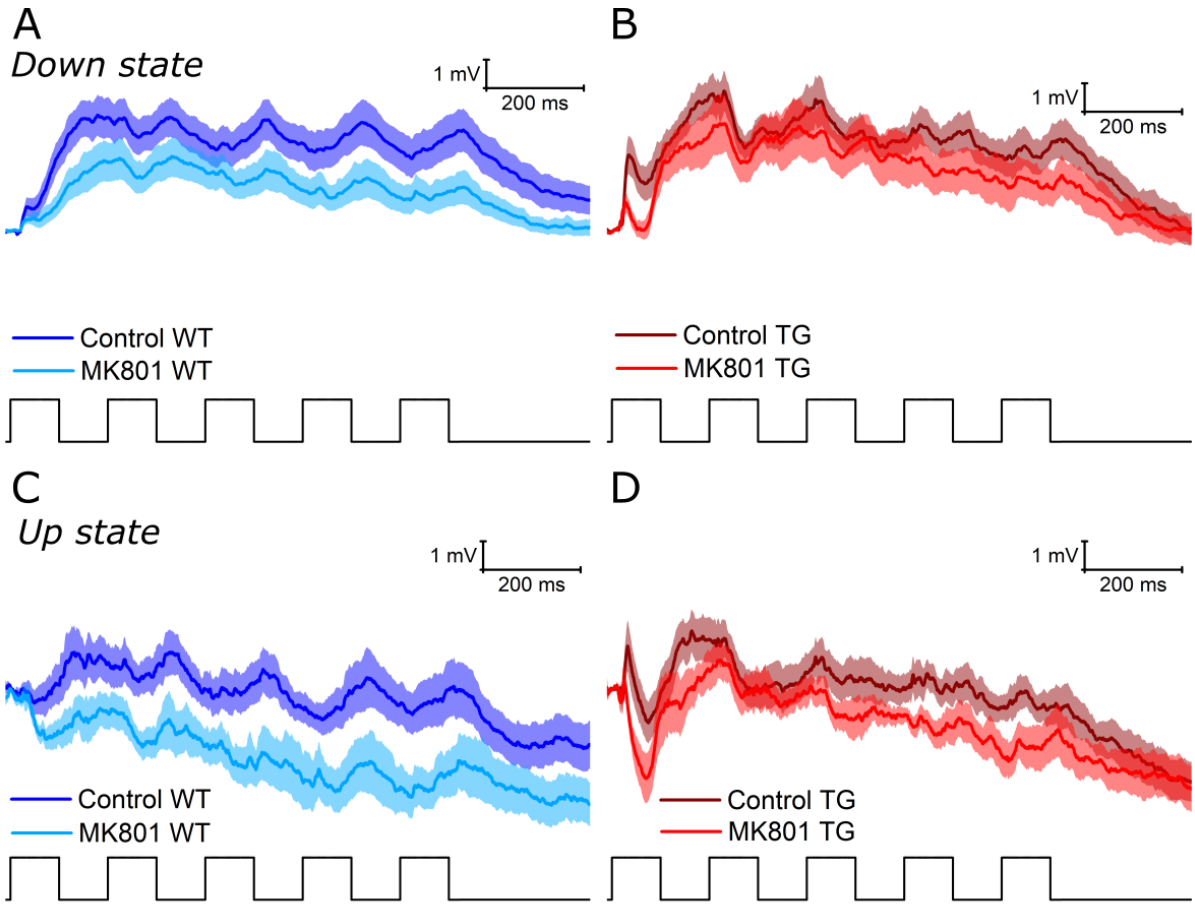

Figure 5.12 The total mean response to whisker stimulation evoked on an up or down states. Evoked neuronal responses to whisker stimulation during a down state (**A** & **B**) and in an up state (**C** & **D**) in WT (**A** & **C**) and TG (**B** & **D**) mice as line plots. Lines are the mean response across all cells within that condition, the shaded area represents SEM. The stimulus waveform is shown beneath each trace in black, with upward square pulses denoting the application of airpuff stimulation.

The overall response evoked on down states by 5 Hz whisker stimulation produced an envelope of depolarisation by the cell, as shown by an AUC greater than 0 (Figure 5.12 A & B, Figure 5.13 A). The AUC was not statistically different between genotypes (p=0.85, ICC=0.32; Figure 5.13 A). NMDAR inhibition by application of MK801 also did not have a significant effect on this evoked response (p=0.29), and there was no interaction between MK801 treatment and genotype (p=0.37). In a similar manner, the SD of the total response was a proxy of the shape of this response, examining whether repeated stimulation led to a more variable evoked response. However, the SD was not significantly different between genotypes (p=0.39) or with MK801 treatment (p=0.31, ICC=0.13; Figure 5.13 B).

The average responses evoked on up states were more hyperpolarised when compared to those on down states (Figure 5.12 C & D). This is reflected by the AUC, which shows the majority of evoked responses had AUC values of less than 0. The AUC of the total response on up states was not significantly different between genotypes (p=0.98) or with MK801 treatment (p=0.24) (Figure 5.13 C). There was also no significant interaction between the two factors (p=0.35). The SD of the response was similar to down states evoked responses ~ around 1.5 μV^2. For the up state average responses, the SD was not significantly different between genotypes (p=0.17) or with MK801 treatment (p=0.1; Figure 5.13 D). There was also no significant interaction between the two factors (p=0.88).

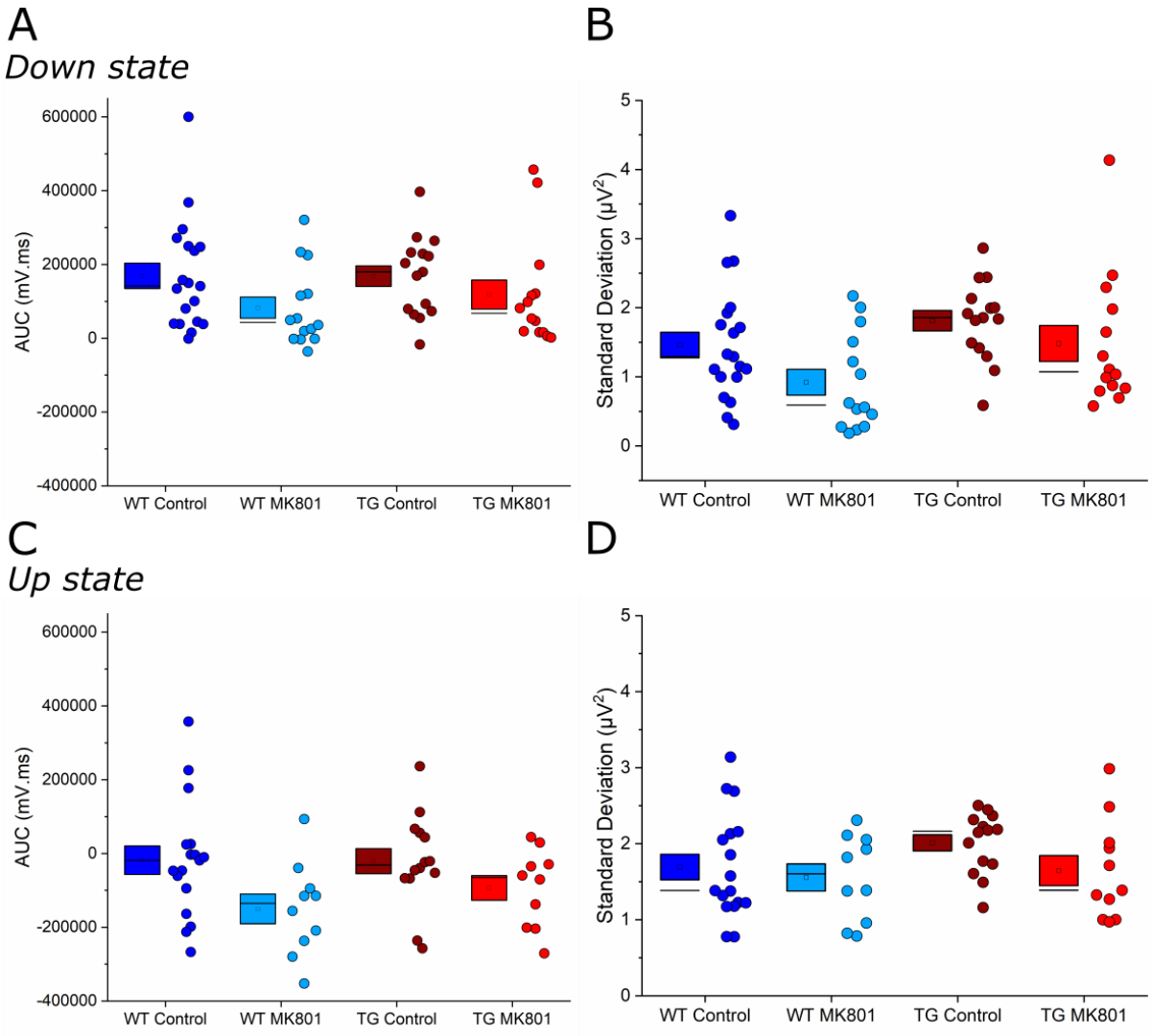

Figure 5.13 SD and AUC of the average response to whisker stimulation when evoked on down or up states. The AUC (the sum of the trace) is shown for responses evoked on down (**A**) and up (**C**) states as box and dot plots. The SD (variance) of the total response is also shown when evoked on down (**B**) or up (**D**) states.

5.4.4 The peak amplitude of the average evoked response to the first stimulus of the stimulus train was increased in TG mice

The first evoked response of the stimulus train was also analysed separately as this response should not be affected by concurrent inhibition/excitation from surrounding barrel fields, along with summation of on and off responses of the cell (Brumberg et al., 1996; Shimegi et al., 1999; Simons, 1983). The peak and PSP components were measured as a proxy for measures of likely AMPAR- and NMDAR- mediated activity (Gambino et al., 2014).

The peak evoked response amplitude on down states was significantly higher in the TG mice compared to WTs (Genotype effect 0.99(0.33), $\chi^2_{(1, 62)}$ = 10.7, p<0.005***; ICC=0.11; Figure 5.14 E). Surprisingly, MK801 treatment also had a significant effect on peak response amplitude, reducing response amplitude (MK801 effect -0.79(0.25), $\chi^2_{(1, 62)}$ = 10.4, p<0.005***). There was no significant interaction between the two factors (p=0.91). Down state PSP responses were not significantly different between genotypes (Figure 5.14 G). As expected, MK801 treatment significantly lowered PSP responses (MK801 effect -1.29(0.66), $\chi^2_{(1, 62)}$ = 3.8, p=0.05*). There was not a significant interaction between the two factors (p=0.82).

The responses of the neuron showed similar changes in up states to those in down states. The peak response amplitude on up states was significantly higher in the TG mice compared to WTs (Genotype effect 0.96(0.42), $\chi^2_{(1, 53)}$ = 5.2, p=0.02*, ICC=0.23; Figure 5.14 F). MK801 treatment also had a significant effect on peak response amplitude, reducing response amplitude (MK801 effect -0.94(0.44), $\chi^2_{(1, 53)}$ = 4.7, p=0.03*). There was no significant interaction between the two factors (p=0.25). The PSP response on up states was not significantly different between genotypes (p=0.53) or with MK801 treatment (p=0.08; Figure 5.14 H). There was also no significant interaction between the two factors (p=0.79).

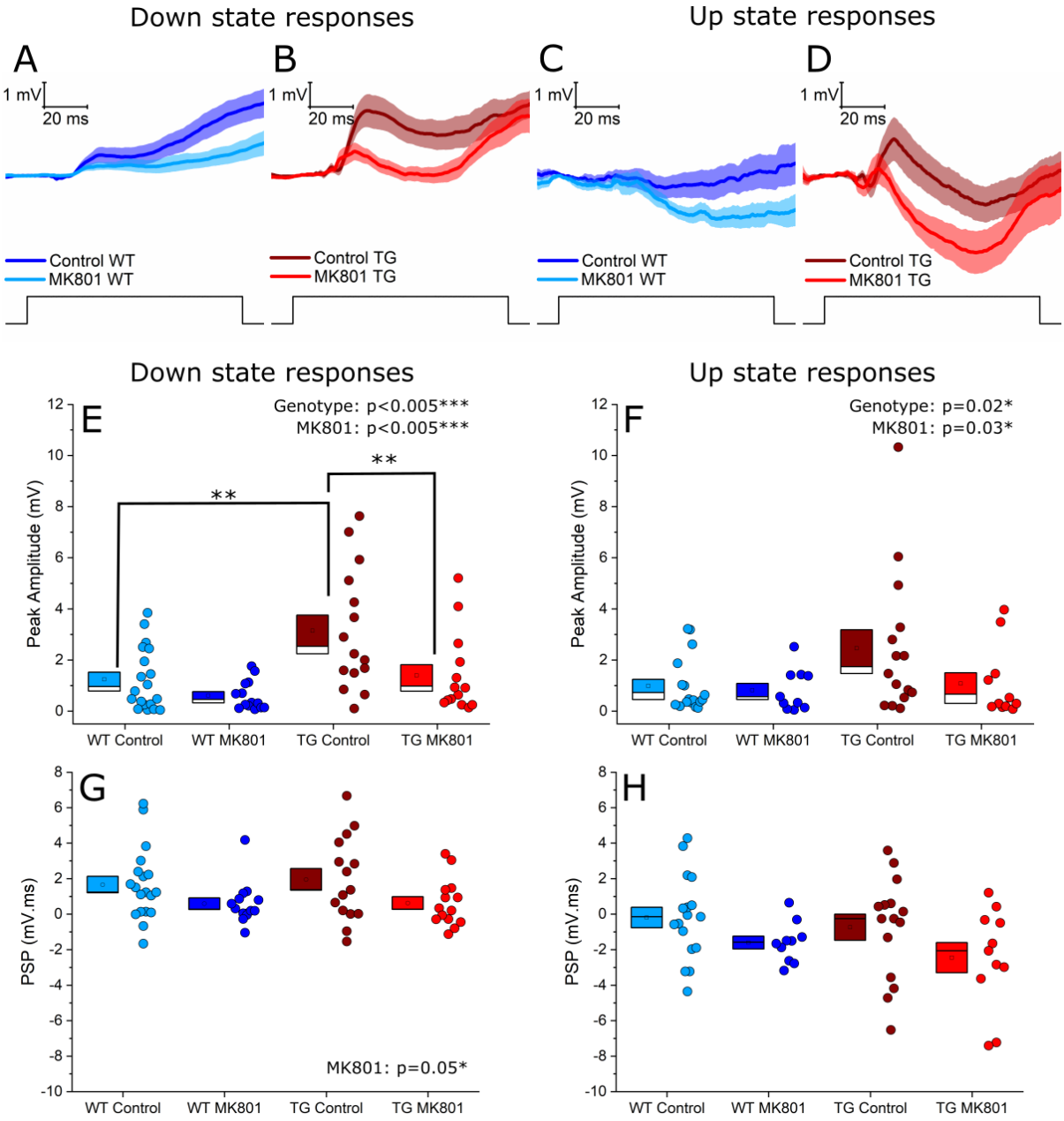

Figure 5.14 Increased peak amplitude on the first stimulus response evoked on up or down states in rTg4510 mice, which was decreased with MK801 application. Mean traces (line) of the first evoked response evoked on up or down states in WT (**A** & **C**) and TG mice (**B** & **D**) with control conditions and MK801 treated recordings overlaid. The shaded area denotes SEM. Box and dot plots of the peak amplitude (**E** & **F**) and mean PSP (**G** & **H**) on down (**E** & **G**) and up states (**F** & **H**) are shown below. *Post hoc* significance is denoted with asterisks (p<0.01 **) with significant effects and interactions listed on the figure calculated from a GLMM with Tukey-Kramer multiple comparisons.

5.4.5 The responses evoked on down states to all five stimuli revealed altered peak and PSP responses with MK801 treatment, with an increased peak response in TG cells

Peak, PSP and AUC of the evoked response to the stimulus train was also analysed per each stimulus (counted as 200 ms per stimulus from stimulus onset, the whisker stimulation was 100 ms long with a 100 ms interstimulus interval). These measures were considered as changes across the overall response per stimulus (normalised to the baseline prior to stimulus 1), and also normalised to the baseline just prior to the individual stimulus to get measures of change as a result of that stimulation specifically.

When responses were normalised to the baseline for stimulus 1, there was no significant effect of genotype (p=0.83) or MK801 treatment (p=0.55) on the AUC when evoked from down states (Figure 5.15 A i & ii). The same was true for the response AUC when normalised to the baseline per stimulus (genotype p=0.44; MK801 p=0.17; Figure 5.15 A iii & vi). Stimulation on down states evoked significantly larger AUC responses compared to stimulus 1 when normalised to the baseline at the start of the stimulation 1 (Stimulation effect $\chi^2_{(4, 310)}$ = 66.1, p<0.005***; Stimulus 2-5 p<0.005***; ICC = 0.74). When baseline normalised per stimulus, stimulation also had a significant effect on evoked AUC responses ($\chi^2_{(4, 310)}$ = 26.8, p<0.005***), with stimulation on down states evoking significantly smaller AUC responses to stimulus 4 and 5 than to stimulus 1 – 3 (Stimulus 4 -9147(3723), p=0.02*; Stimulus 5 -12665(3723), p<0.005***, ICC = 0.1). This would suggest that response size decreases with repeated stimulation at 5 Hz stimulation frequencies. Taken together with the normalised data, this suggests that the first two responses significantly increase in normalised size and then the response plateaus.

For peak amplitude, there was no significant effect of genotype (p=0.08) or MK801 treatment (p=0.07) on peak amplitude response when normalised to stimulation 1 baseline (Figure 5.15 B i & ii). There was also no significant effect of overall stimulation (p=0.31). However, the peak amplitude response to stimulation 2 was significantly larger than stimulus 1 (1.06(0.55), p=0.05*). There was also a significant two-way interaction between stimulation number and genotype ($\chi^2_{(4, 310)}$ = 11.9, p=0.02; stimulation 2, p=0.01**; stimulation 3, p<0.005***; stimulation 4, p<0.005***;

stimulation 5, p<0.005***). There was a significant effect of genotype ($\chi^2_{(1, 310)}$ = 9.2, p<0.005***) and MK801 treatment ($\chi^2_{(1, 310)}$ = 6.8, p=0.009**) on the peak amplitude of evoked responses when normalised to the start of each stimulation (Figure 5.15 A iii & iv). Stimulus also had a significant effect on peak amplitude ($\chi^2_{(4, 310)}$ = 67.7, p<0.005***), with peak amplitude being significantly lower on subsequent stimulations following stimulation 1 (Stimulus 2 0.41(0.09), p<0.005***; Stimulus 3 1.5(0.6), p=0.01**; Stimulus 4 1.2(0.41), p<0.005***; Stimulus 5 1.2(0.39), p<0.005***). There was also a two-way interaction between genotype and stimulus ($\chi^2_{(4, 310)}$ = 11.9, p=0.02*). Overall, the peak amplitude of the response appears was larger in the TG cells, and lower with MK801 treatment. Peak amplitude also reduces over subsequent stimulations, suggesting the peak response depresses to stimulation at 5 Hz frequencies.

For PSP responses normalised to the start of stimulation 1, there was no significant effect of genotype (p=0.8) or MK801 treatment (p=0.15) (Figure 5.15 C i & ii). There was a significant effect of stimulation on PSP response ($\chi^2_{(4, 310)}$ = 29.4, p<0.005***), with stimulations 2-4 evoking significantly larger PSP responses compared to stimulation 1 (stimulation 2, p<0.005***; stimulation 3, p<0.005***, stimulation 4, p=0.02*). PSP responses normalised per stimulation to the stimulation baseline, show no significant effects of genotype (p=0.6), but a significant effect of MK801 treatment ($\chi^2_{(1, 310)}$ = 5.1, p=0.02*) (Figure 5.15 C iii & vi). There was a significant effect of stimulation number on PSP responses ($\chi^2_{(4, 310)}$ = 35.4, p<0.005***), with a significant reduction in PSP stimulation 3 – 5 compared to stimulation 1 and 2 (stimulation 3 -1.6(0.6), p<0.005***; stimulation 4 -2.3(0.6), p<0.005***; stimulation 5 -2.5(0.6), p<0.005***). Altogether, the evoked PSPs were larger compared to the first response which then plateaus. This response was not different between genotypes, but there was an effect of MK801 treatment on the responses normalised per stimulus baseline.

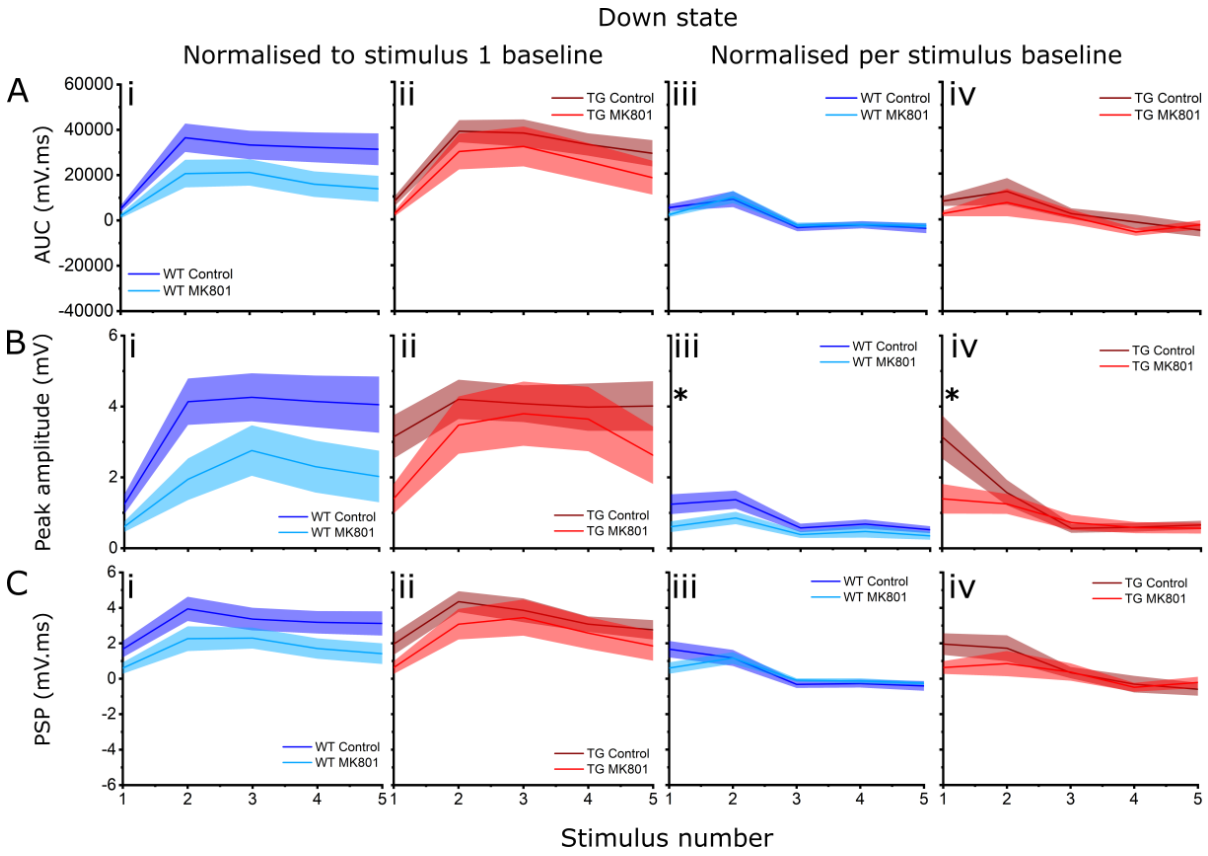

Figure 5.15 Measures from responses evoked on down states to all five stimuli. The mean average AUC (**A**), peak amplitude (**B**) and PSP (**C**) responses represented as a line with shaded SEM. Responses were either baseline normalised to stimulus 1 (**i** - **ii**) or per stimulus (**iii** – **vi**) for down state evoked responses. Statistical significance: GLMM, main effects stated in text, *post hoc* significance was denoted with asterisks, p<0.05*, across genotypes for that stimulus.

5.4.6 The responses evoked on up states to all five stimuli revealed altered peak and PSP responses with MK801 treatment, with an increased peak response in TG cells similar to responses evoked in down states

There was no significant effect of genotype (p=0.99) or MK801 (p=0.45) on up state AUC responses normalised to the start of stimulation 1 (Figure 5.16 A i & ii). Stimulation also significantly increased the up AUC response ($\chi^2_{(4, 265)}$ = 11.8, p=0.02*). There was no significant effect of genotype (p=0.98) or MK801 treatment (p=0.16) on evoked AUC responses on up states normalised per stimulation (Figure 5.16 A iii & vi). Stimulations significantly increased the evoked AUC response ($\chi^2_{(4, 265)}$ = 14.8, p<0.005***). Overall, the evoked AUC on up states was not affected by genotype or MK801 treatment. The response pattern suggests facilitation on stimulation 2, with a return to starting levels afterwards.

There was no significant effect of genotype (p=0.16) or MK801 treatment (p=0.24) on up state stimulation peak amplitude normalised to the baseline at the start of stimulus 1 (Figure 5.16 B i & ii). There was a significant effect of stimulation on the evoked responses ($\chi^2_{(4, 265)}$ = 11.2, p=0.02*), with stimulus 3-5 being significantly lower than stimulus 1 (stimulus 3, p=0.01**; stimulus 4, p =0.02*; stimulus 5, p=0.006**). There was also a significant two-way interaction between genotype and stimulus number ($\chi^2_{(4, 265)}$ = 9.6, p=0.05*;). There was also a significant three-way interaction between genotype, MK801 treatment and stimulus number ($\chi^2_{(4, 265)}$ = 9.6, p=0.05*). There was a significant effect of genotype ($\chi^2_{(1, 265)}$ = 11.7, p<0.005***) and MK801 ($\chi^2_{(1, 265)}$ = 8.5, p<0.005***) on the peak amplitude across all five stimulations evoked on up states when normalised to the baseline of the specific stimulus (Figure 5.16 B iii & vi). From this, this suggests TG responses were significantly higher compared to WT responses and the amplitude was reduced with MK801 treatment. There was a significant effect of stimulations changing the evoked response ($\chi^2_{(4, 265)}$ = 32.6, p<0.005***) with a significant reduction in amplitude of the response from stimulus 3 – 5 compared to stimulus 1 (stimulus 3, p<0.005***; stimulus 4, p<0.005***; stimulus 5, p<0.005***). There were also significant two-way interactions between genotype and stimulus number ($\chi^2_{(4, 265)}$ = 15.8, p<0.005***), and MK801 treatment and stimulus numbers ($\chi^2_{(4, 265)}$ = 9.3, p=0.05). Overall, this would suggest the peak component of evoked

responses is altered with genotype and MK801 treatment, and this response also changes over stimulations.

There was no significant effect of genotype (p=0.54) or MK801 treatment (p=0.08) on evoked up state PSP responses normalised to the baseline prior the first stimulus (Figure 5.16 C i & ii). There was a significant effect of stimulations on the evoked PSP response ($\chi^2_{(4, 265)} = 25.2$, p<0.005***). There was no significant effect of genotype on PSP responses evoked on up states, normalised to the start of each stimulation (Figure 5.16 C iii & vi). However, there was a significant effect of MK801 treatment ($\chi^2_{(1, 265)} = 5.4$, p=0.02*) and a significant effect of stimulations on the evoked PSP responses ($\chi^2_{(4, 265)} = 18.2$, p<0.005***). Overall, stimulation changes the PSP response, and MK801 appears to have a subtle effect on reducing PSP response size on up states.

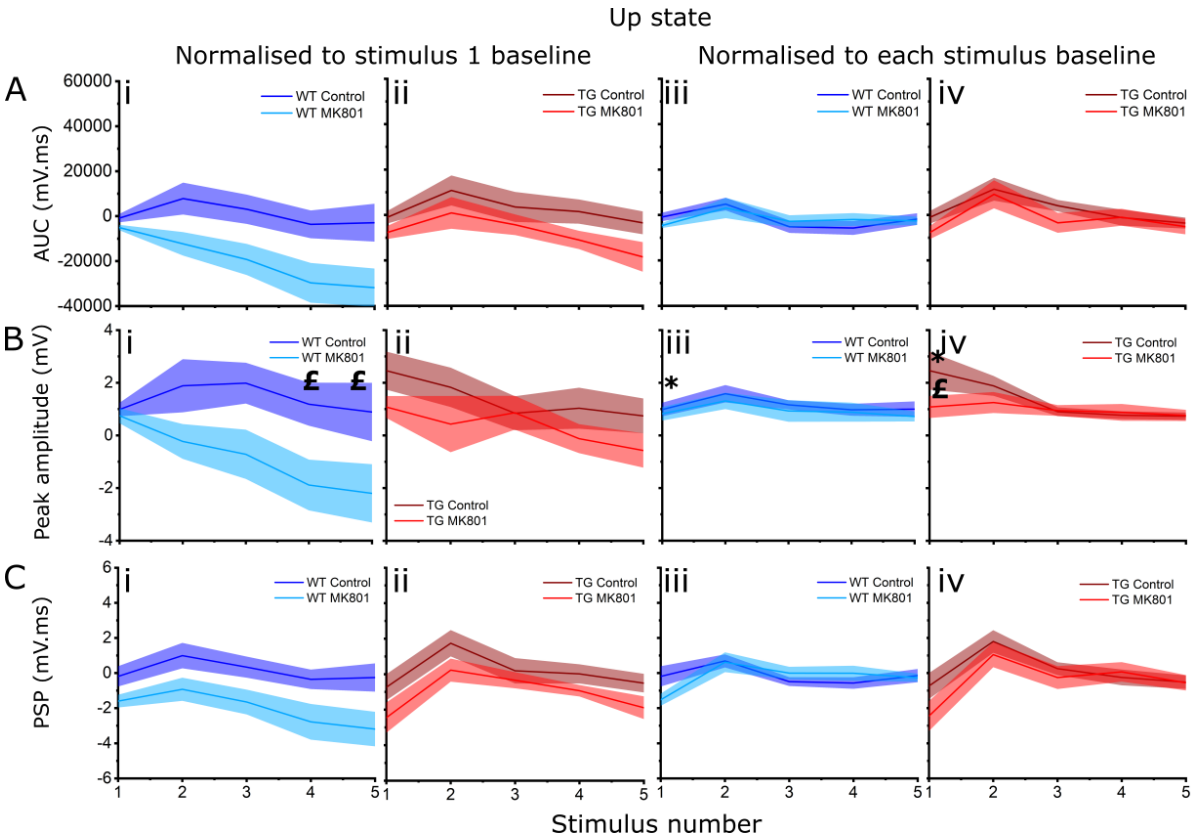

Figure 5.16 Measures from responses evoked on up states to all five stimuli. The mean average AUC (**A**), peak amplitude (**B**) and PSP (**C**) responses with shaded SEM. Responses were either baseline normalised to stimulus 1 (**i** - **ii**) or per stimulus (**iii** – **vi**) for up state evoked responses. Statistical significance: GLMM, main effects stated within the main text, symbols denoted *post hoc* significance: p<0.05 * between genotype control condition for that stimulus; p<0.05 £ within genotype between MK801 treatment condition.

5.4.7 The AUC of average evoked responses to whisker stimulation over time lowers with MK801 treatment after 10-15 minutes

The analyses described above were performed on the mean response across the whole stimulation period. As there was a possibility that changes may occur over time when stimulating, either due to MK801 use dependent antagonism or by plasticity induced changes, the responses were also compared over time. This specific analysis compared SD and AUC of the overall response on down states across the 15 minute stimulation period in 5 minute bins (Figure 5.17).

There was no significant effect of genotype (p=0.5), MK801 (p=0.43) or time (p=0.37) on the AUC of the response (Figure 5.18). However, there was a significant interaction between MK801 and time group ($\chi^2_{(2, 138)}$ = 6, p=0.05*). Specifically, the evoked response at 10-15 minutes was significantly lower in the MK801 treatment group point (-10246(54108), p=0.04*) compared to control conditions. There was no significant effect of genotype (p=0.18), MK801 (p=0.72) or time (p=0.19) on the SD of the signal response (Figure 5.19).

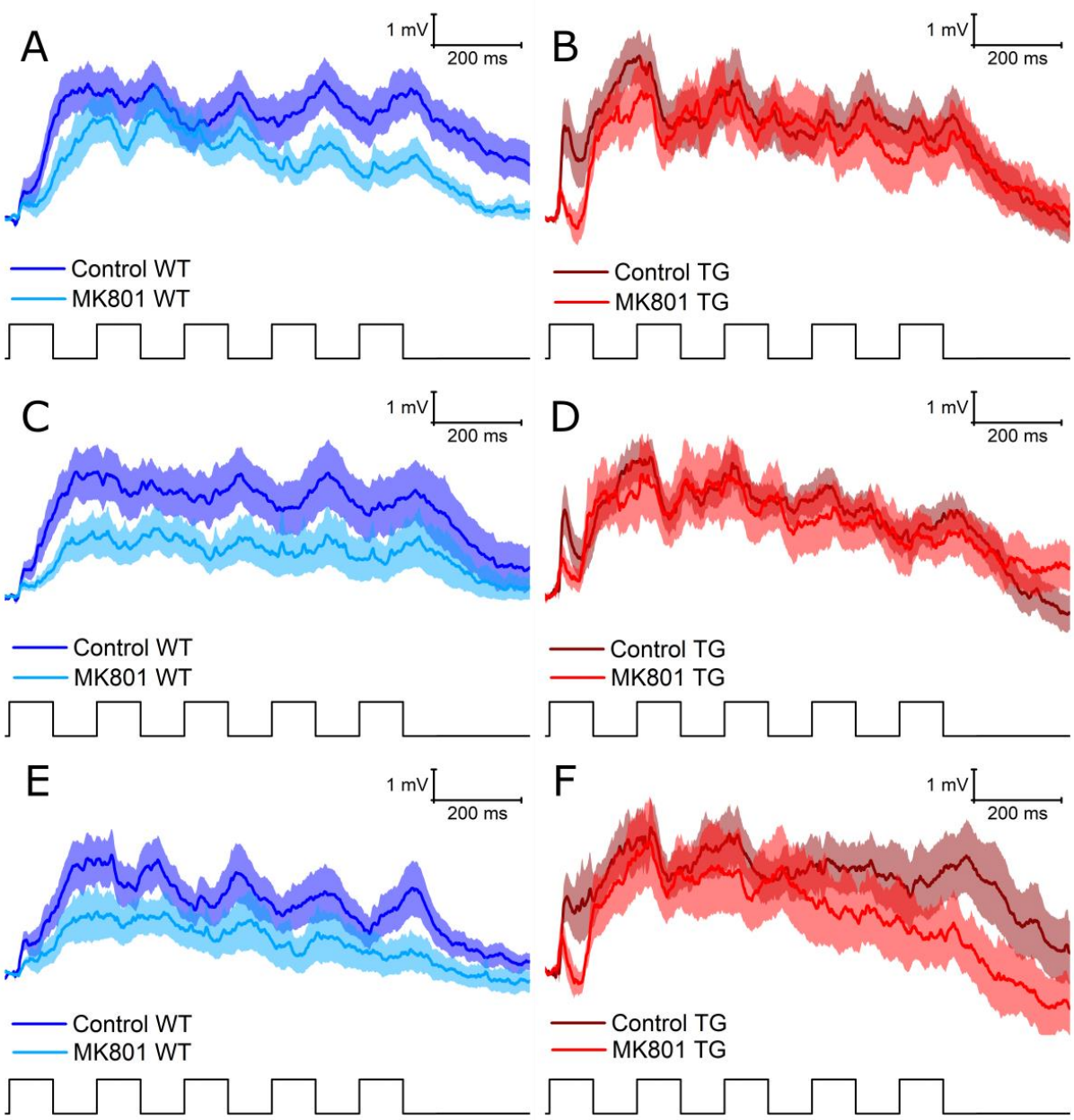

Figure 5.17 Stimulus response over time evoked on down states. Mean traces of the evoked response in down states within 5 minute bins. Data shown from WT (**A**, **C** & **E**) and TG (**B**, **D** & **F**), with or without MK801 treatment at 0-5 minutes (**A** & **B**), 5-10 minutes (**C** & **D**) and 10-15 minutes (**E** & **F**). The mean trace is shown as a thick line and the SEM is the shaded area. The timecourse of the 5 Hz airpuff whisker stimulus is plotted (in black) beneath each set of traces, with upward square pulses denoting the application of airpuff stimulation.

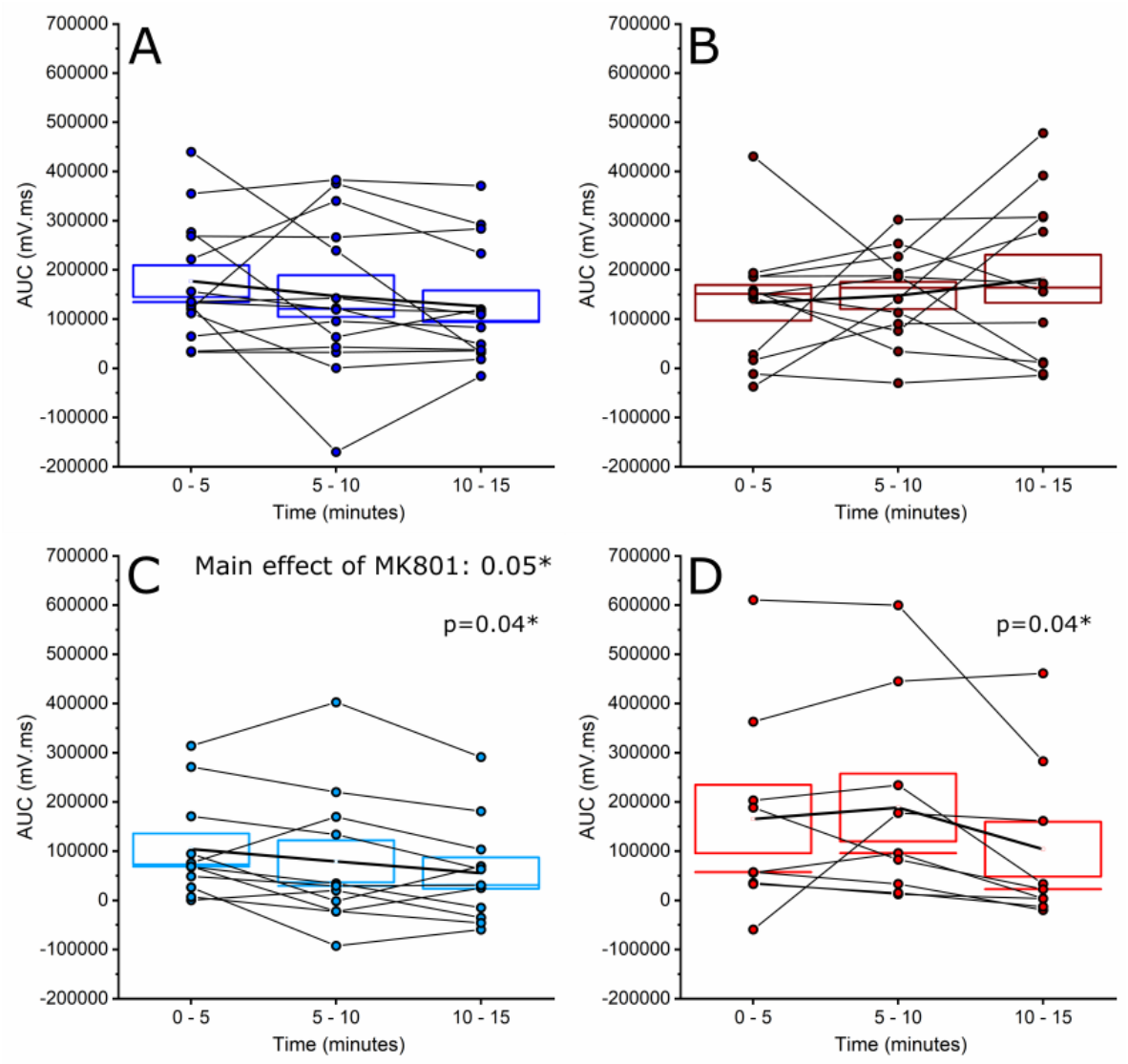

Figure 5.18 The AUC of the average stimulus responses over time evoked on down states. Box and connected dot plots of AUC of the responses in 5 minute bins for WT (**A** & **C**), TG (**B** & **D**) with MK801 (**C** & **D**) and without MK801 (**A** & **B**). Lines connect the same cell. The mean result is also shown as a thick black line. Significant effects are stated on the figure, with *post hoc* significance indicated at the 10-15 minute time point with MK801 treatment compared to control conditions.

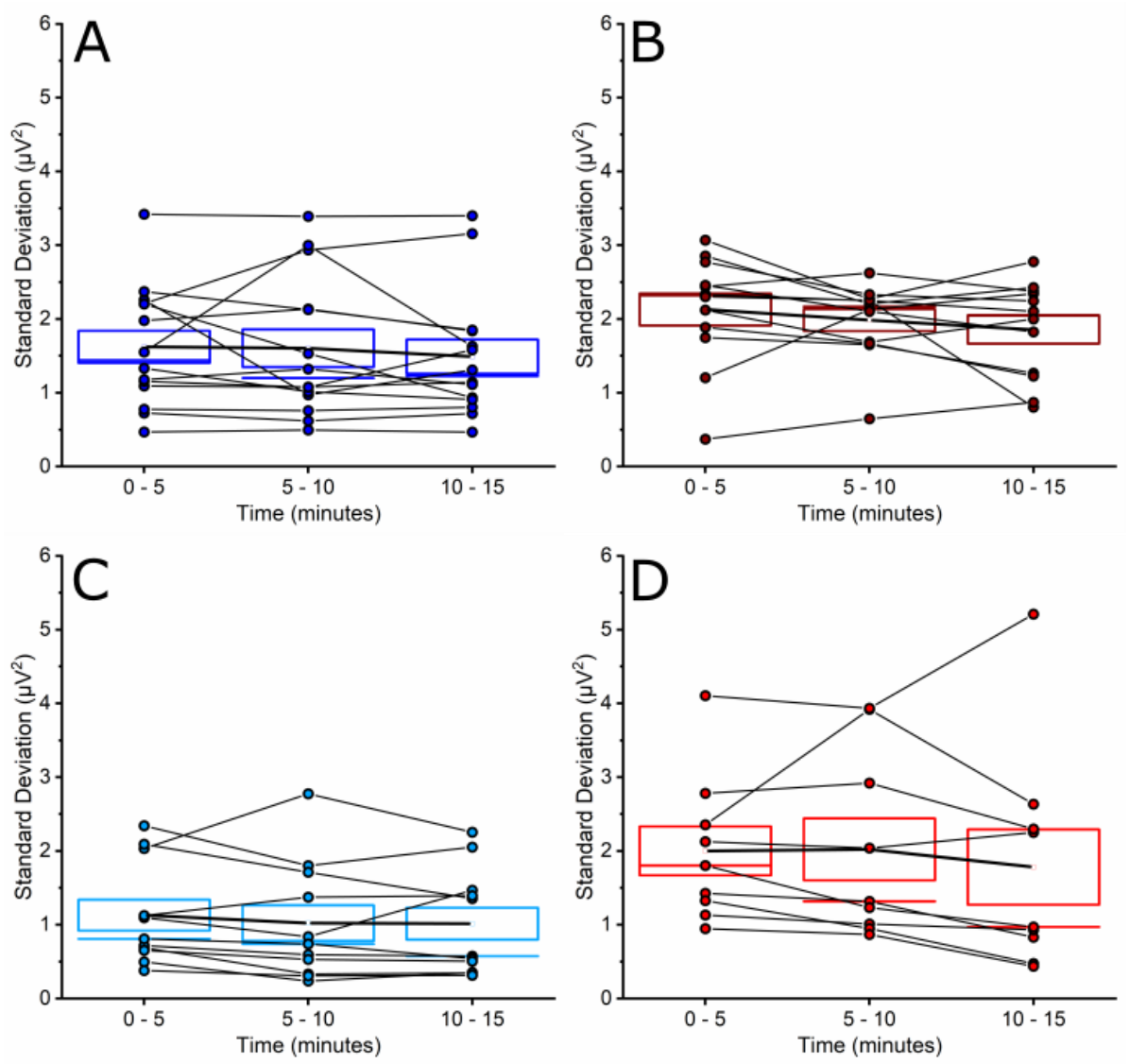

Figure 5.19 The SD of the average stimulus responses over time evoked on down states. Box and connected dot plots of SD of the responses in 5 minute bins for WT (**A** & **C**), TG (**B** & **D**) with MK801 (**C** & **D**) and without MK801 (**A** & **B**). Lines connect the same cell. The mean result is also shown as a thick black line.

5.4.8 Cyclic modulation on up and down states was not statistically different between genotypes, but did alter the evoked response size on up states

The cyclic amplitude modulation of up and down states, discussed in Chapter 4, was quantified by measuring 1 Hz power changes over time (Figure 5.20 A). This cyclic modulation was quantified as periodicity, counted as the mean cycle length. This was measured in: 11 WT animals (15 control cells), 7 WT animals (11 cells treated with MK801), 9 TG animals (13 control cells), 8 TG animals (10 cells treated with MK801). Periodicity was not significantly different between genotypes ($p = 0.67$), or with MK801 treatment ($p=0.96$), and there was no significant interaction between the two factors ($p=0.55$, ICC=0.14; Figure 5.20 B).

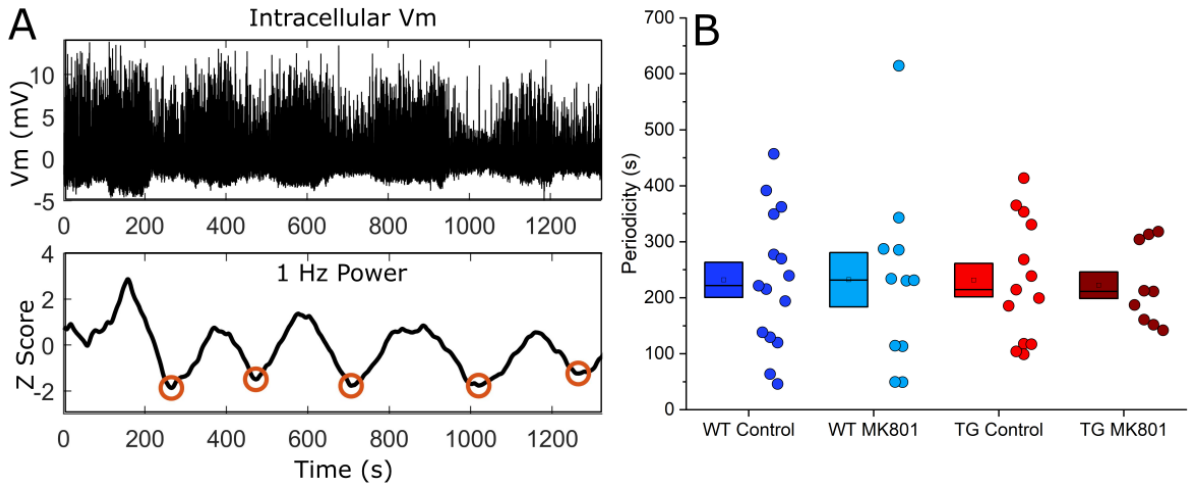

Figure 5.20 Cyclic modulation of up and down states in WT and TG cells. Cyclic modulation of up and down states can be seen in the intracellular Vm, and can be quantified as the 1 Hz power of the oscillation, z-score normalised (**A**). This periodicity can then be quantified, highlighted as orange circles per cycle (**A**). Mean cycle length in seconds (periodicity) is shown as box and dot plots for all groups (**B**).

Evoked response size (peak amplitude) was also compared to the cyclic phase modulation. As up and down states themselves can alter evoked response size, cyclic phase could also alter response size. There was no linear relationship between evoked response and the cyclic phase in either WT or TG cells, with or without MK801 treatment on down states (Figure 5.21 A - D; Table 5.1). In WT cells,

there was a weak negative relationship when cells were stimulated during up states (WT Control, Pearson's rank -0.3, p<0.005 ***; WT MK801, Pearson's rank -0.4, p=0.01**; Figure 5.21 E & G; Table 5.1). This suggests that during points of larger up states (higher 1 Hz power z-score), there was a smaller evoked response. In TG cells, a relationship between cyclic phase and evoked responses on up states was only seen in the control group. In contrast to the WT cells, this revealed a weak positive relationship (Pearson's rank = 0.17, p = 0.02*; Figure 5.21 F; Table 5.1). No linear relationship was observable in the TG MK801 group to responses evoked on up states (Figure 5.21 H; Table 5.1).

Table 5.1 Summary statistics of correlations between cyclic activity and response size amplitude evoked from up or down states. A table showing the summary statistics (F value, Pearson's r and p values) for each of the groups, split into up and down state responses.

Group	*Down state*	*Up state*
WT Control	$F_{1,562}$ 1.14, r = 0.045, p = 0.29	$F_{1,75}$ 9.19, r = -0.33, p <0.005 ***
WT MK801	$F_{1,413}$ 0.49, r = 0.035, p = 0.48	$F_{1,43}$ 6.83, r = -0.37, p = 0.01 **
TG Control	$F_{1,331}$ 0.18, r = 0.024, p = 0.67	$F_{1,175}$ 5.17, r = 0.17, p = 0.02 *
TG MK801	$F_{1,242}$ 0.56, r = -0.048, p = 0.45	$F_{1,154}$ 0.015, r = 0.0099, p = 0.90

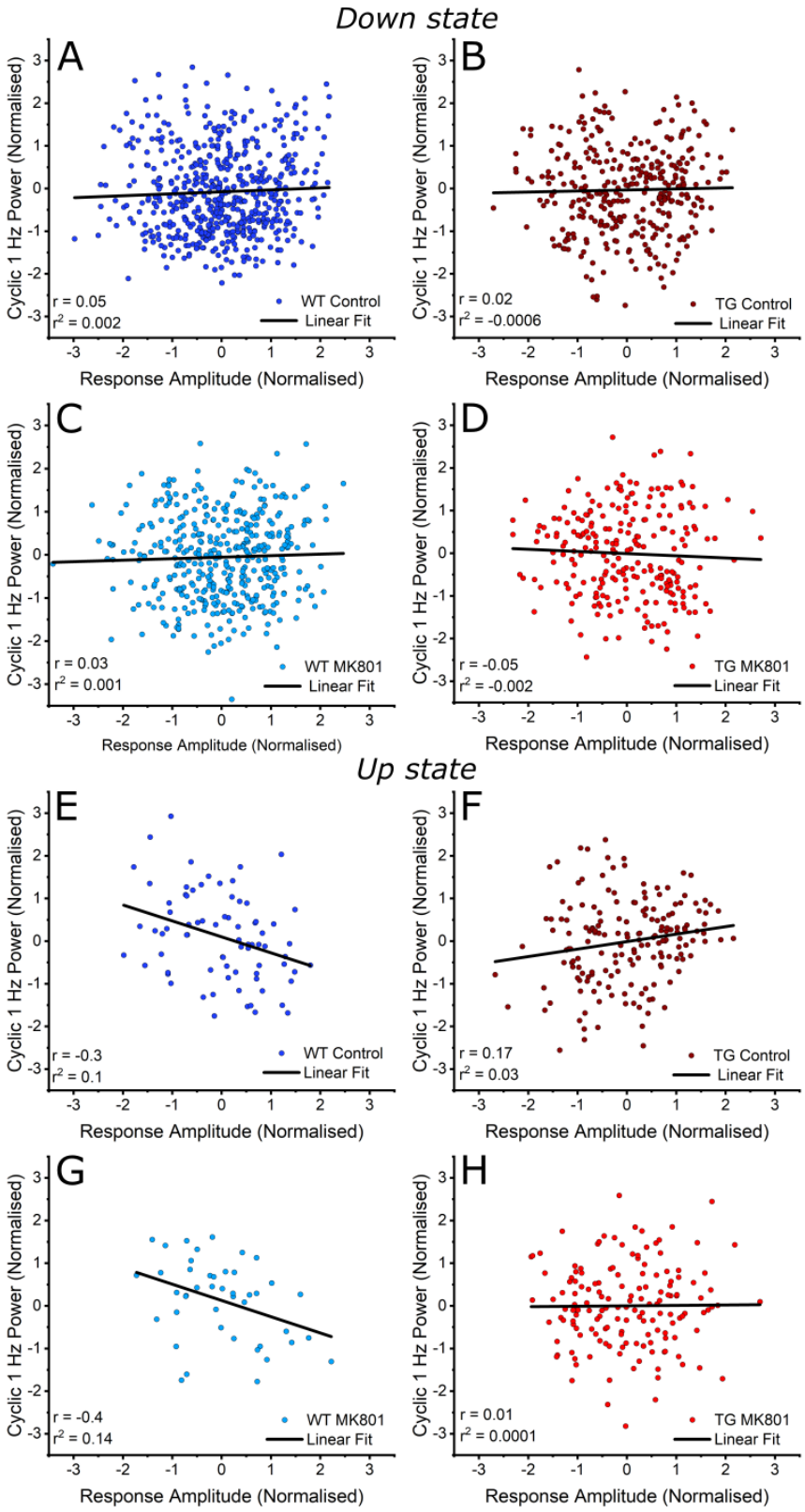

Figure 5.21 Correlations between cyclic phase and evoked responses to whisker stimulation. Cyclic activity phase (based on 1 Hz power normalised by z-score per cell) and how that affects evoked response amplitude (z-score normalised per cell). Scatter plots with lines of best fit for WT (**A**, **C**, **E**, **G**) and TG (**B**, **D**, **F**, **H**) cells with (**C**, **D**, **G**, **H**) and without MK801 (**A**, **B**, **E**, **F**) during down (**A** - **D**) and up (**E** - **H**) states.

5.5 DISCUSSION

In vivo whole-cell recordings were made from layer II/III somatosensory pyramidal neurons in ~5.5M rTg4510 mice and wildtype littermate controls, to reveal significant effects of genotype on evoked activity with some subtle effects of genotype on spontaneous activity. Specifically, the early fast component of whisker deflection evoked responses (peak) was significantly higher in rTg4510 mice than in wildtype littermate counterparts. The application of MK801 had effects on several components of whisker evoked activity (reduction in peak and PSP of evoked responses) and on spontaneous properties (reductions in up state charge).

5.5.1 Dysfunction of spontaneous and evoked activity in the rTg4510 model

5.5.2 Subtle spontaneous dysfunction in the rTg4510 model

There were observed alterations in spontaneous activity, with significant increases in up state charge and power later in the recording time, but not earlier (Figure 5.9 & Figure 5.10). Measures of charge and power are almost synonymous, as larger charge would equate to an increase in up state power, and so it is unsurprising that both are increased. This result however was surprising, as it would perhaps be expected that charge and power would reduce over recording time if the quality of recordings decreased (potentially related to changes in series resistance and cell health as seen by depolarising recordings over time, Figure 5.8). This effect could potentially be related to a persistent effect of intracellular solution perfusion into the extracellular space at 3 minutes following break-in but not at 23 minutes which suppresses the network at this earlier time point. Acute injection of soluble tau has been shown to reduce the power of different oscillatory bands *in vivo* (Ahnaou et al., 2017), which is in contrast with the results in this chapter. However, the rTg4510 model is a model of chronic tauopathy and so the effect of acute vs chronic incubation of tau is likely to be different. Overall, the up state frequency and duration was similar between genotypes (Figure 5.6 & Figure 5.7). Up state initiation within layer II/III is driven from deeper cortical layers with additional thalamic modulation (Beltramo et al., 2013; Neske, 2016). Deeper cortical layers have less pathological tau burden, with the thalamus showing very little pathology at this age in the rTg4510 model. Therefore, this signal

may be less likely to be disrupted leading to a lack of dysfunction in the frequency of these oscillations.

Interestingly, significant reductions in spontaneous activity in the somatosensory cortex in rTg4510 mice at 4-5.5M has been reported, visualised by recording AP-mediated Ca^{2+} transients (Busche et al., 2019; Jackson et al., 2017). However, the work in this chapter and in Chapter 2 would suggest that basal synaptic activity in the model is relatively unimpaired. Whole-cell recordings provide a direct measure of the electrophysiological properties of the cell, whereas Ca^{2+} imaging relies on changes in Ca^{2+} to provide a proxy of neuronal activity. GCaMP Ca^{2+} transients are driven by AP activity, and typically this is bursts of AP activity rather than a single AP. Within layer II/III, all cells show subthreshold activity, but very few fire spontaneous APs, particularly under anaesthesia (Petersen et al., 2003). The activity measured by Ca^{2+} imaging best reflects highly coordinated excitatory synaptic input plus inhibitory modulation eliciting an AP which occurs in a relatively low number of cells. Therefore, these studies were measuring different types of activity in comparison to the work in this study. Another possible explanation for the discrepancies between the different studies could be related to the number of cells sampled with the two methodologies. Two-photon imaging typically allows the experimenter to visualise hundreds of cells at a time, whereas the work in this chapter only measured a couple of neurons per animal, perhaps missing regional effects. However, this is unlikely to be the case as the reduction in spontaneous Ca^{2+} activity was significantly large in the imaging studies, and it would be unlikely that this study recorded from the only neurons that were unaffected.

Menkes-Caspi et al., 2015, also performed *in vivo* whole-cell recordings in the rTg4510 model at 5.5M in the frontal cortex. This study found reductions in the principal frequency (i.e. a reduction in the number of up states) and reductions in spontaneous firing in rTg4510 mice. These changes were not seen in the present study, but this could be due to a number of reasons including differences in anaesthetic (ketamine-xylazine used in Menkes-Caspi vs urethane in this work) to differences in regional severity of tau pathology (frontal expression of transgene) (Harrison et al., 2020).

5.5.3 Increased peak evoked responses to whisker stimulation in the rTg4510 model

In response to whisker stimulations, the peak amplitude of evoked responses was significantly higher in rTg4510 mice compared to wildtypes (Figure 5.14). This was reduced with MK801, suggesting it is modulated in part by NMDAR activity. Interestingly, the whisker evoked response was otherwise similar between genotypes (Figure 5.13 & Figure 5.14). Together this would suggest abnormal increased NMDAR activity at the start of the response in the rTg4510 model, but normal PSP activity thereafter. Evoked Ca^{2+} activity in response to whisker stimulation in the rTg4510 model at 5.5M was significantly reduced in another study, with a low number of neurons responding to stimulation regardless of genotype (Jackson et al., 2017). A strength of using whole-cell recordings is that it allows one to measure subthreshold changes, whereas Ca^{2+} imaging requires action potentials to mediate somatic Ca^{2+} transients. With evoked peak responses being larger in the rTg4510 mice within this study, it is surprising that evoked Ca^{2+} transients were not increased in Jackson et al., 2017. However, the evoked responses in this work were still easily subthreshold responses in most cases. This could suggest alterations in ion channels that regulate Ca^{2+} activity in the model, such as voltage gated Ca^{2+} channels which may lead to reduced Ca^{2+}-mediated activity or intrinsic changes that may impair the conversion of synaptic input to APs (i.e. hypoexcitable). However, work in Chapter 2 hinted at a subtle hyperexcitable phenotype in these cells so it is more likely to be the former.

The evoked response pattern itself appears to faithfully represent the multiple delivered stimuli (Figure 5.15 & Figure 5.16). Evoked activity to 5 Hz whisker stimulation in the somatosensory cortex in the literature shows a similar facilitation over the first two responses followed by a depression of further responses (Kheradpezhouh et al., 2017). Whilst the AUC and PSP were similar between genotypes, the peak amplitude was increased, potentially leading to atypical transfer of information (Figure 5.15 & Figure 5.16). With an increased peak amplitude of responses, this may lead to an increased likelihood of evoking an AP and thus increase downstream synaptic release, altering encoding of the signal.

Changes in inhibition within the local (i.e. principal whisker) and surround barrels may be another contributing factor to the abnormal responses seen in the rTg4510 mice.

Local inhibition governs some of the whisker evoked dynamics with IPSPs measured 10-20ms following stimulus onset (Moore and Nelson, 1998) and inhibition also modulates the amplitude of responses on up vs down states (Sachdev et al., 2004). In addition, stimulation of multiple whiskers leads to altered responses of the cell compared to stimulation of a single whisker that is specific to the barrel where the cell was recorded from (Brumberg et al., 1996; Gambino and Holtmaat, 2012; Shimegi et al., 1999; Simons, 1983). For example, suppression of lateral inhibition from surrounding whiskers facilitated the induction of plasticity and increased the evoked response in neighbouring barrels (Gambino and Holtmaat, 2012). Therefore, alterations in local and surround inhibition could lead to changes in evoked responses, including the facilitation of plasticity induced changes, and is another possible mechanism of dysfunction in rTg4510 mice at 5.5M.

In response to whisker stimulation, responses evoked on down states produced a large envelope of depolarisation, whereas responses evoked on up states elicited a response of reduced amplitude which eventually led to a hyperpolarising response of the cell (Figure 5.14). The balance of excitatory and inhibitory conductance plus changes in the reversal potential of the evoked response in the two states has been suggested to dictate the size and shape of evoked PSP responses, with increased inhibitory conductance and activity during up states (Sachdev et al., 2004). Slow cyclic modulation of up and down states did not seem to alter response dynamics on down states. However, for responses evoked on up states there appeared to be altered response dynamics between genotypes. Whereas larger up states produced smaller evoked responses in wildtype mice, the inverse was true in the rTg4510 mice i.e. bigger up states, bigger amplitude responses (Figure 5.21). MK801 did not modulate response size between these phases and so it is unlikely to be related to NMDAR signalling. However, these were very weak correlations and so caution should be taken with these interpretations. If this were the case, one could hypothesise that increased responses in up states would lead the cell closer to AP threshold and could be related to changes in inhibitory conductance. Controlling the amplitude of these responses would likely be important for regulating synaptic processing. For example, induction of LTP *in vivo* is different during up and down states (González-Rueda et al., 2018) and so loss of this regulation may have dramatic consequences for LTP.

In the rTg4510 model, neurons containing neurofibrillary tangles have been shown to integrate into functional networks with few functional impairments (Kuchibhotla et al., 2014). Whilst the peak responses was altered, other measures were similar and so the same could be said for the results in this chapter from the somatosensory circuit. Overall, the envelope (AUC) of the neuronal response was similar to wildtype responses, suggesting that whisker-based somatosensation could conceivably be unimpaired in the rTg4510 model at the 5.5M age point (Figure 5.13). Perhaps certain neuronal subtypes or circuits are preserved, albeit with more variable or hyperexcitable responses, whilst others are preferentially vulnerable to disruption by tauopathy. This has been seen in other work where head direction cell function was preserved, whereas grid cell functionality within the same region were impaired (Ridler et al., 2019). It would be interesting to see if behaviours dependent on whisker-based somatosensation were also altered (which could be attributed to the increased peak evoked response) or not (perhaps due to no change in AUC of evoked responses) in the rTg4510 model.

5.5.4 The effects of MK801 on spontaneous and evoked activity

MK801 is a use-dependent NMDAR antagonist, with application protocols having a long wash in time or using stimulation protocols to lead to blockade of the channel (Halliwell et al., 1989; Huettner and Bean, 1988; Wong et al., 1986). Application of MK801 via the intracellular solution in whole-cell recordings *in vivo* has been shown to have a wash in time of >5 minutes without the use of NMDAR stimulating protocols (Gambino et al., 2014; Lavzin et al., 2012; Smith et al., 2013). Strikingly, MK801 effects were seen early in the recordings within this chapter, with a significant reduction in up-state charge seen from 3 minutes (Figure 5.6). However, performing targeted patch clamp recordings using the ‘shadow patching’ method results in large amounts of intracellular solution being applied to the surface of the cell to enable visualisation. NMDARs expressed by the recorded call may be blocked even before break-in, and other cells in the local area may also have a partial NMDAR block. Therefore, some of the observed effects could be attributed to widespread NMDAR antagonism in the local area. Consequently, there is a possibility that MK801-mediated effects in this study resulted from the combined intracellular and extracellular local application of MK801.

When compared to spontaneous activity recorded from later time points, changes in variance and power of up and down states were seen with MK801 treatment (Figure 5.8 & Figure 5.10). These properties are inherently linked, as changes in the variability of the signal would lead to changes in oscillatory power. Studies have reported that there are no differences with *in vivo* MK801 application on up and down state properties such as frequency and dwell time (Palmer et al., 2014; Smith et al., 2013) which was also seen within this work. Up and down states are thought to be driven by local network activity and synchronised synaptic activity and therefore it is perhaps unsurprising that there were no changes to frequency or dwell time. Measures that are unrelated to the frequency of the oscillation, but instead measure the shape of how the cell responds such as charge or power, do appear to be different with the application of MK801. This suggests that NMDAR activity does not alter up state frequency or length, but helps shape the envelope of up states *in vivo*. Spontaneous firing frequency was also decreased with intracellular NMDAR antagonist application in other studies (Palmer et al., 2014; Smith et al., 2013), which was not seen in this work. However, spontaneous AP firing frequency is very low under urethane anaesthesia in the somatosensory cortex (Petersen et al., 2003), and so this could be due to a low sample of neurons that were actively firing APs.

Intracellular application of MK801 *in vivo* has been shown to reduce the slow PSP component of evoked whisker stimulation in layer II/III of the somatosensory cortex (Gambino et al., 2014). The PSP component was also decreased by application of MK801 in this work (Figure 5.14). However, the study by Gambino et al., 2014 also observed no change in peak amplitude. This is in direct contrast to the work in this chapter, which saw a significant reduction in peak amplitude with MK801 application, regardless of whether the response was evoked on an up or down state and was seen across multiple stimulations. Other work has observed reductions in the total evoked responses including early and late components (Lavzin et al., 2012), and so it is possible that this discrepancy is due to alterations in recording conditions or animal age (3-4 weeks vs ~5.5M) compared to the Gambino et al., 2014 study. It is also possible that these multi-whisker evoked responses cannot be as cleanly differentiated into AMPAR and NMDAR components as multi-whisker stimulation would drive a barrage of excitatory and inhibitory activity in comparison to the single-whisker evoked responses presented by Gambino et al., 2014.

There was an observable time effect in the evoked response with MK801 application, with a significant reduction in AUC seen by 10-15 minutes (total wash in time of 13-18 minutes; Figure 5.18). However, reductions in the peak amplitude and PSP were observed in the overall average evoked responses compared to no change in AUC in the average evoked response. As MK801 is use-dependent, perhaps there are different pools of NMDA receptors that are active in different components of the evoked responses which are blocked differentially.

5.6 CONCLUSIONS

Overall, this work reveals a role of NMDARs in shaping up states, whilst confirming no change in other up state properties as seen in previous works. Interestingly, these properties were not altered in the rTg4510 mice, although other spontaneous properties were changed. Overall area of evoked responses in the rTg4510 mice were not changed, but the peak subcomponent of this response was significantly increased. NMDARs appear to play a role in mediating this peak, with inhibition reducing the response in rTg4510 mice to the level of the wildtype response. The synaptic population involved in the evoked activity may have differential expression of NMDARs in comparison to the local synaptic population, as a compensatory mechanisms in response to restructuring and loss of local synaptic connections occurring at this age in the rTg4510 mice. Therefore, whilst there is normal function of NMDARs in spontaneous activity, there may be abnormal function in evoked responses, suggesting a role of NMDAR dysfunction in behaviourally relevant circuit disruption in the rTg4510 model. This could be related to differential vulnerability of synaptic populations that contribute to this form of activity. In neurodegenerative diseases, this could reflect the preservation of some synaptic pathways, and therefore behaviours, in comparison to the impairment of others.

6 GENERAL DISCUSSION

6.1 OVERVIEW

The work within this thesis provides an insight into alterations in glutamatergic synaptic and neuronal physiology at an early neurodegenerative phase in tauopathy. Some of these measures were also characterised at a more advanced pathological stage to highlight how physiology may change with the progression of pathology.

6.2 KEY FINDINGS: GLUTAMATERGIC RECEPTOR IMBALANCE AND LOSS DURING PRODROMAL TAUOPATHY

At the 5-6M age point in rTg4510 mice, previous literature has eluded to an aberrant synaptic plasticity phenotype in which synapse density was maintained, with increased spine turnover masking the loss of putative mature dendritic spines with the replacement of immature filopodia spines (Jackson et al., 2017, 2020; Kopeikina et al., 2013a). In addition, it has been suggested that tau pathogenesis induces a loss of glutamatergic receptor localisation to the spine with a corresponding loss of function (Hoover et al., 2010; Suzuki and Kimura, 2017). Even at this earlier neurodegenerative phase of tauopathy in the rTg4510 model, I detected a significant reduction in the regional expression of the post-synaptic marker PSD95 and AMPA receptor (AMPAR) subunits in rTg4510 mice in Chapter 3. Given this global reduction in AMPAR subunit expression, I would have expected a reduction in spontaneous excitatory post-synaptic current (sEPSC) frequency or an increased NMDA:AMPA receptor ratio when in fact the opposite was true, as determined by *in vitro* functional assessment in Chapter 2.

It is possible that the increased proportion of new, filopodia spines that has been previously observed in the rTg4510 model contain silent synapses (i.e. NMDA receptor (NMDAR) only) which are not coupled to a pre-synapse, which could explain the presumed reduction in NMDAR function in contrast to the limited change in regional NMDAR expression seen in Chapters 2 and 3, respectively (Isaac et al., 1995; Jackson et al., 2017; Kopeikina et al., 2013a). One could speculate that because of a significant reduction in PSD95 and AMPAR expression, filopodia cannot be stabilised and strengthened in the rTg4510 mice, as these proteins are thought to be vital for

these processes (Chen et al., 2015b; Granger et al., 2013; Henley and Wilkinson, 2013). rTg4510 neurons were also shown to have a subtle hyperexcitable phenotype in Chapter 2 at ~5.5M (decreased capacitance and depolarised Vm). This may be an intrinsic neuronal mechanism to compensate for a loss of putative AMPAR-mediated sEPSC activity, which could be clarified by measuring miniature EPSCs. Taking into account the increased dendritic restructuring that was also seen in the rTg4510 model in Chapter 3, it would seem that there are multiple aberrant plasticity mechanisms occurring in the early neurodegenerative phases of tauopathy, to likely compensate for loss of synaptic inputs and loss of receptor trafficking to the synapse.

6.3 KEY FINDINGS: ALTERED ENCODING OF EVOKED ACTIVITY *IN VIVO* DURING PRODROMAL TAUOPATHY

Strikingly, these somewhat conflicting deficits seen *in vitro* manifested *in vivo* as increased peak synaptic responses evoked by whisker simulation in ~5.5M rTg4510 mice, shown in Chapter 5. These responses were sensitive to the NMDAR antagonist MK801, while features of spontaneous network activity were seemingly unimpaired. This would suggest increased evoked NMDAR activity, contradicting what I would have expected from the *in vitro* assessment of glutamatergic synaptic function. However, the *in vivo* responses were evoked by simultaneous stimulation of multiple whiskers, which would drive a barrage of excitatory and inhibitory activity, compared to the *in vitro* assessment in which layer IV to layer II/III glutamatergic synapses were selectively driven within an individual barrel field. Therefore, these responses could be interpreted as the global response to incoming sensory information by the cell, where there is a culmination of tauopathy-induced differences in synaptic and neuronal function within an intact network. For example, this could be a product of increased proximal dendritic branching with more NMDAR rich, filopodia-like synapses that when stimulated facilitates the evoked response. In addition, horizontal transcolumnar inputs synapse differentially with apical regions of the dendritic arbor of layer II/III pyramidal neurons in comparison to the basal dendritic layer IV inputs studied *in vitro* (Feldmeyer et al., 2002; Lübke et al., 2000). Therefore, the observed dendritic reshaping may skew the balance of sensory integration towards horizontal inputs which would be stimulated *in vivo* increasing the evoked activity. Regardless of the precise mechanism, altered

glutamatergic receptor expression and function seems to manifest as increased peak evoked activity in this assay, likely altering synaptic encoding of sensory information.

To my knowledge, no other studies have used *in vivo* whole-cell recordings to investigate synaptically-driven evoked activity within a dementia model. This work highlights the importance of quantifying subthreshold dynamics to understand how changes in synaptic and intrinsic neuronal properties contribute to aberrant cellular processing of information. For example, if another *in vivo* electrophysiology technique such as extracellular single unit recordings had been used, these more subtle subthreshold deficits might not have been apparent, as this stimulation paradigm infrequently evokes action potentials.

6.4 KEY FINDINGS: FURTHER GLUTAMATERGIC SYNAPTIC DYSFUNCTION WITH THE PROGRESSION OF NEURODEGENERATIVE TAUOPATHY

Between 5.5M and 7.5M of age in the rTg4510 model, it has been evidenced that there is progressive atrophy of the cortex and hippocampus (Blackmore et al., 2017; Ramsden et al., 2005; SantaCruz et al., 2005; Spires et al., 2006; Yue et al., 2011). Therefore, when comparing between the ~5.5M and ~7.5M age groups in this work, it is likely that some of the differences seen are due to progressive neurodegeneration within the somatosensory cortex. Within the somatosensory cortex, NMDAR expression was significantly reduced (reduced GluN1 subunit expression) with further reductions of PSD95 and AMPAR subunit expression in rTg4510 mice at 7.5M, shown in Chapter 3. Given the role NMDARs play in synaptic plasticity, one could hypothesise that the reduction in NMDAR expression would relate to a reduction in synaptic plasticity, including the formation and stabilisation of new dendritic spines. Within the rTg4510 model at more advanced stages of neurodegeneration, there are large reductions in synapse density and synaptic markers which would fit with this idea (Crimins et al., 2011, 2012; Jackson et al., 2017; Kopeikina et al., 2013a). Functional assessment of synapses in Chapter 2 suggested that putative synaptic AMPAR-mediated currents (sEPSCs) were reduced in frequency with a balanced NMDA:AMPA receptor ratio at ~7.5M in the rTg4510 model, which is contrary to the dysfunction seen at the ~5.5M age point in this model. With the significant loss of regional NMDAR expression in the somatosensory cortex seen in the rTg4510 mice, perhaps the

converse would have been expected. It is also very possible that different synaptic pathways or synapses are differentially affected, such as thalamocortical synapses compared to layer IV synapses. Measuring receptor expression at a finer resolution using histological techniques, and perhaps examining glutamatergic receptor expression at individual synapses using techniques such as super-resolution imaging, would resolve whether local receptor expression and localisation at the synapse is altered. Differences in local expression and synaptic localisation may cause this imbalance of function and global expression, with impairments in synaptic receptor localisation already shown in cultured rTg4510 neurons (Hoover et al., 2010).

6.5 IMPLICATIONS FOR UNDERSTANDING TAUOPATHY-MEDIATED DYSFUNCTION

This work has highlighted the importance of the synapse in maintaining function in tauopathy-mediated neurodegeneration. The synapse plays a vital role in neuronal communication and underpins evoked network activity. Even with the dramatic reductions of glutamatergic receptor expression, there was maintained synaptic and network activity early in the neurodegenerative process (~5.5M age point). Between early and later neurodegenerative phases, there were diverging alterations in glutamatergic receptor expression and function, and further characterisation of how this leads to or predicts synaptic degeneration seems like a critical and unanswered question.

Measuring neuronal and synaptic function in models of tauopathy is fundamental to deconstructing mechanisms of aberrant function prior to degeneration, with this type of intracellular electrophysiological characterisation not possible in humans. For example, whilst I saw reductions in AMPAR subunit expression in the rTg4510 mice, this did not manifest as a reduction in putative AMPAR-mediated function *in vitro*. Of course, different methodologies were used to generate these findings, and comparing single cell data to regional protein expression is not exact. Therefore, whilst it is important to understand pathology-driven molecular changes within the brain, this may not manifest in the expected functional disruption. In fact, the characterisation of NMDAR function *in vitro* suggested reduced NMDAR activity in ~5.5M rTg4510 mice, while there was an increase in evoked synaptic activity which had a large NMDAR-mediated component *in vivo.* This highlights that characterisation of cellular function

using reduced systems such as brain slices may not always translate to the *in vivo* setting, in which diverse sources of excitatory and inhibitory innervation remain intact. Therefore, care should be taken to understand what changes are pathogenic, which are compensatory, and how these changes manifest *in vivo.*

6.6 LIMITATIONS OF THE WORK

6.6.1 Single cell portrayal of a global phenomenon?

Global measures such as reductions in cell density, or total pathological burden within a region, are examples of neuropathological diagnostic criteria used to assess the impact of tauopathy *post-mortem*, inferring a causal link between this and behavioural change (Irwin, 2016; Kishi et al., 2015; Lao et al., 2019). However, this generally assumes a similar expression of pathology within the population of measured cells within a region. Within this population, there is a large variability between the pathological state of each cell with different cells being further along the neurodegenerative process, and some never undergoing neurodegeneration (Crimins et al., 2011, 2012; Rocher et al., 2010). Some cell types, such as excitatory neurons, have also been highlighted as particularly vulnerable compared to others (Fu et al., 2018, 2019). Therefore, it is truly important to understand synaptic and neuronal dysfunction at a single cell level, which enables the analysis of cell-to-cell variability in expression of tauopathy-driven neurophysiological phenotypes.

The majority of my recordings were performed early in the neurodegenerative phase of tauopathy in the rTg4510 model, and so the number of atrophic cells should be low at this disease stage (Blackmore et al., 2017; Crimins et al., 2011; Ramsden et al., 2005; SantaCruz et al., 2005). However, even at this stage, two recorded cells may have very different cellular phenotypes with different pathological burdens. Using visualised whole-cell patch clamp recordings can also lead to targeting healthier cells for recording. However, care was taken to avoid this bias in this work as exclusion criteria was based on technique related measures such as series resistance and not cell health measures such as membrane potential (unless severely depolarised).

Trying to ascribe a defined functional change observed from one cellular subset to a whole network when each cell harbours differing phenotypes is difficult. I have identified various glutamatergic receptor dysfunctions within a subset of cells in layer II/III of the somatosensory cortex. But would this dysfunction lead to network

alterations that could drive altered behavioural phenotypes? In tauopathies, some behaviours or networks have a larger tolerance to cell loss before showing alterations and so these alterations in glutamatergic signalling could be an early or late pathogenic change for these specific cells within the network (Crimins et al., 2013; Perneczky et al., 2019; Stern, 2012). This could also be a compensatory mechanism by healthier cells to account for more pathogenic cells in the local network. This should be considered when discussing therapeutics that target identified single cell dysfunction, as this may inadvertently target compensatory “healthy” cells that show a tauopathy-induced non-pathogenic cellular phenotype.

6.6.2 Can mice model dementia?

Rodents are a key model in neuroscience research, with a wide array of genetic and molecular tools, and broadly similar genetics and physiology, making them an ideal model organism to study normal and disease neurophysiology (Bryda, 2013; Ellenbroek and Youn, 2016). However, rodent models of dementia are limited as they do not fully recapitulate the causal diseases. In fact, research in rodent models of dementia has so far failed to yield successful drugs in the clinic for dementia, thought to be due in part to poor model translatability (Dawson et al., 2018; Drummond and Wisniewski, 2017; Mullane and Williams, 2019; Onos et al., 2016).

Rodent models of dementia typically harbour genetic mutations from familial dementias, the incidence of which is dramatically less than the sporadic forms (Dawson et al., 2018; Götz et al., 2018). These models are qualified as good models based on the expression of the various pathologies that are present within the human disease, but as a field we are still unsure which forms of pathology are toxic or protective (Cowan and Mudher, 2013; D’Orange et al., 2018; Kuchibhotla et al., 2014; Spires-Jones et al., 2011). Within tauopathy research specifically, it is also important to note that mice lack full tau isoform expression found within humans (Dawson et al., 2018; Götz et al., 2018). This can be compensated for with the expression of human tau isoforms within the mouse line, but this may not sufficiently recapitulate human tau physiology (Andorfer et al., 2003; Saito et al., 2019).

In addition, the biggest risk factor for dementia is older age, and thus using rodent models with comparatively short lifespans can be a major limitation for modelling aging-related neurodegenerative diseases (Dawson et al., 2018). Mice are considered

to be mature adults from 3M of age, with the equivalent of old age in mice being from 18M, with mice over 24M considered to be “very old” (Flurkey et al., 2007). However, all of these age points are notably shorter than the lifespan of a human although there are equivalent age points. Within the rTg4510 model specifically, there is a rapid accumulation of pathology and degeneration that occurs within months, compared to a disease that takes years to precipitate from pathology onset. Therefore, we may be missing key changes that occur with aging that we are currently not emulating with this model. Whilst rodent models have their limitations, there is no such thing as the perfect model for human diseases and so rodent models are used to address specific experimental hypothesises that cannot currently be explored in humans.

6.6.2.1 Limitations of the rTg4510 model of tauopathy

rTg4510 mice overexpress the tau P301L mutation up to 13x the typical expression level of murine tau, with neurodegeneration first observed in the cortex and hippocampus at 5/6M (Ramsden et al., 2005; SantaCruz et al., 2005). This overexpression is considered to be highly influential in the resulting pathological phenotype seen (Blackmore et al., 2017). Other models that express mutant tau isoforms at more physiological levels show a more variable and delayed neurodegenerative phenotype in comparison (Andorfer et al., 2003; Gamache et al., 2019; Koss et al., 2016; Saito et al., 2019). For this work, utilising the robust and rapid progression of pathology allowed for assessment of age points that were highly likely to be at a specific disease phase. However, this may not be as physiologically relevant to tauopathy as some of the other rodent models, due to this high overexpression of mutant tau.

Recent work has suggested that the pronounced neurodegenerative phenotype seen in rTg4510 mice is not purely associated with tau overexpression, but is also linked to genetic disruption at the site of transgene insertion (Gamache et al., 2019; Goodwin et al., 2017). However, mutant tau expression within this model is repressible, and work using doxycycline to repress transgene expression provides an appropriate method to assess the contribution of off-target genetic effects. In studies using doxycycline treatment, early repression of tau overexpression was sufficient to prevent neurodegeneration and lowered tau pathology (Blackmore et al., 2017; Holton et al., 2020; Ramsden et al., 2005; SantaCruz et al., 2005; Wang et al., 2018). In addition, direct insertion of the P301L tau mutant transgene without off-target genetic disruption

still caused progressive tauopathy and neurodegeneration, albeit at a slightly later age than in the rTg4510 mice (Gamache et al., 2019). Therefore, whilst I cannot conclude for certain that the results I have observed are not influenced by off-target genetic effects, it is likely that pathological tau is the predominant driver of the observed phenotypes, particularly in experiments conducted at an age point known to precede the onset of cortical neurodegeneration in rTg4510 mice (Blackmore et al., 2017; Ramsden et al., 2005; SantaCruz et al., 2005).

6.7 FUTURE DIRECTIONS

There are still some key unanswered questions that are left to be addressed from this work. Whilst not exhaustive, some of the more pertinent suggestions are:

- **How does altered glutamatergic receptor function and expression manifest at individual synapses?**

  Whilst regional synaptic marker and receptor expression were quantified, this could not be directly linked to the single cell recordings. In addition, synaptic function could only be ascertained as an aggregate value within individual neurons, skewed to activity from more proximal spines (Williams and Mitchell, 2008). *Post hoc* immunohistochemical analysis, perhaps combined with a technique such as super-resolution or expansion microscopy, could be used to quantify synaptic glutamatergic receptor expression and localisation (Chen et al., 2015a). This would confirm whether lowered glutamatergic receptor expression and altered receptor function translates to a different receptor composition within the synapse. An interesting extension of this work would be to examine whether there was a difference in expression and localisation on proximal compared to distal spines as a consequence of the observed dendritic restructuring in the rTg4510 cells.
- **When do the observed changes in glutamatergic receptor expression and function first emerge in rTg4510 mice, and are they specifically driven by cellular or synaptic tauopathy?**

  At the early neurodegenerative age point in rTg4510 mice (~5.5M), there were already apparent changes in glutamatergic receptor function and synaptic marker expression. Examining this at an earlier age would confirm when this phenotype first appears in relation to tau pathology onset, and whether synaptic

marker expression is lowered before or after glutamatergic receptor alterations. Furthermore, the possibility that some phenotypic changes within the rTg4510 model that are related to the off-target gene disruption cannot be ruled out (Gamache et al., 2019). It would be useful to confirm whether the detected alterations were due to the overexpression of mutant tau, which could be controlled for by using doxycycline treated rTg4510 mice as comparators which would repress pathology expression (Blackmore et al., 2017; Ramsden et al., 2005; SantaCruz et al., 2005).

- **What is the role of pathological burden on the observed cellular phenotype?**

  Tau pathology was detected and used to help confirm genotype in the *in vitro* electrophysiology characterisation. However, the amount of tau pathology in the local vicinity of recorded neurons was not directly quantified. There may be differing functional phenotypes observed with variations of the local pathological burden. Also, none of the recorded cells co-expressed markers of tau pathology (MC-1) and so using other markers such as Thioflavin-S which bind to a different tau structure would help confirm this result. For future experiments, fluorescent tau markers such as Thioflavin-S could be used to specifically target cells with that harbor certain pathology isoforms to ensure the inclusion of tau positive cells (de Calignon et al., 2009; Spires-Jones et al., 2008). An alternative way to assess single cell pathology following recordings would be to perform patch-seq to quantify the expression of all tau species expressed within the neuron (Cadwell et al., 2016; Fuzik et al., 2016).

- **What is the impact of altered functional encoding on behavioural output?**

  The *in vivo* whole-cell recordings revealed altered functional encoding of whisker-evoked responses in the rTg4510 model. It would be interesting to see if this affected sensory discrimination for example, by performing awake recordings with the presentation of different textured materials. Another way to examine this would be to measure whether this pathway was capable of undergoing plasticity induced changes such as LTP, particularly as glutamatergic receptor function and mobility is vital for plasticity mechanisms. This could be investigated *in vitro*, or *in vivo* using whisker stimulation (Bartram et al., 2017; Gambino et al., 2014; González-Rueda et al., 2018). If either of

these behavioural outputs were altered, an extension of this work could then be to use an NMDAR antagonist for example, to attempt to normalise aberrant activity.

6.8 FINAL CONCLUSIONS

The work presented in this thesis has provided novel insights into physiological dysfunction at early and more advanced neurodegenerative phases of tauopathy. In the somatosensory cortex of rTg4510 mice, there are clear but discrepant deficits in glutamatergic receptor expression and function, that precipitate as altered functional responses to sensory stimulation early in the neurodegenerative process. Furthermore, with the progression of pathology and neurodegeneration, novel deficits emerge whilst others disappear suggesting transient alterations in glutamatergic receptor function may be critical to help preserve function at these earlier disease phases in tauopathy. Targeting these mechanisms may provide an opportunity for prolonging symptomatic decline and therapeutic recovery prior to overt cell loss in tauopathy-associated dementia.

7 BIBLIOGRAPHY

Abraham, W.C., and Bear, M.F. (1996). Metaplasticity: The plasticity of synaptic plasticity. Trends Neurosci. *19*, 126–130.

Adibi, M. (2019). Whisker-Mediated Touch System in Rodents: From Neuron to Behavior. Front. Syst. Neurosci. *13*, 40.

Agmon, A., and Connors, B.W. (1991). Thalamocortical responses of mouse somatosensory (barrel) cortex in vitro. Neuroscience *41*, 365–379.

Ahmed, Z., Cooper, J., Murray, T.K., Garn, K., McNaughton, E., Clarke, H., Parhizkar, S., Ward, M.A., Cavallini, A., Jackson, S., et al. (2014). A novel in vivo model of tau propagation with rapid and progressive neurofibrillary tangle pathology: the pattern of spread is determined by connectivity, not proximity. Acta Neuropathol. *127*, 667–683.

Ahnaou, A., Moechars, D., Raeymaekers, L., Biermans, R., Manyakov, N. V., Bottelbergs, A., Wintmolders, C., Van Kolen, K., Van De Casteele, T., Kemp, J.A., et al. (2017). Emergence of early alterations in network oscillations and functional connectivity in a tau seeding mouse model of Alzheimer's disease pathology. Sci. Rep. *7*, 1–14.

Akgül, G., and Mcbain, C.J. (2016). Diverse roles for ionotropic glutamate receptors on inhibitory interneurons in developing and adult brain. J. Physiol. J Physiol *594*, 19.

Albieri, G., Barnes, S.J., De Celis Alonso, B., Cheetham, C.E.J., Edwards, C.E., Lowe, A.S., Karunaratne, H., Dear, J.P., Lee, K.C., and Finnerty, G.T. (2015). Rapid bidirectional reorganization of cortical microcircuits. Cereb. Cortex *25*, 3025–3035.

Alldred, M.J., Duff, K.E., and Ginsberg, S.D. (2012). Microarray analysis of CA1 pyramidal neurons in a mouse model of tauopathy reveals progressive synaptic dysfunction. Neurobiol. Dis. *45*, 751–762.

Allen, B., Ingram, E., Takao, M., Smith, M.J., Jakes, R., Virdee, K., Yoshida, H., Holzer, M., Craxton, M., Emson, P.C., et al. (2002). Abundant tau filaments and nonapoptotic neurodegeneration in transgenic mice expressing human P301s tau protein. J. Neurosci. *22*, 9340–9351.

Alonso, A.D.C., Zaidi, T., Grundke-Iqbal, I., and Iqbal, K. (1994). Role of abnormally phosphorylated tau in the breakdown of microtubules in Alzheimer disease. Proc. Natl.

Acad. Sci. U. S. A. *91*, 5562–5566.

Alzheimer's Association (2020). 2020 Alzheimer's disease facts and figures. Alzheimer's Dement. *16*, 391–460.

Alzheimer, A. (1911). Über eigenartige Krankheitsfälle des späteren Alters. Zeitschrift Für Die Gesamte Neurol. Und Psychiatr. *4*, 356.

American Psychiatric Association (2013). Diagnostic and statistical manual of mental disorders (DSM-5®) (American Psychiatric Pub).

Andorfer, C., Kress, Y., Espinoza, M., De Silva, R., Tucker, K.L., Barde, Y.A., Duff, K., and Davies, P. (2003). Hyperphosphorylation and aggregation of tau in mice expressing normal human tau isoforms. J. Neurochem. *86*, 582–590.

Andreadis, A. (2005). Tau gene alternative splicing: Expression patterns, regulation and modulation of function in normal brain and neurodegenerative diseases. Biochim. Biophys. Acta - Mol. Basis Dis. *1739*, 91–103.

Andreadis, A., Brown, W.M., and Kosik, K.S. (1992). Structure and Novel Exons of the Human τ Gene. Biochemistry *31*, 10626–10633.

Anggono, V., and Huganir, R.L. (2012). Regulation of AMPA receptor trafficking and synaptic plasticity. Curr. Opin. Neurobiol. *22*, 461–469.

Anis, N.A., Berry, S.C., Burton, N.R., and Lodge, D. (1983). The dissociative anaesthetics, ketamine and phencyclidine, selectively reduce excitation of central mammalian neurones by N-methyl-aspartate. Br. J. Pharmacol. *79*, 565–575.

Araya, R., Vogels, T.P., and Yuste, R. (2014). Activity-dependent dendritic spine neck changes are correlated with synaptic strength. Proc. Natl. Acad. Sci. U. S. A. *111*, E2895–E2904.

Arieli, A., Shoham, D., Hildesheim, R., and Grinvald, A. (1995). Coherent spatiotemporal patterns of ongoing activity revealed by real- time optical imaging coupled with single-unit recording in the cat visual cortex. J. Neurophysiol. *73*, 2072–2093.

Armstrong-James, M., Welker, E., and Callahan, C.A. (1993). The contribution of NMDA and non-NMDA receptors to fast and slow transmission of sensory information

in the rat SI barrel cortex. J. Neurosci. *13*, 2149–2160.

Ashby, M.C., Daw, M.I., and Isaac, J.T.R. (2008). AMPA Receptors. In The Glutamate Receptors, (Totowa, NJ: Humana Press), pp. 1–44.

Avila, J., Llorens-Martín, M., Pallas-Bazarra, N., Bolós, M., Perea, J.R., Rodríguez-Matellán, A., and Hernández, F. (2017). Cognitive Decline in Neuronal Aging and Alzheimer's Disease: Role of NMDA Receptors and Associated Proteins. Front. Neurosci. *11*, 626.

Bailey, R.M., Howard, J., Knight, J., Sahara, N., Dickson, D.W., and Lewis, J. (2014). Effects of the C57BL/6 strain background on tauopathy progression in the rTg4510 mouse model. Mol. Neurodegener. *9*, 8.

Bang, J., Spina, S., and Miller, B.L. (2015). Frontotemporal dementia. Lancet *386*, 1672–1682.

Barbier, P., Zejneli, O., Martinho, M., Lasorsa, A., Belle, V., Smet-Nocca, C., Tsvetkov, P.O., Devred, F., and Landrieu, I. (2019). Role of tau as a microtubule-associated protein: Structural and functional aspects. Front. Aging Neurosci. *10*, 204.

Barnes, S.J., and Finnerty, G.T. (2010). Sensory experience and cortical rewiring. Neuroscientist *16*, 186–198.

Barnes, S.J., Sammons, R.P., Jacobsen, R.I., Mackie, J., Keller, G.B., and Keck, T. (2015a). Subnetwork-Specific Homeostatic Plasticity in Mouse Visual Cortex In Vivo. Neuron *86*, 1290–1303.

Barnes, S.J., Cheetham, C.E., Liu, Y., Bennett, S.H., Albieri, G., Jorstad, A.A., Knott, G.W., and Finnerty, G.T. (2015b). Delayed and temporally imprecise neurotransmission in reorganizing cortical microcircuits. J. Neurosci. *35*, 9024–9037.

Barnes, S.J., Franzoni, E., Jacobsen, R.I., Erdelyi, F., Szabo, G., Clopath, C., Keller, G.B., and Keck, T. (2017). Deprivation-Induced Homeostatic Spine Scaling In Vivo Is Localized to Dendritic Branches that Have Undergone Recent Spine Loss. Neuron *96*, 871-882.e5.

Barros-Zulaica, N., Villa, A.E.P., and Nuñez, A. (2019). Response adaptation in barrel cortical neurons facilitates stimulus detection during rhythmic whisker stimulation in anesthetized mice. Eneuro *6*.

Barth, A.L., and Poulet, J.F.A. (2012). Experimental evidence for sparse firing in the neocortex. Trends Neurosci. *35*, 345–355.

Bartram, J., Kahn, M.C., Tuohy, S., Paulsen, O., Wilson, T., and Mann, E.O. (2017). Cortical Up states induce the selective weakening of subthreshold synaptic inputs. Nat. Commun. *8*, 665.

Bats, C., Groc, L., and Choquet, D. (2007). The Interaction between Stargazin and PSD-95 Regulates AMPA Receptor Surface Trafficking. Neuron *53*, 719–734.

Bayés, À., Collins, M.O., Galtrey, C.M., Simonnet, C., Roy, M., Croning, M.D.R., Gou, G., Van De Lagemaat, L.N., Milward, D., Whittle, I.R., et al. (2014). Human post-mortem synapse proteome integrity screening for proteomic studies of postsynaptic complexes. Mol. Brain *7*, 88.

Beattie, E.C., Carroll, R.C., Yu, X., Morishita, W., Yasuda, H., Von Zastrow, M., and Malenka, R.C. (2000). Regulation of AMPA receptor endocytosis by a signaling mechanism shared with LTD. Nat. Neurosci. *3*, 1291–1300.

Beaulieu-Laroche, L., and Harnett, M.T. (2018). Dendritic Spines Prevent Synaptic Voltage Clamp. Neuron *97*, 75-82.e3.

Bejanin, A., Schonhaut, D.R., Joie, R. La, Kramer, J.H., Baker, S.L., Sosa, N., Ayakta, N., Cantwell, A., Janabi, M., Lauriola, M., et al. (2017). Tau pathology and neurodegeneration contribute to cognitive impairment in Alzheimer's disease. Brain *140*, 3286–3300.

Belford, G.R., and Killackey, H.P. (1979). Vibrissae representation in subcortical trigeminal centers of the neonatal rat. J. Comp. Neurol. *183*, 305–321.

Beltramo, R., D'Urso, G., Dal Maschio, M., Farisello, P., Bovetti, S., Clovis, Y., Lassi, G., Tucci, V., De Pietri Tonelli, D., and Fellin, T. (2013). Layer-specific excitatory circuits differentially control recurrent network dynamics in the neocortex. Nat. Neurosci. *16*, 227–234.

Benardo, L.S. (1993). GABA A receptor-mediated mechanisms contribute to frequency-dependent depression of IPSPs in the hippocampus. Brain Res. *607*, 81–88.

Benussi, A., Cosseddu, M., Filareto, I., Dell'Era, V., Archetti, S., Sofia Cotelli, M.,

Micheli, A., Padovani, A., and Borroni, B. (2016). Impaired long-term potentiation–like cortical plasticity in presymptomatic genetic frontotemporal dementia. Ann. Neurol. *80*, 472–476.

Benussi, A., Alberici, A., Buratti, E., Ghidoni, R., Gardoni, F., Luca, M. Di, Padovani, A., and Borroni, B. (2019). Toward a glutamate hypothesis of frontotemporal dementia. Front. Neurosci. *13*.

Bettler, B., Boulter, J., Hermans-Borgmeyer, I., O'Shea-Greenfield, A., Deneris, E.S., Moll, C., Borgmeyer, U., Hollmann, M., and Heinemann, S. (1990). Cloning of a novel glutamate receptor subunit, GluR5: Expression in the nervous system during development. Neuron *5*, 583–595.

Bianchi, D., Marasco, A., Limongiello, A., Marchetti, C., Marie, H., Tirozzi, B., and Migliore, M. (2012). On the mechanisms underlying the depolarization block in the spiking dynamics of CA1 pyramidal neurons. J. Comput. Neurosci. *33*, 207–225.

Binder, L.I., Frankfurter, A., and Rebhun, L.I. (1985). The distribution of tau in the mammalian central nervous system. J. Cell Biol. *101*, 1371–1378.

Black, M.M., Slaughter, T., Moshiach, S., Obrocka, M., and Fischer, I. (1996). Tau is enriched on dynamic microtubules in the distal region of growing axons. J. Neurosci. *16*, 3601–3619.

Blackmore, T., Meftah, S., Murray, T.K., Craig, P.J., Blockeel, A., Phillips, K., Eastwood, B., O'Neill, M.J., Marston, H., Ahmed, Z., et al. (2017). Tracking progressive pathological and functional decline in the rTg4510 mouse model of tauopathy. *9*, 77.

Bliss, T.V.P., and Collingridge, G.L. (1993). A synaptic model of memory: long-term potentiation in the hippocampus. Nature *361*, 31–39.

Bliss, T.V.P., and Lømo, T. (1973). Long-lasting potentiation of synaptic transmission in the dentate area of the anaesthetized rabbit following stimulation of the perforant path. J. Physiol. *232*, 331–356.

Booth, C.A., Brown, J.T., and Randall, A.D. (2014). Neurophysiological modification of CA1 pyramidal neurons in a transgenic mouse expressing a truncated form of disrupted-in-schizophrenia 1. Eur. J. Neurosci. *39*, 1074–1090.

Booth, C.A., Witton, J., Nowacki, J., Tsaneva-Atanasova, K., Jones, M.W., Randall, A.D., and Brown, J.T. (2016a). Altered Intrinsic Pyramidal Neuron Properties and Pathway-Specific Synaptic Dysfunction Underlie Aberrant Hippocampal Network Function in a Mouse Model of Tauopathy. J. Neurosci. *36*, 350–363.

Booth, C.A., Ridler, T., Murray, T.K., Ward, M.A., de Groot, E., Goodfellow, M., Phillips, K.G., Randall, A.D., and Brown, J.T. (2016b). Electrical and Network Neuronal Properties Are Preferentially Disrupted in Dorsal, But Not Ventral, Medial Entorhinal Cortex in a Mouse Model of Tauopathy. J. Neurosci. *36*, 312–324.

Borroni, B., Stanic, J., Verpelli, C., Mellone, M., Bonomi, E., Alberici, A., Bernasconi, P., Culotta, L., Zianni, E., Archetti, S., et al. (2017). Anti-AMPA GluA3 antibodies in Frontotemporal dementia: A new molecular target. Sci. Rep. *7*, 1–10.

Boulter, J., Hollmann, M., O'Shea-Greenfield, A., Hartley, M., Deneris, E., Maron, C., and Heinemann, S. (1990). Molecular cloning and functional expression of glutamate receptor subunit genes. Science (80-.). *249*, 1033–1037.

Bourassa, J., Pinault, D., and Deschênes, M. (1995). Corticothalamic Projections from the Cortical Barrel Field to the Somatosensory Thalamus in Rats: A Single-fibre Study Using Biocytin as an Anterograde Tracer. Eur. J. Neurosci. *7*, 19–30.

Bourne, J., and Harris, K.M. (2007). Do thin spines learn to be mushroom spines that remember? Curr. Opin. Neurobiol. *17*, 381–386.

Bourne, J.A., and Rosa, M.G.P. (2006). Hierarchical Development of the Primate Visual Cortex, as Revealed by Neurofilament Immunoreactivity: Early Maturation of the Middle Temporal Area (MT). Cereb. Cortex *16*, 405–414.

Boxer, A.L., Knopman, D.S., Kaufer, D.I., Grossman, M., Onyike, C., Graf-Radford, N., Mendez, M., Kerwin, D., Lerner, A., Wu, C.K., et al. (2013). Memantine in patients with frontotemporal lobar degeneration: A multicentre, randomised, double-blind, placebo-controlled trial. Lancet Neurol. *12*, 149–156.

Braak, H., and Braak, E. (1991). Neuropathological stageing of Alzheimer-related changes. Acta Neuropathol. *82*, 239–259.

Braak, F., Braak, H., and Mandelkow, E.M. (1994). A sequence of cytoskeleton changes related to the formation of neurofibrillary tangles and neuropil threads. Acta

Neuropathol. *87*, 554–567.

Braak, H., Alafuzov, I., Arzberger, T., Kretzschmar, H., Kelly, ·, and Tredici, D. (2006). Staging of Alzheimer disease-associated neurofibrillary pathology using paraffin sections and immunocytochemistry. Acta Neuropathol *112*, 389–404.

Braak, H., Thal, D.R., Ghebremedhin, E., and Del Tredici, K. (2011). Stages of the Pathologic Process in Alzheimer Disease: Age Categories From 1 to 100 Years. J. Neuropathol. Exp. Neurol. *70*, 960–969.

Brecht, M., Roth, A., and Sakmann, B. (2003). Dynamic Receptive Fields of Reconstructed Pyramidal Cells in Layers 3 and 2 of Rat Somatosensory Barrel Cortex. J. Physiol. *553*, 243–265.

Bridi, M.C.D., Zong, F.J., Min, X., Luo, N., Tran, T., Qiu, J., Severin, D., Zhang, X.T., Wang, G., Zhu, Z.J., et al. (2020). Daily Oscillation of the Excitation-Inhibition Balance in Visual Cortical Circuits. Neuron *105*, 621-629.e4.

Brodmann, K. (1909). Vergleichende Lokalisationslehre der Grosshirnrinde in ihren Prinzipien dargestellt auf Grund des Zellenbaues (Barth).

Brumberg, J.C., Pinto, D.J., and Simons, D.J. (1996). Spatial gradients and inhibitory summation in the rat whisker barrel system. J. Neurophysiol. *76*, 130–140.

Brunello, C.A., Merezhko, M., Uronen, R.L., and Huttunen, H.J. (2020). Mechanisms of secretion and spreading of pathological tau protein. Cell. Mol. Life Sci. *77*, 1721–1744.

Bryda, E.C. (2013). The Mighty Mouse: the impact of rodents on advances in biomedical research. Mo. Med. *110*, 207–211.

Burden, D.W. (2012). Guide to the disruption of biological samples-2012. Random Prim. *12*, 1–25.

Burnashev, N., Khodorova, A., Jonas, P., Helm, P.J., Wisden, W., Monyer, H., Seeburg, P.H., and Sakmann, B. (1992). Calcium-permeable AMPA-kainate receptors in fusiform cerebellar glial cells. Science (80-.). *256*, 1566–1570.

Busche, M.A., Wegmann, S., Dujardin, S., Commins, C., Schiantarelli, J., Klickstein, N., Kamath, T. V., Carlson, G.A., Nelken, I., and Hyman, B.T. (2019). Tau impairs

neural circuits, dominating amyloid-β effects, in Alzheimer models in vivo. Nat. Neurosci.

Busse, B., and Smith, S. (2013). Automated Analysis of a Diverse Synapse Population. PLoS Comput. Biol. *9*, e1002976.

Buzsaki, G. (2006). Rhythms of the Brain (Oxford University Press).

Cadwell, C.R., Palasantza, A., Jiang, X., Berens, P., Deng, Q., Yilmaz, M., Reimer, J., Shen, S., Bethge, M., Tolias, K.F., et al. (2016). Electrophysiological, transcriptomic and morphologic profiling of single neurons using Patch-seq. Nat. Biotechnol. *34*, 199–203.

de Calignon, A., Spires-Jones, T.L., Pitstick, R., Carlson, G.A., and Hyman, B.T. (2009). Tangle-Bearing Neurons Survive Despite Disruption of Membrane Integrity in a Mouse Model of Tauopathy. J. Neuropathol. Exp. Neurol. *68*, 757–761.

Cane, M., Maco, B., Knott, G., and Holtmaat, A. (2014). The relationship between PSD-95 clustering and spine stability In Vivo. J. Neurosci. *34*, 2075–2086.

Capone, F., Paolucci, M., Assenza, F., Brunelli, N., Ricci, L., Florio, L., and Di Lazzaro, V. (2016). Canonical cortical circuits: current evidence and theoretical implications. Neurosci. Neuroeconomics *5*, 1–8.

Castanho, I., Murray, T.K., Hannon, E., Jeffries, A., Walker, E., Laing, E., Baulf, H., Harvey, J., Randall, A., Moore, K., et al. (2019). Transcriptional signatures of progressive neuropathology in transgenic tau and amyloid mouse models. BioRxiv 548578.

Castillo, P.E., Malenka, R.C., and Nicoll, R.A. (1997). Kainate receptors mediate a slow postsynaptic current in hippocampal CA3 neurons. Nature *388*, 182–186.

del Castillo, J., and Katz, B. (1954). Quantal components of the end-plate potential. J. Physiol. *124*, 560–573.

del Castillo, J., and Katz, B. (1956a). Localization of active spots within the neuromuscular junction of the frog. J. Physiol. *132*, 630–649.

del Castillo, J., and Katz, B. (1956b). Biophysical aspects of neuromuscular transmission. Prog Biophys Biophys Chem *6*, 121–170.

Cathala, L., Misra, C., and Cull-Candy, S. (2000). Developmental profile of the changing properties of NMDA receptors at cerebellar mossy fiber-granule cell synapses. J. Neurosci. *20*, 5899–5905.

Cauller, L. (1995). Layer I of primary sensory neocortex: where top-down converges upon bottom-up. Behav. Brain Res. *71*, 163–170.

Cauller, L.J., and Connors, B.W. (1994). Synaptic physiology of horizontal afferents to layer I in slices of rat SI neocortex. J. Neurosci. *14*, 751–762.

Cecilia Angulo, M., Lambolez, B., Audinat, E., Hestrin, S., and Rossier, J. (1997). Subunit Composition, Kinetic, and Permeation Properties of AMPA Receptors in Single Neocortical Nonpyramidal Cells. J. Neurosci. *17*, 6685–6696.

Chartier-Harlin, M.C., Crawford, F., Houlden, H., Warren, A., Hughes, D., Fidani, L., Goate, A., Rossor, M., Roques, P., Hardy, J., et al. (1991). Early-onset Alzheimer's disease caused by mutations at codon 717 of the β-amyloid precursor protein gene. Nature *353*, 844–846.

Chatterton, J.E., Awobuluyi, M., Premkumar, L.S., Takahashi, H., Talantova, M., Shin, Y., Cul, J., Tu, S., Sevarino, K.A., Nakanishi, N., et al. (2002). Excitatory glycine receptors containing the NR3 family of NMDA receptor subunits. Nature *415*, 793–798.

Chauvette, S., Volgushev, M., and Timofeev, I. (2010). Origin of active states in local neocortical networks during slow sleep oscillation. Cereb. Cortex *20*, 2660–2674.

Cheetham, C.E.J., Barnes, S.J., Albieri, G., Knott, G.W., and Finnerty, G.T. (2014). Pansynaptic enlargement at adult cortical connections strengthened by experience. Cereb. Cortex *24*, 521–531.

Chen, F., Tillberg, P.W., and Boyden, E.S. (2015a). Expansion microscopy. Science (80-.). *347*, 543–548.

Chen, L., Chetkovich, D.M., Petralia, R.S., Sweeney, N.T., Kawasaki, Y., Wenthold, R.J., Bredt, D.S., and Nicoll, R.A. (2000). Stargazin regulates synaptic targeting of AMPA receptors by two distinct mechanisms. Nature *408*, 936–943.

Chen, Q., Zhou, Z., Zhang, L., Wang, Y., Zhang, Y.W., Zhong, M., Xu, S.C., Chen, C.H., Li, L., and Yu, Z.P. (2012). Tau protein is involved in morphological plasticity in

hippocampal neurons in response to BDNF. Neurochem. Int. *60*, 233–242.

Chen, X., Rochefort, N.L., Sakmann, B., and Konnerth, A. (2013). Reactivation of the Same Synapses during Spontaneous Up States and Sensory Stimuli. Cell Rep. *4*, 31–39.

Chen, X., Levy, J.M., Hou, A., Winters, C., Azzam, R., Sousa, A.A., Leapman, R.D., Nicoll, R.A., and Reese, T.S. (2015b). PSD-95 family MAGUKs are essential for anchoring AMPA and NMDA receptor complexes at the postsynaptic density. Proc. Natl. Acad. Sci. U. S. A. *112*, E6983–E6992.

Cheng, C.H., and Lin, Y.Y. (2013). Aging-related decline in somatosensory inhibition of the human cerebral cortex. Exp. Brain Res. *226*, 145–152.

Chmielowska, J., Carvell, G.E., and Simons, D.J. (1989). Spatial organization of thalamocortical and corticothalamic projection systems in the rat SmI barrel cortex. J. Comp. Neurol. *285*, 325–338.

Choi, D.W. (1988). Glutamate neurotoxicity and diseases of the nervous system. Neuron *1*, 623–634.

Ciabarra, A.M., Sullivan, J.M., Gahn, L.G., Pecht, G., Heinemann, S., and Sevarino, K.A. (1995). Cloning and characterization of χ-1: A developmentally regulated member of a novel class of the ionotropic glutamate receptor family. J. Neurosci. *15*, 6498–6508.

Citri, A., and Malenka, R.C. (2008). Synaptic plasticity: Multiple forms, functions, and mechanisms. Neuropsychopharmacology *33*, 18–41.

Clavaguera, F., Akatsu, H., Fraser, G., Crowther, R.A., Frank, S., Hench, J., Probst, A., Winkler, D.T., Reichwald, J., Staufenbiel, M., et al. (2013). Brain homogenates from human tauopathies induce tau inclusions in mouse brain. Proc. Natl. Acad. Sci. U. S. A. *110*, 9535–9540.

Clement, E.A., Richard, A., Thwaites, M., Ailon, J., Peters, S., and Dickson, C.T. (2008). Cyclic and Sleep-Like Spontaneous Alternations of Brain State Under Urethane Anaesthesia. PLoS One *3*, e2004.

Clements, J.D.D., and Bekkers, J.M.M. (1997). Detection of spontaneous synaptic events with an optimally scaled template. Biophys. J. *73*, 220–229.

Collingridge, G.L., Olsen, R.W., Peters, J., and Spedding, M. (2009). A nomenclature for ligand-gated ion channels. Neuropharmacology *56*, 2–5.

Cossart, R., Aronov, D., and Yuste, R. (2003). Attractor dynamics of network UP states in the neocortex. Nature *423*, 283–288.

Cowan, C.M., and Mudher, A. (2013). Are tau aggregates toxic or protective in tauopathies? Front. Neurol. *4 AUG*, 114.

Crill, W.E., and Schwindt, P.C. (1983). Active currents in mammalian central neurons. Trends Neurosci. *6*, 236–240.

Crimins, J.L., Rocher, A.B., Peters, A., Shultz, P., Lewis, J., and Luebke, J.I. (2011). Homeostatic responses by surviving cortical pyramidal cells in neurodegenerative tauopathy. Acta Neuropathol. *122*, 551–564.

Crimins, J.L., Rocher, A.B., and Luebke, J.I. (2012). Electrophysiological changes precede morphological changes to frontal cortical pyramidal neurons in the rTg4510 mouse model of progressive tauopathy. Acta Neuropathol. *124*, 777–795.

Crimins, J.L., Pooler, A., Polydoro, M., Luebke, J.I., and Spires-Jones, T.L. (2013). The intersection of amyloid beta and tau in glutamatergic synaptic dysfunction and collapse in Alzheimer's disease. Ageing Res. Rev. *12*, 757–763.

D'Orange, M., Aurégan, G., Cheramy, D., Gaudin-Guérif, M., Lieger, S., Guillermier, M., Stimmer, L., Joséphine, C., Hérard, A.S., Gaillard, M.C., et al. (2018). Potentiating tangle formation reduces acute toxicity of soluble tau species in the rat. Brain *141*, 535–549.

D'Souza, I., and Schellenberg, G.D. (2005). Regulation of tau isoform expression and dementia. Biochim. Biophys. Acta - Mol. Basis Dis. *1739*, 104–115.

Dalby, N.O., Volbracht, C., Helboe, L., Larsen, P.H., Jensen, H.S., Egebjerg, J., and Elvang, A.B. (2014). Altered function of hippocampal CA1 pyramidal neurons in the rTg4510 mouse model of tauopathy. J. Alzheimer's Dis. *40*, 429–442.

Danysz, W., and Parsons, C.G. (2003). The NMDA receptor antagonist memantine as a symptomatological and neuroprotective treatment for Alzheimer's disease: Preclinical evidence. In International Journal of Geriatric Psychiatry, (John Wiley & Sons, Ltd), pp. S23–S32.

Dawson, T.M., Golde, T.E., and Lagier-Tourenne, C. (2018). Animal models of neurodegenerative diseases. Nat. Neurosci. *21*, 1370–1379.

Decker, J.M., Krüger, L., Sydow, A., Dennissen, F.J., Siskova, Z., Mandelkow, E., and Mandelkow, E. (2016). The Tau/A152T mutation, a risk factor for frontotemporal-spectrum disorders, leads to NR 2B receptor-mediated excitotoxicity . EMBO Rep. *17*, 552–569.

DeVos, S.L., Corjuc, B.T., Commins, C., Dujardin, S., Bannon, R.N., Corjuc, D., Moore, B.D., Bennett, R.E., Jorfi, M., Gonzales, J.A., et al. (2018). Tau reduction in the presence of amyloid-β prevents tau pathology and neuronal death in vivo. Brain *141*, 2194–2212.

Dewar, D., Chalmers, D.T., Graham, D.I., and McCulloch, J. (1991). Glutamate metabotropic and AMPA binding sites are reduced in Alzheimer's disease: an autoradiographic study of the hippocampus. Brain Res. *553*, 58–64.

Dickson, D.W., Kouri, N., Murray, M.E., and Josephs, K.A. (2011). Neuropathology of frontotemporal lobar degeneration-Tau (FTLD-Tau). J. Mol. Neurosci. *45*, 384–389.

Dickstein, D.L., Brautigam, H., Stockton, S.D., Schmeidler, J., and Hof, P.R. (2010). Changes in dendritic complexity and spine morphology in transgenic mice expressing human wild-type tau. Brain Struct. Funct. *214*, 161–179.

Dieterich, D.C., and Kreutz, M.R. (2016). Proteomics of the synapse - A quantitative approach to neuronal plasticity. Mol. Cell. Proteomics *15*, 368–381.

Dodge, F.A., and Rahamimoff, R. (1967). Co-operative action of calcium ions in transmitter release at the neuromuscular junction. J. Physiol. *193*, 419–432.

Doi, A., Mizuno, M., Katafuchi, T., Furue, H., Koga, K., and Yoshimura, M. (2007). Slow oscillation of membrane currents mediated by glutamatergic inputs of rat somatosensory cortical neurons: in vivo patch-clamp analysis. Eur. J. Neurosci. *26*, 2565–2575.

Douglas, R.J., and Martin, K.A. (1991). A functional microcircuit for cat visual cortex. J. Physiol. *440*, 735–769.

Douglas, R.J., and Martin, K.A.C. (2010). Canonical cortical circuits. Handb. Brain Microcircuits 15–21.

Douglas, R.J., Martin, K.A.C., and Whitteridge, D. (1989). A Canonical Microcircuit for Neocortex. Neural Comput. *1*, 480–488.

Douglas, R.J., Koch, C., Mahowald, M., Martin, K.A.C., and Suarez, H.H. (1995). Recurrent excitation in neocortical circuits. Science (80-.). *269*, 981–985.

Dovzhenok, A., and Kuznetsov, A.S. (2012). Exploring Neuronal Bistability at the Depolarization Block. PLoS One *7*, e42811.

Drummond, E., and Wisniewski, T. (2017). Alzheimer's disease: experimental models and reality. Acta Neuropathol. *133*, 155–175.

Dujardin, S., Bégard, S., Caillierez, R., Lachaud, C., Carrier, S., Lieger, S., Gonzalez, J.A., Deramecourt, V., Déglon, N., Maurage, C.A., et al. (2018). Different tau species lead to heterogeneous tau pathology propagation and misfolding. Acta Neuropathol. Commun. *6*, 132.

Dunkley, P.R., and Robinson, P.J. (2018). Synaptosome preparations: Which procedure should I use? In Neuromethods, (Humana Press Inc.), pp. 27–53.

Dunkley, P.R., Jarvie, P.E., Heath, J.W., Kidd, G.J., and Rostas, J.A.P. (1986). A rapid method for isolation of synaptosomes on Percoll gradients. Brain Res. *372*, 115–129.

Dutar, P., and Nicoll, R.A. (1988). A physiological role for GABAB receptors in the central nervous system. Nature *332*, 156–158.

Eckermann, K., Mocanu, M.-M., Khlistunova, I., Biernat, J., Nissen, A., Hofmann, A., Schö, K., Bujard, H., Haemisch, A., Mandelkow, E., et al. (2007). The β-Propensity of Tau Determines Aggregation and Synaptic Loss in Inducible Mouse Models of Tauopathy. J. Biol. Chem. *282*, 31755–31765.

Edelstein, A.D., Tsuchida, M.A., Amodaj, N., Pinkard, H., Vale, R.D., and Stuurman, N. (2014). Advanced methods of microscope control using μManager software. J. Biol. Methods *1*, 10.

Egorov, A. V., Hamam, B.N., Fransén, E., Hasselmo, M.E., and Alonso, A.A. (2002). Graded persistent activity in entorhinal cortex neurons. Nature *420*, 173–178.

Ehrlich, I., Klein, M., Rumpel, S., and Malinow, R. (2007). PSD-95 is required for activity-driven synapse stabilization. Proc. Natl. Acad. Sci. U. S. A. *104*, 4176–4181.

El-Husseini, A.E., Schnell, E., Chetkovich, D.M., Nicoll, R.A., and Bredt, D.S. (2000). PSD-95 involvement in maturation of excitatory synapses. Science *290*, 1364–1368.

Elias, G.M., Funke, L., Stein, V., Grant, S.G., Bredt, D.S., and Nicoll, R.A. (2006). Synapse-Specific and Developmentally Regulated Targeting of AMPA Receptors by a Family of MAGUK Scaffolding Proteins. Neuron *52*, 307–320.

Ellenbroek, B., and Youn, J. (2016). Rodent models in neuroscience research: Is it a rat race? DMM Dis. Model. Mech. *9*, 1079–1087.

Engert, F., and Bonhoeffer, T. (1999). Dendritic spine changes associated with hippocampal long-term synaptic plasticity. Nature *399*, 66–70.

Erreger, K., Geballe, M.T., Kristensen, A., Chen, P.E., Hansen, K.B., Lee, C.J., Yuan, H., Le, P., Lyuboslavsky, P.N., Micale, N., et al. (2007). Subunit-specific agonist activity at NR2A-, NR2B-, NR2C-, and NR2D-containing N-methyl-D-aspartate glutamate receptors. Mol. Pharmacol. *72*, 907–920.

Erzurumlu, R.S., Bates, C.A., and Killackey, H.P. (1980). Differential organization of thalamic projection cells in the brain stem trigeminal complex of the rat. Brain Res. *198*, 427–433.

Evans, G.J.O. (2015). The synaptosome as a model system for studying synaptic physiology. Cold Spring Harb. Protoc. *2015*, 421–424.

Evans, A.J., Gurung, S., Henley, J.M., Nakamura, Y., and Wilkinson, K.A. (2019). Exciting Times: New Advances Towards Understanding the Regulation and Roles of Kainate Receptors. Neurochem. Res. *44*, 572–584.

Falcon, B., Cavallini, A., Angers, R., Glover, S., Murray, T.K., Barnham, L., Jackson, S., O'Neill, M.J., Isaacs, A.M., Hutton, M.L., et al. (2015). Conformation determines the seeding potencies of native and recombinant Tau aggregates. J. Biol. Chem. *290*, 1049–1065.

Fatt, P., and Katz, B. (1951). An analysis of the end-plate potential recorded with an intra-cellular electrode. J. Physiol. *115*, 320–370.

Fatt, P., and Katz, B. (1952). Spontaneous subthreshold activity at motor nerve endings. J. Physiol. *117*, 109–128.

Fein, J.A., Sokolow, S., Miller, C.A., Vinters, H. V., Yang, F., Cole, G.M., and Gylys, K.H. (2008). Co-localization of amyloid beta and tau pathology in Alzheimer's disease synaptosomes. Am. J. Pathol. *172*, 1683–1692.

Feldmeyer, D., Egger, V., Lübke, J., and Sakmann, B. (1999). Reliable synaptic connections between pairs of excitatory layer 4 neurones within a single 'barrel'of developing rat somatosensory cortex. J. Physiol. *521*, 169–190.

Feldmeyer, D., Lübke, J., Silver, R.A., and Sakmann, B. (2002). Synaptic connections between layer 4 spiny neurone-layer 2/3 pyramidal cell pairs in juvenile rat barrel cortex: physiology and anatomy of interlaminar signalling within a cortical column. J. Physiol. *538*, 803–822.

Feldmeyer, D., Lübke, J., and Sakmann, B. (2006). Efficacy and connectivity of intracolumnar pairs of layer 2/3 pyramidal cells in the barrel cortex of juvenile rats. J. Physiol. *575*, 583–602.

Fell, J., and Axmacher, N. (2011). The role of phase synchronization in memory processes. Nat. Rev. Neurosci. *12*, 105–118.

Fernandez, F.R., Rahsepar, B., and White, J.A. (2018). Differences in the electrophysiological properties of mouse somatosensory layer 2/3 neurons In vivo and slice stem from intrinsic sources rather than a network-generated high conductance state. ENeuro *5*.

Ferrarese, L., Jouhanneau, J.S., Remme, M.W.H., Kremkow, J., Katona, G., Rózsa, B., Schreiber, S., and Poulet, J.F.A. (2018). Dendrite-Specific Amplification of Weak Synaptic Input during Network Activity In Vivo. Cell Rep. *24*, 3455-3465.e5.

Ferreira, T.A., Blackman, A. V, Oyrer, J., Jayabal, S., Chung, A.J., Watt, A.J., Sjöström, P.J., and van Meyel, D.J. (2014). Neuronal morphometry directly from bitmap images. Nat. Methods *11*, 982–984.

Fiero, M.H. (2016). Statistical Approaches for Handling Missing Data in Cluster Randomized Trials Item Type text; Electronic Dissertation. The University of Arizona.

Fioravante, D., and Regehr, W.G. (2011). Short-term forms of presynaptic plasticity. Curr. Opin. Neurobiol. *21*, 269–274.

Fischer, M., Kaech, S., Wagner, U., Brinkhaus, H., and Matus, A. (2000). Glutamate

receptors regulate actin-based plasticity in dendritic spines. Nat. Neurosci. *3*, 887–894.

Flurkey, K., Currer, J.M., and Harrison, D.E. (2007). Mouse Models in Aging Research. In The Mouse in Biomedical Research, (Elsevier Inc.), pp. 637–672.

Foster, M., Sherrington, C.S., and University College, L.L.S. (1897). A Textbook of Physiology. With C.S. Sherrington. Part 3. The Central Nervous System (Macmillan).

Foster, N.L., Wilhelmsen, K., Sima, A.A.F., Jones, M.Z., D'Amato, C.J., and Gilman, S. (1997). Frontotemporal dementia and parkinsonism linked to chromosome 17: A consensus conference. In Annals of Neurology, (John Wiley & Sons, Ltd), pp. 706–715.

Frandemiche, M.L., De Seranno, S., Rush, T., Borel, E., Elie, A., Arnal, I., Lanté, F., and Buisson, A. (2014). Activity-dependent tau protein translocation to excitatory synapse is disrupted by exposure to amyloid-beta oligomers. J. Neurosci. *34*, 6084–6097.

Frere, S., and Slutsky, I. (2018). Alzheimer's Disease: From Firing Instability to Homeostasis Network Collapse. Neuron *97*, 32–58.

Fu, H., Hardy, J., and Duff, K.E. (2018). Selective vulnerability in neurodegenerative diseases. Nat. Neurosci. *21*, 1350–1358.

Fu, H., Possenti, A., Freer, R., Nakano, Y., Villegas, N.C.H.H., Tang, M., Cauhy, P.V.M.M., Lassus, B.A., Chen, S., Fowler, S.L., et al. (2019). A tau homeostasis signature is linked with the cellular and regional vulnerability of excitatory neurons to tau pathology. Nat. Neurosci. *22*, 47–56.

Furukawa, H., Singh, S.K., Mancusso, R., and Gouaux, E. (2005). Subunit arrangement and function in NMDA receptors. Nature *438*, 185–192.

Fuzik, J., Zeisel, A., Mate, Z., Calvigioni, D., Yanagawa, Y., Szabo, G., Linnarsson, S., and Harkany, T. (2016). Integration of electrophysiological recordings with single-cell RNA-seq data identifies neuronal subtypes. Nat. Biotechnol. *34*, 175–183.

Gainey, M.A., Hurvitz-Wolff, J.R., Lambo, M.E., and Turrigiano, G.G. (2009). Synaptic scaling requires the GluR2 subunit of the AMPA receptor. J. Neurosci. *29*, 6479–6489.

Gamache, J., Benzow, K., Forster, C., Kemper, L., Hlynialuk, C., Furrow, E., Ashe, K.H., and Koob, M.D. (2019). Factors other than hTau overexpression that contribute to tauopathy-like phenotype in rTg4510 mice. Nat. Commun. *10*, 1–12.

Gambino, F., and Holtmaat, A. (2012). Spike-timing-dependent potentiation of sensory surround in the somatosensory cortex is facilitated by deprivation-mediated disinhibition. Neuron *75*, 490–502.

Gambino, F., Pagès, S., Kehayas, V., Baptista, D., Tatti, R., Carleton, A., and Holtmaat, A. (2014). Sensory-evoked LTP driven by dendritic plateau potentials in vivo. Nature *515*, 116–119.

Garner, C.C., Kindler, S., and Gundelfinger, E.D. (2000). Molecular determinants of presynaptic active zones. Curr. Opin. Neurobiol. *10*, 321–327.

Gascon, E., Lynch, K., Ruan, H., Almeida, S., Verheyden, J.M., Seeley, W.W., Dickson, D.W., Petrucelli, L., Sun, D., Jiao, J., et al. (2014). Alterations in microRNA-124 and AMPA receptors contribute to social behavioral deficits in frontotemporal dementia. Nat. Med. *20*, 1444–1451.

Gazzina, S., Benussi, A., Premi, E., Paternicò, D., Cristillo, V., Dell'Era, V., Cosseddu, M., Archetti, S., Alberici, A., Gasparotti, R., et al. (2018). Neuroanatomical Correlates of Transcranial Magnetic Stimulation in Presymptomatic Granulin Mutation Carriers. Brain Topogr. *31*, 488–497.

Geiger, J.R.P., Melcher, T., Koh, D.-S., Sakmann, B., Seeburg, P.H., Jonas, P., and Monyer, H. (1995). Relative abundance of subunit mRNAs determines gating and Ca2+ permeability of AMPA receptors in principal neurons and interneurons in rat CNS. Neuron *15*, 193–204.

Gelman, S., Palma, J., Tombaugh, G., and Ghavami, A. (2018). Differences in Synaptic Dysfunction Between rTg4510 and APP/PS1 Mouse Models of Alzheimer's Disease. J. Alzheimer's Dis. *61*, 195–208.

St. George-Hyslop, P.H., Tanzi, R.E., Polinsky, R.J., Haines, J.L., Nee, L., Watkins, P.C., Myers, R.H., Feldman, R.G., Pollen, D., Drachman, D., et al. (1987). The genetic defect causing familial Alzheimer's disease maps on chromosome 21. Science (80-.). *235*, 885–890.

Ghazanfar, A.A., and Schroeder, C.E. (2006). Is neocortex essentially multisensory? Trends Cogn. Sci. *10*, 278–285.

Glenner, G.G., and Wong, C.W. (1984). Alzheimer's disease and Down's syndrome: Sharing of a unique cerebrovascular amyloid fibril protein. Biochem. Biophys. Res. Commun. *122*, 1131–1135.

Goate, A., Chartier-Harlin, M.C., Mullan, M., Brown, J., Crawford, F., Fidani, L., Giuffra, L., Haynes, A., Irving, N., James, L., et al. (1991). Segregation of a missense mutation in the amyloid precursor protein gene with familial Alzheimer's disease. Nature *349*, 704–706.

Goedert, M., and Jakes, R. (2005). Mutations causing neurodegenerative tauopathies. Biochim. Biophys. Acta - Mol. Basis Dis. *1739*, 240–250.

Goedert, M., Spillantini, M.G., Jakes, R., Rutherford, D., and Crowther, R.A. (1989). Multiple isoforms of human microtubule-associated protein tau: sequences and localization in neurofibrillary tangles of Alzheimer's disease. Neuron *3*, 519–526.

Goedert, M., Jakes, R., and Vanmechelen, E. (1995). Monoclonal antibody AT8 recognises tau protein phosphorylated at both serine 202 and threonine 205. Neurosci. Lett. *189*, 167–170.

Goldman, D.E. (1943). Potential, impedance, and rectification in membranes. J. Gen. Physiol. *27*, 37–60.

González-Rueda, A., Pedrosa, V., Feord, R.C., Clopath, C., and Paulsen, O. (2018). Activity-Dependent Downscaling of Subthreshold Synaptic Inputs during Slow-Wave-Sleep-like Activity In Vivo. Neuron *97*, 1244-1252.e5.

Goodwin, L.O., Splinter, E., Davis, T.L., Urban, R., He, H., Braun, R.E., Chesler, E.J., Kumar, V., Min, M. van, Ndukum, J., et al. (2017). Large-scale discovery of mouse transgenic integration sites reveals frequent structural variation and insertional mutagenesis. BioRxiv 236307.

Götz, J., and Ittner, L.M. (2008). Animal models of Alzheimer's disease and frontotemporal dementia. Nat. Rev. Neurosci. *9*, 532–544.

Götz, J., Bodea, L.G., and Goedert, M. (2018). Rodent models for Alzheimer disease. Nat. Rev. Neurosci. *19*, 583–598.

Granger, A.J., and Nicoll, R.A. (2014). LTD expression is independent of glutamate receptor subtype. Front. Synaptic Neurosci. *6*, 15.

Granger, A.J., Shi, Y., Lu, W., Cerpas, M., and Nicoll, R.A. (2013). LTP requires a reserve pool of glutamate receptors independent of subunit type. Nature *493*, 495–500.

Gray, E.G., and Whittaker, V.P. (1962). The isolation of nerve endings from brain: an electron-microscopic study of cell fragments derived by homogenization and centrifugation. J. Anat. *96*, 79–88.

Green, C., Sydow, A., Vogel, S., Anglada-Huguet, M., Wiedermann, D., Mandelkow, E., Mandelkow, E.M., and Hoehn, M. (2019). Functional networks are impaired by elevated tau-protein but reversible in a regulatable Alzheimer's disease mouse model. Mol. Neurodegener. *14*, 13.

Grosskreutz, J., Zoerner, A., Schlesinger, F., Krampfl, K., Dengler, R., and Buffer, J. (2003). Kinetic properties of human AMPA-type glutamate receptors expressed in HEK293 cells. Eur. J. Neurosci. *17*, 1173–1178.

Grundke-Iqbal, I., Iqbal, K., Tung, Y.C., Quinlan, M., Wisniewski, H.M., and Binder, L.I. (1986). Abnormal phosphorylation of the microtubule-associated protein tau (tau) in Alzheimer cytoskeletal pathology. Proc. Natl. Acad. Sci. U. S. A. *83*, 4913–4917.

Guillery, R.W., and Sherman, S.M. (2002). Thalamic relay functions and their role in corticocortical communication: Generalizations from the visual system. Neuron *33*, 163–175.

Gupta, N., Singh, S.S., and Stopfer, M. (2016). Oscillatory integration windows in neurons. Nat. Commun. *7*.

Haider, B., Duque, A., Hasenstaub, A.R., and McCormick, D.A. (2006). Neocortical network activity in vivo is generated through a dynamic balance of excitation and inhibition. J. Neurosci. *26*, 4535–4545.

Halliwell, R.F., Peters, J.A., and Lambert, J.J. (1989). The mechanism of action and pharmacological specificity of the anticonvulsant NMDA antagonist MK-801: a voltage clamp study on neuronal cells in culture. Br. J. Pharmacol. *96*, 480–494.

Hansen, K.B., Yi, F., Perszyk, R.E., Furukawa, H., Wollmuth, L.P., Gibb, A.J., and

Traynelis, S.F. (2018). Structure, function, and allosteric modulation of NMDA receptors. J. Gen. Physiol. *150*, 1081–1105.

Hara, K., and Harris, R.A. (2002). The Anesthetic Mechanism of Urethane: The Effects on Neurotransmitter-Gated Ion Channels. Anesth. Analg. *94*, 313–318.

Hardingham, G.E., and Bading, H. (2010). Synaptic versus extrasynaptic NMDA receptor signalling: Implications for neurodegenerative disorders. Nat. Rev. Neurosci. *11*, 682–696.

Hardy, J.A., and Higgins, G.A. (1992). Alzheimer's Disease: The Amyloid Cascade Hypothesis. Science (80-.). *256*.

Harris, K.D., and Shepherd, G.M.G. (2015). The neocortical circuit: Themes and variations. Nat. Neurosci. *18*, 170–181.

Harris, S.S., Wolf, F., De Strooper, B., and Busche, M.A. (2020). Tipping the Scales: Peptide-Dependent Dysregulation of Neural Circuit Dynamics in Alzheimer's Disease. Neuron.

Harrison, I.F., Ismail, O., Machhada, A., Colgan, N., Ohene, Y., Nahavandi, P., Ahmed, Z., Fisher, A., Meftah, S., Murray, T.K., et al. (2020). Impaired glymphatic function and clearance of tau in an Alzheimer's disease model. Brain *143*, 2576–2593.

Hatch, R.J., Wei, Y., Xia, D., and Götz, J. (2017). Hyperphosphorylated tau causes reduced hippocampal CA1 excitability by relocating the axon initial segment. Acta Neuropathol. *133*, 717–730.

Hebb, D.O. (1949). The organization of behavior: a neuropsychological theory (J. Wiley; Chapman & Hall).

Hebb, C.O., and Whittaker, V.P. (1958). Intracellular distributions of acetylcholine and choline acetylase. J. Physiol. *142*, 187–196.

Heimer, L. (2012). The human brain and spinal cord: functional neuroanatomy and dissection guide (Springer Science & Business Media).

Henderson, D., and Miller, R.F. (2002). Evidence for low-voltage-activated (LVA) calcium currents in the dendrites of tiger salamander retinal ganglion cells. Vis. Neurosci. *20*, 141.

Henley, J.M. (2003). Proteins interactions implicated in AMPA receptor trafficking: A clear destination and an improving route map. Neurosci. Res. *45*, 243–254.

Henley, J.M., and Wilkinson, K.A. (2013). AMPA receptor trafficking and the mechanisms underlying synaptic plasticity and cognitive aging. Dialogues Clin. Neurosci. *15*, 11–27.

Herrup, K. (2015). The case for rejecting the amyloid cascade hypothesis. Nat. Neurosci. *18*, 794–799.

Heuser, J.E., and Reese, T.S. (1973). Evidence for recycling of synaptic vesicle membrane during transmitter release at the frog neuromuscular junction. J. Cell Biol. *57*, 315–344.

Hill, E., Karikari, T.K., Moffat, K.G., Richardson, M.J.E., and Wall, M.J. (2019). Introduction of Tau oligomers into cortical neurons alters action potential dynamics and disrupts synaptic transmission and plasticity. ENeuro *6*.

Hodgkin, A.L., and Huxley, A.F. (1952). A quantitative description of membrane current and its application to conduction and excitation in nerve. J. Physiol. *117*, 500–544.

Hodgkin, A.L., and Katz, B. (1949). The effect of sodium ions on the electrical activity of the giant axon of the squid. J. Physiol. *108*, 37–77.

Hoffmann, N.A., Dorostkar, M.M., Blumenstock, S., Goedert, M., and Herms, J. (2014). Impaired plasticity of cortical dendritic spines in P301S tau transgenic mice. Acta Neuropathol. Commun. *2*.

Hollmann, M., and Heinemann, S. (1994). Cloned Glutamate Receptors. Annu. Rev. Neurosci. *17*, 31–108.

Hollmann, M., O'Shea-Greenfield, A., Rogers, S.W., and Heinemann, S. (1989). Cloning by functional expression of a member of the glutamate receptor family. Nature *342*, 643–648.

Hollmann, M., Hartley, M., and Heinemann, S. (1991). Ca2+ permeability of KA-AMPA - gated glutamate receptor channels depends on subunit composition. Science (80-.). *252*, 851–853.

Holton, C., Hanley, N., Shanks, E., Oxley, P., McCarthy, A., Eastwood, B., Murray, T., Nickerson, A., and KA, W. (2020). Longitudinal changes in EEG power, sleep cycles and behaviour in a tau model of neurodegeneration. Alzheimers. Res. Ther. *12*.

Hoover, B.R., Reed, M.N., Su, J., Penrod, R.D., Kotilinek, L.A., Grant, M.K., Pitstick, R., Carlson, G.A., Lanier, L.M., Yuan, L.L., et al. (2010). Tau Mislocalization to Dendritic Spines Mediates Synaptic Dysfunction Independently of Neurodegeneration. Neuron *68*, 1067–1081.

Hubel, D.H., and Wiesel, T.N. (1959). Receptive fields of single neurones in the cat's striate cortex. J. Physiol. *148*, 574–591.

Hubel, D.H., and Wiesel, T.N. (1962). Receptive fields, binocular interaction and functional architecture in the cat's visual cortex. J. Physiol. *160*, 106–154.

Huettner, J.E., and Bean, B.P. (1988). Block of N-methyl-D-aspartate-activated current by the anticonvulsant MK-801: Selective binding to open channels. Proc. Natl. Acad. Sci. U. S. A. *85*, 1307–1311.

Hugo, J., and Ganguli, M. (2014). Dementia and Cognitive Impairment. Epidemiology, Diagnosis, and Treatment. Clin. Geriatr. Med. *30*, 421–442.

Huttner, W.B., Schiebler, W., Greengard, P., and De Camilli, P. (1983). Synapsin I (protein I), a nerve terminal-specific phosphoprotein. III. Its association with synaptic vesicles studied in a highly purified synaptic vesicle preparation. J. Cell Biol. *96*, 1374–1388.

Hutton, M. (2001). Missense and splice site mutations in tau associated with FTDP-17: Multiple pathogenic mechanisms. Neurology *56*, S21–S25.

Hutton, M., Lendon, C.L., Rizzu, P., Baker, M., Froelich, S., Houlden, H., Pickering-Brown, S., Chakraverty, S., Isaacs, A., Grover, A., et al. (1998). Association of missense and 5′-splice-site mutations in tau with the inherited dementia FTDP-17. Nature *393*, 702–705.

Iijima, K., Abe, H., Okazawa, M., Moriyoshi, K., and Nakanishi, S. (2008). Dual regulation of NR2B and NR2C expression by NMDA receptor activation in mouse cerebellar granule cell cultures. Proc. Natl. Acad. Sci. U. S. A. *105*, 12010–12015.

Iqbal, K., Del C. Alonso, A., Chen, S., Chohan, M.O., El-Akkad, E., Gong, C.X.,

Khatoon, S., Li, B., Liu, F., Rahman, A., et al. (2005). Tau pathology in Alzheimer disease and other tauopathies. Biochim. Biophys. Acta - Mol. Basis Dis. *1739*, 198–210.

Iqbal, K., Liu, F., Gong, C.-X., and Grundke-Iqbal, I. (2010). Tau in Alzheimer Disease and Related Tauopathies. Curr. Alzheimer Res. *7*, 656–664.

Irvine, G.B., El-Agnaf, O.M., Shankar, G.M., and Walsh, D.M. (2008). Protein aggregation in the brain: The molecular basis for Alzheimer's and Parkinson's diseases. Mol. Med. *14*, 451–464.

Irwin, D.J. (2016). Tauopathies as clinicopathological entities. Park. Relat. Disord. *22*, S29–S33.

Isaac, J.T.R., Nicoll, R.A., and Malenka, R.C. (1995). Evidence for silent synapses: Implications for the expression of LTP. Neuron *15*, 427–434.

Isaac, J.T.R., Ashby, M., and McBain, C.J. (2007). The Role of the GluR2 Subunit in AMPA Receptor Function and Synaptic Plasticity. Neuron *54*, 859–871.

Isaacson, J.S., and Scanziani, M. (2011). How inhibition shapes cortical activity. Neuron *72*, 231–243.

Ittner, L.M., and Götz, J. (2011). Amyloid-β and tau - A toxic pas de deux in Alzheimer's disease. Nat. Rev. Neurosci. *12*, 67–72.

Ittner, L.M., Ke, Y.D., Delerue, F., Bi, M., Gladbach, A., van Eersel, J., Wölfing, H., Chieng, B.C., Christie, M.J., Napier, I.A., et al. (2010). Dendritic function of tau mediates amyloid-β toxicity in alzheimer's disease mouse models. Cell *142*, 387–397.

Jack, C.R., Knopman, D.S., Jagust, W.J., Shaw, L.M., Aisen, P.S., Weiner, M.W., Petersen, R.C., and Trojanowski, J.Q. (2010). Hypothetical model of dynamic biomarkers of the Alzheimer's pathological cascade. Lancet Neurol. *9*, 119–128.

Jack Jr, C.R., Lowe, V.J., Weigand, S.D., Wiste, H.J., Senjem, M.L., Knopman, D.S., Shiung, M.M., Gunter, J.L., Boeve, B.F., Kemp, B.J., et al. (2009). Serial PIB and MRI in normal, mild cognitive impairment and Alzheimer's disease: implications for sequence of pathological events in Alzheimer's disease. Brain *132*, 1355–1365.

Jackson, J., Jambrina, E., Li, J., Marston, H., Menzies, F., Phillips, K., and Gilmour,

G. (2019). Targeting the synapse in Alzheimer's disease. Front. Neurosci. *13*.

Jackson, J.S., Witton, J., Johnson, J.D., Ahmed, Z., Ward, M., Randall, A.D., Hutton, M.L., Isaac, J.T., O'Neill, M.J., and Ashby, M.C. (2017). Altered Synapse Stability in the Early Stages of Tauopathy. Cell Rep. *18*, 3063–3068.

Jackson, J.S., Johnson, J.D., Meftah, S., Murray, T.K., Ahmed, Z., Fasiolo, M., Hutton, M.L., Isaac, J.T.R., O'Neill, M.J., and Ashby, M.C. (2020). Differential aberrant structural synaptic plasticity in axons and dendrites ahead of their degeneration in tauopathy. BioRxiv 2020.04.29.067629.

Jadhav, S., Cubinkova, V., Zimova, I., Brezovakova, V., Madari, A., Cigankova, V., and Zilka, N. (2015). Tau-mediated synaptic damage in Alzheimer's disease. Transl. Neurosci. *6*, 214–226.

Jaworski, T., Lechat, B., Demedts, D., Gielis, L., Devijver, H., Borghgraef, P., Duimel, H., Verheyen, F., Kgler, S., and Van Leuven, F. (2011). Dendritic degeneration, neurovascular defects, and inflammation precede neuronal loss in a mouse model for tau-mediated neurodegeneration. Am. J. Pathol. *179*, 2001–2015.

Jicha, G., Bowser, R., Kazam, I., and Davies, P. (1997). Alz-50 and MC-1, a new monoclonal antibody raised to paired helical filaments, recognize conformational epitopes on recombinant tau. J. Neurosci. Res. *48*.

Jicha, G.A., Berenfeld, B., and Davies, P. (1999). Sequence requirements for formation of conformational variants of tau similar to those found in Alzheimer's disease. J. Neurosci. Res. *55*, 713–723.

Johnston, D., and Wu, S.M.-S. (1994). Foundations of cellular neurophysiology (MIT press).

Jonas, P., Racca, C., Sakmann, B., Seeburg, P.H., and Monyer, H. (1994). Differences in Ca2+ permeability of AMPA-type glutamate receptor channels in neocortical neurons caused by differential GluR-B subunit expression. Neuron *12*, 1281–1289.

Jouhanneau, J.S., Ferrarese, L., Estebanez, L., Audette, N.J., Brecht, M., Barth, A.L., and Poulet, J.F.A. (2014). Cortical fos GFP expression reveals broad receptive field excitatory neurons targeted by pom. Neuron *84*, 1065–1078.

Kaas, J.H. (1987). The Organization of Neocortex in Mammals: Implications for

Theories of Brain Function. Annu. Rev. Psychol. *38*, 129–151.

Kandel, E.R., Schwartz, J.H., Jessell, T.M., Jessell, D. of B. and M.B.T., Siegelbaum, S., and Hudspeth, A.J. (2000). Principles of neural science (McGraw-hill New York).

Kaphzan, H., Buffington, S.A., Jung, J.I., Rasband, M.N., and Klann, E. (2011). Neurobiology of Disease Alterations in Intrinsic Membrane Properties and the Axon Initial Segment in a Mouse Model of Angelman Syndrome. J. Neurosci. *31*, 17637–17648.

Karavanova, I., Vasudevan, K., Cheng, J., and Buonanno, A. (2007). Novel regional and developmental NMDA receptor expression patterns uncovered in NR2C subunit-β-galactosidase knock-in mice. Mol. Cell. Neurosci. *34*, 468–480.

Karran, E., Mercken, M., and Strooper, B. De (2011). The amyloid cascade hypothesis for Alzheimer's disease: An appraisal for the development of therapeutics. Nat. Rev. Drug Discov. *10*, 698–712.

Katz, B. (1969). The release of neural transmitter substances. Liverpool Univ. Press 5–39.

Keinänen, K., Wisden, W., Sommer, B., Werner, P., Herb, A., Verdoorn, T.A., Sakmann, B., and Seeburg, P.H. (1990). A family of AMPA-selective glutamate receptors. Science (80-.). *249*, 556–560.

Kerr, J.N.D., De Kock, C.P.J., Greenberg, D.S., Bruno, R.M., Sakmann, B., and Helmchen, F. (2007). Spatial organization of neuronal population responses in layer 2/3 of rat barrel cortex. J. Neurosci. *27*, 13316–13328.

Kew, J.N.C., and Kemp, J.A. (2005). Ionotropic and metabotropic glutamate receptor structure and pharmacology. Psychopharmacology (Berl). *179*, 4–29.

Kheradpezhouh, E., Adibi, M., and Arabzadeh, E. (2017). Response dynamics of rat barrel cortex neurons to repeated sensory stimulation. Sci. Rep. *7*.

Kimm, T., Khaliq, Z.M., and Bean, B.P. (2015). Cellular/Molecular Differential Regulation of Action Potential Shape and Burst-Frequency Firing by BK and Kv2 Channels in Substantia Nigra Dopaminergic Neurons. J. Neurosci. *35*, 16404–16417.

Kishi, T., Matsunaga, S., and Iwata, N. (2015). Memantine for the treatment of

frontotemporal dementia: A meta-analysis. Neuropsychiatr. Dis. Treat. *11*, 2883–2885.

Kitamura, K., Judkewitz, B., Kano, M., Denk, W., and Häusser, M. (2008). Targeted patch-clamp recordings and single-cell electroporation of unlabeled neurons in vivo. Nat. Methods *5*, 61–67.

Kodandaramaiah, S.B., Flores, F.J., Holst, G.L., Singer, A.C., Han, X., Brown, E.N., Boyden, E.S., and Forest, C.R. (2018). Multi-neuron intracellular recording in vivo via interacting autopatching robots. Elife *7*.

Köhr, G. (2006). NMDA receptor function: Subunit composition versus spatial distribution. Cell Tissue Res. *326*, 439–446.

Konorski, J. (1948). Conditioned reflexes and neuron organization.

Kopeikina, K.J., Hyman, B.T., and Spires-Jones, T.L. (2012). Soluble forms of tau are toxic in Alzheimer's disease. Transl. Neurosci. *3*, 223–233.

Kopeikina, K.J., Polydoro, M., Tai, H.-C.C., Yaeger, E., Carlson, G.A., Pitstick, R., Hyman, B.T., and Spires-Jones, T.L. (2013a). Synaptic alterations in the rTg4510 mouse model of tauopathy. J. Comp. Neurol. *521*, 1334–1353.

Kopeikina, K.J., Wegmann, S., Pitstick, R., Carlson, G.A., Bacskai, B.J., Betensky, R.A., Hyman, B.T., and Spires-Jones, T.L. (2013b). Tau Causes Synapse Loss without Disrupting Calcium Homeostasis in the rTg4510 Model of Tauopathy. PLoS One *8*, e80834.

Kopke, E., Tung, Y.-C., Shaikh, S., Alonso, A.D.C., Iqbal, K., and Grundke-Iqbals, I. (1993). Microtubule-associated protein tau. Abnormal phosphorylation of a non-paired helical filament pool in Alzheimer disease. J. Biol. Chem. *268*, 24374–24384.

Koralek, K. -A, Olavarria, J., and Kellackey, H.P. (1990). Areal and laminar organization of corticocortical projections in the rat somatosensory cortex. J. Comp. Neurol. *299*, 133–150.

Koralek, K.A., Jensen, K.F., and Killackey, H.P. (1988). Evidence for two complementary patterns of thalamic input to the rat somatosensory cortex. Brain Res. *463*, 346–351.

Koss, D.J., Robinson, L., Drever, B.D., Plucińska, K., Stoppelkamp, S., Veselcic, P., Riedel, G., and Platt, B. (2016). Mutant Tau knock-in mice display frontotemporal dementia relevant behaviour and histopathology. Neurobiol. Dis. *91*, 105–123.

Kovacs, G.G. (2015). Neuropathology of tauopathies: Principles and practice. Neuropathol. Appl. Neurobiol. *41*, 3–23.

Krnjević, K., and Schwartz, S. (1967). The action of γ-Aminobutyric acid on cortical neurones. Exp. Brain Res. *3*, 320–336.

Kuchibhotla, K. V, Wegmann, S., Kopeikina, K.J., Hawkes, J., Rudinskiy, N., Andermann, M.L., Spires-Jones, T.L., Bacskai, B.J., and Hyman, B.T. (2014). Neurofibrillary tangle-bearing neurons are functionally integrated in cortical circuits in vivo. Proc. Natl. Acad. Sci. U. S. A. *111*, 510–514.

Kunishima, N., Shimada, Y., Tsuji, Y., Sato, T., Yamamoto, M., Kumasaka, T., Nakanishi, S., Jingami, H., and Morikawa, K. (2000). Structural basis of glutamate recognition by a dimeric metabotropic glutamate receptor. Nature *407*, 971–977.

Küppenbender, K.D., Standaert, D.G., Feuerstein, T.J., Penney, J.B., Young, A.B., and Landwehrmeyer, G.B. (2000). Expression of NMDA receptor subunit mRNAs in neurochemically identified projection and interneurons in the human striatum. J. Comp. Neurol. *419*, 407–421.

Kwon, S.E., and Chapman, E.R. (2011). Synaptophysin Regulates the Kinetics of Synaptic Vesicle Endocytosis in Central Neurons. Neuron *70*, 847–854.

LaFerla, F.M., and Green, K.N. (2012). Animal models of Alzheimer disease. Cold Spring Harb. Perspect. Med. *2*.

Lampl, I., Reichova, I., and Ferster, D. (1999). Synchronous membrane potential fluctuations in neurons of the cat visual cortex. Neuron *22*, 361–374.

Land, P.W., Buffer, S.A., and Yaskosky, J.D. (1995). Barreloids in adult rat thalamus: Three-dimensional architecture and relationship to somatosensory cortical barrels. J. Comp. Neurol. *355*, 573–588.

Lao, K., Ji, N., Zhang, X., Qiao, W., Tang, Z., and Gou, X. (2019). Drug development for Alzheimer's disease: review. J. Drug Target. *27*, 164–173.

Lasagna-Reeves, C.A., Castillo-Carranza, D.L., Sengupta, U., Clos, A.L., Jackson, G.R., and Kayed, R. (2011). Tau oligomers impair memory and induce synaptic and mitochondrial dysfunction in wild-type mice. Mol. Neurodegener. *6*, 39.

Lau, C.G., Takeuchi, K., Rodenas-Ruano, A., Takayasu, Y., Murphy, J., Bennett, M.V.I., and Zukin, R.S. (2009). Regulation of NMDA receptor Ca2+ signalling and synaptic plasticity. Biochem. Soc. Trans. *37*, 1369–1374.

Laube, B., Kuhse, J., and Betz, H. (1998). Evidence for a tetrameric structure of recombinant NMDA receptors. J. Neurosci. *18*, 2954–2961.

Lavzin, M., Rapoport, S., Polsky, A., Garion, L., and Schiller, J. (2012). Nonlinear dendritic processing determines angular tuning of barrel cortex neurons in vivo. Nature *490*, 397–401.

Lazic, S.E. (2010). The problem of pseudoreplication in neuroscientific studies: Is it affecting your analysis? BMC Neurosci. *11*, 1–17.

Lebedeva, J., Zakharov, A., Burkhanova, G., Chernova, K., and Khazipov, R. (2019). The Effects of NMDA Receptor Blockade on Sensory-Evoked Responses in Superficial Layers of the Rat Barrel Cortex. Front. Cell. Neurosci. *13*, 259.

Lee, K.J., and Woolsey, T.A. (1975). A proportional relationship between peripheral innervation density and cortical neuron number in the somatosensory system of the mouse. Brain Res. *99*, 349–353.

Lee, L.J., Lo, F.S., and Erzurumlu, R.S. (2005). NMDA receptor-dependent regulation of axonal and dendritic branching. J. Neurosci. *25*, 2304–2311.

Lee, M.-C., Ting, K.K., Adams, S., Brew, B.J., Chung, R., and Guillemin, G.J. (2010). Characterisation of the Expression of NMDA Receptors in Human Astrocytes. PLoS One *5*, e14123.

Lefort, S., and Petersen, C.C.H. (2017). Layer-Dependent Short-Term Synaptic Plasticity Between Excitatory Neurons in the C2 Barrel Column of Mouse Primary Somatosensory Cortex. Cereb. Cortex *27*, 3869–3878.

Lefort, S., Tomm, C., Floyd Sarria, J.C., and Petersen, C.C.H. (2009). The Excitatory Neuronal Network of the C2 Barrel Column in Mouse Primary Somatosensory Cortex. Neuron *61*, 301–316.

Lerma, J., and Marques, J.M. (2013). Kainate receptors in health and disease. Neuron *80*, 292–311.

Léveillé, F., El gaamouch, F., Gouix, E., Lecocq, M., Lobner, D., Nicole, O., and Buisson, A. (2008). Neuronal viability is controlled by a functional relation between synaptic and extrasynaptic NMDA receptors. FASEB J. *22*, 4258–4271.

Levy, E., Carman, M.D., Fernandez-Madrid, I.J., Power, M.D., Lieberburg, I., Van Duinen, S.G., Bots, G.T.A.M., Luyendijk, W., and Frangione, B. (1990). Mutation of the Alzheimer's disease amyloid gene in hereditary cerebral hemorrhage, Dutch type. Science (80-.). *248*, 1124–1126.

Lindwall, G., and Cole, D.R. (1984). Phosphorylation Affects the Ability of Tau Protein to Promote Microtubule Assembly. J. Biol. Chem. *259*, 5301–5305.

Liu, F., and Gong, C.X. (2008). Tau exon 10 alternative splicing and tauopathies. Mol. Neurodegener. *3*, 8.

Liu, J., Chang, L., Song, Y., Li, H., and Wu, Y. (2019). The role of NMDA receptors in Alzheimer's disease. Front. Neurosci. *13*.

Liu, Y., Tak, P.W., Aarts, M., Rooyakkers, A., Liu, L., Ted, W.L., Dong, C.W., Lu, J., Tymianski, M., Craig, A.M., et al. (2007). NMDA receptor subunits have differential roles in mediating excitotoxic neuronal death both in vitro and in vivo. J. Neurosci. *27*, 2846–2857.

Lomeli, H., Mosbacher, J., Melcher, T., Höger, T., Geiger, J.R.P., Kuner, T., Monyer, H., Higuchi, M., Bach, A., and Seeburg, P.H. (1994). Control of kinetic properties of AMPA receptor channels by nuclear RNA editing. Science (80-.). *266*, 1709–1713.

Longair, M.H., Baker, D.A., and Armstrong, J.D. (2011). Simple Neurite Tracer: open source software for reconstruction, visualization and analysis of neuronal processes. Bioinformatics *27*, 2453–2454.

Van Der Loos, H. (1976). Barreloids in mouse somatosensory thalamus. Neurosci. Lett. *2*, 1–6.

Lopresti, P. (2002). Regulation and differential expression of tau mRNA isoforms as oligodendrocytes mature in vivo: Implications for myelination. Glia *37*, 250–257.

Lopresti, P., Szuchet, S., Papasozomenos, S.C., Zinkowski, R.P., and Binder, L.I. (1995). Functional implications for the microtubule-associated protein tau: Localization in oligodendrocytes. Proc. Natl. Acad. Sci. U. S. A. *92*, 10369–10373.

Lőrincz, M.L., Gunner, D., Bao, Y., Connelly, W.M., Isaac, J.T.R., Hughes, S.W., and Crunelli, V. (2015). A distinct class of slow (~0.2-2 Hz) intrinsically bursting layer 5 pyramidal neurons determines UP/DOWN state dynamics in the neocortex. J. Neurosci. *35*, 5442–5458.

Lovestone, S., and McLoughlin, D.M. (2002). Protein aggregates and dementia: Is there a common toxicity? J. Neurol. Neurosurg. Psychiatry *72*, 152–161.

Lu, S.M., and Lin, R.C.S. (1993). Thalamic afferents of the rat barrel cortex: A light- and electron-microscopic study using phaseolus vulgaris leucoagglutinin as an anterograde tracer. Somatosens. Mot. Res. *10*, 1–16.

Lu, W., Shi, Y., Jackson, A.C., Bjorgan, K., During, M.J., Sprengel, R., Seeburg, P.H., and Nicoll, R.A. (2009). Subunit Composition of Synaptic AMPA Receptors Revealed by a Single-Cell Genetic Approach. Neuron *62*, 254–268.

Lübke, J., and Feldmeyer, D. (2007). Excitatory signal flow and connectivity in a cortical column: focus on barrel cortex. Brain Struct. Funct. *212*, 3–17.

Lübke, J., Egger, V., Sakmann, B., and Feldmeyer, D. (2000). Columnar organization of dendrites and axons of single and synaptically coupled excitatory spiny neurons in layer 4 of the rat barrel cortex. J. Neurosci. *20*, 5300–5311.

Luebke, J.I., Medalla, M., Amatrudo, J.M., Weaver, C.M., Crimins, J.L., Hunt, B., Hof, P.R., and Peters, A. (2015). Age-related changes to layer 3 pyramidal cells in the rhesus monkey visual cortex. Cereb. Cortex *25*, 1454–1468.

MacDonald, J.F., Miljkovic, Z., and Pennefather (1987). Use-dependent block of excitatory amino acid currents in cultured neurons by ketamine. J. Neurophysiol. *58*, 251–266.

MacDonald, J.F., Jackson, M.F., and Beazely, M.A. (2006). Hippocampal long-term synaptic plasticity and signal amplification of NMDA receptors. Crit. Rev. Neurobiol. *18*, 71–84.

Maeda, S., Djukic, B., Taneja, P., Yu, G., Lo, I., Davis, A., Craft, R., Guo, W., Wang,

X., Kim, D., et al. (2016). Expression of A152T human tau causes age-dependent neuronal dysfunction and loss in transgenic mice. EMBO Rep. *17*, 530–551.

Mahanty, N.K., and Sah, P. (1998). Calcium-permeable AMPA receptors mediate long-term potentiation in interneurons in the amygdala. Nature *394*, 683–687.

Mandelkow, E.M., Biernat, J., Drewes, G., Gustke, N., Trinczek, B., and Mandelkow, E. (1995). Tau domains, phosphorylation, and interactions with microtubules. Neurobiol. Aging *16*, 355–362.

Mansour, M., Nagarajan, N., Nehring, R.B., Clements, J.D., and Rosenmund, C. (2001). Heteromeric AMPA receptors assemble with a preferred subunit stoichiometry and spatial arrangement. Neuron *32*, 841–853.

Marcello, E., Epis, R., Saraceno, C., Gardoni, F., Borroni, B., Cattabeni, F., Padovani, A., and di Luca, M. (2012). SAP97-mediated local trafficking is altered in Alzheimer disease patients' hippocampus. Neurobiol. Aging *33*, 422.e1-422.e10.

Margrie, T., Brecht, M., and Sakmann, B. (2002). In vivo, low-resistance, whole-cell recordings from neurons in the anaesthetized and awake mammalian brain. Pflügers Arch. Eur. J. Physiol. *444*, 491–498.

Margrie, T.W., Meyer, A.H., Caputi, A., Monyer, H., Hasan, M.T., Schaefer, A.T., Denk, W., and Brecht, M. (2003). Targeted Whole-Cell Recordings in the Mammalian Brain In Vivo. Neuron *39*, 911–918.

Marinković, P., Blumenstock, S., Goltstein, P.M., Korzhova, V., Peters, F., Knebl, A., and Herms, J. (2019). In vivo imaging reveals reduced activity of neuronal circuits in a mouse tauopathy model. Brain *142*, 1051–1062.

Markram, H., Muller, E., Ramaswamy, S., Reimann, M.W., Abdellah, M., Sanchez, C.A., Ailamaki, A., Alonso-Nanclares, L., Antille, N., Arsever, S., et al. (2015). Reconstruction and Simulation of Neocortical Microcircuitry. Cell *163*, 456–492.

Masamoto, K., and Kanno, I. (2012). Anesthesia and the quantitative evaluation of neurovascular coupling. J. Cereb. Blood Flow Metab. *32*, 1233–1247.

Masu, M., Tanabe, Y., Tsuchida, K., Shigemoto, R., and Nakanishi, S. (1991). Sequence and expression of a metabotropic glutamate receptor. Nature *349*, 760–765.

Mazzo, F., Zwart, R., Serratto, G.M., Gardinier, K.M., Porter, W., Reel, J., Maraula, G., and Sher, E. (2016). Reconstitution of synaptic Ion channels from rodent and human brain in Xenopus oocytes: a biochemical and electrophysiological characterization. J. Neurochem. *138*, 384–396.

Mcbain, C.J., and Mayer, M.L. (1994). N-methyl-D-aspartic acid receptor structure and function. Physiol. Rev. *74*, 723–760.

McCullagh, P. (2018). Generalized linear models (Routledge).

McInnes, J., Wierda, K., Snellinx, A., Bounti, L., Wang, Y.C., Stancu, I.C., Apóstolo, N., Gevaert, K., Dewachter, I., Spires-Jones, T.L., et al. (2018). Synaptogyrin-3 Mediates Presynaptic Dysfunction Induced by Tau. Neuron *97*, 823-835.e8.

Meguro, H., Mori, H., Araki, K., Kushiya, E., Kutsuwada, T., Yamazaki, M., Kumanishi, T., Arakawa, M., Sakimura, K., and Mishina, M. (1992). Functional characterization of a heteromeric NMDA receptor channel expressed from cloned cDNAs. Nature *357*, 70–74.

Menkes-Caspi, N., Yamin, H., Kellner, V., Spires-Jones, T.L., Cohen, D., and Stern, E.A. (2015). Pathological tau disrupts ongoing network activity. Neuron *85*, 959–966.

Merino-Serrais, P., Benavides-Piccione, R., Blazquez-Llorca, L., Kastanauskaite, A., Rábano, A., Avila, J., and Defelipe, J. (2013). The influence of phospho-tau on dendritic spines of cortical pyramidal neurons in patients with Alzheimer's disease. Brain *136*, 1913–1928.

Miller, K.D., Pinto, D.J., and Simons, D.J. (2001). Processing in layer 4 of the neocortical circuit: New insights from visual and somatosensory cortex. Curr. Opin. Neurobiol. *11*, 488–497.

Mirabella, G., Battiston, S., and Diamond, M.E. (2001). Integration of multiple-whisker inputs in rat somatosensory cortex. Cereb. Cortex *11*, 164–170.

Miyamoto, T., Stein, L., Thomas, R., Djukic, B., Taneja, P., Knox, J., Vossel, K., and Mucke, L. (2017). Phosphorylation of tau at Y18, but not tau-fyn binding, is required for tau to modulate NMDA receptor-dependent excitotoxicity in primary neuronal culture. Mol. Neurodegener. *12*, 1–19.

Mo, C., Petrof, I., Viaene, A.N., and Sherman, S.M. (2017). Synaptic properties of the

lemniscal and paralemniscal pathways to the mouse somatosensory thalamus. Proc. Natl. Acad. Sci. U. S. A. *114*, E6212–E6221.

Moen, E.L., Fricano-Kugler, C.J., Luikart, B.W., and O'Malley, A.J. (2016). Analyzing Clustered Data: Why and How to Account for Multiple Observations Nested within a Study Participant? PLoS One *11*, e0146721.

Mondragón-Rodríguez, S., Trillaud-Doppia, E., Dudilot, A., Bourgeois, C., Lauzon, M., Leclerc, N., and Boehm, J. (2012). Interaction of endogenous tau protein with synaptic proteins is regulated by N-methyl-D-aspartate receptor-dependent tau phosphorylation. J. Biol. Chem. *287*, 32040–32053.

Montine, T.J., Phelps, C.H., Beach, T.G., Bigio, E.H., Cairns, N.J., Dickson, D.W., Duyckaerts, C., Frosch, M.P., Masliah, E., Mirra, S.S., et al. (2012). National institute on aging-Alzheimer's association guidelines for the neuropathologic assessment of Alzheimer's disease: A practical approach. Acta Neuropathol. *123*, 1–11.

Monyer, H., Sprengel, R., Schoepfer, R., Herb, A., Higuchi, M., Lomeli, H., Burnashev, N., Sakmann, B., and Seeburg, P.H. (1992). Heteromeric NMDA receptors: Molecular and functional distinction of subtypes. Science (80-.). *256*, 1217–1221.

Monyer, H., Burnashev, N., Laurie, D.J., Sakmann, B., and Seeburg, P.H. (1994). Developmental and Regional Expression in the Rat Brain and Functional Properties of Four NMDA Receptors. Neuron *12*, 529–540.

Moore, C.I., and Nelson, S.B. (1998). Spatio-temporal subthreshold receptive fields in the vibrissa representation of rat primary somatosensory cortex. J. Neurophysiol. *80*, 2882–2892.

Moriyoshi, K., Masu, M., Ishii, T., Shigemoto, R., Mizuno, N., and Nakanishi, S. (1991). Molecular cloning and characterization of the rat NMDA receptor. Nature *354*, 31–37.

Mosbacher, J., Schoepfer, R., Monyer, H., Burnashev, N., Seeburg, P.H., and Ruppersberg, J.P. (1994). A molecular determinant for submillisecond desensitization in glutamate receptors. Science (80-.). *266*, 1059–1062.

Mota, S.I., Ferreira, I.L., and Rego, A.C. (2013). Dysfunctional synapse in Alzheimer's disease - A focus on NMDA receptors. Neuropharmacology *76*, 16–26.

Mountcastle, V.B. (1957). Modality and topographic properties of single neurons of

cat’s somatic sensory cortex. J. Neurophysiol. *20*, 408–434.

Mountcastle, V.B. (1997). The columnar organization of the neocortex. Brain *120*, 701–722.

Mullane, K., and Williams, M. (2019). Preclinical Models of Alzheimer’s Disease: Relevance and Translational Validity. Curr. Protoc. Pharmacol. *84*, e57.

Müller, T., Albrecht, D., and Gebhardt, C. (2009). Both NR2A and NR2B subunits of the NMDA receptor are critical for long-term potentiation and long-term depression in the lateral amygdala of horizontal slices of adult mice. Learn. Mem. *16*, 395–405.

Murrell, J., Farlow, M., Ghetti, B., and Benson, M.D. (1991). A mutation in the amyloid precursor protein associated with hereditary Alzheimer’s disease. Science (80-.). *254*, 97–99.

Nagy, A., and Delgado-Escueta, A. V. (1984). Rapid Preparation of Synaptosomes from Mammalian Brain Using Nontoxic Isoosmotic Gradient Material (Percoll). J. Neurochem. *43*, 1114–1123.

Narayanan, R.T., Udvary, D., and Oberlaender, M. (2017). Cell Type-Specific Structural Organization of the Six Layers in Rat Barrel Cortex. Front. Neuroanat. *11*, 91.

Naundorf, B., Wolf, F., and Volgushev, M. (2006). Unique features of action potential initiation in cortical neurons. Nature *440*, 1060–1063.

Nelder, J.A., and Wedderburn, R.W.M. (1972). Generalized linear models. J. R. Stat. Soc. Ser. A *135*, 370–384.

Neske, G.T. (2016). The slow oscillation in cortical and thalamic networks: Mechanisms and functions. Front. Neural Circuits *9*, 88.

Nilsen, L.H., Rae, C., Ittner, L.M., Götz, J., and Sonnewald, U. (2013). Glutamate metabolism is impaired in transgenic mice with tau hyperphosphorylation. J. Cereb. Blood Flow Metab. *33*, 684–691.

Nishimune, A., Isaac, J.T.R., Molnar, E., Noel, J., Nash, S.R., Tagaya, M., Collingridge, G.L., Nakanishi, S., and Henley, J.M. (1998). NSF binding to GluR2 regulates synaptic transmission. Neuron *21*, 87–97.

Niswender, C.M., and Conn, P.J. (2010). Metabotropic Glutamate Receptors: Physiology, Pharmacology, and Disease. Annu. Rev. Pharmacol. Toxicol. *50*, 295–322.

Noel, J., Ralph, G.S., Pickard, L., Williams, J., Molnar, E., Uney, J.B., Collingridge, G.L., and Henley, J.M. (1999). Surface expression of AMPA receptors in hippocampal neurons is regulated by an NSF-dependent mechanism. Neuron *23*, 365–376.

O'Brien, J.T., and Thomas, A. (2015). Vascular dementia. Lancet *386*, 1698–1706.

O'Rourke, N.A., Weiler, N.C., Micheva, K.D., and Smith, S.J. (2012). Deep molecular diversity of mammalian synapses: Why it matters and how to measure it. Nat. Rev. Neurosci. *13*, 365–379.

Oberlaender, M., De Kock, C.P.J., Bruno, R.M., Ramirez, A., Meyer, H.S., Dercksen, V.J., Helmstaedter, M., and Sakmann, B. (2012). Cell type-specific three-dimensional structure of thalamocortical circuits in a column of rat vibrissal cortex. Cereb. Cortex *22*, 2375–2391.

Okun, M., Naim, A., and Lampl, I. (2010). The Subthreshold Relation between Cortical Local Field Potential and Neuronal Firing Unveiled by Intracellular Recordings in Awake Rats. J. Neurosci. *30*, 4440–4448.

Onos, K.D., Sukoff Rizzo, S.J., Howell, G.R., and Sasner, M. (2016). Toward more predictive genetic mouse models of Alzheimer's disease. Brain Res. Bull. *122*, 1–11.

Opazo, P., Labrecque, S., Tigaret, C.M., Frouin, A., Wiseman, P.W., De Koninck, P., and Choquet, D. (2010). CaMKII triggers the diffusional trapping of surface AMPARs through phosphorylation of stargazin. Neuron *67*, 239–252.

Orr, M.E., Sullivan, A.C., and Frost, B. (2017). A Brief Overview of Tauopathy: Causes, Consequences, and Therapeutic Strategies. Trends Pharmacol. Sci. *38*, 637–648.

Owens, D.F., and Kriegstein, A.R. (2002). Is there more to GABA than synaptic inhibition? Nat. Rev. Neurosci. *3*, 715–727.

Pachernegg, S., Strutz-Seebohm, N., and Hollmann, M. (2012). GluN3 subunit-containing NMDA receptors: Not just one-trick ponies. Trends Neurosci. *35*, 240–249.

Pagliardini, S., Greer, J.J., Funk, G.D., and Dickson, C.T. (2012). State-dependent

modulation of breathing in urethane-anesthetized rats. J. Neurosci. *32*, 11259–11270.

Pagliardini, S., Gosgnach, S., and Dickson, C.T. (2013). Spontaneous Sleep-Like Brain State Alternations and Breathing Characteristics in Urethane Anesthetized Mice. PLoS One *8*, e70411.

Palacio, S., Chevaleyre, V., Brann, D.H., Murray, K.D., Piskorowski, R.A., and Trimmer, J.S. (2017). Neuronal Excitability Heterogeneity in Kv2 Channel Expression Shapes Action Potential Characteristics and Firing Patterns in CA1 versus CA2 Hippocampal Pyramidal Neurons. Eneuro *4*.

Pallas-Bazarra, N., Draffin, J., Cuadros, R., Antonio Esteban, J., and Avila, J. (2019). Tau is required for the function of extrasynaptic NMDA receptors. Sci. Rep. *9*, 9116.

Palmer, L.M., Shai, A.S., Reeve, J.E., Anderson, H.L., Paulsen, O., and Larkum, M.E. (2014). NMDA spikes enhance action potential generation during sensory input. Nat. Neurosci. *17*, 383–390.

Palop, J.J., Chin, J., Roberson, E.D., Wang, J., Thwin, M.T., Bien-Ly, N., Yoo, J., Ho, K.O., Yu, G.Q., Kreitzer, A., et al. (2007). Aberrant Excitatory Neuronal Activity and Compensatory Remodeling of Inhibitory Hippocampal Circuits in Mouse Models of Alzheimer's Disease. Neuron *55*, 697–711.

Paxinos, G., and Franklin, K.B.J. (2001). The Mouse Brain in Stereotaxic Coordinates (Academic Press).

Pelkey, K.A., Barksdale, E., Craig, M.T., Yuan, X., Sukumaran, M., Vargish, G.A., Mitchell, R.M., Wyeth, M.S., Petralia, R.S., Chittajallu, R., et al. (2015). Pentraxins coordinate excitatory synapse maturation and circuit integration of parvalbumin interneurons. Neuron *85*, 1257–1272.

Penfield, W., and Rasmussen, T. (1950). The cerebral cortex of man; a clinical study of localization of function. (Oxford, England: Macmillan).

Perez-Nievas, B.G., Stein, T.D., Tai, H.-C., Dols-Icardo, O., Scotton, T.C., Barroeta-Espar, I., Fernandez-Carballo, L., Lopez De Munain, E., Perez, J., Marquie, M., et al. (2013). Dissecting phenotypic traits linked to human resilience to Alzheimer's pathology. BRAIN 2510–2526.

Perneczky, R., Kempermann, G., Korczyn, A.D., Matthews, F.E., Ikram, M.A.,

Scarmeas, N., Chetelat, G., Stern, Y., and Ewers, M. (2019). Translational research on reserve against neurodegenerative disease: Consensus report of the International Conference on Cognitive Reserve in the Dementias and the Alzheimer's Association Reserve, Resilience and Protective Factors Professional Interest Ar. BMC Med. *17*, 1–15.

Petersen, C.C.H. (2007). The functional organization of the barrel cortex. Neuron *56*, 339–355.

Petersen, C.C.H., G Hahn, T.T., Mehta, M., Grinvald, A., and Sakmann, B. (2003). Interaction of sensory responses with spontaneous depolarization in layer 2/3 barrel cortex. PNAS *100*, 13638–13643.

Pierret, T., Lavallee, P., and Deschenes, M. (2000). Parallel streams for the relay of vibrissal information through thalamic barreloids. J. Neurosci. *20*, 7455–7462.

Pinheiro, P., and Mulle, C. (2006). Kainate receptors. Cell Tissue Res. *326*, 457–482.

Pooler, A.M., Phillips, E.C., Lau, D.H.W., Noble, W., and Hanger, D.P. (2013). Physiological release of endogenous tau is stimulated by neuronal activity. EMBO Rep. *14*, 389–394.

Pooler, A.M., Noble, W., and Hanger, D.P. (2014). A role for tau at the synapse in Alzheimer's disease pathogenesis. Neuropharmacology *76*, 1–8.

Poorkaj, P., Bird, T.D., Wijsman, E., Nemens, E., Garruto, R.M., Anderson, L., Andreadis, A., Wiederholt, W.C., Raskind, M., and Schellenberg, G.D. (1998). Tau is a candidate gene for chromosome 17 frontotemporal dementia. Ann. Neurol. *43*, 815–825.

Prince, M.J. (2015). World Alzheimer Report 2015: the global impact of dementia: an analysis of prevalence, incidence, cost and trends (Alzheimer's Disease International).

Prince, M., Bryce, R., Albanese, E., Wimo, A., Ribeiro, W., and Ferri, C.P. (2013). The global prevalence of dementia: A systematic review and metaanalysis. Alzheimer's Dement. *9*, 63-75.e2.

Prince, M., Knapp, M., Guerchet, M., McCrone, P., Prina, M., Comas-Herrera, A., Wittenberg, R., Adelaja, B., Hu, B., King, D., et al. (2014). Dementia UK Second edition - Overview.

Rall, W. (2011). Core Conductor Theory and Cable Properties of Neurons. In Comprehensive Physiology, (Hoboken, NJ, USA: John Wiley & Sons, Inc.), pp. 39–97.

Ramon y Cajal, S. (1911). Histologie du système nerveux de l'homme et des vertébrés. Maloine *2*, 153–173.

Ramsden, M., Kotilinek, L., Forster, C., Paulson, J., Mcgowan, E., Santacruz, K., Guimaraes, A., Yue, M., Lewis, J., Carlson, G., et al. (2005). Age-Dependent Neurofibrillary Tangle Formation, Neuron Loss, and Memory Impairment in a Mouse Model of Human Tauopathy (P301L). J. Neurosci. *25*, 10637–10647.

Randall, A.D., Witton, J., Booth, C., Hynes-Allen, A., and Brown, J.T. (2010). The functional neurophysiology of the amyloid precursor protein (APP) processing pathway. Neuropharmacology *59*, 243–267.

Randall, A.D., Booth, C., and Brown, J.T. (2012). Age-related changes to Na+ channel gating contribute to modified intrinsic neuronal excitability. Neurobiol. Aging *33*, 2715–2720.

Ranjbar-Slamloo, Y., and Arabzadeh, E. (2019). Diverse tuning underlies sparse activity in layer 2/3 vibrissal cortex of awake mice. J. Physiol. *597*, 2803–2817.

Rao, V.R., and Finkbeiner, S. (2007). NMDA and AMPA receptors: old channels, new tricks. Trends Neurosci. *30*, 284–291.

Renart, A., De La Rocha, J., Bartho, P., Hollender, L., Parga, N., Reyes, A., and Harris, K.D. (2010). The asynchronous state in cortical circuits. Science (80-.). *327*, 587–590.

Renner, M.C., Albers, E.H., Gutierrez-Castellanos, N., Reinders, N.R., van Huijstee, A.N., Xiong, H., Lodder, T.R., and Kessels, H.W. (2017). Synaptic plasticity through activation of GluA3-containing AMPA-receptors. Elife *6*.

Reyes, A., and Sakmann, B. (1999). Developmental switch in the short-term modification of unitary EPSPs evoked in layer 2/3 and layer 5 pyramidal neurons of rat neocortex. J. Neurosci. *19*, 3827–3835.

Rice, F.L., Mance, A., and Munger, B.L. (1986). A comparative light microscopic analysis of the sensory innervation of the mystacial pad. I. Innervation of vibrissal follicle-sinus complexes. J. Comp. Neurol. *252*, 154–174.

Ridler, T., Witton, J., Phillips, K.G., Randall, A.D., and Brown, J.T. (2019). Impaired speed encoding is associated with reduced grid cell periodicity in a mouse model of tauopathy. BioRxiv 595652.

De Robertis, E., Pellegrino De Iraldi, A., Rodriguez, G., and Gomez, C.J. (1961). On the isolation of nerve endings and synaptic vesicles. J. Biophys. Biochem. Cytol. *9*, 229–235.

Rocher, A.B., Crimins, J.L., Amatrudo, J.M., Kinson, M.S., Todd-Brown, M.A., Lewis, J., and Luebke, J.I. (2010). Structural and functional changes in tau mutant mice neurons are not linked to the presence of NFTs. Exp. Neurol. *223*, 385–393.

Rockel, A.J., Hiorns, R.W., and Powell, T.P.S. (1980). The basic uniformity in structure of the neocortex. Brain *103*, 221–244.

Rodríguez-Moreno, A., Kohl, M.M., Reeve, J.E., Eaton, T.R., Collins, H.A., Anderson, H.L., and Paulsen, O. (2011). Presynaptic induction and expression of timing-dependent long-term depression demonstrated by compartment-specific photorelease of a use-dependent NMDA receptor antagonist. J. Neurosci. *31*, 8564–8569.

Rothman, S.M., and Olney, J.W. (1986). Glutamate and the pathophysiology of hypoxic–ischemic brain damage. Ann. Neurol. *19*, 105–111.

Sachdev, R.N.S., Ebner, F.F., and Wilson, C.J. (2004). Effect of Subthreshold Up and Down States on the Whisker-Evoked Response in Somatosensory Cortex. J Neurophysiol *92*, 3511–3521.

Sahara, N., Murayama, M., Higuchi, M., Suhara, T., and Takashima, A. (2014). Biochemical distribution of tau protein in synaptosomal fraction of transgenic mice expressing human p301l tau. Front. Neurol. *5*.

Saito, T., Matsuba, Y., Mihira, N., Takano, J., Nilsson, P., Itohara, S., Iwata, N., and Saido, T.C. (2014). Single App knock-in mouse models of Alzheimer's disease. Nat. Neurosci. *17*, 661–663.

Saito, T., Mihira, N., Matsuba, Y., Sasaguri, H., Hashimoto, S., Narasimhan, S., Zhang, B., Murayama, S., Higuchi, M., Lee, V.M.Y., et al. (2019). Humanization of the entire murine Mapt gene provides a murine model of pathological human tau propagation. J. Biol. Chem. *294*, 12754–12765.

Sanchez-Vives, M. V., and McCormick, D.A. (2000). Cellular and network mechanisms of rhytmic recurrent activity in neocortex. Nat. Neurosci. *3*, 1027–1034.

Sans, N., Vissel, B., Petralia, R.S., Wang, Y.X., Chang, K., Royle, G.A., Wang, C.Y., O'Gorman, S., Heinemann, S.F., and Wenthold, R.J. (2003). Aberrant Formation of Glutamate Receptor Complexes in Hippocampal Neurons of Mice Lacking the GluR2 AMPA Receptor Subunit. J. Neurosci. *23*, 9367–9373.

SantaCruz, K., Lewis, J., Spires, T., Paulson, J., Kotilinek, L., Ingelsson, M., Guimaraes, A., DeTure, M., Ramsden, M., McGowan, E., et al. (2005). Tau Suppression in a Neurodegenerative Mouse Model Improves Memory Function. Science (80-.). *309*, 476–481.

Scannevin, R.H., and Huganir, R.L. (2000). Postsynaptic organisation and regulation of excitatory synapses. Nat. Rev. Neurosci. *1*, 133–141.

Sceniak, M.P., and Maciver, M.B. (2006). Cellular Actions of Urethane on Rat Visual Cortical Neurons In Vitro. J Neurophysiol *95*, 3865–3874.

Schaler, A.W., Runyan, A.M., Fowler, S.L., Figueroa, H.Y., Shioda, S., Santa-Maria, I., Duff, K.E., and Myeku, N. (2020). GPCR-mediated clearance of tau in post-synaptic compartments attenuates tau pathology in vivo. BioRxiv 2020.01.21.914135.

Scheff, S.W., Price, D.A., Schmitt, F.A., and Mufson, E.J. (2006). Hippocampal synaptic loss in early Alzheimer's disease and mild cognitive impairment. Neurobiol. Aging *27*, 1372–1384.

Scheff, S.W., Price, D.A., Schmitt, F.A., Dekosky, S.T., and Mufson, E.J. (2007). Synaptic alterations in CA1 in mild Alzheimer disease and mild cognitive impairment. Neurology *68*, 1501–1508.

Schindelin, J., Arganda-Carreras, I., Frise, E., Kaynig, V., Longair, M., Pietzsch, T., Preibisch, S., Rueden, C., Saalfeld, S., Schmid, B., et al. (2012). Fiji: an open-source platform for biological-image analysis. Nat. Methods *9*, 676–682.

Schnitzler, A., and Gross, J. (2005). Normal and pathological oscillatory communication in the brain. Nat. Rev. Neurosci. *6*, 285–296.

Schramm, A.E., Marinazzo, D., Gener, T., and Graham, L.J. (2014). The touch and zap method for in Vivo whole-cell patch recording of intrinsic and visual responses of

cortical neurons and glial cells. PLoS One *9*, 97310.

Schweizer, F.E., and Ryan, T.A. (2006). The synaptic vesicle: cycle of exocytosis and endocytosis. Curr. Opin. Neurobiol. *16*, 298–304.

Serrano-Pozo, A., Frosch, M.P., Masliah, E., and Hyman, B.T. (2011). Neuropathological alterations in Alzheimer disease. Cold Spring Harb. Perspect. Med. *1*.

Sheroziya, M., and Timofeev, I. (2014). Global intracellular slow-wave dynamics of the thalamocortical system. J. Neurosci. *34*, 8875–8893.

Shimegi, S., Ichikawa, T., Akasaki, T., and Sato, H. (1999). Temporal characteristics of response integration evoked by multiple whisker stimulations in the barrel cortex of rats. J. Neurosci. *19*, 10164–10175.

Shimojo, M., Takuwa, H., Takado, Y., Tokunaga, M., Tsukamoto, S., Minatohara, K., Ono, M., Seki, C., Maeda, J., Urushihata, T., et al. (2020). Selective disruption of inhibitory synapses leading to neuronal hyperexcitability at an early stage of tau pathogenesis in a mouse model. J. Neurosci. *40*, 3491–3501.

Sibson, N.R., Dhankhar, A., Mason, G.F., Rothman, D.L., Behar, K.L., and Shulman, R.G. (1998). Stoichiometric coupling of brain glucose metabolism and glutamatergic neuronal activity. Proc. Natl. Acad. Sci. U. S. A. *95*, 316–321.

Simons, D.J. (1983). Multi-whisker stimulation and its effects on vibrissa units in rat Sml barrel cortex. Brain Res. *276*, 178–182.

Singer, W., and Gray, C.M. (1995). Visual Feature Integration and the Temporal Correlation Hypothesis. Annu. Rev. Neurosci. *18*, 555–586.

Smith, S.L., Smith, I.T., Branco, T., and Häusser, M. (2013). Dendritic spikes enhance stimulus selectivity in cortical neurons in vivo. Nature *503*, 115–120.

Sohn, P.D., Tracy, T.E., Son, H.I., Zhou, Y., Leite, R.E.P., Miller, B.L., Seeley, W.W., Grinberg, L.T., and Gan, L. (2016). Acetylated tau destabilizes the cytoskeleton in the axon initial segment and is mislocalized to the somatodendritic compartment. Mol. Neurodegener. *11*, 1–13.

Spillantini, M.G., Murrell, J.R., Goedert, M., Farlow, M.R., Klug, A., and Ghetti, B.

(1998). Mutation in the tau gene in familial multiple system tauopathy with presenile dementia. Proc. Natl. Acad. Sci. U. S. A. *95*, 7737–7741.

Spires-Jones, T.L., De Calignon, A., Matsui, T., Zehr, C., Pitstick, R., Wu, H.-Y., Osetek, J.D., Jones, P.B., Bacskai, B.J., Feany, M.B., et al. (2008). In Vivo Imaging Reveals Dissociation between Caspase Activation and Acute Neuronal Death in Tangle-Bearing Neurons. J. Neurosci. *28*, 862–867.

Spires-Jones, T.L., Stoothoff, W.H., de Calignon, A., Jones, P.B., and Hyman, B.T. (2009). Tau pathophysiology in neurodegeneration: a tangled issue. Trends Neurosci. *32*, 150–159.

Spires-Jones, T.L., Kopeikina, K.J., Koffie, R.M., De Calignon, A., and Hyman, B.T. (2011). Are tangles as toxic as they look? J. Mol. Neurosci. *45*, 438–444.

Spires, T.L., Orne, J.D., Santacruz, K., Pitstick, R., Carlson, G.A., Ashe, K.H., and Hyman, B.T. (2006). Region-specific Dissociation of Neuronal Loss and Neurofibrillary Pathology in a Mouse Model of Tauopathy. Am. J. Pathol. *168*, 1598–1607.

Stancu, I.C., Vasconcelos, B., Ris, L., Wang, P., Villers, A., Peeraer, E., Buist, A., Terwel, D., Baatsen, P., Oyelami, T., et al. (2015). Templated misfolding of Tau by prion-like seeding along neuronal connections impairs neuronal network function and associated behavioral outcomes in Tau transgenic mice. Acta Neuropathol. *129*, 875–894.

Standaert, D.G., Landwehrmeyer, G.B., Kerner, J.A., Penney, J.B., and Young, A.B. (1996). Expression of NMDAR2D glutamate receptor subunit mRNA in neurochemically identified interneurons in the rat neostriatum, neocortex and hippocampus. Brain Res. Mol. Brain Res. *42*, 89–102.

Steriade, M., Nuiiez, A., and Amzica, F. (1993a). A Novel Slow (<1 Hz) Oscillation of Neocortical Neurons in viva: Depolarizing and Hyperpolarizing Components. J. Neurosci. *73*, 3252–3285.

Steriade, M., Nunez, A., and Amzica, F. (1993b). Intracellular analysis of relations between the slow (<1 Hz) neocortical oscillation and other sleep rhythms of the electroencephalogram. J. Neurosci. *13*, 3266–3283.

Steriade, M., Nunez, A., and Amzica, F. (1993c). A novel slow (< 1 Hz) oscillation of

neocortical neurons in vivo: Depolarizing and hyperpolarizing components. J. Neurosci. *13*, 3252–3265.

Stern, Y. (2012). Cognitive reserve in ageing and Alzheimer's disease. Lancet Neurol. *11*, 1006–1012.

Stern, E.A., Kincaid, A.E., and Wilson, C.J. (1997). Spontaneous Subthreshold Membrane Potential Fluctuations and Action Potential Variability of Rat Corticostriatal and Striatal Neurons In Vivo. J. Neurophysiol. *77*, 1697–1715.

Sucher, N.J., Akbarian, S., Chi, C.L., Leclerc, C.L., Awobuluyi, M., Deitcher, D.L., Wu, M.K., Yuan, J.P., Jones, E.G., and Lipton, S.A. (1995). Developmental and regional expression pattern of a novel NMDA receptor- like subunit (NMDAR-L) in the rodent brain. J. Neurosci. *15*, 6509–6520.

Suzuki, M., and Kimura, T. (2017). Microtubule-associated protein tau contributes to intra-dendritic trafficking of AMPA receptors in multiple. Neurosci. Lett. *653*, 276–282.

Sydow, A., Van Der Jeugd, A., Zheng, F., Ahmed, T., Balschun, D., Petrova, O., Drexler, D., Zhou, L., Rune, G., Mandelkow, E.E.-M.M., et al. (2011). Tau-Induced Defects in Synaptic Plasticity, Learning, and Memory Are Reversible in Transgenic Mice after Switching Off the Toxic Tau Mutant. J. Neurosci. *31*.

Tai, H.C., Wang, B.Y., Serrano-Pozo, A., Frosch, M.P., Spires-Jones, T.L., and Hyman, B.T. (2014). Frequent and symmetric deposition of misfolded tau oligomers within presynaptic and postsynaptic terminals in Alzheimer's disease. Acta Neuropathol. Commun. *2*, 146.

Takahashi, N., Oertner, T.G., Hegemann, P., and Larkum, M.E. (2016). Active cortical dendrites modulate perception. Science (80-.). *354*, 1587–1590.

Tamagnini, F., Walsh, D.A., Brown, J.T., Bondulich, M.K., Hanger, D.P., and Randall, A.D. (2017). Hippocampal neurophysiology is modified by a disease-associated C-terminal fragment of tau protein. Neurobiol. Aging *60*, 44–56.

Tanzi, R.E., and Bertram, L. (2005). Twenty years of the Alzheimer's disease amyloid hypothesis: A genetic perspective. Cell *120*, 545–555.

Tenreiro, P., Rebelo, S., Martins, F., Santos, M., Coelho, E.D., Almeida, M., Alves de Matos, A.P., and da Cruz e Silva, O.A.B. (2017). Comparison of simple sucrose and

percoll based methodologies for synaptosome enrichment. Anal. Biochem. *517*, 1–8.

Terashima, A., Suh, Y.H., and Isaac, J.T.R. (2019). The AMPA Receptor Subunit GluA1 is Required for CA1 Hippocampal Long-Term Potentiation but is not Essential for Synaptic Transmission. Neurochem. Res. *44*, 549–561.

Teravskis, P.J., Oxnard, B.R., Miller, E.C., Kemper, L., Ashe, K.H., and Liao, D. (2019). Phosphorylation in two discrete tau domains regulates a stepwise process leading to postsynaptic dysfunction. J. Physiol. JP277459.

Thompson, C.L., Drewery, D.L., Atkins, H.D., Stephenson, F.A., and Chazot, P.L. (2000). Immunohistochemical localization of N-methyl-D-aspartate receptor NR1, NR2A, NR2B and NR2C/D subunits in the adult mammalian cerebellum. Neurosci. Lett. *283*, 85–88.

Timofeev, I., Grenier, F., Bazhenov, M., Sejnowski, T.J., and Steriade, M. (2000). Origin of slow cortical oscillations in deafferented cortical slabs. Cereb. Cortex *10*, 1185–1199.

Tomita, S., Chen, L., Kawasaki, Y., Petralia, R.S., Wenthold, R.J., Nicoll, R.A., and Bredt, D.S. (2003). Functional studies and distribution define a family of transmembrane AMPA receptor regulatory proteins. J. Cell Biol. *161*, 805–816.

Tovar, K.R., and Westbrook, G.L. (1999). The incorporation of NMDA receptors with a distinct subunit composition at nascent hippocampal synapses in vitro. J. Neurosci. *19*, 4180–4188.

Tovar, K.R., and Westbrook, G.L. (2002). Mobile NMDA receptors at hippocampal synapses. Neuron *34*, 255–264.

Tozzi, A., Sclip, A., Tantucci, M., de Iure, A., Ghiglieri, V., Costa, C., Di Filippo, M., Borsello, T., and Calabresi, P. (2015). Region- and age-dependent reductions of hippocampal long-term potentiation and NMDA to AMPA ratio in a genetic model of Alzheimer's disease. Neurobiol. Aging *36*, 123–133.

Trachtenberg, J.T., Chen, B.E., Knott, G.W., Feng, G., Sanes, J.R., Welker, E., and Svoboda, K. (2002). Long-term in vivo imaging of experience-dependent synaptic plasticity in adult cortex. Nature *420*, 788–794.

Tracy, T.E., and Gan, L. (2018). Tau-mediated synaptic and neuronal dysfunction in

neurodegenerative disease. Curr. Opin. Neurobiol. *51*, 134–138.

Traynelis, S.F., Wollmuth, L.P., Mcbain, C.J., Menniti, F.S., Vance, K.M., Ogden, K.K., Hansen, K.B., Yuan, H., Myers, S.J., and Dingledine, R. (2010). Glutamate Receptor Ion Channels: Structure, Regulation, and Function. Pharmacol. Rev. *62*, 405–496.

Tristan, C., Shahani, N., Sedlak, T.W., and Sawa, A. (2011). The diverse functions of GAPDH: Views from different subcellular compartments. Cell. Signal. *23*, 317–323.

Tsuno, Y., Chapman, G.W., and Hasselmo, M.E. (2015). Rebound spiking properties of mouse medial entorhinal cortex neurons *in vivo*. Eur. J. Neurosci. *42*, 2974–2984.

Turrigiano, G.G. (2008). The Self-Tuning Neuron: Synaptic Scaling of Excitatory Synapses. Cell *135*, 422–435.

Valbuena, S., and Lerma, J. (2020). Kainate Receptors, Homeostatic Gatekeepers of Synaptic Plasticity. Neuroscience.

Veinante, P., and Deschênes, M. (1999). Single- and multi-whisker channels in the ascending projections from the principal trigeminal nucleus in the rat. J. Neurosci. *19*, 5085–5095.

Ventura, R., and Harris, K.M. (1999). Three-dimensional relationships between hippocampal synapses and astrocytes. J. Neurosci. *19*, 6897–6906.

Vercelletto, M., Boutoleau-Bretonnière, C., Volteau, C., Puel, M., Auriacombe, S., Sarazin, M., Michel, B.F., Couratier, P., Thomas-Antérion, C., Verpillat, P., et al. (2011). Memantine in behavioral variant frontotemporal dementia: Negative results. J. Alzheimer's Dis. *23*, 749–759.

Verkhratsky, A., and Kirchhoff, F. (2007). Glutamate-mediated neuronal-glial transmission. J. Anat. *210*, 651–660.

Vicini, S., Wang, J.F., Li, J.H., Zhu, W.J., Wang, Y.H., Luo, J.H., Wolfe, B.B., and Grayson, D.R. (1998). Functional and Pharmacological Differences Between Recombinant N -Methyl- d -Aspartate Receptors. J. Neurophysiol. *79*, 555–566.

Villemagne, V.L., Burnham, S., Bourgeat, P., Brown, B., Ellis, K.A., Salvado, O., Szoeke, C., Macaulay, S.L., Martins, R., Maruff, P., et al. (2013). Amyloid β deposition, neurodegeneration, and cognitive decline in sporadic Alzheimer's disease: A

prospective cohort study. Lancet Neurol. *12*, 357–367.

Vogel, J.W., Iturria-Medina, Y., Strandberg, O.T., Smith, R., Levitis, E., Evans, A.C., and Hansson, O. (2020). Spread of pathological tau proteins through communicating neurons in human Alzheimer's disease. Nat. Commun. *11*, 2612.

Walker, Z., Possin, K.L., Boeve, B.F., and Aarsland, D. (2015). Lewy body dementias. Lancet *386*, 1683–1697.

Wang, R., and Reddy, P.H. (2017). Role of Glutamate and NMDA Receptors in Alzheimer's Disease. J. Alzheimer's Dis. *57*, 1041–1048.

Wang, J.-Z., Xia, Y.-Y., Grundke-Iqbal, I., Iqbal, K., Vingtdeux, V., Davies, P., Dickson, D.W., Marambaud, P., Pritchard, S.M., Dolan, P.J., et al. (2011). Tau in Alzheimer disease and related tauopathies. Front. Neurol. *4*, 122.

Wang, X., Smith, K., Pearson, M., Hughes, A., Cosden, M.L., Marcus, J., Hess, J.F., Savage, M.J., Rosahl, T., Smith, S.M., et al. (2018). Early intervention of tau pathology prevents behavioral changes in the rTg4510 mouse model of tauopathy. PLoS One *13*, e0195486.

Wang, Y., Liu, Y.Z., Wang, S.Y., and Wang, Z. (2016). In vivo whole-cell recording with high success rate in anaesthetized and awake mammalian brains. Mol. Brain *9*, 86.

Ward, G., Murray, A., and Wilms, C. (2017). Open-Source Software for Controlling Two-Photon Laser Scanning Microscopes. Micros. Today *25*, 12–17.

Warmus, B.A., Sekar, D.R., McCutchen, E., Schellenberg, G.D., Roberts, R.C., McMahon, L.L., and Roberson, E.D. (2014). Tau-mediated NMDA receptor impairment underlies dysfunction of a selectively vulnerable network in a mouse model of frontotemporal dementia. J. Neurosci. *34*, 16482–16495.

Waters, J., and Helmchen, F. (2006). Background synaptic activity is sparse in neocortex. J. Neurosci. *26*, 8267–8277.

Waters, J., Larkum, M., Sakmann, B., and Helmchen, F. (2003). Supralinear Ca2+ influx into dendritic tufts of layer 2/3 neocortical pyramidal neurons in vitro and in vivo. J. Neurosci. *23*, 8558–8567.

Watt, A.J., Van Rossum, M.C.W., MacLeod, K.M., Nelson, S.B., and Turrigiano, G.G. (2000). Activity coregulates quantal AMPA and NMDA currents at neocortical synapses. Neuron *26*, 659–670.

Weingarten, M.D., Lockwood, A.H., Hwo, S.Y., and Kirschner, M.W. (1975). A protein factor essential for microtubule assembly. Proc. Natl. Acad. Sci. U. S. A. *72*, 1858–1862.

Welker, C. (1971). Microelectrode delineation of fine grain somatotopic organization of SmI cerebral neocortex in albino rat. Brain Res. *26*, 259–275.

Wenthold, R.J., Petralia, R.S., Blahos, J., and Niedzielski, A.S. (1996). Evidence for multiple AMPA receptor complexes in hippocampal CA1/CA2 neurons. J. Neurosci. *16*, 1982–1989.

Whitehead, G., Regan, P., Whitcomb, D.J., and Cho, K. (2017). Ca2+-permeable AMPA receptor: A new perspective on amyloid-beta mediated pathophysiology of Alzheimer's disease. Neuropharmacology *112*, 221–227.

Whittaker, V.P. (1959). The isolation and characterization of acetylcholine-containing particles from brain. Biochem. J. *72*, 694–706.

Whittaker, V.P. (1993). Thirty years of synaptosome research. J. Neurocytol. *22*, 735–742.

Wilhelmsen, K.C., Lynch, T., Pavlou, E., Higgins, M., and Nygaard, T.G. (1994). Localization of disinhibition-dementia-parkinsonism-amyotrophy complex to 17q21-22. Am. J. Hum. Genet. *55*, 1159–1165.

Williams, S.R., and Mitchell, S.J. (2008). Direct measurement of somatic voltage clamp errors in central neurons. Nat. Neurosci. *11*, 790–798.

Williams, M.N., Zahm, D.S., and Jacquin, M.F. (1994). Differential Foci and Synaptic Organization of the Principal and Spinal Trigeminal Projections to the Thalamus in the Rat. Eur. J. Neurosci. *6*, 429–453.

Wilson, C. (2008). Up and down states. Scholarpedia J. *3*, 1410.

Wilson, C.J., and Groves, P.M. (1981). Spontaneous firing patterns of identified spiny neurons in the rat neostriatum. Brain Res. *220*, 67–80.

Wilson, H.R., and Cowan, J.D. (1972). Excitatory and Inhibitory Interactions in Localized Populations of Model Neurons. Biophys. J. *12*, 1–24.

Witman, G.B., Cleveland, D.W., Weingarten, M.D., and Kirschner, M.W. (1976). Tubulin requires tau for growth into microtubule initiating sites. Proc. Natl. Acad. Sci. U. S. A. *73*, 4070–4074.

Witton, J., Staniaszek, L.E., Bartsch, U., Randall, A.D., Jones, M.W., and Brown, J.T. (2016). Disrupted hippocampal sharp-wave ripple-associated spike dynamics in a transgenic mouse model of dementia. J. Physiol. *594*, 4615–4630.

Wolf, J.A., Moyer, J.T., Lazarewicz, M.T., Contreras, D., Benoit-Marand, M., O'donnell, P., and Finkel, L.H. (2005). NMDA/AMPA Ratio Impacts State Transitions and Entrainment to Oscillations in a Computational Model of the Nucleus Accumbens Medium Spiny Projection Neuron. J. Neurosci. *25*, 9080–9095.

Wong, E.H.F., Kemp, J.A., Priestley, T., Knight, A.R., Woodruff, G.N., and Iversen, L.L. (1986). The anticonvulsant MK-801 is a potent N-methyl-D-aspartate antagonist. Proc. Natl. Acad. Sci. U. S. A. *83*, 7104–7108.

Woodward, J.J., and Pava, M.J. (2009). Effects of ethanol on persistent activity and up-States in excitatory and inhibitory neurons in prefrontal cortex. Alcohol. Clin. Exp. Res. *33*, 2134–2140.

Woolsey, T.A., and Van der Loos, H. (1970). The structural organization of layer IV in the somatosensory region (SI) of mouse cerebral cortex. The description of a cortical field composed of discrete cytoarchitectonic units. Brain Res. *17*, 205–242.

Xia, D., Li, C., and Götz, J. (2015). Pseudophosphorylation of Tau at distinct epitopes or the presence of the P301L mutation targets the microtubule-associated protein Tau to dendritic spines. Biochim. Biophys. Acta - Mol. Basis Dis. *1852*, 913–924.

Yasuda, R.P., Ikonomovic, M.D., Sheffield, R., Rubin, R.T., Wolfe, B.B., and Armstrong, D.M. (1995). Reduction of AMPA-selective glutamate receptor subunits in the entorhinal cortex of patients with Alzheimer's disease pathology: a biochemical study. Brain Res. *678*, 161–167.

Yoshiyama, Y., Higuchi, M., Zhang, B., Huang, S.M., Iwata, N., Saido, T.C.C., Maeda, J., Suhara, T., Trojanowski, J.Q., and Lee, V.M.Y. (2007). Synapse Loss and

Microglial Activation Precede Tangles in a P301S Tauopathy Mouse Model. Neuron *53*, 337–351.

Yu, C., Derdikman, D., Haidarliu, S., and Ahissar, E. (2006). Parallel Thalamic Pathways for Whisking and Touch Signals in the Rat. PLoS Biol. *4*, e124.

Yue, M., Hanna, A., Wilson, J., Roder, H., and Janus, C. (2011). Sex difference in pathology and memory decline in rTg4510 mouse model of tauopathy. Neurobiol. Aging *32*, 590–603.

Yuste, R. (2013). Electrical Compartmentalization in Dendritic Spines. Annu. Rev. Neurosci. *36*, 429–449.

Zhang, W., and Bruno, R.M. (2019). High-order thalamic inputs to primary somatosensory cortex are stronger and longer lasting than cortical inputs. Elife *8*.

Zhou, L., McInnes, J., Wierda, K., Holt, M., Herrmann, A.G., Rosemary, J., Wang, Y.-C.C., Swerts, J., Beyens, J., Miskiewicz, K., et al. (2017). Tau association with synaptic vesicles causes presynaptic dysfunction. Nat. Commun. *8*, 1–29.

Zhou, Y., Shi, J., Chu, D., Hu, W., Guan, Z., Gong, C.-X., Iqbal, K., and Liu, F. (2018). Relevance of Phosphorylation and Truncation of Tau to the Etiopathogenesis of Alzheimer's Disease. Front. Aging Neurosci. *10*, 27.

Zhu, J.J., Esteban, J.A., Hayashi, Y., and Malinow, R. (2000). Postnatal synaptic potentiation: Delivery of GluR4-containing AMPA receptors by spontaneous activity. Nat. Neurosci. *3*, 1098–1106.